UC Irvine
UC Irvine Electronic Theses and Dissertations

Title
Synthesis, Characterization and Applications of Plasmonic Gold Nanocrystals for Catalysis

Permalink
https://escholarship.org/uc/item/3jd138bw

Author
Yang, Andy Yue

Publication Date
2022

Peer reviewed|Thesis/dissertation

eScholarship.org Powered by the California Digital Library
University of California

UNIVERSITY OF CALIFORNIA,
IRVINE

SYNTHESIS, CHARACTERIZATION AND APPLICATIONS OF PLASMONIC GOLD NANOCRYSTALS FOR CATALYSIS

DISSERTATION

submitted in partial satisfaction of the requirements
for the degree of

DOCTOR OF PHILOSOPHY

in Chemistry

by

Andy Yue Yang

Dissertation Committee:
Professor Matthew D. Law, Chair
Professor Eric O. Potma
Assistant Professor Joseph P. Patterson

2022

© 2022 Andy Yue Yang

DEDICATION

To

My Mother and Father for your inspiring efforts to encourage and support me

TABLE OF CONTENTS

LIST OF FIGURES

LIST OF TABLES

ACKNOWLEDGEMENTS

I am very grateful for the amazing opportunity to conduct research in Professor Matt Law's group for the past five years. He has truly been one of the most knowledgeable persons I've known. The progress that I've made during my doctorate program could not have been accomplished without the methodologies he's suggested.

I want to give a special thank you to my advancement and defense committee members, Professor Eric Potma, Professor Michael Green, Assistant Professor Joe Patterson, Professor Zuzanna Ziwy, Professor Lorenzo Valdevit, and of course Professor Matt Law.

There have been many colleagues who I've worked with. Among the Law group, I very much appreciated Dr. Yash Gargasya, Dr. Caroline Qian, Dr. Alex Abelson, Dr. Zhongyue Luan, Dr. Christian Engelbrekt, and Logan Brennan. Not only were they brilliant minds, but they were great friends. I am also very grateful for having very supportive neigbors in the Penner and Siwy groups, Dr. Eric Choi, Dr. Josh Zeigler, Dr. Apurva Bhasin, Dr. Ilektra Andoni, Dr. Jake Polster and Vivian Chen. And last but not least, I want to thank Dr. Xingyue Li for helping me getting my first project started. I could not have had the success with my freeze-drying project if not for his help in the early years.

My many days and nights were spent gathering data, but the kind scientists at IMRI made the process much smoother. Thank you Dr. Qiyin Lin, Dr. Xiaofeng Lui, Dr. Mingjie Xu, Dr, Li Xing, Dr. Jiang-Guo Zheng, Dr. Ich Tran, and Dr. Toshihiro Aoki.

I am also very fortunate to have funding during my doctorate career. I could not have achieved this without the assistance of Prof. V. Ara Apkarian, CaSTL and the NSF.

I am forever thankful for our loving relationship with my partner, Jonnie Luong.

VITA

ANDY YUE YANG

EDUCATION

UNIVERSITY OF CALIFORNIA, IRVINE
Doctor of Philosophy in Chemistry 2022
Advisor: Matthew D. Law

UNIVERSITY OF CALIFORNIA, IRVINE
Master of Science in Chemistry 2019

UNIVERSITY OF CALIFORNIA, DAVIS
Bachelor of Science in Chemistry 2013

UNIVERSITY OF CALIFORNIA, DAVIS
Bachelor of Science in Physics 2013

EXPERIENCE

UNIVERSITY OF CALIFORNIA, IRVINE
Graduate Research Assistant 2017-2022
Graduate Teaching Assistant 2017-2022

TRICIDA, SOUTH SAN FRANCISCO
Sr. Research Associate 2014-2017

PUBLICATIONS

A. Y. Yang, L. Brennan, M. Xu, M. Law. *Iridium and Platinum Decorated Gold Nanocrystals for Plasmonic Hydrogen Dissociation.*

A. Y. Yang, M. Law. *Uniform Supported Metal Nanocrystal Catalysts Prepared by Slurry Freeze-Drying*. Chemistry of Materials, **2021**, 33, 256-265

S. A. Mauger, J. Li, Ö. T. Özmen, **A. Y. Yang**, S. Friedrich, M. D. Rail, L. A. Berben, A. J. Moulé. *High Work-function Hole Transport Layers by Self-assembly Using a Fluorinated Additive*. Journal of Materials Chemistry C, **2014**, 2, 115-123

ABSTRACT OF THE DISSERTATION

Synthesis, Characterization and Applications of Plasmonic Gold Nanocrystals for Catalysis

by

Andy Yue Yang

Doctor of Philosophy in Chemistry

University of California, Irvine, 2022

Professor Matthew D. Law, Chair

Plasmonic metals are materials that strongly interact with incident light to produce oscillating waves of electrons. In nanomaterials, these plasmon waves are localized, having brilliant optical absorbance and scattering behavior. Harnessing this light capture can be key to drive many important chemical transformations. However, engineering stable and efficient catalytic material is not simple, due to synthesis challenges, and a lack of understanding of the true dominant mechanism at play.

Heterogeneous plasmonic photocatalysis requires intact noble nanocrystals to maintain a stable localized surface plasmon resonance (LSPR) for solar energy conversion. Even in conventional catalysts, recovering and reusing nanoparticle is crucial to reducing industrial cost and waste as well as improving efficiency. Many studies successfully show supported plasmonic photocatalyze reactions but very few studies utilize precisely colloidally controlled plasmonic nanocrystals on support. Here, 12-14 nm colloidally synthesized Au nanospheres and 55-60 nm triangular nanoprisms are deposited onto Microcrystalline cellulose (MCC) and TiO_2 by lyophilization. Transmission electron microscope (TEM) images show high dispersity of nanocrystals

across the surface of MCC and TiO_2. Sodium citrate additive enhances the dispersity of Au nanosphere (NS) and support material during the lyophilization process. UV-vis spectra of highly dispersed supported material show significant optical resemblance with their respective colloidal Au nanoparticles. Catalytic reduction of 4-Nitrophenol with sodium borohydride was utilized to show surface availability of Au. Additionally, platinum deposited on 5 wt% Au nanospheres on MCC demonstrate surface accessibility to reactive species for adsorption. 4-nitrophenol reduction was used as a model reaction for assessing Au nanocrystal (NC) performance. TiO_2 supported Au showed higher degradation rate than MCC. This result was attributed to diffusion-limited in the zone near Au NCs. Citrate additive improved degradation for Au-TiO_2 but not Au-MCC.

Furthermore, we applied this method of immobilizing nanocrystals on supports to conduct photocatalytic reactions. For revealing mechanisms, we adapted a model reaction to experimentally measure the photoactivity of the catalysts. Moreover, decorating the Au nanocrystals with iridium and platinum showed significant enhanced catalytic activity. We have discovered that there are two dominant regimes of photocatalytic activity. Below ~5-6 W/cm^2, thermal effects govern the rate of reaction while above this intensity, high energy charged carriers dictate the reaction rate. The core-shell design allows great flexibility in engineering light capture wavelength through nanocrystal size and geometry design while driving reactions can be tailored by decorating specific types of active metals to the Au particle. This designer core-shell catalyst can be optimized for many applications.

Lastly, we briefly explored high valued applications for sustainable chemical production. We have investigated Au@Pt colloids for photocatalytic water reduction to hydrogen. Our mass spectrometer was able to detect hydrogen signals in real time upon illumination. Also, this system was applied to nitrogen fixation, a method to synthesize

ammonia from nitrogen and water. The work conducted were only foundational experiments exploring real world applications but will be very important for influencing future work.

SYNTHESIS, CHARACTERIZATION AND APPLICATIONS OF PLASMONIC GOLD NANOCRYSTALS FOR CATALYSIS

Chapter 1. Introduction and Background

1.1. Motivation

Harnessing solar energy has gained considerable attention because of increasing concerns over climate change from carbon emissions. Capturing light efficiently is ultimately the cleanest renewable source to power cities, industries and economies so photovoltaic has been developed enough to be economically viable over fossil fuels in the last decade.[1] Attention has primarily centered towards photovoltaics; however, a growing research area is focusing on solar to chemical conversion including photochemical water splitting and epoxide synthesis.[2,3] Semiconductors have traditionally been considered because of its uses as photovoltaics but high band gap material such as TiO_2 only captures less than 5% of the solar spectrum.[4] Engineering semiconducting material for direct photochemical conversion is very difficult as it must have a low band gap to harness significant portions of the solar spectrum, have correct band positions to efficiently inject hot charge carriers, and be chemically inert to maintain stability and usability.[1] It is unlikely that a single material encompasses all these requirements, so research has been focusing on combining layers of materials each to perform specific roles like photo capture, charge transport, and catalytic adsorption.[5]

Artificial photosynthesis research recently gained major traction as climate change advocates have taken the spotlight. Oil cannot be extracted indefinitely so fuels and chemicals must be synthesized from abundant carbon waste molecules. Hydrogen as fuel and ammonia as fertilizer and an energy storage medium are highly valuable chemicals needed in a renewable society.[6] Carbon dioxide reduction to carbon monoxide and formic acid research powered by plasmonics are well underway with promising results.[7] Plasmonics can be the engine that powers the energy conversion of

water to hydrogen and potentially synthesize ammonia.[8] Metallic nanocrystals are ideal to drive the conversion because it can be colloidally shaped into a variety of geometries and sizes depending on synthetic conditions.[9] Colloidal synthesis is the most efficient method of creating great quantities of plasmonic nanoparticles with absorption spectra capable of harnessing the solar spectrum.

The advantage of gold is its chemical inertness that it remains intact colloidally under illumination and in a wide pH range but, its nobility is its weakness as small molecule precursors rarely interact with its surface. Uniting catalytic semiconductor like TiO_2 with plasmonic nanocrystals allows an efficient and stable system for solar fuels production. Under illumination, coherent oscillation of conduction electrons form for a short lifetime before decaying to an athermal distribution of hot carriers within 100 femtoseconds.[10] This athermal distribution of energetic electrons scatter with electrons within 1 picosecond to Fermi-Dirac thermalized distribution followed by lattice phonons scattering to heat.[10] The short duration makes harnessing energetic carriers difficult for meaningful chemical conversion to occur. Fusing semiconductor interface to plasmonic nanocrystals injects hot electron into the conduction band thereby extending its lifetime giving sufficient time to transfer to electron acceptors.[11]

The fabrication of supported nanocrystals has been dominated by deposition-precipitation and co-precipitation methods.[9] Deposition-precipitation involves depositing noble metal precursor onto suspended metal oxide nanocrystals followed by precipitation on metal oxide surfaces. Co-precipitation starts with soluble salts of metal oxide like magnesium nitrate with noble metal precursor. Reduction the precursor coincides with the precipitation of the support to oxide. Plasmonic nanocrystals form but particle size distribution cannot be controlled as precisely as colloidally synthesized methods which limits spectrum tunability. Plasmonic photochemistry is an expanding topic utilizing nanoparticles to capture light through localized surface plasmon

resonance (LSPR). Commonly used plasmonic nanocrystals are solution synthesized from organometallic or ionic precursor of gold, silver, copper, or aluminum.[12] The different dielectric constants from these metals determine its interacting resonance with electromagnetic waves. For spherical nanocrystals, silver strongly interacts with near UV photons while gold resonates with visible green light.[13] Size and shape change these resonating properties allowing optical absorption to be tuned for maximum solar capture and conversion. While tunability of resonance is trivial, determining the fundamental mechanism of chemical transformation is not. Because of the very brief plasmon lifetime, it makes observing charge transfer to adsorbates extremely challenging. The rapid plasmon decay through scattering with electrons and phonons can increase temperature which increases the reaction rate and interfering with the hot electron injection mechanism.[10] Many high profile publications showed hot electrons to be the dominant method with gas-phase oxygen dissociation and ammonia decomposition.[3,14] Probing the local surface temperature of plasmonic nanoparticles proved to be a challenging task so many argue thermal effects are the dominant rate enhancing mechanism over hot carriers.[15]

1.2. Plasmon Resonance

1.2.1. Surface Plasmon Resonance

The interactions between charged particles and electromagnetic waves can produce unique phenomena. Electrons in metals behave uniquely than insulators because electrons populate the valance band energy states without any stimulations. The delocalized electrons in the crystal lattice of metals can strongly interact with electromagnetic fields, specifically electromagnetic waves. Free electrons oscillate with the coherent incoming plane waves of the electromagnetic oscillations.[16,17] During periods of oscillations, collections of charges, electrons and holes, will bunch and form oscillations on the surface.[16] This is known as surface plasmon polaritons (SPP).

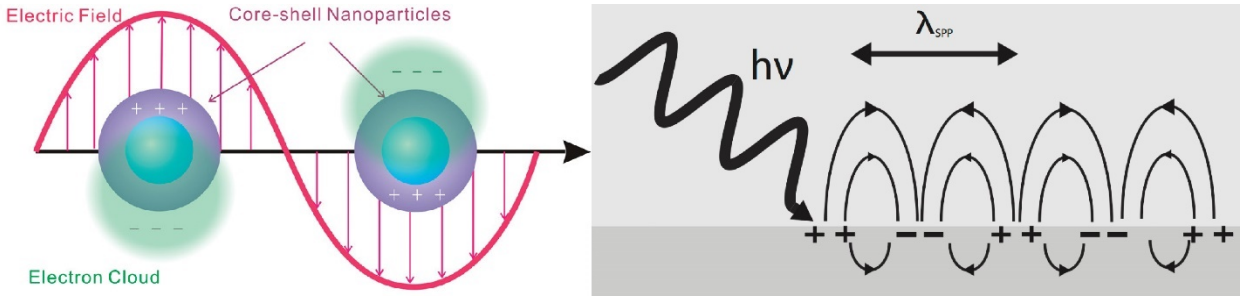

Figure 1.1 Interactions between electromagnetic waves and a metallic medium. Surface plasmon polaritons created by interactions of surface valance electrons with incident oscillating waves (Right). Oscillation of plasmons in nanoparticle metals with oscillating EM waves (Left). (Reprinted with permission from Ref.[18] Copyright 2011 by American Chemical Society.)

The mechanism is illustrated in Figure 1.1. When the interaction between EM waves and bulk metal, SPP forms along the surface. The compressed regions of positive and negative waves are collectively known as plasmons. Incident plasmon propagates along the surface for microns while penetration sharply attenuates by 1/e on the order of 200 nm.[19] When the dimensions of the medium becomes much smaller than the wavelength of the incoming EM wave, localized surface plasmon resonance (LSPR) can develop. Figure 1.1 demonstrates the mechanism of this phenomenon. The oscillation of plasmons will oscillate normal to the direction of wave propagation with the electric field direction. Coupling between the EM wave and plasmon oscillation allows efficient energy transfer to the free electrons.

Maxwell's equations can be used to derive the kinematics of motion for an electron in an electron gas with an external electric field.[20]

$$m\ddot{\mathbf{x}} + m\gamma\dot{\mathbf{x}} = -e\mathbf{E}$$

$\mathbf{E}$ is the time dependent external electric driving field, $\dot{\mathbf{x}}$ and $\ddot{\mathbf{x}}$ represent the first and second derivatives of position with respect to time respectively, m is the effective optical mass of each electron, γ is the collision frequency on the order of 100 THz.[20]

Solving the differential equation for the electron position then combining with the macroscopy polarization gives[20]

$$\mathbf{D} = \omega_0 \left(1 - \frac{\omega_p^2}{\omega^2 + i\gamma\omega}\right)\mathbf{E}$$

The plasma frequency is given by[20]

$$\omega_p^2 = \frac{ne^2}{\varepsilon_0 m}$$

The dielectric function of the free electron gas[20]

$$\varepsilon(\omega) = 1 - \frac{\omega_p^2}{\omega^2 + i\gamma\omega}$$

where the complex dielectric constant has a real and complex component. When w << 1/t, the complex dielectric function overtakes the real component. Given this condition, the absorption coefficient α is given by[20]

$$\alpha = \left(\frac{2\omega_p^2 \tau\omega}{c^2}\right)^{1/2}$$

where τ is the relaxation time and c is the speed of light.

The electrodynamics of plasmonic is well known well enough to simulate the complex intricacies of concentrated electric fields at the nanoscale and attosecond regime.[21] The equations describe a simple damped, driven harmonic oscillator where the incident EM wave drive the oscillation of free electron while the electron-electron scattering decay energy into the bound electrons. A consequence of the damping EM wave creates a concentrated hotspot of intense electric and magnetic fields at the poles for dipolar resonance.[22] If a small organic molecule happens to be in the region of intense EM fields, enhanced Raman scattering will occur.[23] Fleischmann et al. observed the first Raman enhancement using a silver electrode for detecting pyridine adsorption on the surface. The Raman peak intensities observed was much higher than what the analyte concentration allowed. In 1977, Jeanmaire and Van Duyne first proposed an electromagnetic theory to explain the enhancement.[24] This theory has now been

established as the primary mechanism of the surface enhanced Raman spectroscopy (SERS) effect. Because the plasmonic interaction process transpires at the atomic length scale and femtosecond time regime, concrete evidence for this mechanism is difficult to produce. A combination of transmission electron microscopy and finite element analysis simulations can probe the space and time limits.[25]

Smaller particles are able to more effectively absorb the light and convert the energy into plasmons their larger counterparts.[26] A nanoparticle's reach is much larger than it's diameter. Bohren explained that the nanoparticle can act as an antenna that redirects light towards the surface. Field lines show the poynting vector towards the particle.[10] Figure 1.2 bottom left shows the field lines converging towards the surface such that the particle's reach is many times its diameter. For larger particles with diameters on the order of the wavelength of light, a much higher fraction of the energy is reradiated (scattered) as described by Mie theory.[27] Thus only much smaller particles are able to harness the EM energy.

1.2.2. Energy Transfer

Figure 1.2 illustrates energy flow from light absorption to heat conversion. Energy is first transferred into plasmons on the 0-10 femtosecond time-scale.[10,28] This is because the plasmon phase and the incident light must match. Decay of the plasmon is immediate, between 1-100 fs.[10] This is because of the high electron density in the metal increasing the probability of plasmon-electron scattering interactions. The election energy distribution becomes athermal, show in Figure 1.2b. A block (in orange) of electrons suddenly has elevated energy above the fermi energy with corresponding holes (in blue) via the Landau damping process. It is this high energy charged carriers that is hypothesized to drive chemical reactions[29–31] and drive photovoltaics.[32–34] In the next panel, a thermalized distribution of carriers formed from electron-electron scattering of the initial athermal hot carriers. Due to the strength of electron-electron

coupling, much of the redistribution of energy will normalize in less than 1 picosecond. The multiplication of hot carriers increases the number of high energy electrons and holes but will have an average energy less than the athermal population. Between the generation of athermal carriers and thermalization, decay and energy loss will occur through re-emission from electron-hole recombination.[10] In the final phase, thermalized hot carriers couple with lattice phonons from 0.1 to 10 ps timescale resulting in room temperature electrons and a warmer bulk material. The full thermodynamic transformation converts EM radiation into heat in a very efficient and fairly direct process.

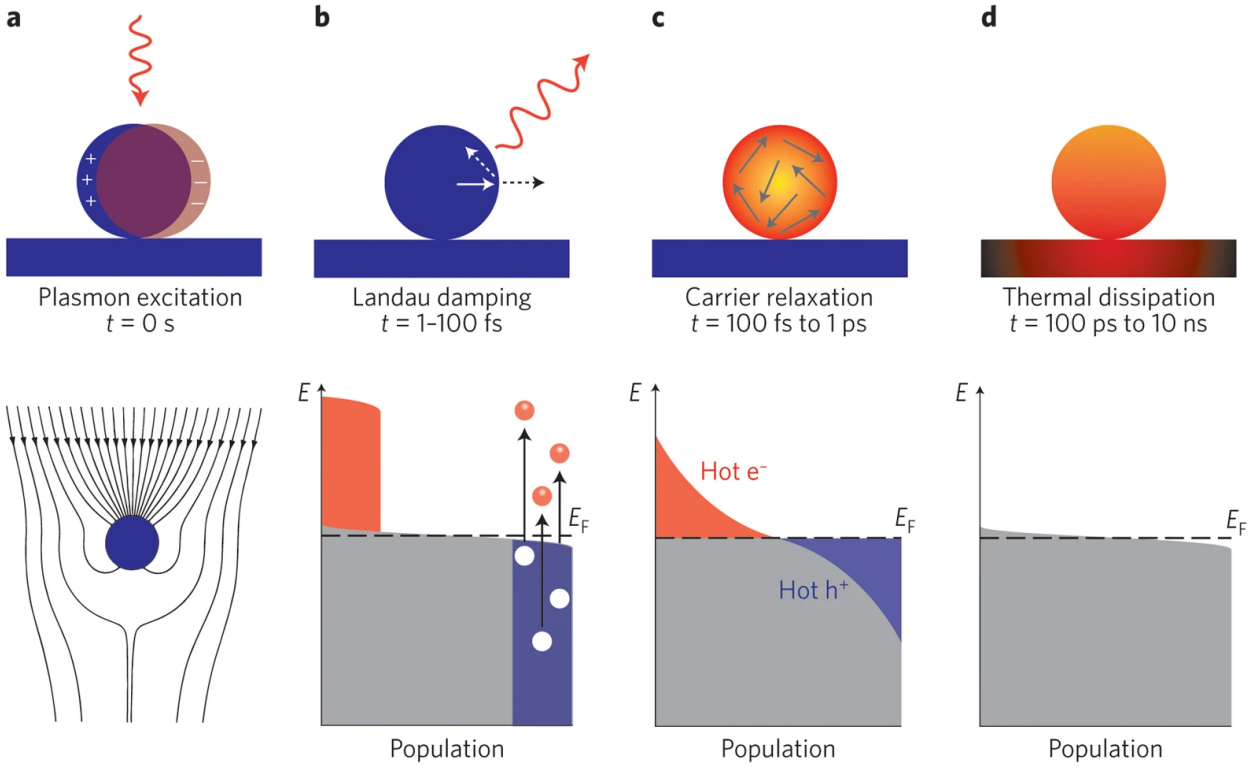

Figure 1.2 Illustration of plasmonic energy flow in a nanoparticle. (a) Initial excitation of plasmons by the incident light. (b) Landau damping occurs which converts plasmons to an athermal distribution of excited charged carriers. (c) Scattering between excited charged carriers with all other electrons during thermalization. (d) Thermalized

charged carriers scatter off lattice phonons to dissipate energy as heat. (Reprinted with permission from Ref.[10] Copyright 2015 Springer Nature Limited)

The energy dissipation as described above describes a simple nanocrystal in vacuum under ideal conditions where the nanocrystal diameter matches with its corresponding plasmon resonance frequency. However, additional energy transfer pathways can occur. Figure 1.3 illustrates the variety of energy transfer mechanism from decaying plasmons. Plasmon-electron interactions excite electrons within the metal to above the fermi energy. This hot electron can subsequently indirectly transfer into a physisorbed or chemisorbed small molecule, or a bound layer of semiconductor material with appropriate conduction band energy. If the hot electron has sufficient energy to match with the lowest unoccupied molecular orbital (LUMO), there is a probability that the hot electron will shift to the coupled energy state in the small molecule.[28] The same mechanism applies to fused semiconductor where excited electrons jump from the bulk lattice into the conduction band via indirect electron transfer.[28]

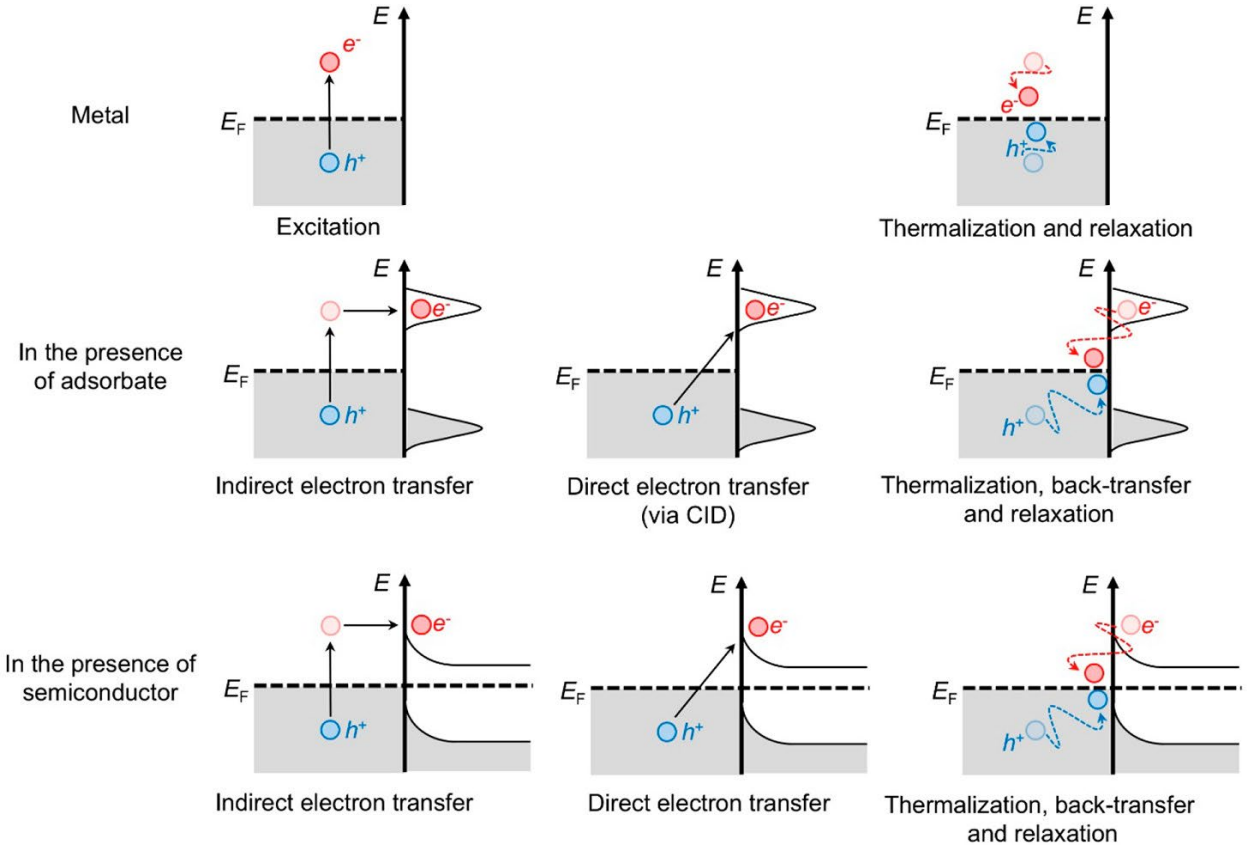

Figure 1.3 Diagrams of several different plasmon dissipation pathways. Initially, hot electrons and holes are generated from Landau damping of plasmons. The typical thermalization pathway occurs as carriers scatter off lattice phonons. The second row shows how electrons can transfer to small molecule adsorbates. The third row illustrates the electron transfer can hop into the conduction band of bound semiconductors. (Reprinted with permission from Ref.[28] Copyright 2018 American Chemical Society)

Direct electron injection can also occur through a process called chemical interface damping (CID).[28,35–37] Through this process, coupling of unoccupied energy states mix with plasmons to directly transfer electrons. This process is thought to promote cleavage of very strongly couple atomic bonds like carbon monoxide and diatomic nitrogen. By injecting electrons into the LUMO or antibonding orbitals, molecular bonds can be broken through this catalytic process.

1.3. Applications for Plasmonics

1.3.1. Plasmonic Nanocrystal Synthesis

The most widespread and popular condition to harness plasmon generation is through noble metal nanocrystals. Nanocrystals of gold, silver, platinum, copper, and aluminum have all been used for plasmonic applications in academic and industrial settings.[38–42] The tunability of optical properties from plasmonic metallic nanocrystals can be simulated based on Maxwell's equations of electrodynamics. Fundamental light scattering theory such as Mie and Rayleigh theories can be applied to predict the behaviors of light attenuation as a function of wavelength.[42–44] Simulations methods like finite difference time domain (FDTD) and discrete dipole approximation (DDA) solve Maxwell's equations numerically instead of analytically to calculate the electric field intensities of EM waves interacting with plasmonic spheres or other simple geometric shaped particles.[42,45] Techniques like these provide a simple model to predict the light absorption profile as a function of wavelength. With known real and complex dielectric constants for metals, this method can very accurately model the plasmonic absorption, electric field strength, and enhancement properties of simple spherical nanoparticle or complex systems with interfaces.[41,46]

Experimentally, progress has advanced significantly in the synthetic space where nanocrystal design encompasses many different geometric shapes, elemental composition and morphologies, core-shell structures, and ligand coverages.[39,47] The most basic nanoparticle are spheroidal shaped particles with some level of monodispersity. One of the most early and basic synthetic techniques is the citrate stabilized gold nanoparticle method developed by Turkevich *et al* in 1951.[48,49] This method involves combining aqueous solutions of sodium citrate and tetrachloroauric acid at subboiling temperatures for a period of time until all auric acid ions have reduced to metallic gold.[48] The simplicity of this synthetic technique made gold

nanoparticle usage very popular. Additionally, the plasmonic absorptive behavior of spherical gold particles absorbs approximately 520-540 nm depending on the particle's diameter.[41,46,47]

Other noble metal nanoparticles are also commonly used like silver and platinum.[3,50,51] Because the plasmonic behavior fundamentally depends on the dielectric constant, the resonant frequency of silver and platinum nanoparticles are different than gold's. Silver nanospheres typically absorbs ultraviolet and blue light with a different extinction coefficient versus gold nanospheres. Moreover, chemical inertness has a key role over its applicability. Silver nanoparticles are more easily oxidized versus its gold counterpart making some catalytic applications limited due to its reactivity with reagents. Having a smaller particle size increases the surface area to volume ratio which negatively affects its oxidation rate.

Nanoparticle growth is easily adjusted depending on nucleation rate and ligand coverage. For instance, very fine gold nanoseed with approximately 2-3 nm diameter are synthesized using very strong reducing reagents like sodium borohydride.[52] The strength of the reducing reagent on Au^{3+} determines the rate of Au^{0} formation leading to incredibly fast nucleation rate. Cetyltrimethylammonium chloride (CTAC), an organic charged surfactant stabilizes the rapidly formed particles by forming a bilayer similar to the phospholipid membrane in cells. Increasing the size of the seed particles can be done by adding more gold reagent with a less reactive reducing reagent, ascorbic acid, sodium citrate or salicylic acid.[52,53] Using less reactive reducing reagent is critical because the rapid reduction of Au^{3+} to Au^{0} will result the formation of additional seed as the solubilized gold concentration exceeds the nucleation concentration.[54–56]

Synthesis of exotic shaped gold nanoparticles can display wildly different behavior than its spherical particle. Triangular gold nanoprisms and nanorods have multiple modes of resonance due to the directionality of the polarization.[52,53] These

particles are considered anisotropic. Colloidal nanoprisms appear blue when purified. The primary plasmonic absorption is due to its longitudinal resonant mode along its plane while the transverse mode matches the spherical frequency. The tunability of the nanocrystal shape is exceedingly valuable as its light capture ability can be adapted to match solar wavelengths. A mixture of gold spheres, prisms and rods can nearly capture all the solar spectrum below 500 nm.[52,53] Figure 1.4 shows Au nanoprism under TEM imaging. Purified precipitate can reach phenomenal purity and uniformity of gold nanoprisms. The corresponding spectra illustrates the absorption of the longitudinal plasmon near 640 nm. Because the supernatant contains higher proportions of spheroidal particles, the spectra (d-f) is clearly dominated by the primary plasmon resonance near 530 nm while the precipitate spectra shows the opposite (a-c).[52]

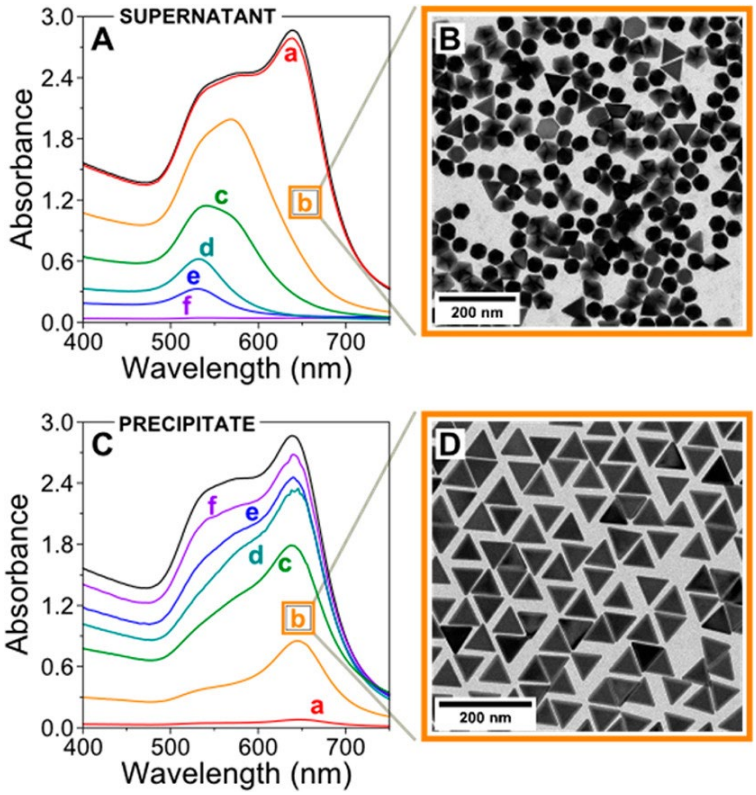

Figure 1.4 Supernatant and precipitate of Au nanoprism colloid. (a) Spectra of supernatant of synthesized nanoprisms with varying concentrations of CTAC. (b)

Corresponding TEM image of the supernatant showing the dispersity of particle geometry and purity of spheroids compared to prisms. (c) Spectra of the purified precipitate containing highly concentrated nanoprism. (d) TEM image of the precipitate nanoprism. (Reprinted with permission from Ref.[52] Copyright 2014 American Chemical Society)

The synthesis of anisotropic gold nanocrystals relies on the facets of the face centered cubic structure of gold. Prisms, cubes, rods, and multipoles have been synthesized by regulating the reaction conditions to control the kinetics of nucleation on different gold facets.[53,57–59] In addition to regulating the kinetics, the ligand stabilizer also is crucial to the growth process. It has been shown that sodium dodecyl sulfate (SDS) can produce highly faceted pentagonal and hexagonal gold particles while poly(vinylpyrrolidone) (PVP) yields cubic structures.[57,58] These sharp faceted structures allow highly concentrated EM fields at the vertices. Applications are primarily pointed at sensing and catalysis.

Overall, the tunability of plasmonic nanostructures is extensive to fit countless applications. Absorption profiles can be engineered, chemical inertness can be strengthened by using noble metals, and sharp pointed particles can be synthesized by configuring the right reaction conditions.

1.3.2. Sensing

The sensing field in plasmonic chemistry has exploded with popularity in recent decades. This is focused on the mechanism of using concentrated electric fields from nanoconfined light to enhance dipole interaction in Raman spectroscopy. SERS has popularized the use of plasmonic nanocrystals for the detection of small organic molecules, proteins, nucleic acids and viral vectors.[60–63] Diagnostics has benefited greatly from the development of this technology as biomarkers can be detected in extremely low concentrations. Two different techniques, surface plasmon resonance

microscopy (SPRM) and SERS, rely on the fundamental principle of plasmon resonance on surfaces. SPRM takes advantage of surface oscillation of a metallic surface while SERS enhances the dipole modes from electric fields. Colorimetric sensors based on the proximity of colloidal and adhered gold nanoparticles can also be reliably constructed into a sensor. However, the specificity of such devices is a major drawback as it can produce significant numbers of false positives.[64]

In SPRM, dampening of electric fields is highly sensitive to the refractive index and dielectric constant of the adsorbing species to the metallic interface.[60] The incident light must have high lateral momentum in order to achieve sufficiently strong surface plasmon polariton waves to match the configuration of total internal reflection. To achieve a high angle incident, a high index prism, optical fiber, gratings, and waveguides are used be used to redirect light at a low contact angle relative to the interface.[60,65] Sensitivities of the assay depend on the refractive indices of the bound and unbound states of surface proteins. Much of the applications are attributed towards biomacromolecules detection and small molecule binding kinetics in immunoassays.[60,66] Merging the specificities from antibodies and sensitivities of SPRM can be a potent method for conducting a quick and simple quantification of pesticides down to parts per trillion concentrations.[66]

SERS is by far the more commonly used technique for plasmonic sensing with widespread adoption in chemistry, biology, and engineering. As discussed previously, enhanced electric fields strongly interact with Raman capable bonds in molecules that can be detected at extremely low concentration, sometimes single molecule detection.[67] Plasmonic colloids and substrates can be synthesized and fabricated in a wide variety of techniques. Solution synthesized nanoparticles produces clean, uniform stable suspension of plasmonic nanoparticles.[62,68,69] Nanostructure lithography can be used to fabricate perfectly clean surface with relatively strong plasmonic behavior. Although

the fabrication process is more demanding, this gives the cleanest surfaces to reduce interactions and contamination. Sample measurement is straightforward, combine the plasmonic nanoparticles or nanoarray device with the analyte solution.[70] This solution or substrate can be directly measured with a Raman microscope. More advanced applications can produce 2D spatial maps of Raman signal of interest for studies of cells.[71,72]

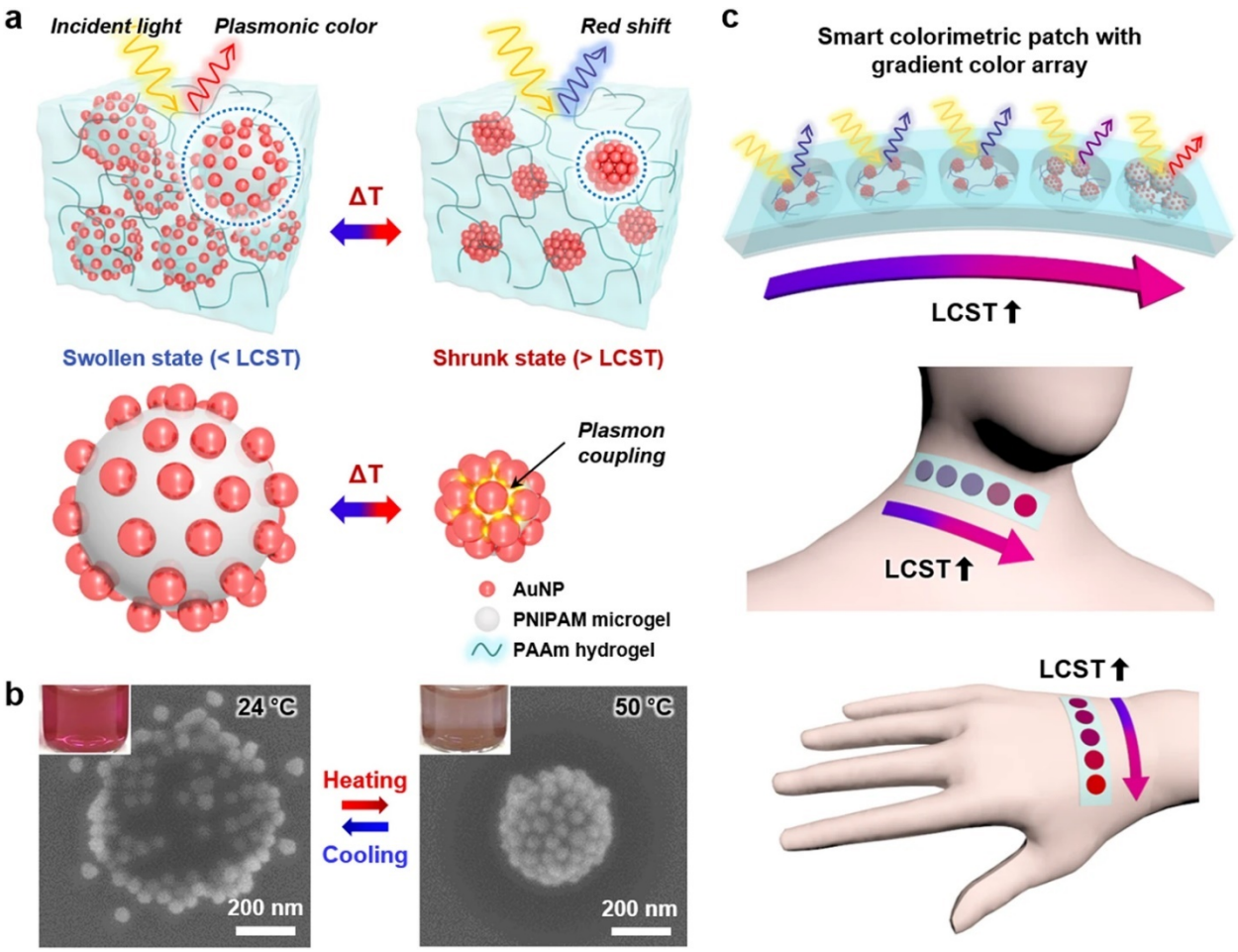

Figure 1.5 Plasmonic colorimetric temperature sensor. (a) Gold nanoparticles attached to microgel will change from the swollen state to a shrunken state resulting in changes in plasmon resonance. (b) SEM images of the swollen and shrunken microgel affecting the nanoparticle proximity to other particles. (c) A patch of an array of sensor

demonstrating a gradient of color. (Reprinted with permission from Ref.[73] Copyright 2018 Springer Nature Limited)

Colorimetric sensing is the simplest method of detecting analytes with some capacities for quantification. It involves mixing colloidal plasmonic nanoparticles with the analyte of interest, enzymes, antibodies, DNA, and small molecules or ions.[74–77] Additionally, physical properties like temperature can be monitored by exploiting thermodynamic of temperature dependence on solubility of polymers.[73] The inherit mechanism are all based on gold nanoparticle coupling. As synthesized gold nanoparticle colloid appear as a wine-red color solution. The addition of analytes triggers aggregation of surface molecules to permanently link the particles. The shift in color from wine-red towards blue or violet denotes this effect visually. This method can be adapted for simple qualification assay or quantification with additional UV-vis measurement of absorption. For highly specific assays for detecting antigens, DNA, and aptamers, the nanoparticle must be functionalized with specific antibodies or oligonucleotides to high specificity.[76,78] Noble metal plasmonic nanoparticles are best due to its chemical inertness for bioconjugation and stability. Highly reactive metals like copper can exhibit plasmon behavior in the visible spectrum but its reactivity is not suitable for *in vitro* assays.

Figure 1.5 shows the viability of a colorimetric sensor for temperature detection near body temperature.[73] The authors attached gold nanoparticles on polymer microgel beads suspended in a hydrogel. By manipulating thermodynamic properties of polymer solubility, swelling of the microgel was engineered to change near body temperature. Various surfactant and ion additives can alter the lower critical solution temperature (LCST) of the microgel which allows controllability of the microgel swelling temperature. Gold nanoparticles act as the visual indicator as it will appear red in the

swollen state compared to purple in the shrunken state. The proximity of nanoparticles can be well controlled by engineering the swelling properties of the polymer microbead.

1.3.3. Plasmonic Photocatalysis

A major developing application for plasmonics involves the active acceleration due to light. Traditional means of photocatalysis primarily remain in the small molecule and semiconductor fields. Small molecule photocatalysis, typically homogeneous catalysis, can be solution phase and gas phase.[79,80] Heterogenous photocatalysis are commonly semiconductor based that fundamentally harness energetic electrons and holes generated from the photoexcitation from the valance band to the conduction band.[28] Subsequently charge-transfer occurs to electron or hole scavengers that produce energetic intermediates. Here however, plasmonic is more like semiconductor heterogeneous photocatalysis but the time scale of reaction is shifted. Excited semiconductors have electron-hole lifetime on the order or picoseconds to nanoseconds. Plasmonics on the other hand, have much shorter hot carrier lifetime from femtoseconds to picoseconds. This shift requiring ultrafast charge transport is a significant hurdle in the field of plasmon hot carrier driven chemical change.

Light-driven plasmonic catalysis recently gained traction in the early 2010s when Linic *et al*. showed that plasmonic silver nanocubes can drive gaseous ethylene epoxidation by electron transfer to the LUMO of bound diatomic oxygen to then assist the cleavage of the oxygen double bond.[3] Numerous other heterogenous solid-gas reactions have been done like ammonia decomposition to H_2 and N_2,[14] hydrogen dissociation,[81] and nitrous oxide decomposition to O_2 and N_2.[82] Many of these reactions require surface atoms to strongly interact via chemisorption to precursors for strong reaction rates to occur. Gold is typically too inert to undergo many catalytic reactions because its orbital energy level is different than that of molecular highest occupied molecular orbital (HOMO) and LUMO. So, many of the reactions Halas *et al* carried out

have decoration of catalytic metals like iridium, ruthenium, or palladium on Au, Cu, or Al.[14,82,83] Many of these can be connected to the chemical interface damping scheme from Figure 1.3. (CID) involves direct electron injection into the LUMO of molecular adsorbates. Much of these studies have been measured by SERS due to the surface enhancement of Raman signals.[84,85] Because plasmons decay into excited carriers and are accompanied by strong electric fields, the pump laser can be used to drive chemical change and can probe the interactions via SERS, making it a strong candidate for photocatalysis studies. A popular reaction is a surface reaction of para-nitrothiophenol dimerization on gold.[84,86] The strong linkage between thiols and surface gold atoms allow self-assembled monolayers of organic moieties to be studied with reliability.

Figure 1.6 shows plasmonic ammonia decomposition.[14] Cu nanoparticles decorated with ruthenium are hot carrier driven to catalytically decompose ammonia to hydrogen and nitrogen. Zhou et al showed experimental and computational evidence pointing towards hot carrier driven mechanism. Temperature was measured with an infrared (IR) camera showing that photothermal did not play a key role in this reaction. The authors applied Arrhenius equation to model the activation barrier of the reaction showing a catalytic effect from hot carriers. They observed the greatest reduction in activation energy from 1.21 eV to 0.35 eV. A significant driving force from the simulation showed that desorption was the rate limiting step which can be overcome with desorption induced by electronic transition (DIET).[14]

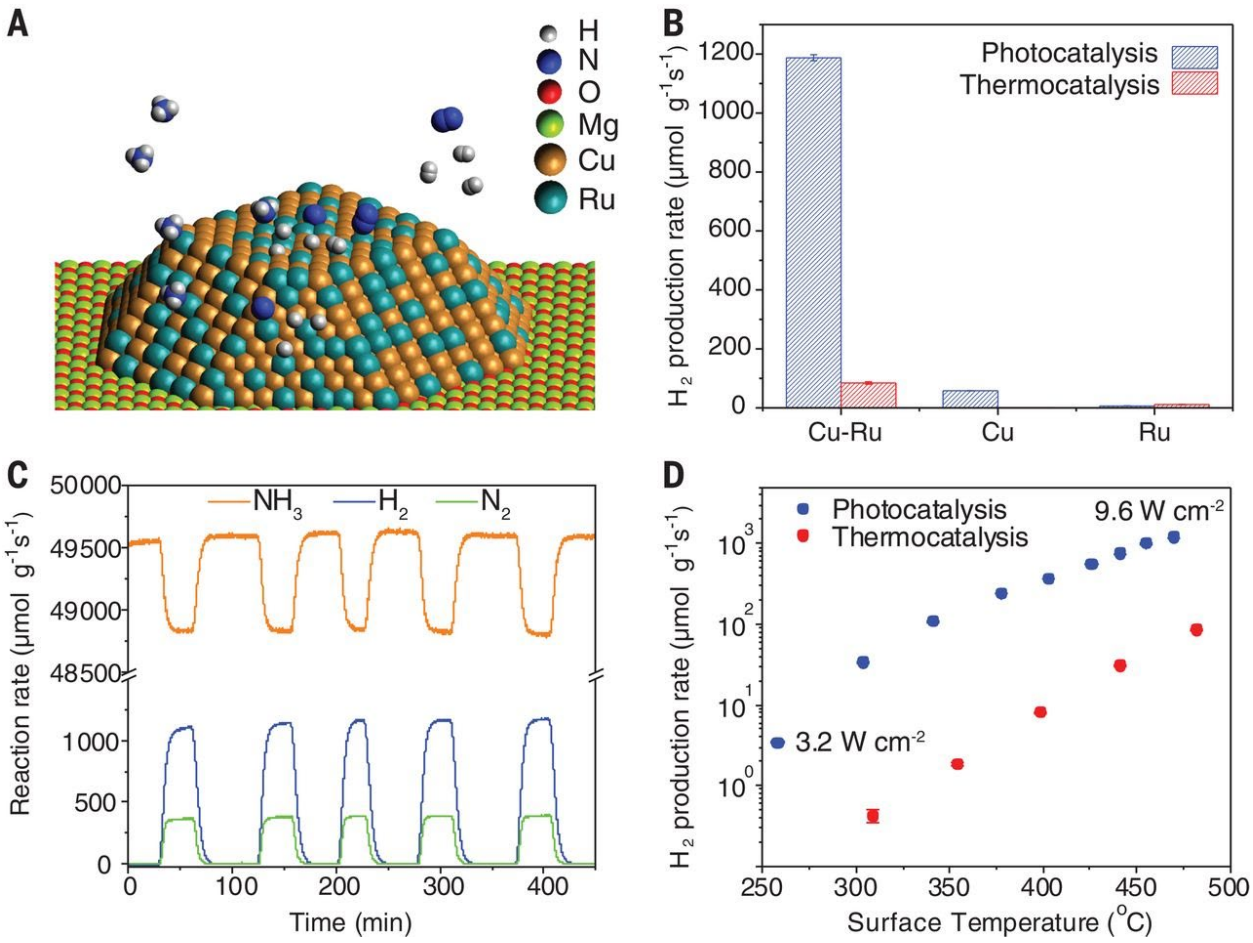

Figure 1.6 Plasmonic Photocatalytic Ammonia Decomposition. (a) Nanostructure illustration of Ru doped Cu nanoparticles deposited on MgO. Ammonia molecules adsorb to ruthenium sites and under decomposition to diatomic H_2 and N_2 gases. (b) Rates of hydrogen production comparing Cu only, Ru only, and alloyed Cu-Ru nanoparticles. (c) Real-time mass spectrometry traces of ammonia, hydrogen and nitrogen demonstrating illuminated and dark rates of hydrogen and nitrogen formation. (Reprinted with permission from Ref.[14] Copyright 2018 American Association for the Advancement of Science)

Excitation of semiconductors can also be driven with plasmonic nanoparticle. Many synthetic pathways exist for combining semiconductors for photocatalysis and plasmonic nanoparticles. One of the most commonly used semiconductors is TiO_2 and

water reduction to generate clean hydrogen. Many combinations of plasmonic nanoparticle shape from colloidal nanospheres, nanorods, and device centered nanostructures have been linked with TiO_2 have been studied to show photocatalytic hydrogen production.[2,87,88] The coupling between plasmonics with TiO_2 has always been to increase solar absorption and efficiency of the photocatalytic water splitting process. With TiO_2's band gap at 3.2 eV, much of the solar radiation cannot be utilized as lower energy photons cannot excite the band gap. By bridging the tunability nature of plasmonics to capture 2.4 eV or lower energy photons, achieving higher efficiency is more likely. [88,89] Engineering this combination of plasmonic nanoparticle with semiconductor is not always straightforward. We must consider the semiconductor's band gap and positions, the fermi energy of the plasmonic metal, and the plasmon resonance frequency. A mismatch in energy levels would not yield any appreciable charge transport which will not catalyze any reaction reliably.

Alloyed or bimetallic nanostructures have amazing potential as a simple formulation to drive photocatalysis by skipping the engineering of band structure completely. Alloyed nanoparticles have mixtures of the parent plasmonic metal with some lower concentration of chemically active metals like iron, copper, ruthenium, platinum, iridium, or palladium.[14,90–94] Plasmon energy flow has been revealed to dephase into the surface nanostructure of secondary metal.[95,96] Efficient energy channeling of hot carriers to the surface atoms of catalytic metals can dramatically accelerate the rate of reaction by hot carriers. Synthesis of transition metal decorated onto aluminum nanoparticles has been shown to be a simple process.[97] This functionality adds to another capacity to the controllability of plasmon based nanoparticles for catalysis. These decorated nanoparticles can improve traditional dark heterogeneous catalysis due to the increase mass efficiencies of the surface area.

Economic viability is a major driving force for the research and development of catalyst on the billion dollar per year chemicals industry.

1.3.4. Thermoplasmonics

Photothermal harnessing has a limited range of applications but can be highly targetable and efficient. Hot carrier relaxation efficiently converts light into heat through plasmon damping pathways. Basic applications involve chemical reaction acceleration at the nanoscale interface of the particle's surface. Mechanistically, thermoplasmonics heat is generated at on the nanosecond which then dispersed to the surrounding medium fairly quickly.

Basic applications involve solar thermal desalination by simply evaporating water the gold colloid is surrounded by.[98,99] Arrays of solar concentrators elevate the intensity to upwards of 20 suns can increase efficiency enhancement by 60%.[99] One particular challenge could be the formation of voids during the sudden onset of plasmon heating. Expanding water can be quickly superheated and vaporize creating a significant cavitation which consequently alter the surrounding dielectric environment thereby changing the absorptive behavior of the particle.[100] It has been shown that having a cavitation of 200 nm radius can decrease the absorption by approximately 40%. The resulting insulating layer decreases the water/gold interface nearly stopping thermal transport restricting the energy to continuously increase the to over 900 ˚C above the ambient temperature.[101] Concentration of light can only be increased so much before morphological changes start appearing. At extreme power densities (10^6 – 10^7 W/cm^2) from a continuous wave (CW) laser, the plasmonic nanoparticle disintegrates into many fragmented smaller nanoparticles.[102] Outcomes for the nanoparticle in water showed no difference compared to those in air.[102] Eventually, temperatures reaching ~1200K would start evaporation of gold atoms.[102] Another study simulated a gold nanoparticle under extreme illumination power densities with molecular dynamics.

Amorphization of gold initially occurred from the crystalline starting state at 500 to 700 nW. At 1000 nW, the nanoparticle disintegrated into fragments, supporting experimental evidence of nanoparticle destruction.[103] Careful engineering must be done to maintain stability of the absorbing nanoparticles while maximizing efficiency.

Chemical reactions can also be accelerated without resorting to heating to significant temperatures. Photothermal chemical reactions have been used for Suzuki coupling reactions and chemical decomposition.[29,104,105] These reactions can be done at much lower average temperatures as the local temperature is significantly higher than the surrounding that cannot be reasonably achieved. Because local temperatures can be several hundred degrees above ambient, high potential energy barriers can be overcome allowing simple synthetic methods to be applied for intensive methods.

Wang *et al* showed Pd decorated nanoparticles can perform Suzuki coupling reactions when illuminated with 809 nm laser at 1.68 W.[29] At 1.68 W, photothermal conversion efficiency was observed to be 95.8% with the bulk solvent temperature of 62 ˚C. The Suzuki coupling reaction between bromobenzene and m-Tolylboronic acid gave a yield of 99% at 1.68 W.[29] Figure 1.7 shows the particles used for this particular reaction. TEM images indicate the core-shell nature of the nanostructures used. The bulk solution temperature shows how it increases over time under high power laser irradiation.

Solar radiation was also used but reaction time was extended due to the lower intensity. Nonetheless, yield was still surprisingly high at 99%.[29] Fasciani et al showed photoexcitation of gold nanoparticles can decompose dicumyl peroxide in under one minute exposure time to 532 nm laser.[106] The decomposition reaction of dicumyl peroxide is endothermic requiring temperatures above 140 ˚C. This reaction's activation energy was determined to be 34.3 kcal/mol from calculated rate constants against temperature.[106] Combining reaction kinetics, the investigators calculated that the local

temperature needed to be above 500 ˚C.[105] These photothermal techniques should improve efficiency and yield while reducing energy cost and complex reaction conditions.

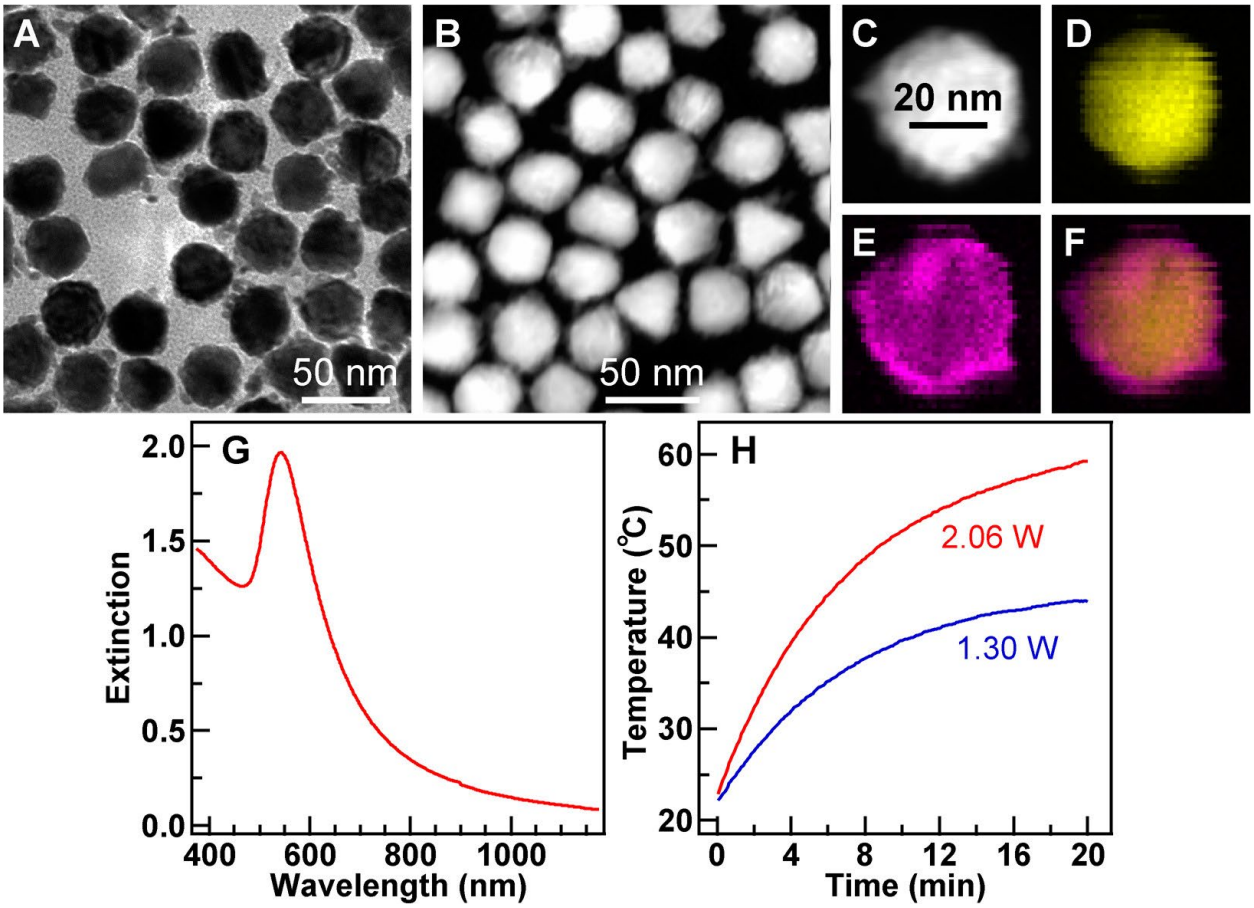

Figure 1.7 Au-Pd nanoparticles for photothermal driven reactions. (a-b) TEM and Scanning Transmission Electron Microscope (STEM) images of Au core and Pd shelled nanostructures. (c-f) Elemental maps of gold core in yellow, Pd in pink and a composite image. (g) Absorption spectra of the reaction solution containing the Au-Pd nanoparticles. (h) Temperature change of the solution under two different laser irradiation powers. (Reprinted with permission from Ref.[29] Copyright 2013 American Chemical Society)

A major advancement for thermoplasmonics is photothermal therapy for cancer treatment. Nanorods have been engineered to absorb infrared radiation outside the absorption window of organisms. Longitudinal plasmons oscillate strongly with the applied laser only IR radiation thereby inducing isolated hyperthermia and irreversible damage in the solid tumor region.[104,107] Gold nanorods of particular aspect ratios have the absorption profile to absorb within this optical window of 790-800 nm.[107] Gold nanospheres can also be applied even though the plasmon resonant wavelength is 530 nm. At higher doses, aggregation of nanoparticles at the tumors shifts the absorption profile towards the infrared. Numerous *in vitro* studies have been able to quantify cell death using a variety of plasmon absorbers, cell lines, laser irradiation conditions, and exposure settings.[107] One study used aptamer-functionalized gold/silver bimetallic nanoparticles on MCF-7 breast cancer cell line that killed 97% of cancer cells at 0.25 W/cm^2 irradiation of CW 808 nm light.[107,108] The pristine nanoparticle absorbed only 580 nm light but *in vivo* conditions exhibited supercoiling, aggregation and crosslinking of the nanoparticles and aptamer complex.[108] *In vivo* studies have been dominated by studies on genetically designed tumor susceptible mice.[107] Ke *et al* injected the mice with polyethylene glycol-functionalized gold nanoshelled nanocapsules with significant absorption in the visible and near infrared. U87MG tumor mice were irradiated with a CW 808 nm laser at 1.3 W/cm^2 for 10 minutes. One study observed a 35 ˚C increase in tumor temperature followed by 67.6% decrease in solid tumor volume while control mice all had tumor growth of approximately 1000% within the same period.[109] Although these studies appear to be promising, key challenges still lie in the functionalization of nanoparticles. A major hurdle appears to be forcing nanoparticles to specifically adsorb near or on the tumor cells. This area will likely see major development towards DNA or antibody coupled nanoparticles.

1.4. Driving Forces of Chemical Reactions

Because of the extremely short timescale and small dimensions plasmons take place, pinning the exact mechanism for chemical reactions can be especially challenging. Photocatalysis driven by plasmons have been studied extensively using on diverse set of reactions and a variety of plasmonic engines from colloidal nanoparticles to scanning tunneling microscopy. The three primary hypotheses for photocatalytic driven reactions are field enhancement effects, hot carrier transfer, and photothermal acceleration.

1.4.1. Field Enhancement

Incident electromagnetic waves interacting with plasmonic metals will generate strong electric fields due to the dielectric difference between the metal and the outside medium. This type of lensing concentrates the field in particular modes that behave similar to standing waves. For spherical particles, the dipolar mode produces the strongest field and is the dominant absorber that most studies are based around. Higher order resonances do occur in more complex nanomaterials like cubes, and prisms with higher order symmetry.[110]

The highly controlled nature of tip enhanced Raman spectroscopy (TERS) can be a valuable method for studying field enhancement effects of chemical transformation. Kazuma et al adapted a scanning tunneling microscope with Raman spectroscopy to study real time single molecule dissociation of dimethyl disulfide.[111] A fine silver tip with a 60 nm radius of curvature was positioned over a smooth silver surface covered with dimethyl disulfide as shown in Figure 1.8. Scanning tunneling microscope (STM) images show bright spots where the intact dimers are located prior to the laser stimulation. The silver tip confines the light within the nanogap to induce plasmonic chemical reactions. After irradiation, the once brightly lit signals appear dimmer dimers of the dissociated molecule. The study shows significant rate of dissociation where the

field is strongest with substantial drop-off only a few nm from the center of the tip. Simulations of the silver tip with substrate indicated electric field enhancements of up to 60 times the incident field.[111] Of course there are additional mechanisms at play including hot carriers that excite the LUMO of the molecule so this study cannot single handedly show field dominated nor hot carrier induced mechanism.

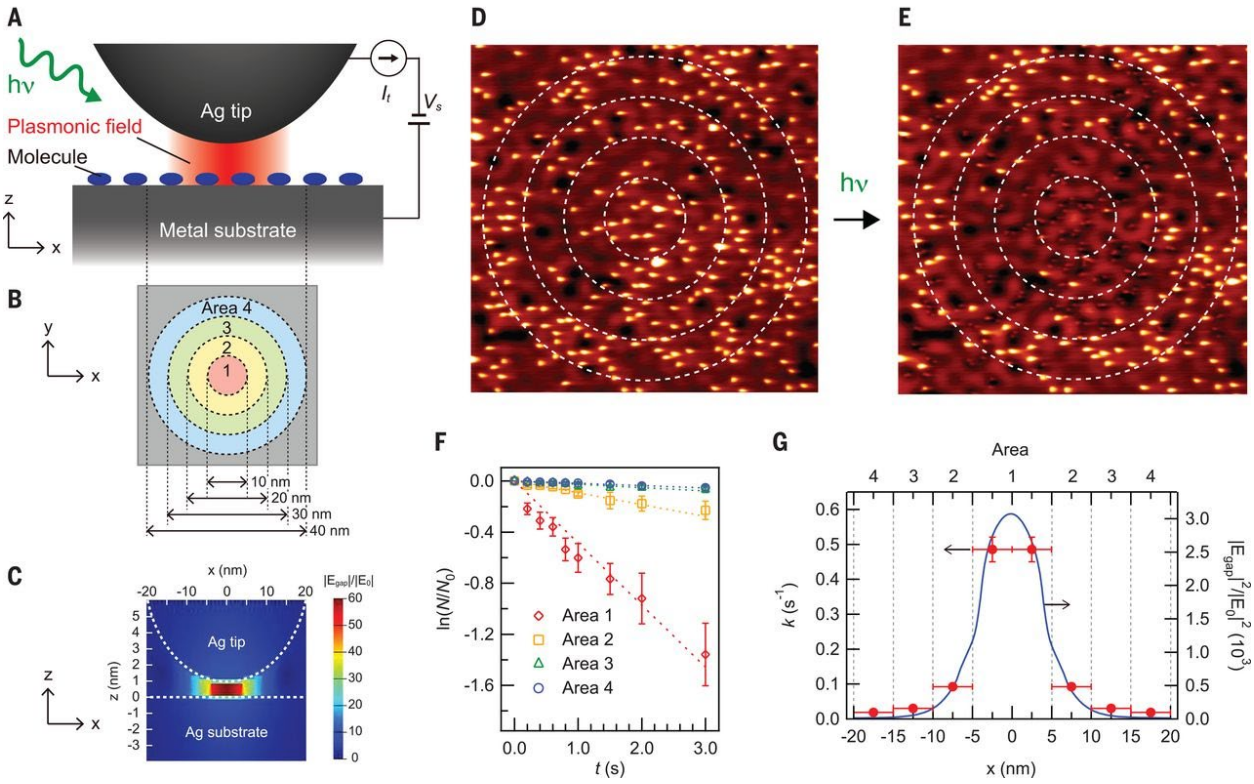

Figure 1.8 Observing real space plasmon driven dimethyl sulfide dissociation. (a) Tip enhanced plasmonic field showing adsorbed species under a scanning tunneling microscope. (b-c) Zones showing level of enhanced fields as a function of radius from the tip. (d-e) Before and after STM image of adsorbed dimethyl sulfide. (f) Kinetics of dimethyl sulfide dissociation at different areas of the tip location. (g) Rates of reaction in relation to distance from the tip. (Reprinted with permission from Ref.[111] Copyright 2011 American Association for the Advancement of Science)

The get an accurate understanding behind near-field enhanced reactions, modeling provides the clearest view. Huang et al studied the mechanism of near field enhancement effect of plasmon-driven water splitting.[112] They used real space real time dependent density functional theory to model the electronic structure of Au_{20} molecule in a pyramid with a water molecule on a vertex. Upon illumination, they noticed the bond length increase significantly within 30 fs. This time regime is extremely short that is dominated by electric field presence. Excited carriers are produced from plasmons long after this point by hundreds of fs. It was hypothesized that the strong near-field interactions with water induces O-H cleavage and induces fragmentation of the water molecules.[112]

Of the three possible mechanisms, near-field enhancement is the least supported mechanism. Nonlinear optical effects start occurring when electric field strength approaches hundreds of millions of volts per meter. This provides enough energy density to potentially excite molecular bonds in the eV/nm intensities. Applying this behavior to plasmonic nanoconfinement, it appears that high intensity stimulation will induce nonlinear excitation.

1.4.2. Hot Carriers

Hot carrier mechanism is the most popular explanation for describing chemical reaction acceleration by plasmonics. Many groups like Halas, Linic, Christopher, and Nordlander have explored this area in great detail with a considerable collection of reactions and models. One of the earliest works came from Linic's oxygen dissociation using plasmonic silver nanocubes.[3] Product species of a heterogenous plasmonic reaction are measured with an online mass spectrometer sampling gaseous molecules in real time. This experimental setup became the hallmark for detecting chemical reactions from plasmonics. Supporting evidence often came in the form of FDTD modeling of electric fields and DFT depicting electronic transitions due to excited carriers.

One of Halas' later studies looked at hot carrier multiplication in plasmonic photocatalysis.[113] Figure 1.9 shows the hot carrier dynamics as a function laser intensity of hydrogen dissociation reaction. The study centered around hydrogen deuterium scrambling reaction to serve as a model for plasmonic activity on copper nanoparticles. Intensity dependent measurements showed a sigmoidal relationship against the HD rate under white light illumination. Activation energy was calculated by conducting thermocatalytic measurements at a series of temperatures. DFT modeling confirmed a possible pathway of reducing the activation energy from 1.10 eV to 0.63 eV which was in line with the experimental measurement of 0.54 eV. A series of vibration excitations were hypothesized to occur for electrons proceeding through the activation barrier. Combining quantum yield calculations and a model of vibration energy level showed that the vibrational energy gap was 0.17 eV. Linan et at showed that the over unity of the quantum yield was due to thermalized hot carrier through a multiplication process. The athermal distribution is created upon initial plasmon decay. Then thermalization occur with the bulk electrons to generate a Fermi-Dirac distribution of hot electrons. It is this thermalized hot carrier that produced a higher quantum efficiency than an athermal collection of hot electrons would. Their model also showed that there is an interesting light intensity dependent contribution factor from hot carriers versus photothermal effects. At low intensities (less than 5 W/cm^2), photothermal dominates the HD production rate while hot carriers dictate the higher intensities.[113]

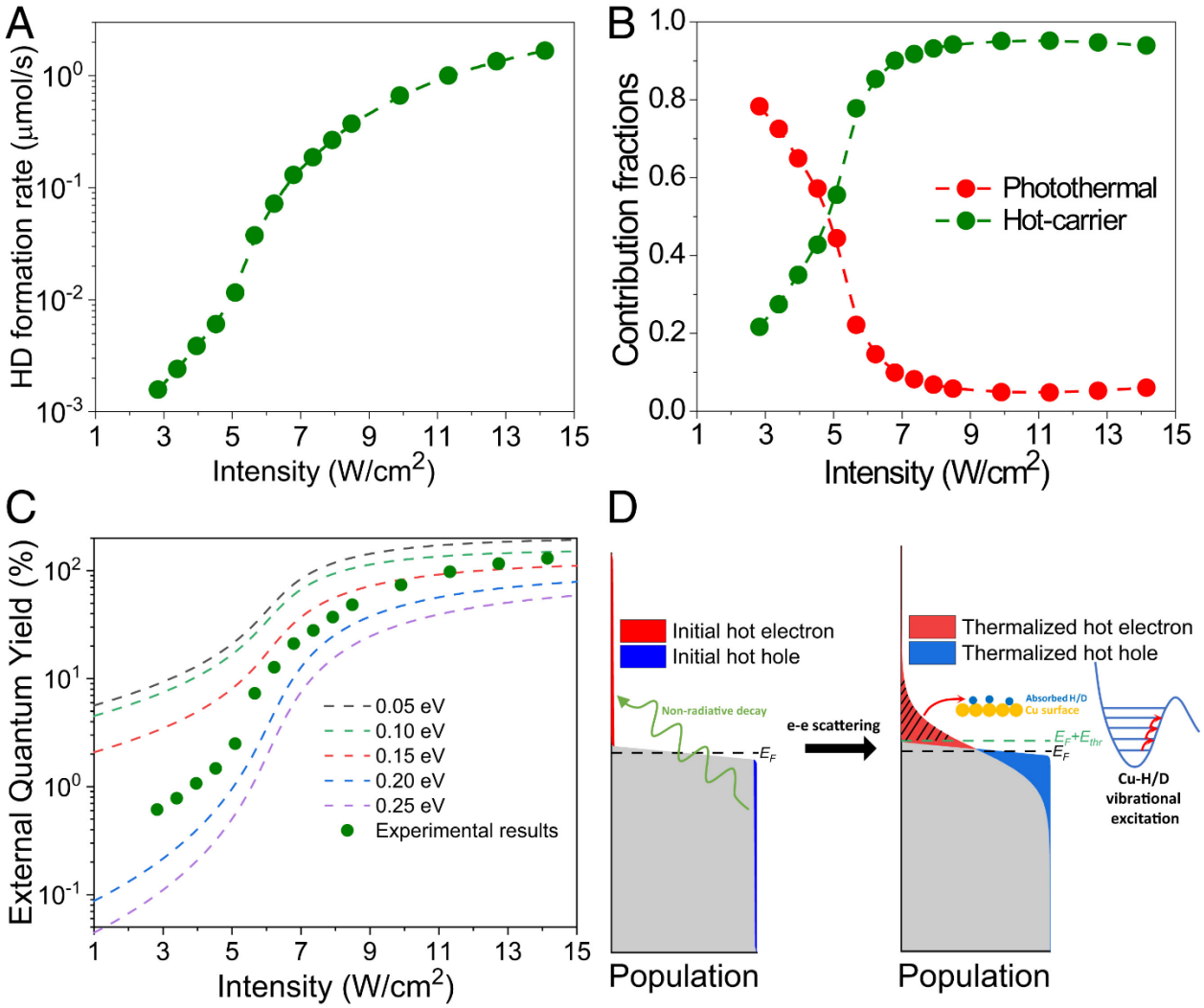

Figure 1.9 Plasmonic Hydrogen Dissociation Reaction. (a) Intensity dependence of HD formation of plasmonic copper nanoparticles. (b) Contribution ratio due to photothermal and hot carrier effects on HD production rate. (c) External quantum yield dependence as a function of intensity comparing experimental to modelled results. (d) illustration of hot carrier multiplication dynamics inducing catalytic hydrogen dissociation. (Reprinted with Permission from Ref.[113] Copyright 2021 National Academy of Science)

Plasmonic photochemical nitrogen fixation has also been demonstrated. Yang et al prepared gold nanoparticle decorated TiO_2 nanosheets with oxygen vacancies to

drive nitrogen fixation and hydrogen evolution.[8] Colloidal gold nanoparticles are impregnated on solution prepared TiO_2 nanosheets from 0% to 5% loadings. Photochemical reactions were conducted with only visible light in the presence of water, bubbling nitrogen, and methanol as the hole acceptor. After 90 minutes of illumination time, ammonia concentrations were significantly higher at 150 μM in the Au/TiO_2 with oxygen vacancies while all other measurements yielded less than 5 μM. Yang et al hypothesized that the excited carriers where simultaneous being transferred. Gold-adsorbed methanol were oxidized directly by holes to oxidized products while hot electrons migrated to the TiO_2 nanosheet's conduction band. With the extended lifetimes of excited electrons on TiO_2, electrons eventually migrate towards the oxygen vacancies where diatomic nitrogen were bound. These electrons are transferred onto the nitrogen π antibonding orbitals. Proton in solution couple to the negatively charged N_2 intermediate generating ad-HN_2. After several charge transfer steps, 2 equivalents of ammonia are released into solution.

These two studies show the diversity of engineering photochemical reactions from heterogenous plasmonic nanoparticles. The more direct electron injection pathway and hot carrier multiplication of the copper nanoparticle to adsorbed hydrogen radically increased the efficiency of the reaction to over 100% quantum yield. In the nitrogen fixation reaction, the authors measured a 0.82% apparently quantum efficiency.

1.4.3. Photothermal Acceleration

As discussed in the section above on thermoplasmonics, reactions can be driven purely due to local photothermal heating. This concentrated local high temperature heater from the nanoparticle can dramatically increase kinetics of thermally driven reactions. However, measuring the local temperature is no small feat as the surrounding support will rapidly dissipate any heat generated.

One method to directly measure local temperature uses Stokes and anti-Stokes Raman spectroscopy.[114] Raman lines are determined by differences in emitted radiation compared to the pumped laser wavelength. Stokes lines have energies below the excitation energy as the energy difference is from the electron population of the vibrational levels before excitation. At higher temperatures, thermodynamic equilibration of electron population shifts towards higher energy vibrational states. Consequently, more vibrationally excited electrons are promoted to virtual states that when relaxed will emit higher energy photons than the initial excitation photon. This phenomenon is observed as the anti-Stokes shift in Raman spectroscopy and can be used to measure the temperature of small Raman active molecules on surfaces.

Halas attempted to measure the nanoscale thermoplasmonic behavior of engineered gold nano-antennas.[115] Figure 1.10 details the experimental setup used to funnel extremely high intensity light towards gold nanorod (reactor). They fabricated large antenna-reactor system to funnel light directed towards a gold nanorod in an attempt to observe changes in its structure. A gold nanorod reactor sits at the center of two larger wing-shaped gold trapezoidal prisms acting as light funneling antennas maximizing the EM enhancement to maximize temperature of the reactor while minimizing temperature increase of the antennas. The nanostructure substrate will either be a layer of thermally insulating alumina or more thermally conductive silicon to compare the maximum attainable temperature. An 808 nm IR laser focused to near the diffraction limit illuminated the antenna-reactor with power densities upwards of 1.2 MW/cm^2. Nanothermometry was conducted by Stokes-anti-Stokes ratio measured with SERS signal from reactor-adsorbed para-mercaptobenzoid acid (pMBA). SERS peaks at 1075 cm^{-1} were gaussian fitted and the respective Stokes and anti-Stokes intensities were used to determine the local temperature. When illuminated with 435.5 kW/cm^2 light, Stokes-anti-Stokes ratio yielded an increase of 54.3 $^\circ$C.[115] Illuminated

samples were compared to thermally annealed at up to 540 ˚C. Reactor shape deformation was measured by SEM imaging to calculate the aspect ratio. Changes to the nanorod aspect ratio only occurred for the 470 ˚C and 540 ˚C samples. When compared to illuminated samples, shape changes did not occur until the intensity was above 716.2 kW/cm^2. These power densities studied span several orders of magnitude higher than standard AM 1.5G solar simulator illumination or typical plasmonic photocatalysis irradiated with lasers. So, Halas *et al* concluded that at power densities around 10 W/cm^2, local temperatures should not a significant factor.

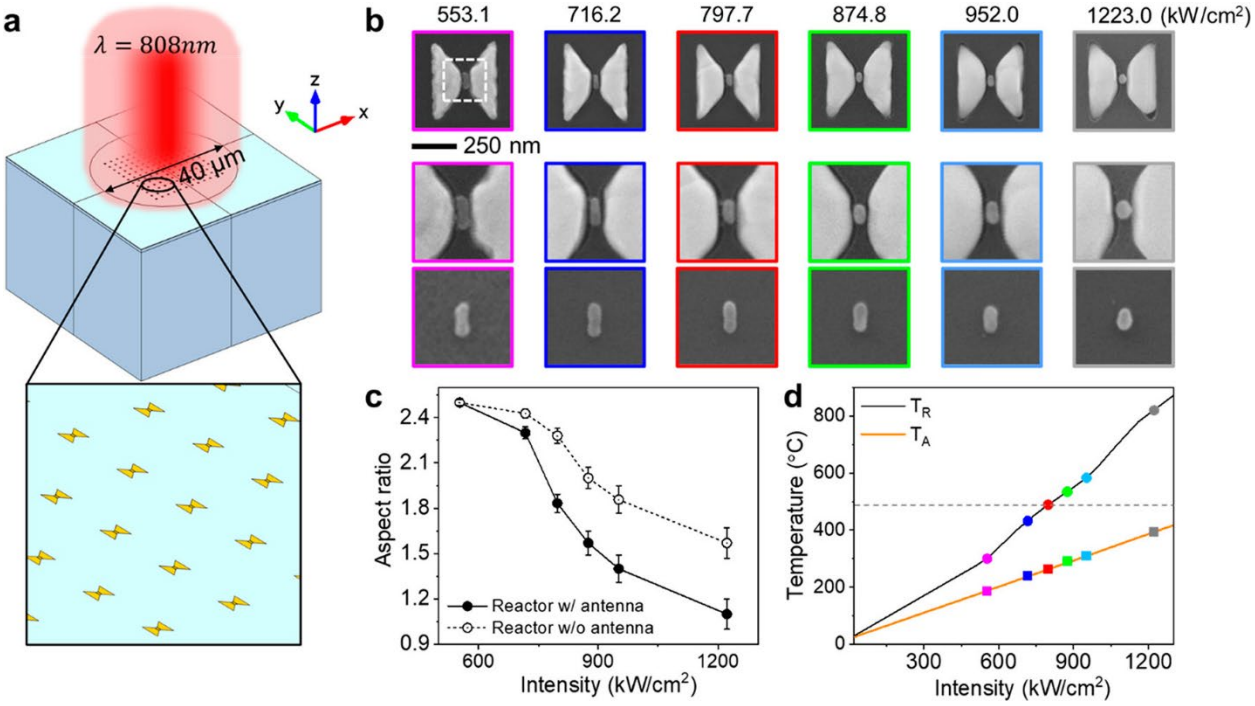

Figure 1.10 Photothermal effects from gold antenna reactor system. (a) illustration of fabricated gold plasmonic bowtie antenna reactor absorbing light at 808 nm. (b) SEM images of reactor nanorod changes under extremely intense laser power densities. (c) Changes in aspect ratios of nanorod reactors after laser illumination. (d) Predicted and measured temperatures from Stokes-anti-Stokes ratio of adsorbed small molecule. (Reprinted with permission from Ref.[115] Copyright 2021 American Chemical Society)

One of the traditional methods to probe the mechanism was a simple light intensity dependence on the rate of product formation. This precise relationship should be predictive of the dominant mechanism whether it is thermal or hot carrier.[116] Linic et al observed the rate of ethylene epoxidation by plasmonic photocatalytic nanocubes. Their power density dependence data was fitted to a linear regression that seemed reasonable at the time.[3] However, when fitted to an exponential, the deviation was not dissimilar to the linear fit suggesting that photothermal could also be a candidate for the dominant mechanism.[116] A linear dependence shows direct hot carrier generation as the quantity of charge carrier generated is directly proportional to the light intensity. A supralinear or exponential dependence should show Arrhenius behavior conforming to temperature driven reaction. One possibility is to extend the power dependence measurement through several orders of magnitude from 0.1 W/cm^2 to 100 W/cm^2. With hot carrier multiplication, it was shown that the sigmoidal intensity-rate curve was due to photothermal behavior 5 W/cm^2 while hot carrier dominated at the higher power regime.

Traditionally, Halas et al supported their studies for hot carrier dominated photocatalytic reactions by measuring the temperature with a thermal camera.[14] However, this method was met with criticism as this only measures the bulk average temperature. Additionally, the intensity of IR radiation depends on the black body emissivity of the material, but a reliable calibration was not performed. Of course, the strongest misjudgment might be assuming the local nanoparticle temperature to be the same as the bulk material temperature. Logically, the light absorbing material is the nanoparticles that must then dissipate the heat into the supporting material. So, the local plasmonic nanoparticles must be at a higher temperature, with the question of how much higher precisely is still unknown.

1.5. Overview of Dissertation

This dissertation summarizes experiments for the synthesis, fabrication, characterization, and performance of supported gold nanocrystal catalysts. My first goal was to design a robust system to consistently yield high quality nanocrystals to then load it onto a support medium. This was carried out by adapting the Turkevich synthetic method as it was robust and reproducible. Citrate capped gold nanocrystals are monodispersed and colloidally stable for storage making it ideal for long term catalysis use. We combined colloidally stable nanocrystals with supporting nanopowder metal oxides by lyophilization or freeze-drying to yield highly random, disperse and homogenous catalysts with significant impact on the nanocatalysis community. The supported nanocrystal catalyst was characterized by a whole host of analytical techniques designed to probe the nanostructure of the material. We extensively imaged the particles using a world-class transmission electron microscopy facility at UC Irvine Materials Research Institute (IMRI). Concurrently, we have constructed a top to bottom expandable and modifiable photocatalysis reactor with real time product detection. We have overcome numerous challenges during the assembly of the photocatalysis reactor by improving through successive iterations of improvements to the flow controllers, reactor, transport lines, and detector. Performance of the photocatalyst was done by repurposing a high power 520 nm laser to illuminate the plasmonic nanocrystals under gas flow. Highly purified hydrogen and deuterium dissociation reaction was use as a model to elucidate the mechanism of plasmon induced catalysis. Products can be quantified in real time with a mass spectrometer sampling small quantities of product exhaust. We have determined that platinum can undergo background autocatalytic hydrogen dissociation at room temperature. However, the stability of platinum can be poisoned by chemisorbed hydrogen over a period under continuous hydrogen exposure. We have investigated

the enhancement effect of Iridium and platinum decorate core-shell nanocrystals of this reaction to show possible mechanisms of hot carrier dynamics within the subnanometer shell of the particle.

The following chapter details the background, synthesis, structure, characterization, and performance of supported gold nanocrystal catalyst by slurry freeze-drying. We have developed a novel approach to the fabrication of homogenous metal nanocrystal on a variety of organic and inorganic supports. The results obtained show a uniform nanocrystal dispersion with tunable loading with retention of original size and shape of the gold particle. We showed that sodium citrate suppresses the clustering of gold NCs on cellulose and TiO_2 and can be subsequently rinsed away to yield supported NCs with cleaner surfaces, avoiding the need for high-temperature calcination that can degrade NC monodispersity. Two model reactions were used to establish the catalytic activity of the supported NCs in water. The generality of the method was demonstrated by depositing triangular Au nanoprisms onto cellulose and TiO_2. Due to its many advantages, slurry freeze-drying should prove useful for making a wide variety of uniform supported NC catalysts from chemically synthesized colloidal NCs. We anticipate that the freeze-drying of colloidal mixture can be extended beyond metal NCs to load many other types of colloids (inorganic NCs, organic nanoparticles, nanowires, etc.) onto a wide variety of support materials (carbon, metal oxides, polymers, etc.) for applications in catalysis, energy conversion and storage, optoelectronics, and sensing.

Chapter three compiles the development work done throughout the assembly of the photoreactor. The iterative process has shown that the adaptability of the mass spectrometer can be used to measure gaseous products from a diverse set of reactions including heterogenous gaseous mixture to headspace sampling of solution reactions.

Early uses of the residual gas analyzer were to attempt to measure potential hydrogen production from colloidal plasmonic core-shell catalysts.

Chapter four branches our studies towards assessing the performance of the core-shell nanocrystals. Our method was to use a model reaction involving the dissociation of hydrogen and deuterium gases accelerated by our core-shell supported catalyst. We showed that the iridium and platinum core-shell structure is indeed a gold core and an iridium or platinum shell. While the iridium was spotty on the surface, we did conclude that it was primarily surface bound.

The concluding chapter closes the dissertation with a comprehensive summary of highlights from all studies done. Furthermore, there is a section describing an experiment to determine the fundamental mechanism of the hotly debate photothermal versus hot carrier mechanisms within the plasmonic community. It involves measuring the equilibrium constant of the hydrogen and deuterium mixture in an isolated container. The equilibrium constant is temperature dependent such that it only depends on the surface temperature of the reaction site. So, in principle, nanoparticle's temperature can be potentially measured against the intensity of the laser illumination. Modifications to the reactor would be minimal and there would only need to be a sizable sealed contained with a transparent viewport for the laser to penetrate through. If this experiment is successful, we imagine this method could revolutionize the way temperature is measure on the nanoscale.

Chapter 2. Supported Nanocrystals by Freeze-drying

2.1. Introduction

Metal nanocrystals (NCs) supported on high-surface-area solids are an important class of heterogeneous catalysts.[9,117–120] Supported metal NCs are made either by growing NCs directly on a support (often by liquid-phase metal salt deposition and reduction) or immobilizing pre-formed colloidal NCs on a support. The direct NC growth methods (salt deposition,[117] co-precipitation,[9] deposition-precipitation,[118,119] ion exchange, chemical vapor deposition, co-sputtering, etc.) can yield metal NCs with clean surfaces and interfaces, but control of NC size, shape, and coverage on the support is usually poor and NC polydispersity, clustering, and coverage non-uniformity are common problems.[9,118,120,121,122] In contrast, the deposition of pre-formed, highly-monodisperse colloidal NCs offers excellent control of NC size and shape, but depositing colloidal NCs uniformly throughout a support is challenging because (*i*) NC binding to the support is often too weak or too strong and difficult to control[123–127] and (*ii*) when NCs are weakly bound to the support, conventional drying allows motion of the solvent, NCs, and support particles that results in NC/support unmixing and non-uniform NC loading.[9,117,128–130] In addition, the ligands used in NC synthesis tend to inhibit catalyst activity and decrease stability.[131,132] Attempts to clean the NC surface by exchanging or removing the ligands with chemical or thermal treatments usually degrade the NC monodispersity,[117,127,131,133–136] although size/shape changes can be suppressed if the NCs are encapsulated within nanostructured materials such as mesoporous silica.[132,137–139]

The advent of a general, scalable approach to uniformly load colloidal NCs onto solid supports while preserving NC size and shape would be valuable for the

development of improved catalysts. This is particularly true for plasmonic photocatalysts,[140] whose optical absorption spectra and local electromagnetic field enhancements depend sensitively on NC size, shape, and coupling with other NCs and the support. To avoid contamination that can reduce catalyst activity and stability, the new approach should employ purified NCs and achieve uniform, tunable NC loading without the need for additives to promote NC-support binding.[132,140–144]

Freeze-drying (lyophilization) offers a way to make uniform supported NCs by avoiding the need to adsorb NCs from a liquid onto a support and preventing unmixing of the NCs and support during drying. Freeze-drying employs rapid freezing at low temperature followed by *in vacuo* sublimation of water to gently produce dehydrated solids. It is a mature technology common in many sectors, most notably the food and pharmaceutical industries.[28] Freeze-drying has been used to dry colloidal NC dispersions to prepare reconstitutable NC powders for improved storage, transport and shelf life.[8,145–149] In addition to NC powders, freeze-drying has been utilized to make supported metal NC catalysts by mixing a support material with a dissolved or molten metal salt, freeze-drying the mixture, and then reducing the metal salt at high temperature to grow metal NCs on the support.[150–154] Kim *et al*. modified this process by chemically reducing the metal salt while it stirred with the support, then filtering, washing, and freeze-drying the resulting solid.[155,156] The application of freeze-drying in these direct NC growth methods generally improves the uniformity of NC loading, but the NC size and shape distributions remain broad and uncontrolled. By employing monodisperse colloidal NCs instead of metal salts, it should be possible to use freeze-drying to produce uniform supported NC catalysts with excellent control of NC size and shape.

Here we show that freeze-drying of aqueous slurries of gold (Au) NCs and a powdered support (cellulose, TiO_2, Al_2O_3, SiO_2, carbon) yields highly-uniform

supported Au NC catalysts with retention of the original NC monodispersity. This freeze-drying process is effective for a range of NC loadings (to at least 20 wt%) and batch sizes (to at least 1 g). By using NCs with a weakly-bound ligand that readily desorbs in water (citrate), we eliminate the calcination step that is normally needed to activate catalysts prepared by NC deposition. The resulting solids are demonstrated to be catalytically active for solution-phase reductive platinum deposition and reduction of 4-nitrophenol to 4-aminophenol. The applicability of the process to different types of NCs is illustrated by preparing gold triangular nanoprisms supported on cellulose and TiO_2. Our work shows that slurry freeze-drying is a simple, reproducible, general, and scalable method to make uniform and active supported NC catalysts from monodisperse colloidal NCs.

2.2. Materials and Methods

2.2.1. Chemicals

All chemicals were used as received unless otherwise noted. 18.2 MΩ water (Millipore Milli-Q Gradient) was used throughout the study. Hydrogen tetrachloroaurate(III) trihydrate ($HAuCl_4 \bullet 3H_2O$, 99.99%) and potassium iodide (KI, 99.9%) were purchased from Alfa Aesar. Trisodium citrate dihydrate (>99.8%) was purchased from MP Biomedical. Microcrystalline cellulose (90 μm average particle size), titanium(IV) oxide (Aeroxide P25), and sodium borohydride ($NaBH_4$, 99%) were purchased from Acros. Cetyltrimethylammonium chloride solution (CTAC, 25 wt% in H_2O), 4-nitrophenol (≥99%), aluminum(III) oxide nanopowder (Al_2O_3 <50 nm) and hexachloroplatinic(IV) acid hydrate ($H_2PtCl_6 \bullet xH_2O$, ≥99.9%) were purchased from Sigma Aldrich. Silicon dioxide (SiO_2) nanopowder (US3435, 98%+, 60-70 nm diameter) and activated carbon nanopowder (US1078, >95%, <100 nm diameter) were purchased from U.S. Research Nanomaterials. L-ascorbic acid and methanol (99.9%) were purchased from Fisher Scientific.

2.2.2. *Synthesis of Spheroidal Au Nanocrystals*

A modified citrate reduction method[157] was used to synthesize spheroidal Au NCs of 12-14 nm diameter. 130 mg of trisodium citrate dihydrate was dissolved in 200 mL of water and heated to boiling on a hot plate with moderate stirring. 4 mL of 25 mM aqueous $HAuCl_4$ was then quickly added to this solution and, after 20 minutes of stirring, the resulting dark red NC dispersion was cooled in an ice bath. The NCs were purified by dialysis filtration using Amicon Ultra-15 Centrifugal Filter Units (UFC905024, 50 kDa cutoff)[158] to remove solutes and loosely-bound ligands (i.e., citrate, NaCl, and other by-products) without subjecting the NCs to precipitation and redispersion cycling that can cause incomplete NC recovery and an altered size distribution. Briefly, 12.5 mL aliquots of the reaction mixture were centrifuge filtered at 3000 rcf for three minutes and the resulting concentrated colloidal retentate (<1 mL volume) was re-diluted to 12.5 mL with water. Each aliquot was filtered again, diluted again, and filtered a third time to give a >2000-fold reduction in solute concentrations with no loss of NCs. The purified aliquots were then combined and diluted with water to a total volume of 20 mL (final NC concentration of ~1 mg/mL).

2.2.3. *Synthesis of Triangular Au Nanoprisms*

We used the seeded growth and purification method of Scarabelli *et al*. to synthesize triangular Au nanoprisms.[52] Spheroidal Au NC seeds were prepared by mixing 50 μL of 25 mM aqueous $HAuCl_4$ with 4.7 mL of 100 mM aqueous CTAC in a 20 mL scintillation vial at room temperature, and then injecting 100 μL of a freshly-made, ice-cold 30 mM $NaBH_4$ solution under vigorous stirring. The seed dispersion was stirred continuously for 2 hours, then diluted tenfold with a 100 mM CTAC solution. To grow the seeds into larger NCs, 200 μL of the seed dispersion was added to a vial containing 80 μL of 25 mM $HAuCl_4$, 1.6 mL of 100 mM CTAC, 15 μL of 10 mM KI, 40 μL of 100 mM ascorbic acid, and 8 mL of water and shaken for 1 second. To grow the large

NCs into triangular nanoprisms of 55-60 nm edge length, 3.2 mL of this colloid was immediately transferred to a 50 mL flask containing 1 mL of 25 mM $HAuCl_4$, 2.86 mL of 25% CTAC, 0.3 mL of 10 mM KI, 400 μL of 100 mM ascorbic acid, and 37.14 mL of water and shaken for several seconds. The flask was left undisturbed for 1 hour at ambient conditions, resulting in a mixed dispersion of nanoprisms and spheroidal NCs. The nanoprisms were selectively flocculated by adding 10 mL of 25% CTAC and allowed to precipitate overnight (16 hours) in a conical-bottom centrifuge tube. The supernatant was removed, and the precipitate redispersed in 20 mL of water, yielding a bright blue dispersion of nanoprisms. In contrast to the NCs, the nanoprisms were not further purified by diafiltration because the centrifuge filters were clogged by CTAC.

2.2.4. Preparation of Supported Nanocrystals

NCs supported on MCC were prepared by adding 0-9 mL of water to 100 mg of MCC powder in a vial, then injecting 0-5 mL of 50 mM aqueous trisodium citrate followed by 1-10 mL of the Au NC dispersion (1 mg/mL NCs), producing a series of slurries with 1, 2, 5, and 10 wt% NCs and 0-25 mM citrate at a total volume of 10 mL. Samples with 20 wt% NC loading were made by adding 50 mg of MCC to 10 mL of the NCs. Each slurry was sonicated for 60 minutes, briefly shaken for 2 seconds to homogenize the slurry, frozen at -78 °C in crushed dry ice for at least 30 minutes, and then freeze-dried in a homebuilt lyophilizer (20 mTorr base pressure) until completely dry (~48 hours). The resulting solids were pink to deep maroon in color (depending on the NC and citrate concentrations) with a sponge-like texture. The BET surface area of the sonicated and freeze-dried MCC (without Au NCs) was measured by nitrogen gas adsorption to be 7 m^2/g.

TiO_2-supported and Al_2O_3-supported NCs with 1 wt% and 5 wt% NCs were made in a similar fashion by mixing 100 mg of P25 TiO_2 or Al_2O_3 nanocrystals in 0-9 mL of water and adding 0-5 mL of 50 mM aqueous trisodium citrate followed by 1-5 mL of

Au NCs for a total volume of 10 mL. The mixtures were shaken to form homogeneous slurries, as sonication was not needed to disperse the TiO_2 and Al_2O_3 nanopowders. The final freeze-dried products were fine to coarse powders with a violet to deep maroon color (depending on the NC and citrate concentrations). The BET surface area of the freeze-dried TiO_2 (without Au NCs or citrate) was measured by nitrogen gas adsorption to be 51 m^2/g. SiO_2-supported NCs (1% NCs) were prepared using an identical procedure.

To prepare carbon-supported NCs (1% NCs), 1 g of carbon nanopowder was added to 20 mL of 8 M aqueous HNO_3 in a scintillation vial. The mixture was briefly shaken and aged at room temperature for 90 minutes. The slurry was then neutralized with excess sodium bicarbonate (Macron Fine Chemicals, 7412-06), vacuum filtered, washed with water, and dried in an oven at 100 ºC for 1 hour. Next, a NC/support slurry was made by mixing 100 mg of the support, 9 mL of water, and 1 mL of the 1 mg/mL NC dispersion. The slurry was freeze-dried as described above.

2.2.5. Preparation of Supported Nanoprisms

Nanoprisms supported on MCC were prepared by adding 100 mg of sonicated and freeze-dried MCC powder to 10 mL of the nanoprism dispersion. This slurry was shaken to suspend the cellulose particles, frozen in crushed dry ice for at least 30 minutes, and then freeze-dried as described above. Sonication of the slurry was avoided to prevent possible changes to the shape of the nanoprisms. The product was a fine powder light blue in color. TiO_2-supported nanoprisms were prepared similarly, using 100 mg of P25 TiO_2 powder and 10 mL of the nanoprism dispersion. The final freeze-dried product was a fine powder with a vivid light blue color. No citrate was added to either nanoprism slurry.

2.2.6. Materials Characterization

Transmission electron microscopy (TEM) was performed on JEOL JEM-2100 and JEOL JEM-2800 TEMs at accelerating voltages of 200 kV. Samples were prepared by drop casting and drying 5 μL of the supported nanocrystal/nanoprism suspension on a standard TEM grid (#01824, Ted Pella) in air. Samples for optical extinction spectra were made by sandwiching 100 μL of supported nanocrystal/nanoprism suspension between two microscope cover slips and allowing the suspension to dry overnight. Optical transmittance (T) and reflectance (R) spectra (λ = 400-800 nm) were acquired on a PerkinElmer Lambda 950 spectrophotometer equipped with a 60 mm integrating sphere. Optical absorbance was calculated using the following equation: absorbance $= -\log(R + T)$. 4-nitrophenol reduction experiments were carried out in 4.5 mL polystyrene cuvettes (759071D, BrandTech) in standard transmission geometry.

Attenuated total reflectance Fourier transform infrared (ATR-FTIR) spectra were measured with Nicolet 6700 FTIR spectrometer with GladiATR™ diamond ATR module (Pike Technologies) using 256 scans at 2 cm^{-1} resolution. The samples presented in Figure 2.8 were made by depositing 100 μL of solution onto the ATR crystal and drying in a stream of nitrogen. The samples presented in Figure 2.14 were prepared by drop casting and drying 20 μL of a 20 mg/mL suspension of the supported NCs onto the ATR crystal. *In situ* water rinsing was performed by covering the sample with 20 μL of pure water, gently wicking the water away with a Kimwipe after 5 minutes, and allowing the sample to dry.

Thermogravimetric analysis (TGA) was performed on a TA Q500 TGA. Samples were placed on tared platinum pans and heated at a ramp rate of 20 °C/min from room temperature to 500 °C under constant nitrogen purge. Powder X-ray diffraction (XRD) was performed on a Rigaku SmartLab in Bragg-Brentano geometry using zero background plates. Samples were scanned from 10 to 60 degrees with a step

size of 0.05 degree at a scan rate of 6 degrees/min. The surface area of the freeze-dried MCC and TiO_2 supports was measured with a Micromeritics 3Flex Surface Characterization Analyzer using nitrogen as the adsorption gas.

2.2.7. Thermal Reduction of Platinum on Supported Au Nanocrystals

Pt nanocrystals were deposited on MCC-supported Au NCs (5 wt%) by adding 40 mg of the supported NCs, 500 μL of 10 mM H_2PtCl_6, and 1 mL of methanol to 8.5 mL of water in a 25 mL two-neck round bottom flask fitted with a condenser. This mixture was degassed and refluxed at 65 °C for six hours with constant argon purging and stirring. The resulting dark grey solid was collected by centrifugation and washed three times with water to remove residual Pt salts, by-products, and methanol.

2.2.8. Catalytic Reduction of 4-nitrophenol to 4-aminophenol

Reduction of 4-nitrophenol to 4-aminophenol on the surface of the Au NCs was studied by *in situ* optical extinction spectroscopy in stirred cuvettes cooled to 15 °C with a recirculating bath (LT ecocool 150, Grant Instruments). Experiments were performed at both 1 wt% and 5 wt% NC loadings. 1 mg/mL suspensions of the MCC- and TiO_2-supported NCs were prepared by adding 4 mg of the supported NC powder to 4 mL of water and stirring. In the 5 wt% tests, 1.0 mL of freshly-made 45 mM $NaBH_4$ and 60 μL of the supported NC suspension were added to 1.88 mL of water in a 4.5 mL cuvette and stirred for five minutes at 15 °C, at which time 60 μL of a 5 mM 4-nitrophenol solution was injected into the cuvette to initiate the reaction. The 1 wt% NC tests used 1.64 mL of water and 300 μL of the supported NC suspension. Control experiments with unsupported colloidal NCs were performed using 1.91 mL of water, 1.0 mL of 45 mM $NaBH_4$, 30 μL of a 100 μg/mL NC dispersion, and 60 μL of 5 mM 4-nitrophenol. Initial reactant and NC concentrations were the same in all cases (100 μM 4-nitrophenol, 15 mM $NaBH_4$, and 1 μg/mL NCs). Loss of 4-nitrophenolate was monitored by

recording its absorption peak at λ = 400 nm under continuous temperature control and stirring.

2.3. Results

2.3.1. Process of Fabricating Supported Nanocrystals

Figure 2.1a outlines the process used here to load pre-formed gold NCs onto solid supports. Spheroidal, citrate-capped Au NCs with a diameter of 12-14 nm were synthesized in water using a published method[159] and purified by centrifuge dialysis filtration, which removes molecular solutes without causing aggregation or loss of NCs (see Materials and Methods and Figure 2.8).[160–162]

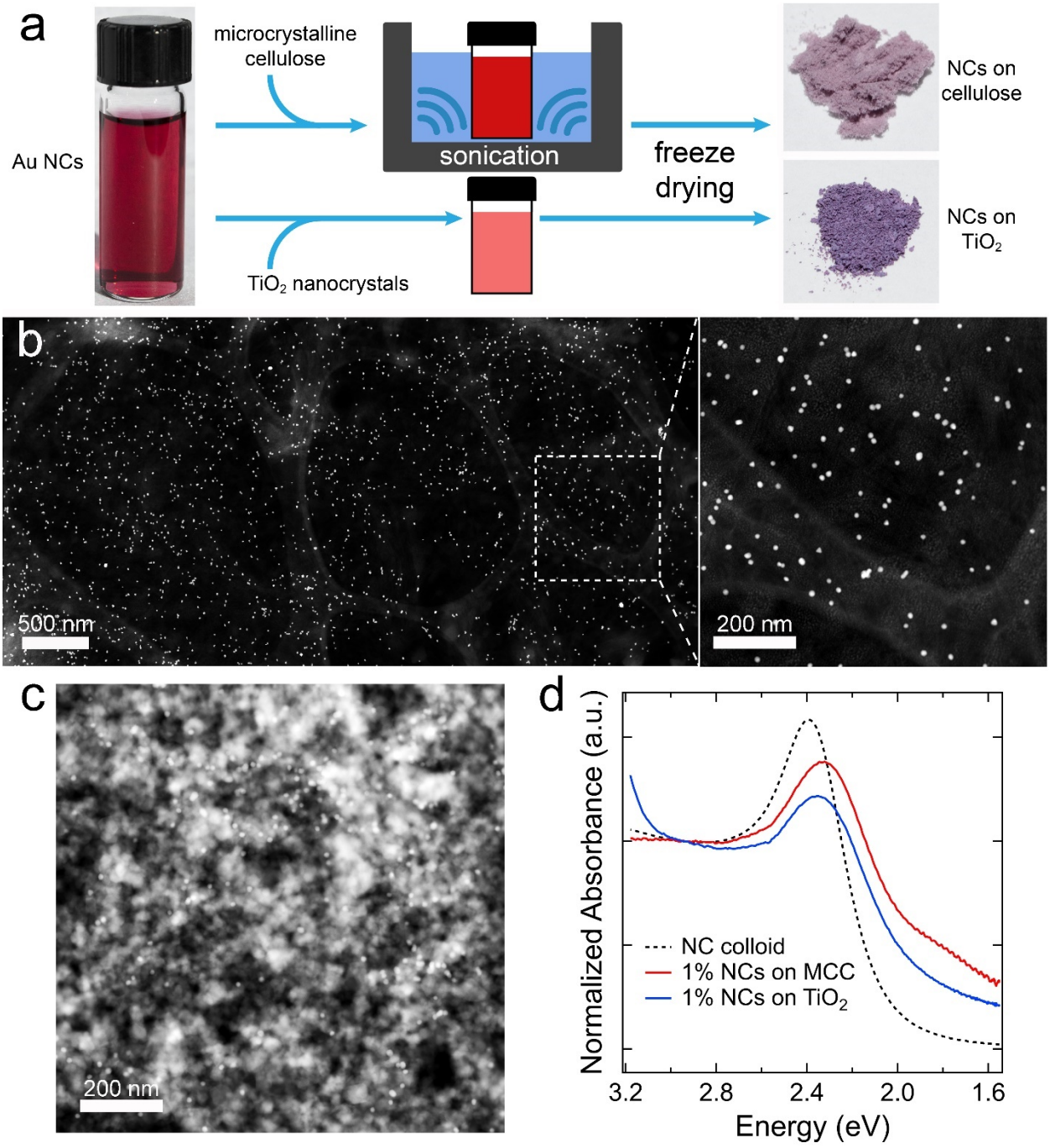

Figure 2.1 Preparation of well-dispersed gold NCs on high surface area solid supports by freeze-drying. (a) The process flow. Purified gold NCs in water are mixed with a powder of the support (microcrystalline cellulose, TiO_2 nanocrystals or Al_2O_3, SiO_2 or carbon nanoparticles), sonicated (for cellulose only) and shaken, and then freeze-dried to yield a porous, high surface area solid uniformly loaded with well-

dispersed NCs. (b) Low-magnification dark-field STEM image of 1 wt% Au NCs on MCC prepared without added citrate. This image shows a particularly flat region of the sample so that all of the NCs are in focus. At right is a magnified view of the region outlined in the dashed box. (c) Dark-field STEM image of 1 wt% NCs on nanocrystalline TiO_2, also prepared without added citrate. The small whitish spheroids are the NCs. (d) Optical absorbance spectra of dried layers of these NC/MCC and NC/TiO_2 samples. A spectrum of the aqueous dispersion of the NCs is shown for comparison. All spectra are normalized at λ = 420 nm ($h\nu$ = 2.95 eV). (Reprinted with permission from Ref.[163] Copyright 2021 American Chemical Society)

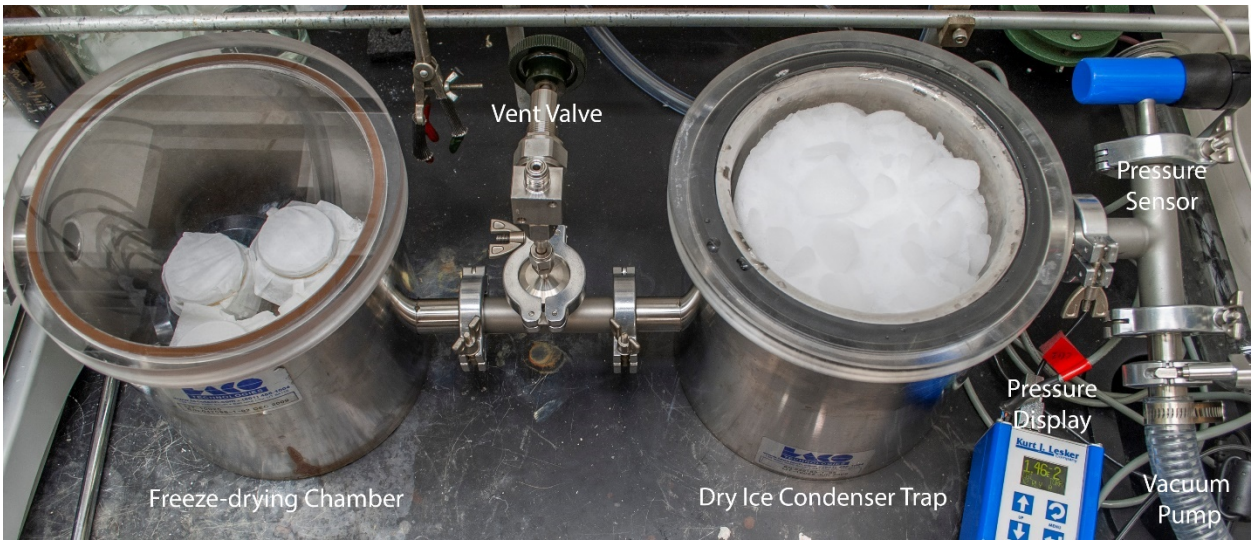

Figure 2.2 Photograph of the homebuilt lyophilizer apparatus used in this work. The base pressure of this setup is ~20 mTorr. (Reprinted with permission from Ref.[163] Copyright 2021 American Chemical Society)

A known amount of a powdered support material (microcrystalline cellulose (MCC), TiO_2 nanocrystals, γ-Al_2O_3 nanocrystals, SiO_2 nanoparticles, or carbon nanopowder) was then added to the purified NC dispersion and the mixture shaken (for TiO_2, Al_2O_3, SiO_2, and carbon) or sonicated and then shaken (for MCC) to make a

homogeneous slurry, frozen in dry ice at -78 °C, and freeze-dried in a homebuilt lyophilizer Figure 2.2.

MCC was selected for study because it is an insoluble, chemically robust, and low-cost organic support, while TiO_2, γ-Al_2O_3, SiO_2 and activated carbon are common inorganic supports. We found that sonication was necessary to form homogeneous MCC slurries by decreasing the MCC particle size, but sonication also partially amorphized the cellulose, which probably decreases its thermal and chemical stability Figure 2.3. Sonication was not needed for the TiO_2, Al_2O_3, SiO_2 and activated carbon slurries because these supports formed stable suspensions upon brief shaking.

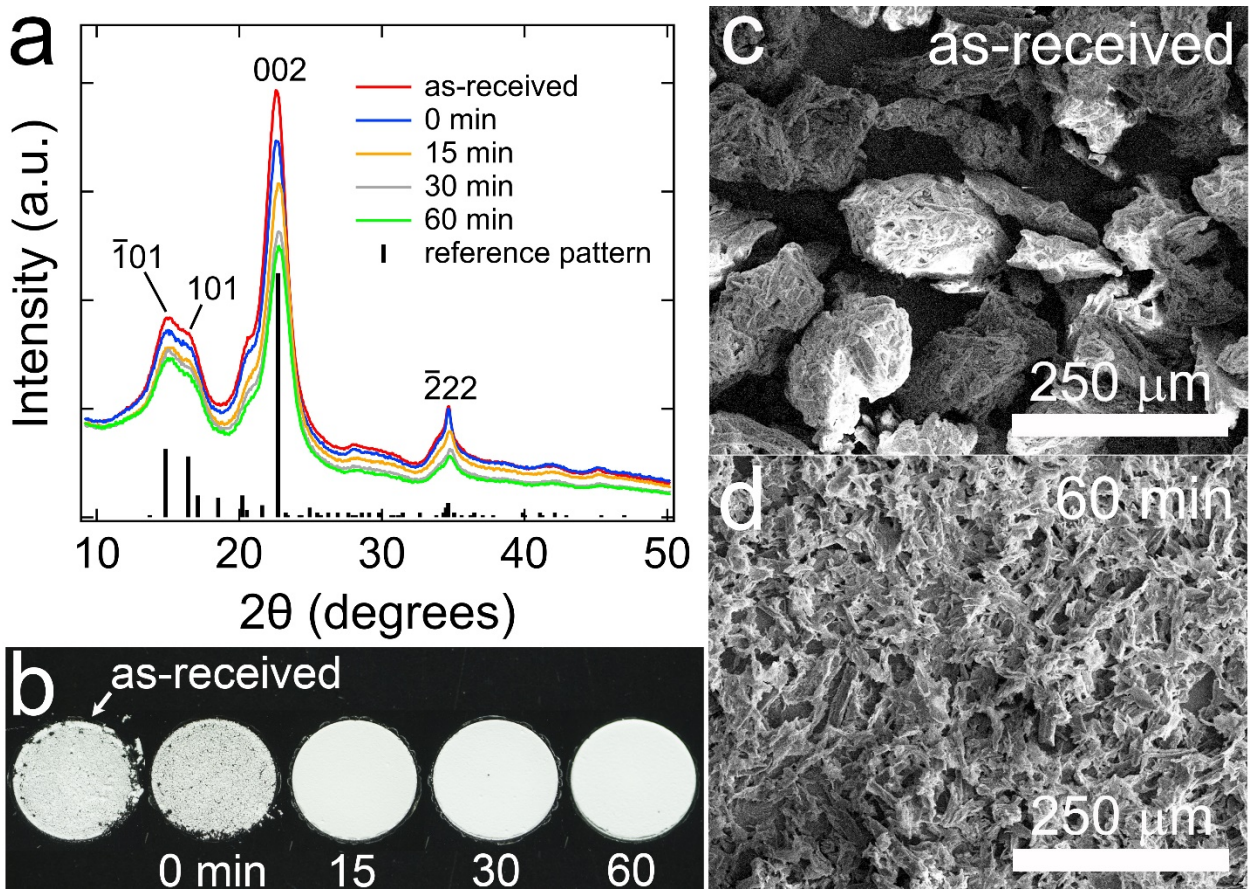

Figure 2.3 Sonication and freeze-drying reduces the crystallinity and alters the particle size and morphology of microcrystalline cellulose (MCC). (a) X-ray diffraction patterns of as-received MCC powder and MCC powder that was sonicated for 0, 15, 30

or 60 minutes and then freeze-dried. The data show a progressive loss of crystallinity with increasing sonication time. A standard powder pattern for cellulose Iβ (PDF# 0-060-1502) is shown for reference. (b) Photographs of as-received MCC powder and freeze-dried MCC powder prepared with 0, 15, 30 or 60 minutes of sonication. The powders were suspended in water and drop cast onto a glass microscope slide. (c) SEM image of drop-cast as-received MCC powder on a silicon substrate. (d) SEM image of MCC powder after 60 minutes of sonication and freeze-drying. Sonication reduced the MCC particle size, increased the porosity, and yielded more stable MCC suspensions, thereby enhancing the uniformity of Au NC loading during freeze-drying. (Reprinted with permission from Ref.[163] Copyright 2021 American Chemical Society)

The resulting freeze-dried products are uniform in color and texture. For example, MCC and TiO_2 loaded with 1 wt% NCs and no added sodium citrate (*vide infra*) have a uniform pink and violet color, respectively, suggesting that the NCs are distributed homogeneously throughout both supports (Figure 2.1a). Scanning transmission electron microscopy (STEM) images confirm that the NCs are intact and well dispersed on both MCC and TiO_2 (Figure 2.1b-c and Figure 2.4). A comparison of secondary electron and dark-field STEM images shows that the NCs are distributed over all of the solution-accessible surfaces of the support rather than being located only on the outer surface of the support agglomerates (Figure 2.4 and Figure 2.5).

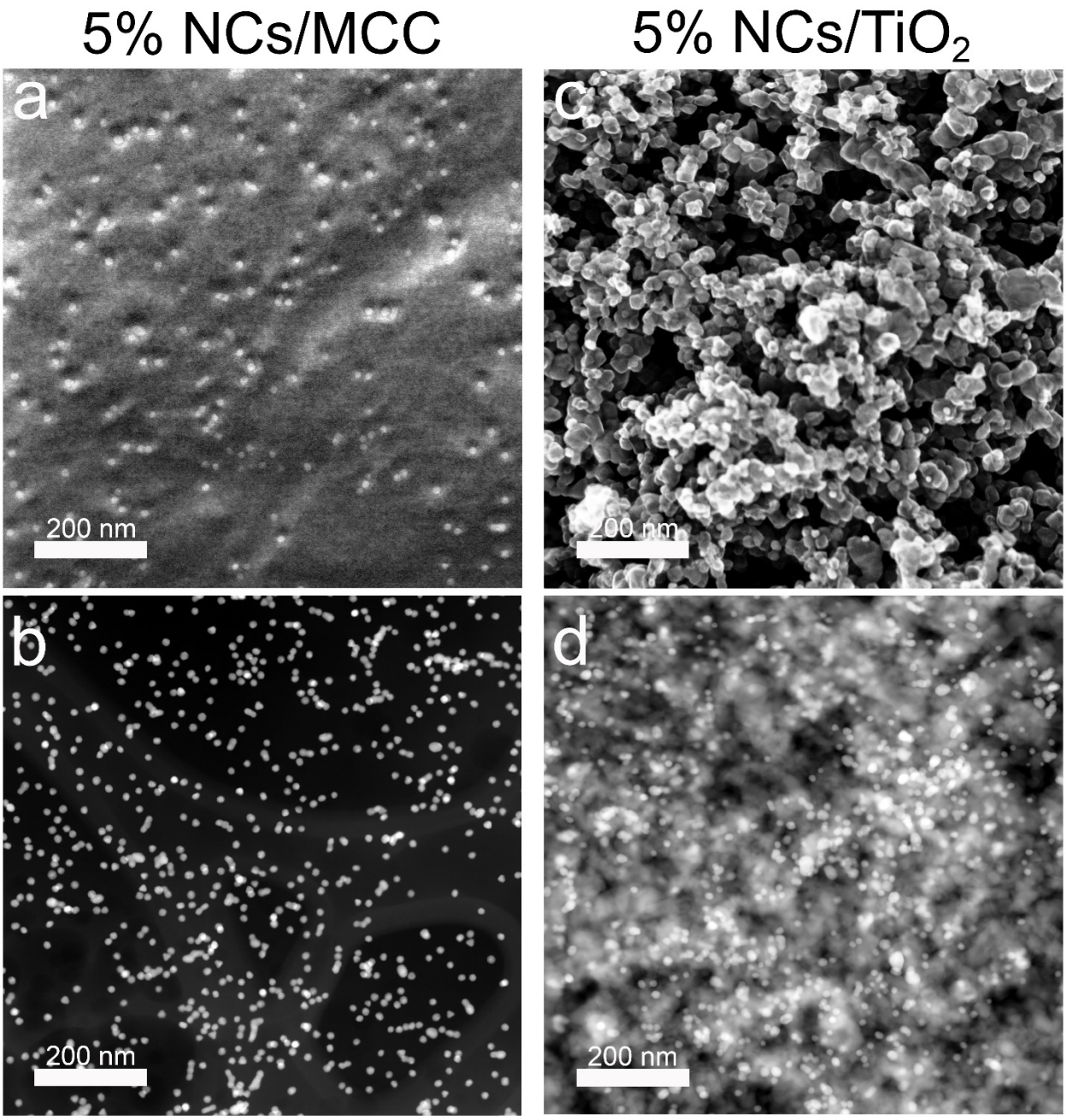

Figure 2.4 STEM images of 5% NCs on MCC and TiO_2 supports made without added citrate. (a) Secondary electron image (SEI) of the top surface of a representative NC/MCC sample. (b) Dark-field STEM image of the same region, revealing all of the Au NCs (bright spots) in projection. (c-d) Corresponding SEI and dark-field STEM images of a NC/TiO_2 sample. Most of the NCs are buried amongst the TiO_2 crystallites and

therefore obstructed in the SE image. (Reprinted with permission from Ref.[163] Copyright 2021 American Chemical Society)

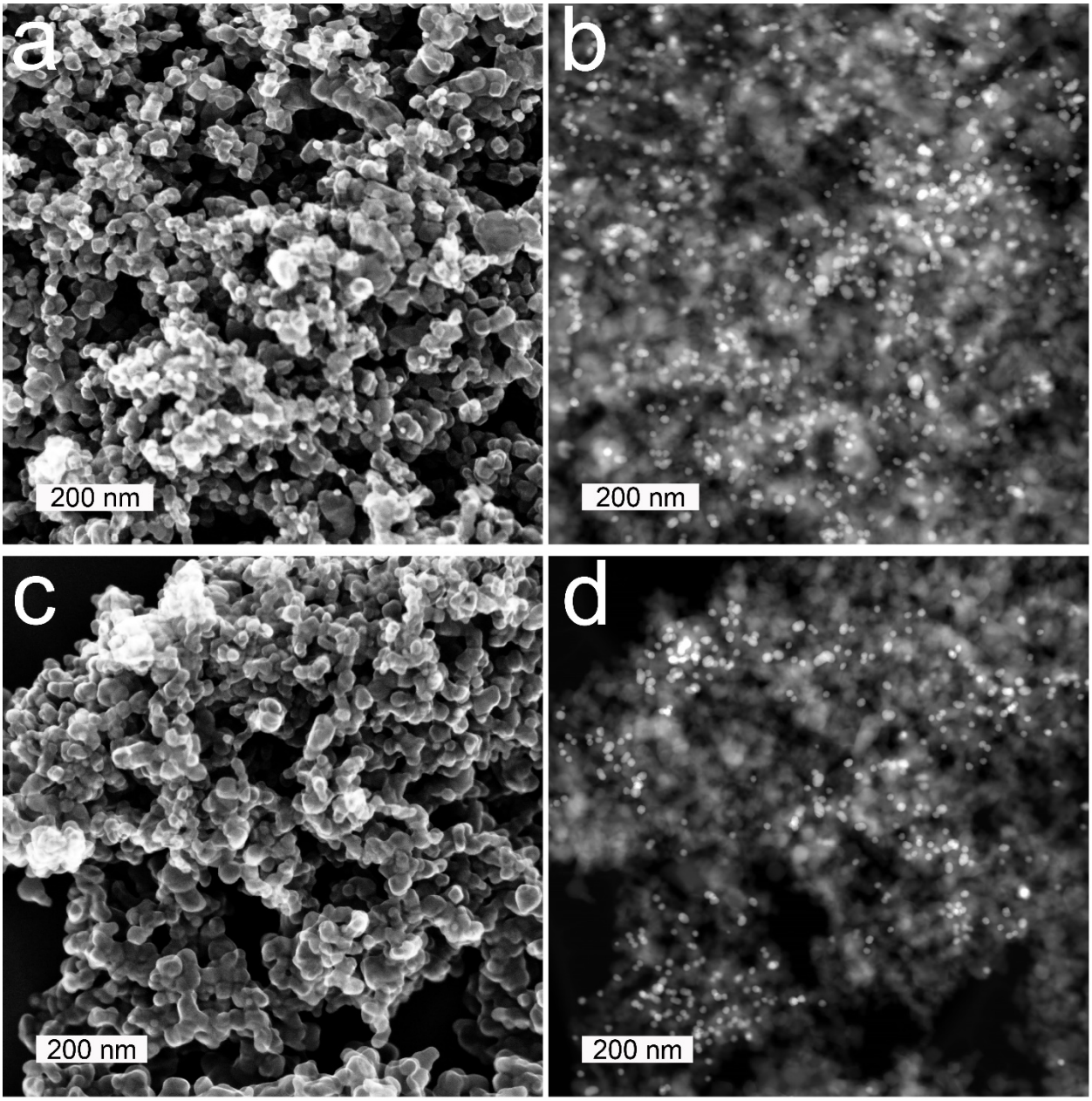

Figure 2.5 Additional STEM images of 5% NCs on TiO_2 made without added citrate. (a) Secondary electron image (SEI) of the top surface of one area of the sample. Only the Au NCs near to or on the top surface of the sample are visible. (b) Corresponding dark-field image of the same region, revealing all of the Au NCs (bright spots) in projection.

Comparison with the SEI proves that most of the NCs are buried amongst the TiO_2 crystallites rather than sitting on the outer surface of the support. (c-d) Secondary electron and dark-field images of another area of the sample. (Reprinted with permission from Ref.[163] Copyright 2021 American Chemical Society)

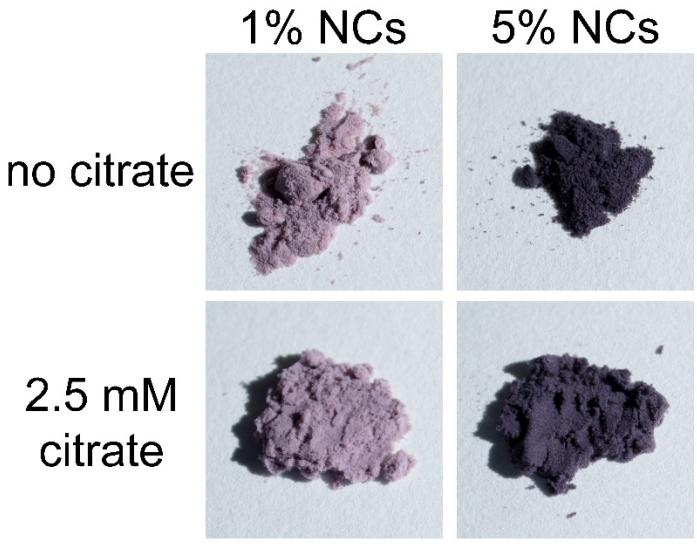

Figure 2.6 Photographs of Au NCs loaded onto γ-Al_2O_3 nanopowder by freeze-drying. 1 or 5 wt% NCs were loaded with or without 2.5 mM sodium citrate onto ~50 nm γ-Al_2O_3 nanocrystal powder. (Reprinted with permission from Ref.[163] Copyright 2021 American Chemical Society)

The NC/MCC solids have a fluffy, sponge-like texture, while the NC/TiO_2 solids are coarse, free-flowing powders. Slurry freeze-drying also yielded uniform loading of the 12-14 nm diameter NCs onto nanocrystalline γ-Al_2O_3 (Figure 2.6), SiO_2 and carbon supports (Figure 2.7), as well as ~3.5 nm diameter citrated-capped NCs on MCC and TiO_2 supports (Figure 2.7), further demonstrating the versatility of this method for making supported NCs on different supports.

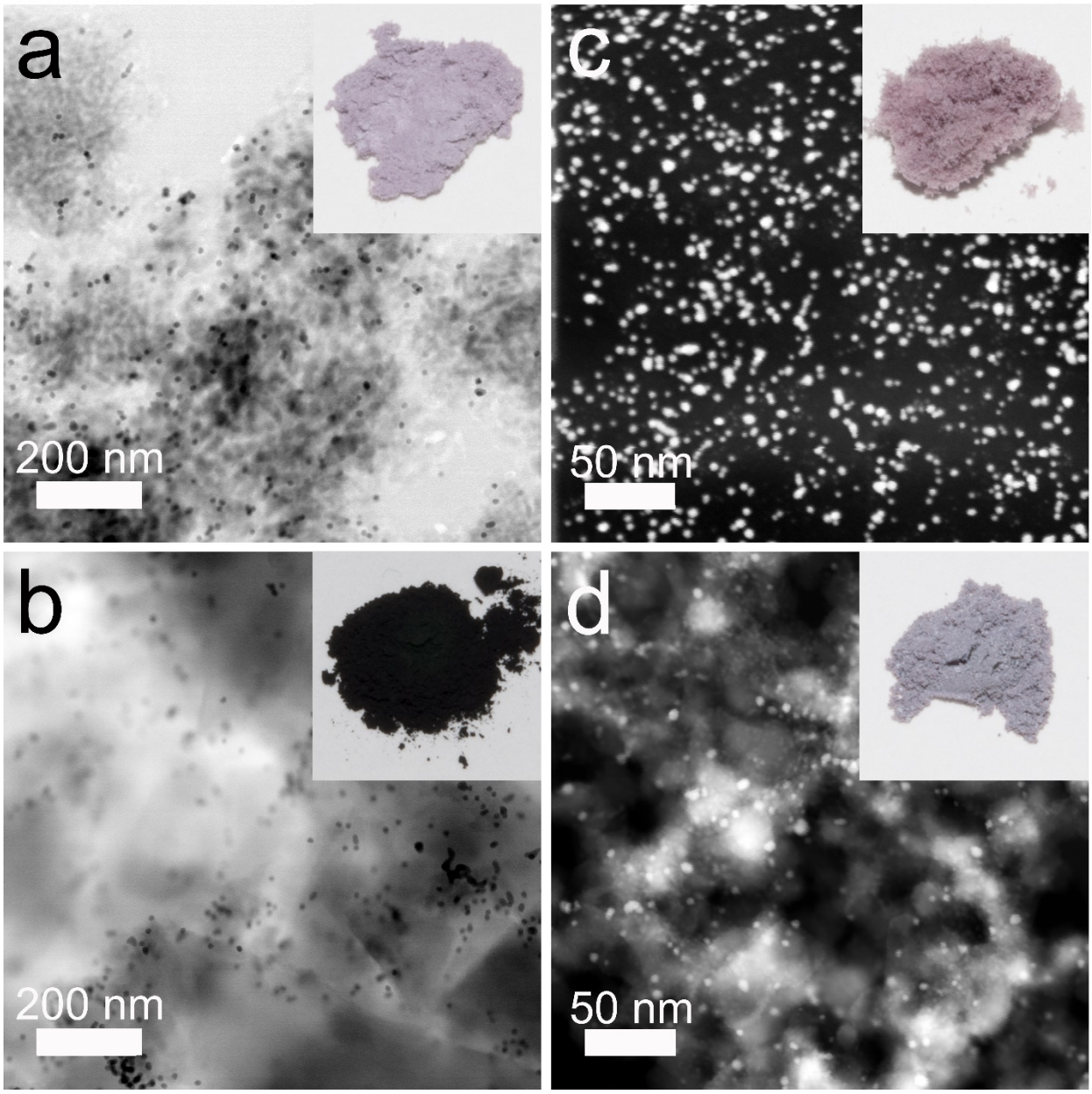

Figure 2.7 Additional STEM images of NC/support combinations. Dark-field STEM images of (a) the normal Au NCs on SiO_2, (b) the normal Au NCs on carbon, (c) 3.5 ± 0.5 nm diameter citrated-capped Au NCs on MCC, and (d) 3.5 ± 0.5 nm diameter citrate-capped Au NCs on TiO_2. Inset are photographs of each sample. All samples are 1% NCs by mass. The small NCs were synthesized using a modified published procedure.[164] (Reprinted with permission from Ref.[163] Copyright 2021 American Chemical Society)

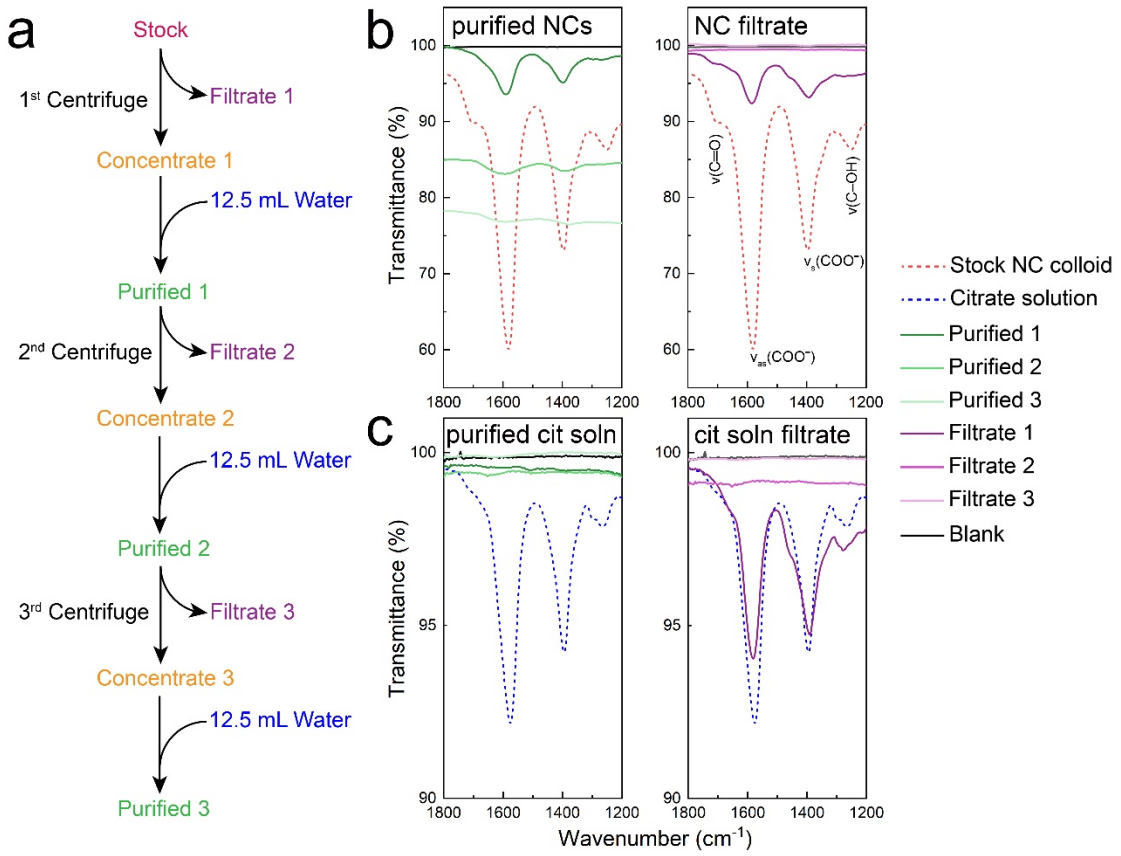

Figure 2.8 Purification of colloidal Au NCs by centrifuge dialysis filtration. (a) Diagram of the experimental workflow. A stock NC dispersion was concentrated ~10× by centrifuge filtration and then re-diluted to its original volume with ultrapure water. This cycle was repeated a total of three times to remove molecular impurities from the colloid without the need for NC precipitation and redispersion that can cause NC aggregation, loss of NCs and an altered NC size distribution. Based on the liquid volumes involved, we estimate that the concentration of molecular solutes in the triply-purified NCs was decreased by approximately a factor of 10^3. (b) ATR-FTIR spectra of a dried droplet of the purified colloid (green traces) and filtrate (purple curves) after each cycle. The spectrum of a dried droplet of the stock colloid is also shown (dashed red line). Several citrate peaks are labeled,[165,166] including the symmetric and asymmetric RCOO- stretches at 1396 cm^{-1} and 1580 cm^{-1}, respectively, the RC-OH stretch of the central citrate carbon at 1250 cm^{-1}, and the carbonyl (C=O) stretch at ~1700 cm^{-1}. The

decrease in baseline transmittance with each NC purification cycle is caused by increased light scattering from the larger NC aggregates that form upon drying dispersions with successively lower citrate concentration. (c) ATR-FTIR spectra of the purified fractions (green traces) and filtrate fractions (purple traces) of a 2.2 mM aqueous sodium citrate solution (no NCs). The spectrum of a dried droplet of the stock citrate solution is also shown (dashed blue line). In each cycle, the same amount of solution was passed through the filter and the same amount of pure water added to re-dilute the sample as in (b). Since no citrate peaks were detected in the purified or filtrate fractions after the first cycle, we conclude that the free citrate in solution was effectively removed by this filtering process and assign the small citrate signal in the spectrum of the triply-purified NCs in (b) to residual citrate ligand that remains bound to the NCs, rather than free citrate. (Reprinted with permission from Ref.[163] Copyright 2021 American Chemical Society)

2.3.2. Optical Behavior

Optical absorbance spectra of 1% NCs on MCC and TiO_2 determined using an integrating sphere are shown in Figure 2.1d (see Materials and Methods). The spectra are normalized at a wavelength of 420 nm to roughly equalize the volume of gold in each spectrum[53,167] and emphasize differences in the energy, intensity, and linewidth of the localized surface plasmon resonance (LSPR) compared to the LSPR of the dispersed NCs (dashed spectrum in Figure 2.1d). The spectra were fit to the following expression:

Equation 1
$$\mathrm{Abs}(E) = \frac{c_0}{\pi}\frac{\gamma_0/2}{(E-E_0)^2+(\gamma_0/2)^2} + \frac{c_1}{1+e^{-\left(\frac{E-E_1}{\gamma_1}\right)}} + \frac{c_2}{1+e^{-\left(\frac{E-E_2}{\gamma_2}\right)}}$$

consisting of a Lorentzian LSPR with peak energy E_0 and linewidth (FWHM) $\gamma 0$ and sp←d interband transitions (ITs) described by switching functions at E_1 = 2.4 eV (visible IT) and E_2 = 3.4 eV (UV IT) with transition widths γ_1 and γ_2, respectively.[96,168] The NC colloid has a single-component Lorentzian LSPR with E_0 = 2.37 eV and γ_0 = 0.32 eV. The

LSPR of the NCs supported on MCC and TiO_2 is also reasonably well fit by a single Lorentzian peak, but the peak is redshifted and broadened compared to the LSPR of the NCs in solution (Figure 2.9 and Table 2.1). We attribute this redshifting and broadening primarily to (*i*) the larger dielectric constant of the environment of the supported NCs[38,169,170] (the real part of the dielectric constants of water, cellulose, and TiO_2 at 520 nm are 1.78, 2.17,[171] and ~8,[172,173] respectively), (*ii*) the more heterogeneous dielectric environment of the supported NCs, and (*iii*) electromagnetic coupling between some of the supported NCs in each sample. Absorbance tails in the red (<2 eV) are caused by a small population of clustered NCs on each support, which are visible in the TEM images (Figure 2.1b-c). The shoulder at ~1.8 eV in the NC/MCC spectrum may indicate a greater number of strongly-coupled NCs on MCC than on TiO_2, possibly due a larger number of small NC clusters (i.e., dimers and trimers) that form on the large, sheet-like, low-surface-area MCC particles (see Figure 2.1 and Figure 2.3). The absorbance tail at >3 eV (<415 nm) in the NC/TiO_2 spectrum results from light absorption by TiO_2.

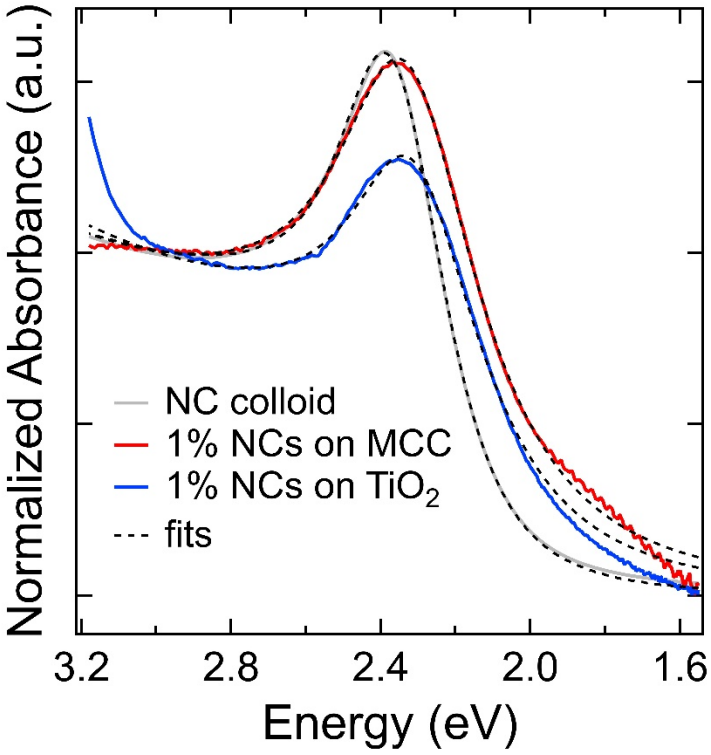

Figure 2.9 Fits of the three absorbance spectra in Figure 2.1. (Reprinted with permission from Ref.[163] Copyright 2021 American Chemical Society)

Sample	LSPR			Visible IT			UV IT		
	E_0 (eV)	γ_0 (eV)	c_0 (OD)	E_1 (eV)	γ_1 (eV)	c_1 (OD)	E_2 (eV)	γ_2 (eV)	c_2 (OD)
1% NCs/MCC	2.33	0.470	0.899	2.40	0.192	0.800	3.30	0.238	0.485
1% NCs/TiO_2	2.31	0.439	0.640	2.38	0.185	0.826	3.25	0.216	0.500
NC colloid	2.37	0.324	0.456	2.25	0.082	0.819	3.30	0.265	0.500

Table 2.1 Fitting parameters from fits of absorbance spectra.

2.3.3. Nanocrystal Distribution

Figure 2.10 shows images and spectra of NC/MCC samples with NC loadings of 1, 5 and 20 wt%. With increasing NC loading, the sample color changes from mauve to

deep violet and then nearly black (Figure 2.10a-c). TEM images show that the NCs remain well dispersed but form an increasing number of small NC clusters at higher NC loading. The normalized absorbance spectra (Figure 2.1d) show a progressive weakening of the LSPR of the isolated NCs (at 2.35-2.4 eV) and growing absorption at lower energies as a result of increased inter-NC optical coupling due to the higher NC density and more prevalent clustering. The high-energy LSPR decreases in intensity because there are fewer isolated NCs and more clusters that lack strong plasmon modes at this energy (e.g., non-linear trimers and larger aggregates). At the same time, NC coupling and clustering produce a multitude of new plasmon modes at low energy, eventually resulting in strong panchromatic absorption across the visible and near infrared spectrum that yields a black material at 20% NC loading.

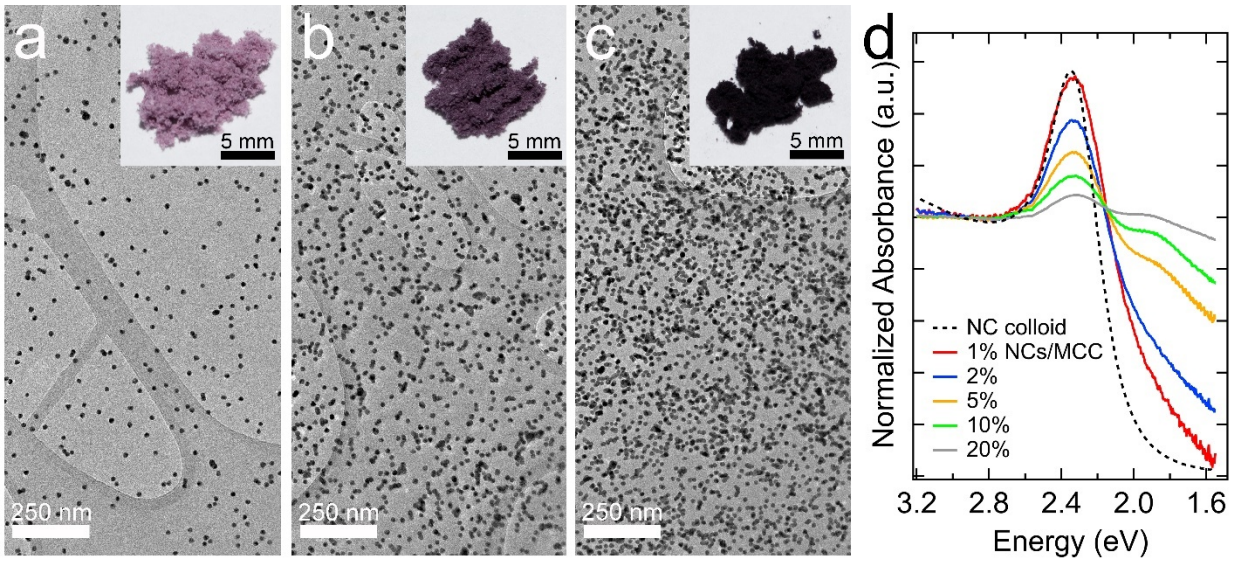

Figure 2.10 NC/MCC powders as a function of NC loading. TEM images and photographs of samples with (a) 1 wt%, (b) 5 wt%, and (c) 20 wt% NC loading. Higher NC loading results in more NC clustering. Some of the NCs within the cluster appear to have fused together into larger NCs, probably as a result of electron beam heating. (d) Optical absorbance spectra of dried layers of NC/MCC samples with 1, 2, 5, 10, and 20 wt% NCs compared to a spectrum of the aqueous dispersion of the NCs. The spectra

are normalized for total gold volume at λ = 420 nm. All samples were prepared without added citrate. See Figure 2.11 for for photographs of MCC samples with 0-20 wt% NCs. (Reprinted with permission from Ref.[163] Copyright 2021 American Chemical Society)

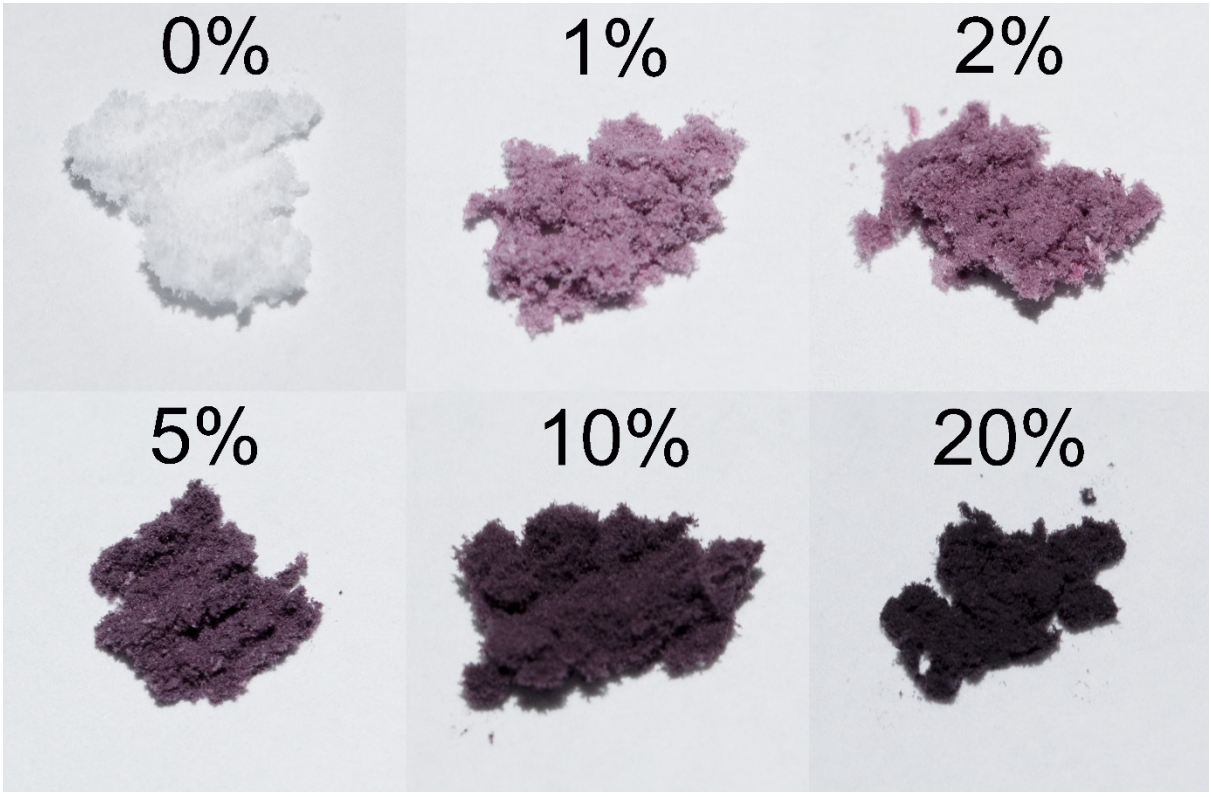

Figure 2.11 Photographs of NC/MCC samples with 0, 1, 2, 5, 10, and 20 wt% NCs. All samples were prepared without added citrate. (Reprinted with permission from Ref.[163] Copyright 2021 American Chemical Society)

2.3.4. Effect of Citrate Addition

The extent of NC clustering on MCC and TiO_2 could be reduced by adding trisodium citrate to the slurries prior to freeze-drying. As an anionic ligand, citrate can enhance inter-NC electrostatic repulsion[173] and thereby reduce the tendency for NCs to aggregate during the freeze-drying process. Citrate adsorption also reduced the aggregation of the support particles. Figure 2.12 compares photographs, absorbance spectra, and TEM images of NC/MCC and NC/TiO_2 samples (1% NC loading) made

with 0 versus 2.5 mM citrate. Citrate addition changes the color of the powders from mauve (for MCC) or violet (for TiO_2) to red-violet, much closer to the color of the colloidal NC dispersion. The optical spectra show decreased absorption at low energy and narrower LSPRs, consistent with less NC clustering in the citrate-spiked samples. TEM images verified that the number and size of the NC clusters are reduced upon citrate addition. The effect of citrate increased with citrate concentration and was larger for (*i*) 5% than 1% NC loading and (*ii*) TiO_2 than MCC supports because NC clustering and support particle aggregation are more significant in such samples (Figure 2.13).

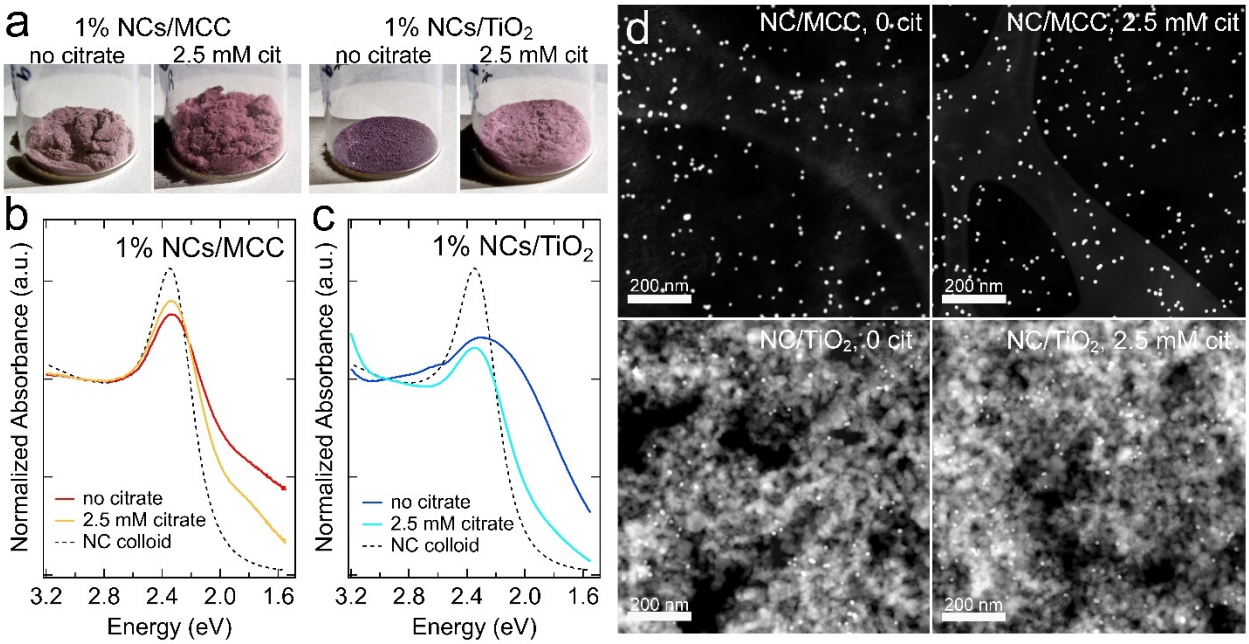

Figure 2.12 The effect of citrate addition on Au NC clustering and support porosity. (a) Photographs, (b-c) absorbance spectra, and (d) representative dark-field STEM images of 1% NC/MCC and NC/TiO_2 samples made with 0 or 2.5 mM citrate. The spectrum of an aqueous dispersion of the NCs is also shown. All spectra are normalized at λ = 420 nm. (Reprinted with permission from Ref.[163] Copyright 2021 American Chemical Society)

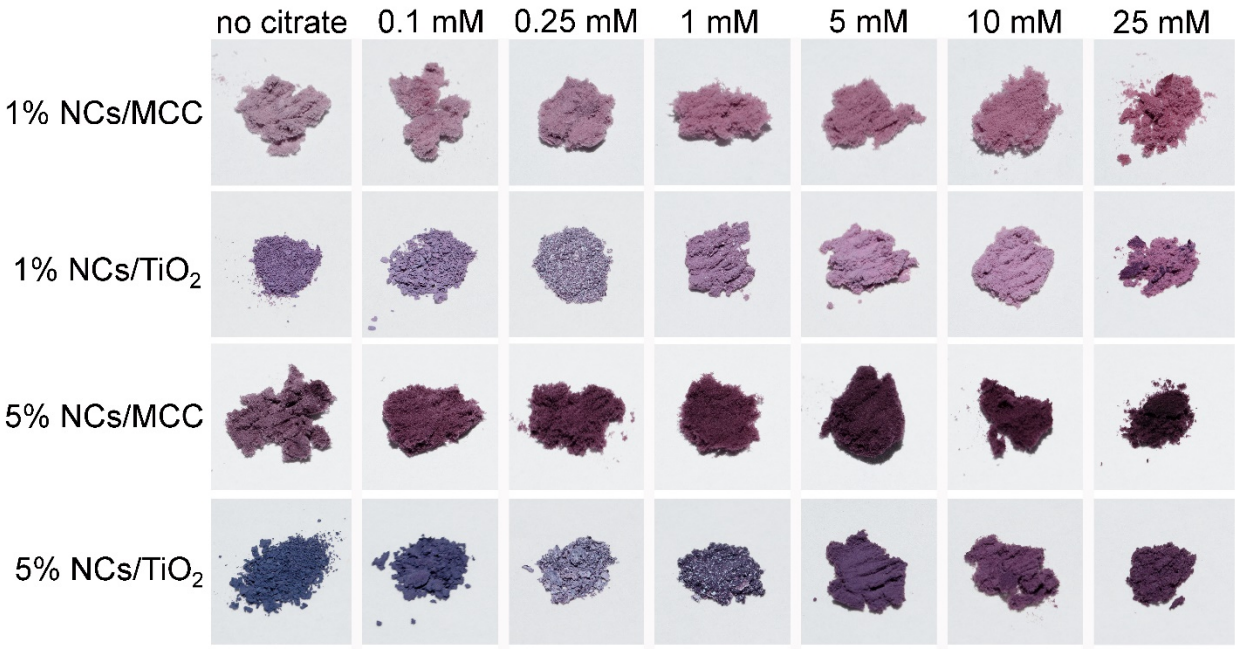

Figure 2.13 Photographs of NC/MCC and NC/TiO_2 samples (1% and 5% NC loading) as a function of the amount of citrate added prior to freeze-drying (0-25 mM). (Reprinted with permission from Ref.[163] Copyright 2021 American Chemical Society)

Importantly, the added citrate was easily removed after freeze-drying by rinsing the supported NCs with water at room temperature to yield cleaner NC surfaces.[140] Attenuated total reflectance Fourier transform infrared (ATR-FTIR) spectra show that water rinsing (solvent extraction) lowers the citrate concentration below the instrument detection limit (Figure 2.14). Moreover, the color of the rinsed samples was unchanged, indicating that citrate removal was achieved without causing significant NC clustering. A major advantage of using a charged, weakly-bound, and soluble ligand like citrate is that it can be added to tune the degree of NC clustering on the support and then removed with a mild treatment (such as rinsing in water at room temperature) to expose the NC surfaces for catalysis.

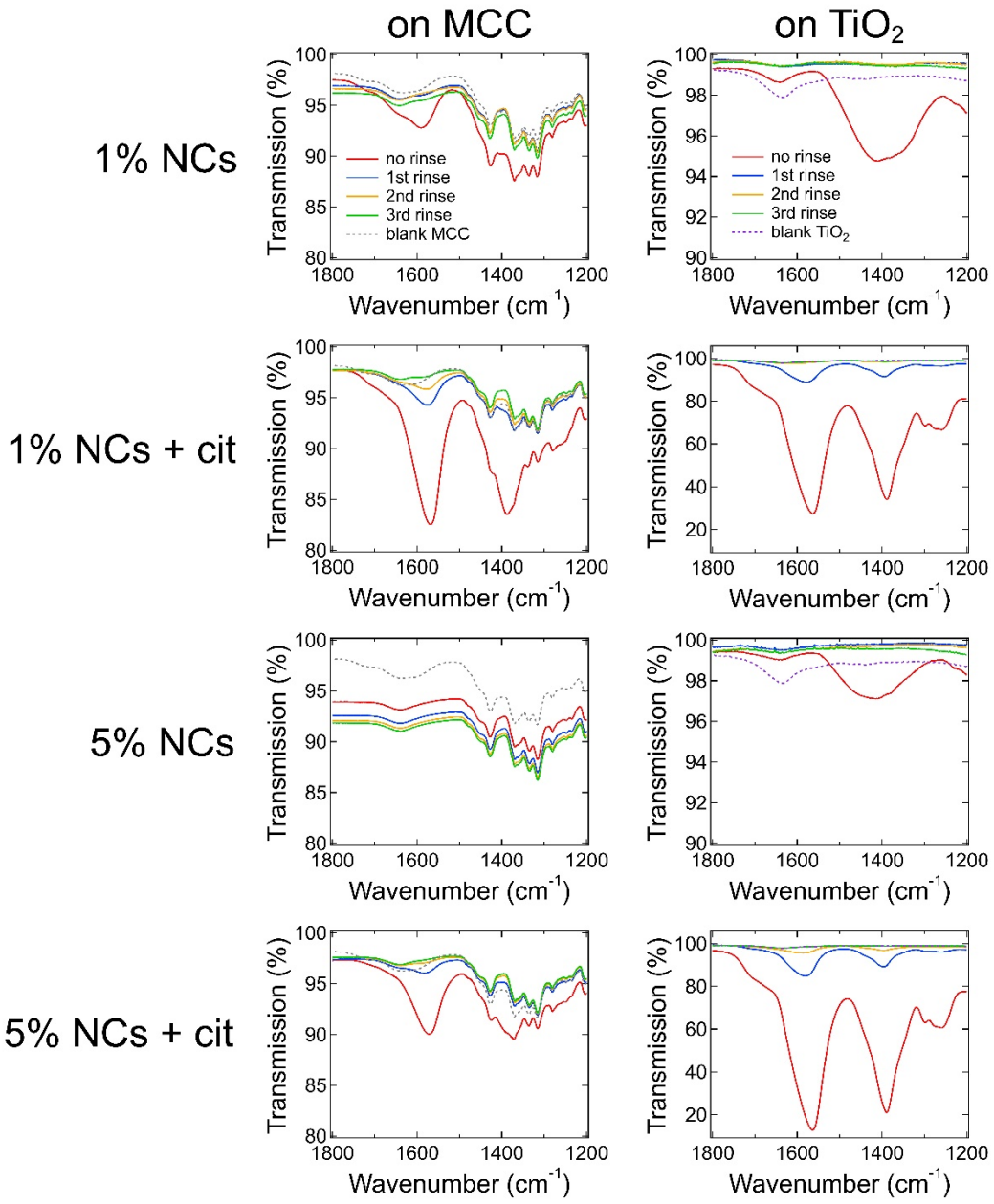

Figure 2.14 ATR-FTIR transmission spectra of NC/MCC and NC/TiO_2 samples as a function of water rinsing. Samples were prepared by drop casting and drying 20 µL of a 20 mg/mL suspension of the supported NCs onto a clean ATR crystal. Spectra of the as-made samples before water rinsing (red lines) show the presence of citrate in all samples but one (5% NCs on MCC). The prominent citrate peaks occur at 1390-1400 cm^{-1} and 1565-1580 cm^{-1} (see Figure 2.8). Water rinsing was performed by covering the

sample with 20 μL of pure water, gently wicking the water away with a Kimwipe after 5 minutes, and allowing the sample to dry. This procedure minimized mechanical disturbance to the samples and prevented loss of any of the supported NCs from the ATR crystal. The spectra show that repeated water rinsing lowers the citrate signal (bound and free citrate) below the instrument detection limit. Spectra of pure MCC and TiO_2 without NCs or citrate are shown for reference (dashed lines). (Reprinted with permission from Ref.[163] Copyright 2021 American Chemical Society)

2.3.5. Platinum Deposition

We used solution-phase reductive deposition of platinum to establish that the supported NCs are catalytically active. In these experiments, NC/MCC powders prepared without added citrate were suspended in water and heated in the presence of H_2PtCl_6 and 10% methanol (a reducing agent) at 65 °C in the dark (see Materials and Methods). Similar chemistries have been previously used to grow Pt on other Au nanostructures.[174–177] TEM images show the selective growth of Pt nodules on the gold NCs, with no Pt detected on the cellulose support (Figure 2.15).

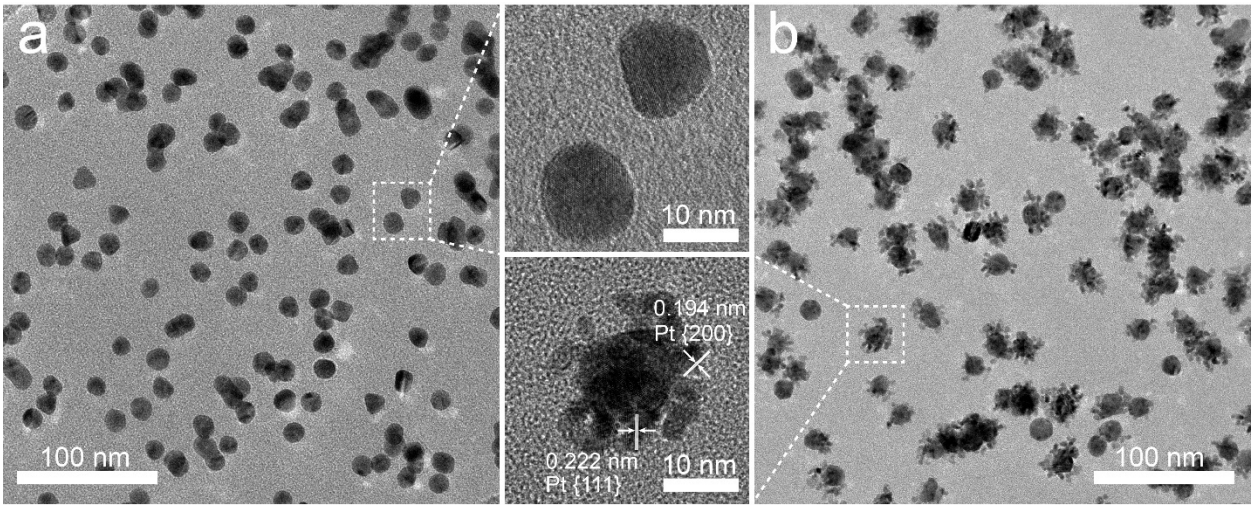

Figure 2.15 Platinum deposition on the supported NCs. TEM images (a) before and (b) after heating a NC/MCC suspension (5 wt% NCs) with H_2PtCl_6 in a 10:90 methanol-water mixture at 65 °C for six hours in the dark. Magnified images of several of the NCs

are also shown. The measured spacing of the lattice fringes indicate that the nodules are crystalline Pt. (Reprinted with permission from Ref.[163] Copyright 2021 American Chemical Society)

Analysis of several images indicates that at least 95% of the NCs had Pt nodules after six hours of reaction. In contrast, no Pt deposition was observed in the absence of methanol (Figure 2.16) because methanol is the sacrificial electron donor needed to sustain the reduction of Pt on the NC surface. In control reactions without NCs, Pt deposition was evident only in a few areas of the MCC, indicating that Pt deposition is mediated by the Au surface. The deposition of Pt onto the supported gold NCs shows that the NCs are in contact with the surrounding solution and not blocked by the cellulose support or residual citrate ligands.

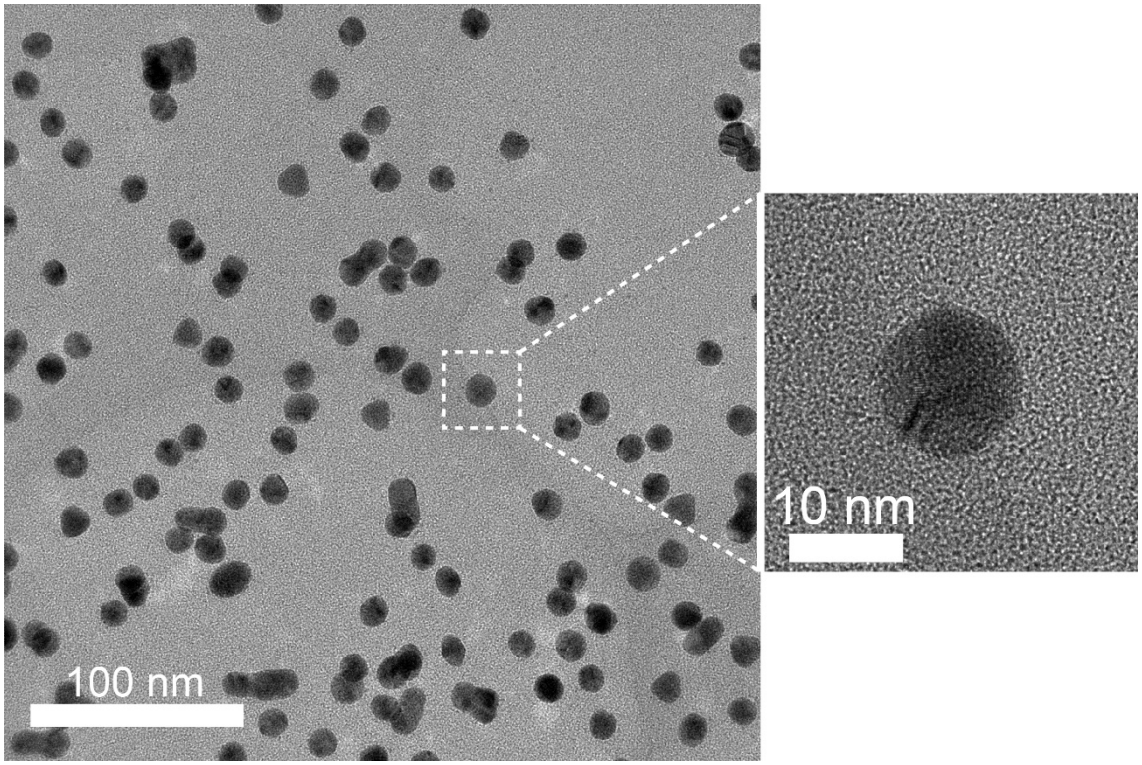

Figure 2.16 TEM image of control methanol-free platinum deposition. TEM images of a NC/MCC powder (5 wt% NCs) that was suspended in water and heated in the presence of H_2PtCl_6 but without methanol at 65 °C for six hours in the dark. The images

show no evidence for Pt deposition in the absence of methanol. (Reprinted with permission from Ref.[163] Copyright 2021 American Chemical Society)

2.3.6. Kinetics of Nitrophenol Reduction

To better understand the catalytic activity of the freeze-dried supported NCs, we measured their ability to catalyze the solution-phase reduction of 4-nitrophenol to 4-aminophenol by sodium borohydride (Figure 2.17a). This is a well-known model reaction that can be conveniently monitored via optical extinction spectroscopy by measuring the decay of the 4-nitrophenolate absorption peak at 400 nm (Figure 2.17b).[178]

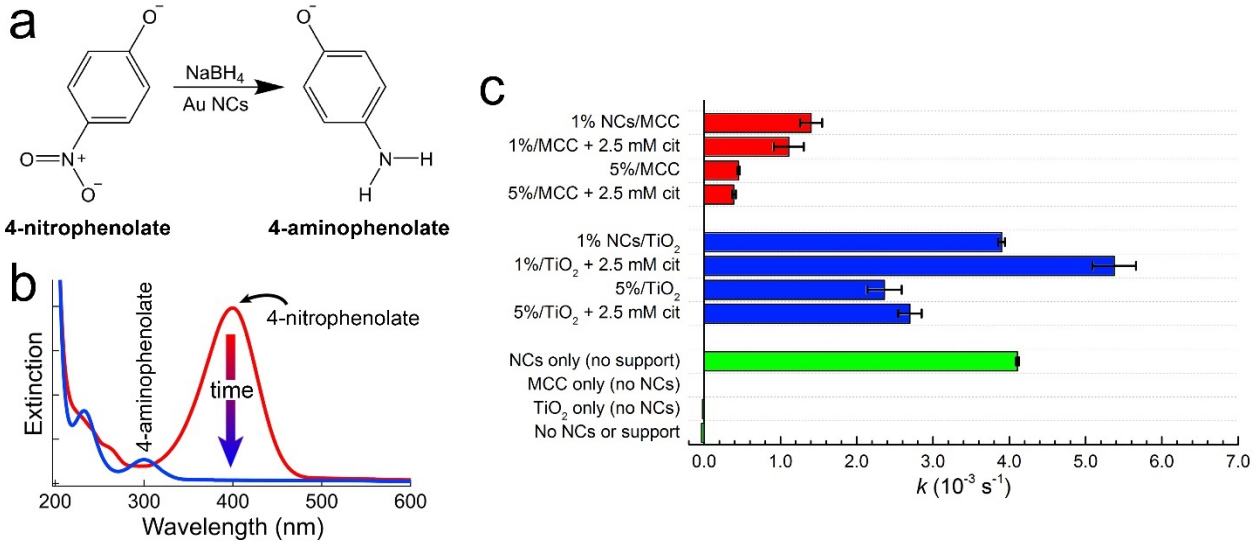

Figure 2.17 Catalyzed reduction of 4-nitrophenol by Au NCs. (a) Reaction scheme for the reduction of 4-nitrophenolate to 4-aminophenolate by sodium borohydride on the surface of Au NCs. (b) Solution extinction spectra before and after 4-nitrophenolate reduction. Reaction kinetics were monitored via the decay of the nitrophenolate absorbance peak at 400 nm. (c) Pseudo first-order rate constants for the reduction reaction carried out in excess $NaBH_4$ for suspensions of NC/MCC (red bars) or NC/TiO_2 (blue bars) with 1% or 5% NC loading and 0 or 2.5 mM citrate added prior to freeze-drying. These powders were re-suspended without washing off the added citrate. Also shown are data for colloidal (unsupported) NC samples without added citrate and

several negative control experiments without NCs (green bars). All samples contained the same concentrations of 4-nitrophenol and $NaBH_4$, and all samples with NCs contained the same mass of NCs (1 μg/mL). Error bars denote the standard deviation of three measurements. See Figure 2.18 for raw data and fits. (Reprinted with permission from Ref.[163] Copyright 2021 American Chemical Society)

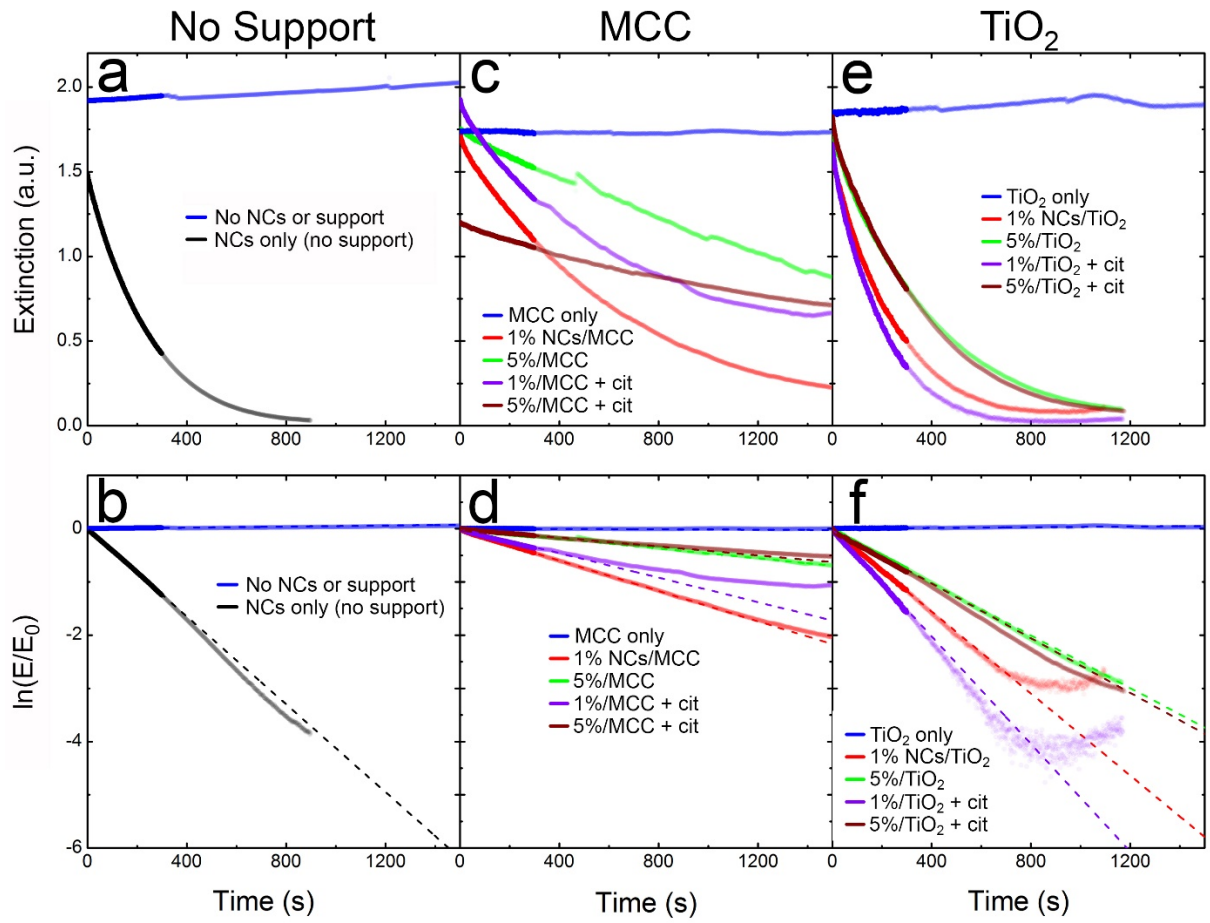

Figure 2.18 Kinetics data and pseudo first-order fits for 4-nitrophenol reduction. (a) Optical extinction at λ = 400 nm versus time for colloidal (unsupported) NCs with no added citrate, compared to a negative control without NCs or support material. (b) Corresponding log-linear plots of these data with pseudo first-order fits (dashed lines) of the initial 300 seconds of the reaction (darker data points). (b-c) Extinction data and fits for NC/MCC samples and for MCC alone (no NCs). (e-f) Extinction data for

NC/TiO_2 samples and for TiO_2 alone (no NCs). All experiments were conducted with the same initial concentrations of 4-nitrophenol (100 μM) and $NaBH_4$ (15 mM), and all samples with NCs contained the same concentration of NCs (1 μg/mL). Any background signal not due to 4-nitrophenol absorption was subtracted from each plot and $t = 0$ was shifted to account for the induction period that is typically observed in this reaction.[178] Fluctuations in the data are due to light scattering by hydrogen bubbles that form intermittently on the walls of the cuvette as borohydride decomposes. The slow upward drift in extinction for several of the control experiments may result from increased light scattering by microscopic bubbles that gradually accumulate in the solutions. (Reprinted with permission from Ref.[163] Copyright 2021 American Chemical Society)

In our experiments, aqueous 4-nitrophenol was added to a suspension of the supported NCs in aqueous $NaBH_4$ and the extinction at 400 nm was measured *in situ* with constant stirring at 15 °C (see Materials and Methods). Measurements were conducted in triplicate on samples with 1% or 5% NC loading on MCC or TiO_2 at equal total concentrations of NCs (1 μg/mL), $NaBH_4$ and 4-nitrophenol (with [$NaBH_4$]/[4-nitrophenol] = 150). Pseudo first-order rate constants extracted from fits of the resulting 4-nitrophenolate concentration versus time data are shown in Figure 2.17c. We found that NC/MCC and NC/TiO_2 samples catalyze nitrophenol reduction at different rates, with the reaction proceeding significantly faster on TiO_2 than on MCC. We attribute the larger rate constants on TiO_2 to (*i*) favorable metal-support interactions for Au/TiO_2,[179–181] (*ii*) the smaller size of the TiO_2 particles, which is expected to allow freer diffusion of molecular reactants and products compared to the larger, more aggregated and occluded MCC particles (see Figure 2.3), and (*iii*) reduced NC clustering on the larger-surface-area TiO_2 support (51 m2/g vs. 7 m2/g for MCC). The NC/TiO_2 samples with 1% NC loading had about the same rate constant as the unsupported NC colloid,

confirming the existence of a cooperative NC/TiO_2 effect that counterbalances the reduction in NC surface area due to adsorption on the support. Increasing the NC loading to 5% resulted in smaller rate constants on both supports, probably due to increased NC clustering, occlusion, and competition between the NCs for 4-nitrophenol. Citrate addition had an insignificant effect on the rates except in the case of 1% NCs/TiO_2 samples, where it resulted in a 30% larger rate constant, likely by suppressing NC cluster formation. Overall, these experiments demonstrate that the supported NCs are catalytically active and that the rate of this model reaction depends strongly on the support material and NC loading.

2.3.7. Stability and Miscellaneous

In contrast to freeze-drying, conventional evaporative drying of the NC/MCC and NC/TiO_2 slurries resulted in inhomogeneous solids. Four methods of conventional drying were explored as control experiments. Evaporative drying at room temperature in unstirred open vials led to a large vertical gradients in NC loading (more NCs near the top of the solids) as a consequence of the different suspendability limits and precipitation dynamics of the NCs and support material. This process was also irreproducible and very slow (4-5 weeks to evaporate 10 mL of water). Drying at 60 °C in a vacuum oven (no stirring) was faster (1 week) but gave similarly inhomogeneous products. We also investigated the use of rotary evaporation to dry the slurries. Rotary evaporation at 50 °C improved sample homogeneity compared to ambient and vacuum oven drying, but the directional drying inherent to rotary evaporation still resulted in a pronounced NC concentration gradient from the top to the bottom of the vials (more NCs near the bottom of the vials; Figure 2.19).

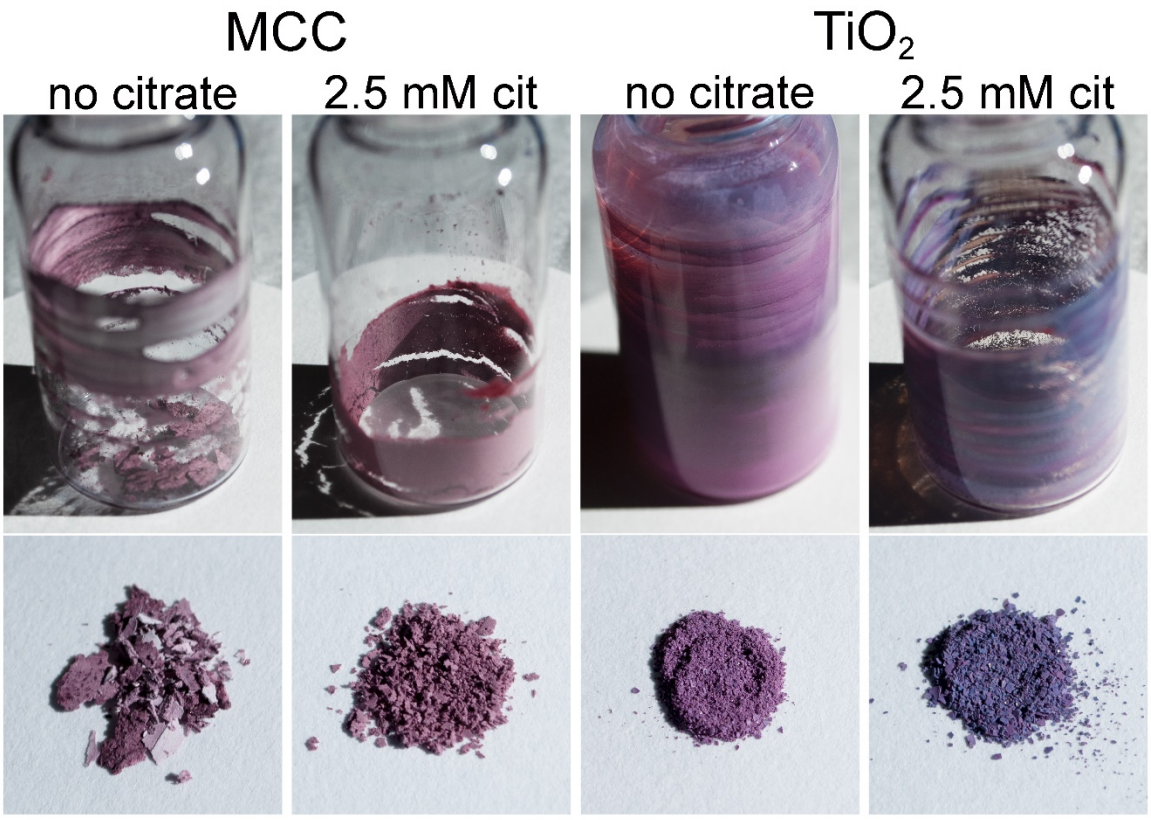

Figure 2.19 Results of evaporative drying control experiments conducted in 20 mL scintillation vials with a rotary evaporator. 10 mL aqueous slurries of MCC or TiO_2 powder and 1 wt% NCs were dried at 50 °C, 60 rpm, and 100 mbar dynamic vacuum. Most of the as-dried products had an inhomogeneous color (bands of different color on the vial wall) due in part to non-uniform loading of NCs on the support. The bottom row of images shows the powders collected by scraping the solids out of the vials. (Reprinted with permission from Ref.[163] Copyright 2021 American Chemical Society)

Finally, we tested vacuum filtration as a way to collect and dry the slurries on nanoporous filters. We made a series of slurries (1 wt% NCs), thoroughly mixed them by brief shaking, and then filtered each within ~1 minute through a 0.2 μm nylon membrane filter using a Buchner funnel. This procedure resulted in uniformly-colored retentates only for NC/TiO_2 slurries without added citrate. The other five types of

slurries that we tested produced layered or otherwise inhomogeneous solids (Figure 2.20).

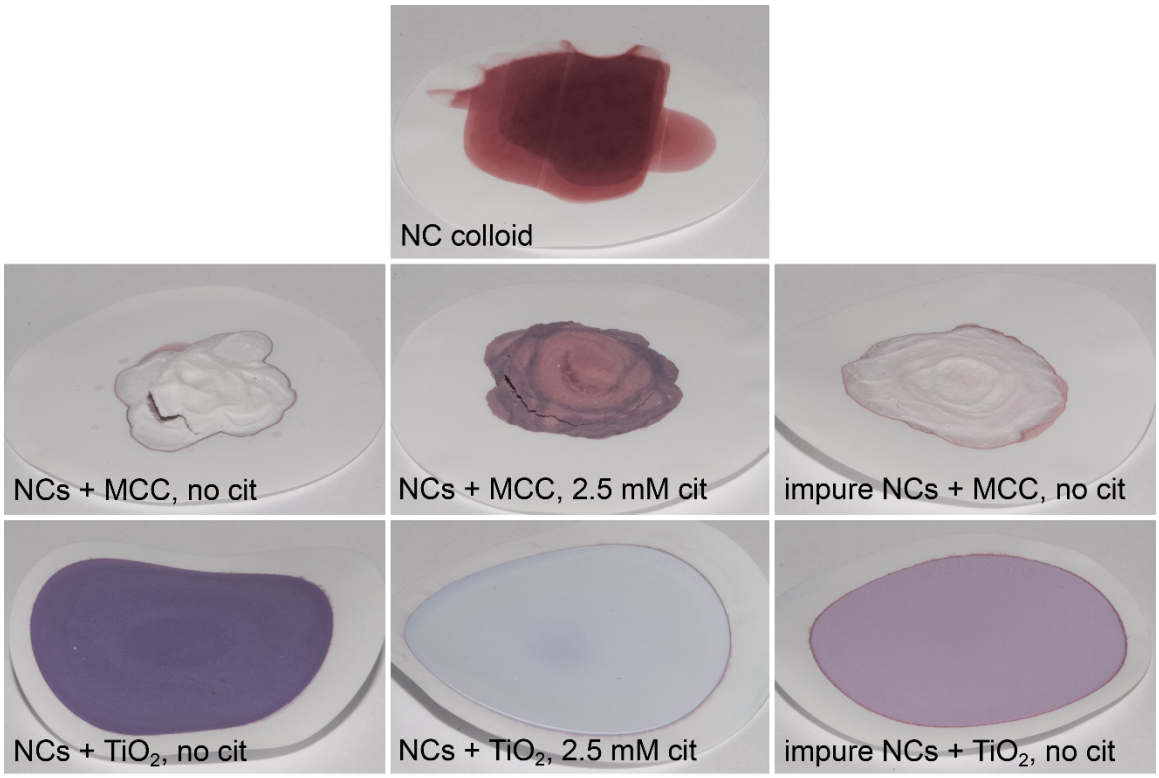

Figure 2.20 Vacuum filtration of NC/MCC and NC/TiO_2 slurries. Photographs of the solids collected by filtering NC slurries (1 wt% NCs) through 0.2 μm nylon membrane filters using a Buchner funnel. *Top row*: Result of filtering the purified Au NC colloid (no MCC or TiO_2 support). All of the NCs were retained by the filter, with none passing through the filter. *Middle row*: Result of filtering various NC/MCC slurries. Each slurry was made, shaken for a few seconds and then filtered within a minute. Without added citrate (left image), the retentate consisted of a layer of NCs captured within the filter under a layer of MCC. With added citrate (2.5 mM, center image), the retentate was more homogeneous but still showed a pronounced radial and vertical gradient of NC concentration. Slurries made with unpurified NCs and no additional citrate (right image) gave retentates with an intermediate degree of homogeneity, with some NCs mixed into the layer of MCC on top of the NC layer. *Bottom row*: Result of filtering

NC/TiO_2 slurries. Without added citrate (left image), the retentate was homogeneous but purple in color, indicating clustering of the NCs during the filtering process. With added citrate (center image), the retentate was highly stratified, with a layer of NCs under a layer of TiO_2. We note that citrate addition has opposite effects on MCC and TiO_2. Slurries made with unpurified NCs and no additional citrate (right image) again gave retentates with an intermediate degree of homogeneity, with many NCs mixed into the TiO_2 but most still passing through the TiO_2 layer and captured by the filter. These data show that the NCs are strongly adsorbed only to TiO_2 in the absence of citrate and, to a lesser extent, to MCC in the presence of citrate, within the time frame of the experiments. (Reprinted with permission from Ref.[163] Copyright 2021 American Chemical Society)

The difficulty in obtaining uniform NC loading by these conventional drying methods shows that the NCs often have little tendency to adsorb to the support particles while stirred together as a slurry. To further test this notion, we stirred NC/TiO_2, NC/MCC, and NC/Al_2O_3 slurries continuously for two days at room temperature and then visually checked the extent of NC uptake by the support particles. We found complete NC uptake in only three of the six types of slurries tested, with the other three slurries showing little or no NC uptake (Figure 2.21). Although spontaneous NC adsorption by simple stirring of NC/support mixtures has been successfully used to make several types of supported NCs,[128–131,133,134] such adsorption occurs only for certain combinations of NCs, support and solution composition (e.g., pH, ionic strength, ligands). By rapidly freezing well-mixed slurries and removing the frozen solvent by sublimation rather than evaporation, freeze-drying sidesteps the difficulties associated with NC adsorption from the liquid and prevents segregation of the NCs and support during drying, yielding more homogeneous products for a wider

range of NC/support materials with less effort and time compared to conventional approaches.

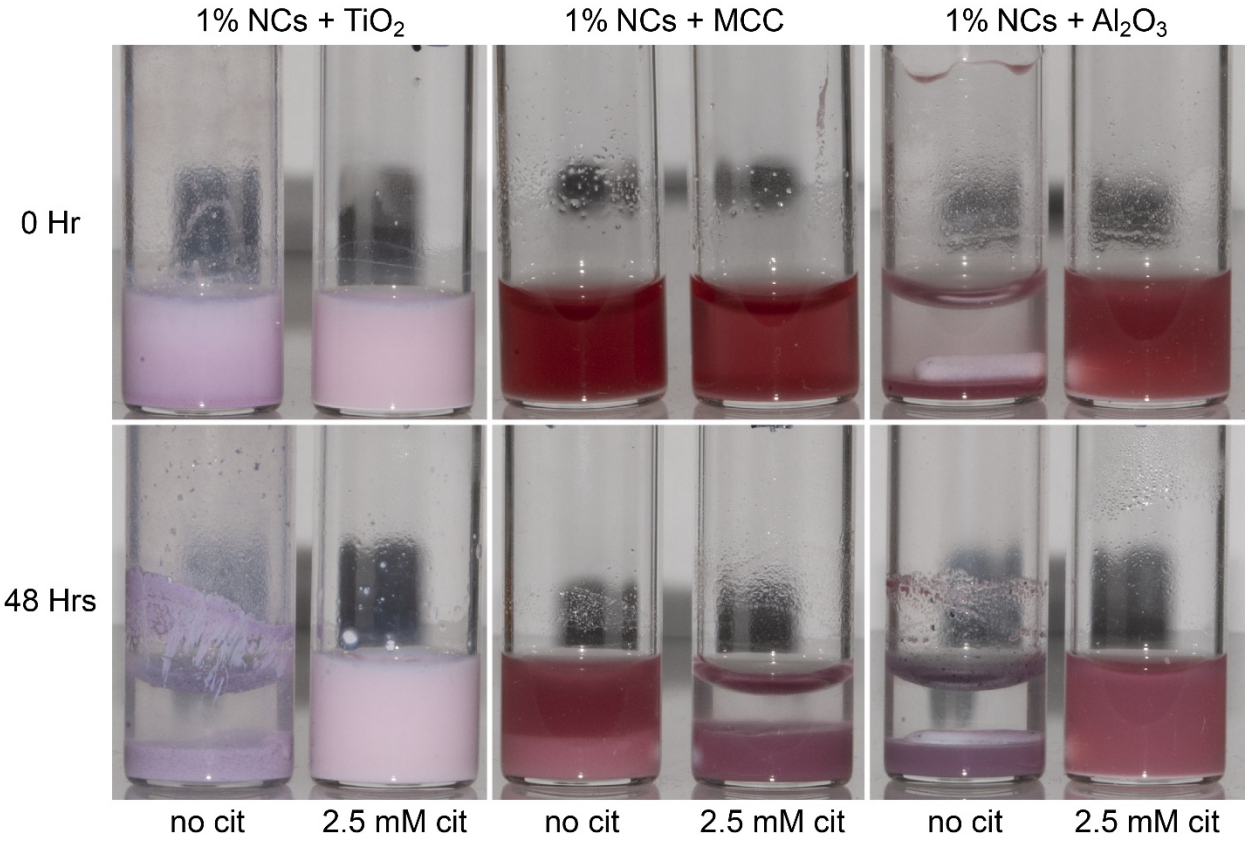

Figure 2.21 Tests for spontaneous NC adsorption onto the support particles during slurry stirring. (*top row*) Photographs of freshly-prepared slurries of Au NCs and either TiO_2, MCC or Al_2O_3 particles with or without 2.5 mM added citrate (1 wt% NCs). Each sample was briefly shaken, allowed to sit without stirring for 10 min, and then photographed. (*bottom row*) Photographs of these slurries after 48 hours of continuous stirring at 400 rpm followed by a 10 min sit time. We see that in the absence of added citrate, the NCs adsorb completely to TiO_2 and Al_2O_3 (note the strongly-colored precipitates and colorless supernatants), while NC adsorption to MCC is poor (weakly-colored precipitate and strongly-colored supernatant). We noticed that NC adsorption is faster on Al_2O_3 than TiO_2. In the presence of added citrate, the NCs adsorb poorly to TiO_2 and Al_2O_3 but completely to MCC. Longer sit times resulted in the slow settling of

white TiO_2 and Al_2O_3 precipitates, with the vast majority of the Au NCs remaining in suspension. (Reprinted with permission from Ref.[163] Copyright 2021 American Chemical Society)

Although often the NCs did not adsorb to the support particles while wet in the slurry, they always became strongly immobilized on the support once freeze-dried. Immersing the freeze-dried solids in water resulted in no visible leeching of NCs into the liquid. Furthermore, after re-suspending the freeze-dried NC/MCC or NC/TiO_2 powders by shaking, the support particles retained their NCs as they slowly settled, leaving colorless supernatants free of NCs (Figure 2.22). We believe that a combination of electrostatic and van der Waals forces anchor the NCs to the supports as the solvent sublimes away during freeze-drying. The immobilized NCs facilitate the washing of these solids to remove or replace surface ligands without causing NC leaching or aggregation.

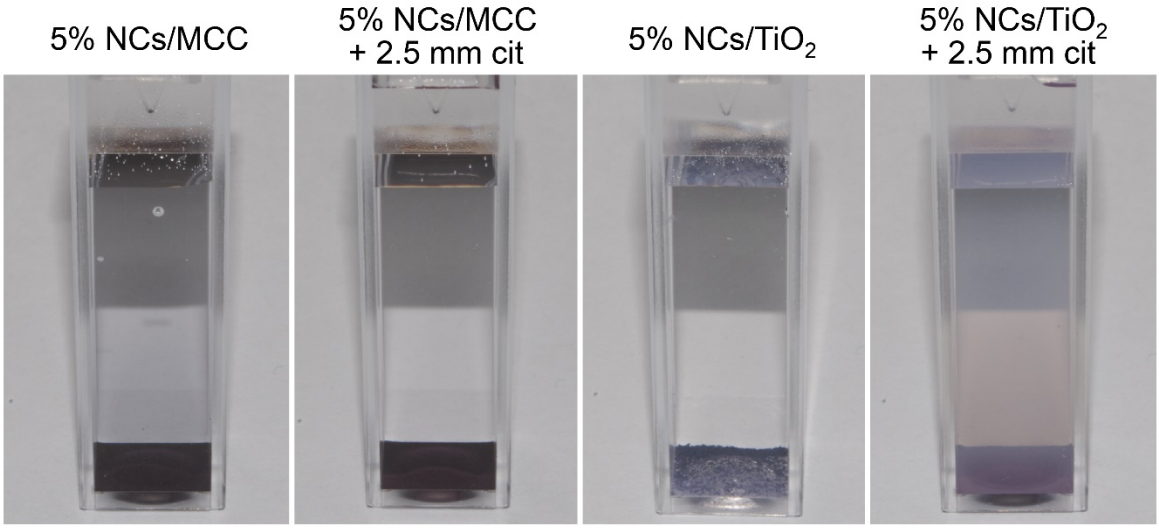

Figure 2.22 Tests of NC immobilization on MCC and TiO_2. Photographs of freeze-dried NC/MCC and NC/TiO_2 samples that were re-suspended in pure water by shaking for 10 seconds and then allowed to settle undisturbed for 24 hours. The NCs remain attached to the MCC and TiO_2 particles and settle with them to the bottom of the

cuvette, leaving a colorless or nearly-colorless supernatant. The light pink color of the NC/TiO_2 sample made with 2.5 mM citrate (rightmost image) is caused by incomplete precipitation of the TiO_2 particles as a result of improved charge stabilization of TiO_2 by adsorbed citrate. We believe that most of this faint color is due to suspended supported NCs rather than free (unsupported) NCs, a conclusion that is consistent with Figure 2.8. (Reprinted with permission from Ref.[163] Copyright 2021 American Chemical Society)

Thermal stability is an important requirement for practical supported metal NC catalysts, especially plasmonic photocatalysts. We investigated the bulk thermal stability of NC/MCC and NC/TiO_2 samples by thermogravimetric analysis (TGA) in inert atmosphere (nitrogen) from room temperature to 500 °C. For NC/MCC samples without added citrate, pyrolysis of the support began at ~225 °C and was largely complete by ~350 °C, leaving a black residue of carbon and gold (Figure 2.23a,c). NC/MCC samples containing ~6 wt% sodium citrate showed slightly greater total mass loss but over a significantly wider temperature range (175-450 °C). Thus, citrate should be removed from NC/MCC catalysts not only to boost NC catalytic activity, but also to avoid degrading the already low thermal stability of MCC. In contrast, NC/TiO_2 samples showed only small mass losses (primarily due to dehydration and citrate pyrolysis), while the color of these materials changed from mauve to violet as a result of mild NC ripening/fusion at elevated temperatures (Figure 2.23b,c).

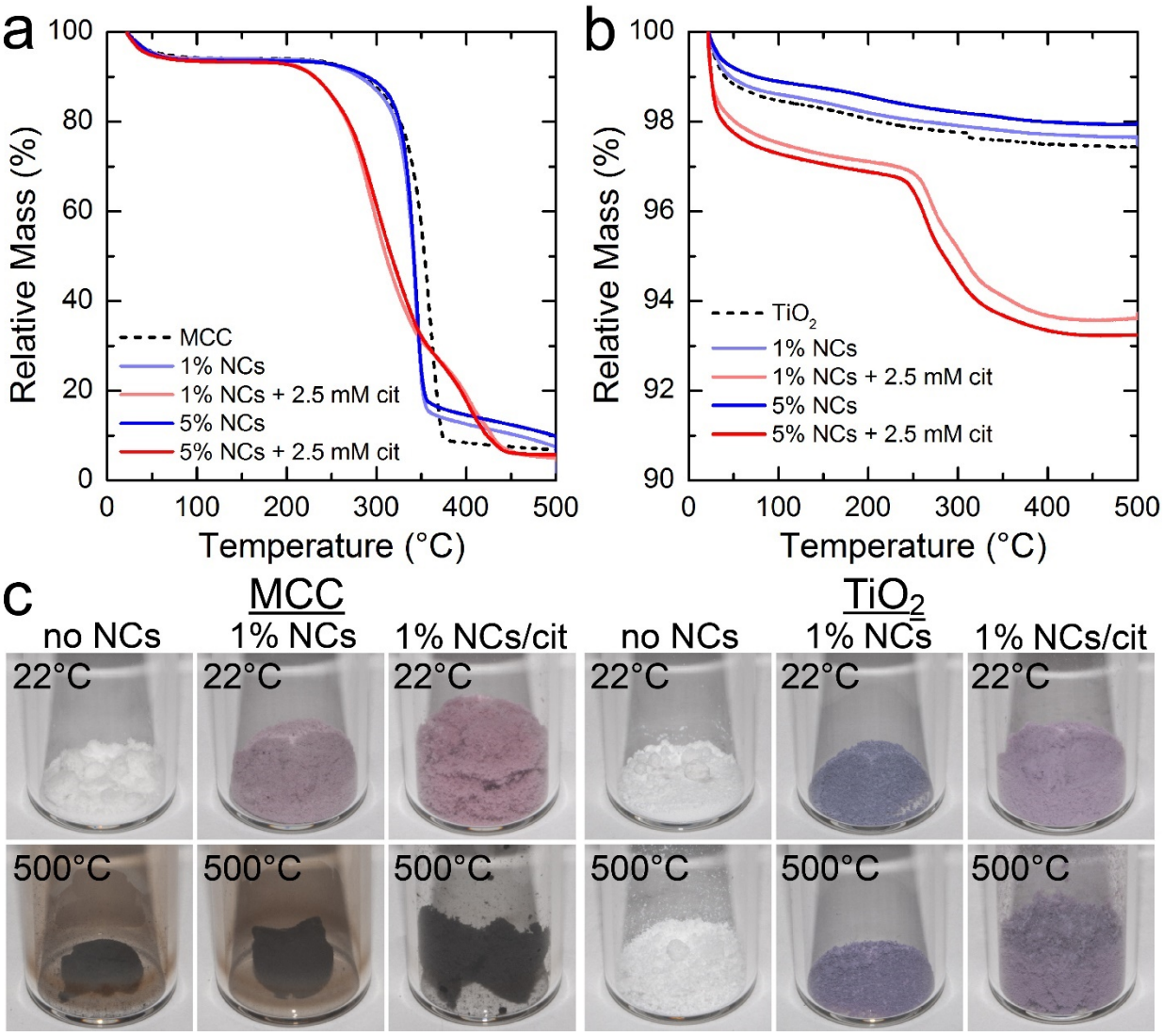

Figure 2.23 Thermogravimetric analysis of the supported NCs. (a) TGA traces for NC/MCC samples (1% or 5% NCs with or without 2.5 mM citrate) in flowing nitrogen. Data for pure MCC are also shown. The initial mass loss (up to ~200 °C) is caused by water desorption. MCC and citrate pyrolysis occurred above ~200 °C. (b) Corresponding data for NC/TiO_2 samples and pure TiO_2. The citrate-spiked samples showed greater water loss below 200 °C (from citrate hydrates) and citrate pyrolysis above ~250 °C. (c) Photographs of NC/MCC and NC/TiO_2 samples (1% NCs with and without citrate) before and after annealing at 500 °C in nitrogen for 15 minutes in a tube furnace. Photos of pure MCC and TiO_2 are also shown for reference. See Figure 2.24 for

TEM images of one of the NC/TiO_2 samples after the 500 °C anneal. (Reprinted with permission from Ref.[163] Copyright 2021 American Chemical Society)

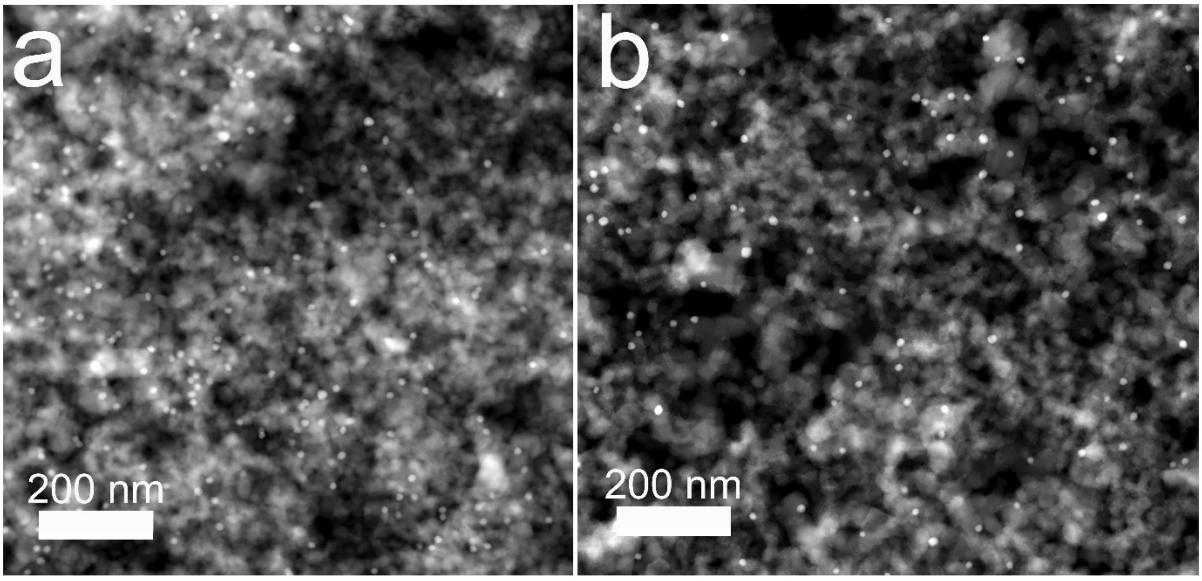

Figure 2.24 STEM images of NC/TiO_2. Morphology of a NC/TiO_2 powder (1% NCs with 2.5 mM citrate) before and after annealing at 500 °C in nitrogen for 15 minutes in a tube furnace. (a) Dark-field STEM image before annealing. (b) Image after annealing. (Reprinted with permission from Ref.[163] Copyright 2021 American Chemical Society)

Finally, we show that freeze-drying can be scaled to larger batch sizes and extended to other types of metal NCs, making it an attractive general method for preparing supported NC catalysts. As a demonstration, we increased the batch size from 0.1 g to 1 g of 1% NC/MCC and NC/TiO_2 and obtained products identical in color and microstructure to those shown in Figure 1 (Figure 2.25). Further increases in batch size are possible by employing larger lyophilizers.

Figure 2.25 Scaled-up freeze-drying of 1 wt% NCs on MCC and TiO_2. Each image shows a 1 gram batch of supported NCs. Batches made on the 0.1 g (see Figure 2.1) and 1 g scale appear identical. These samples were made without added citrate. (Reprinted with permission from Ref.[163] Copyright 2021 American Chemical Society)

We also used freeze-drying to deposit triangular Au nanoprisms (55-60 nm edge length and capped with CTAC, see Materials and Methods) on MCC and TiO_2 supports (Figure 2.26). As with the spheroidal Au NCs, the supported nanoprisms were well dispersed and retained their original shape and colloidal color (blue in this case). The presence of CTAC had no obvious impact on the freeze-drying process. Absorbance spectra of the supported nanoprisms show weaker, broader, and slightly blueshifted LSPRs compared to the colloidal (unsupported) nanoprisms, which may reflect some blunting/rounding of the prism corners during the freeze-drying process.[38] The exact cause of these spectral changes is the subject of ongoing investigations in our laboratory.

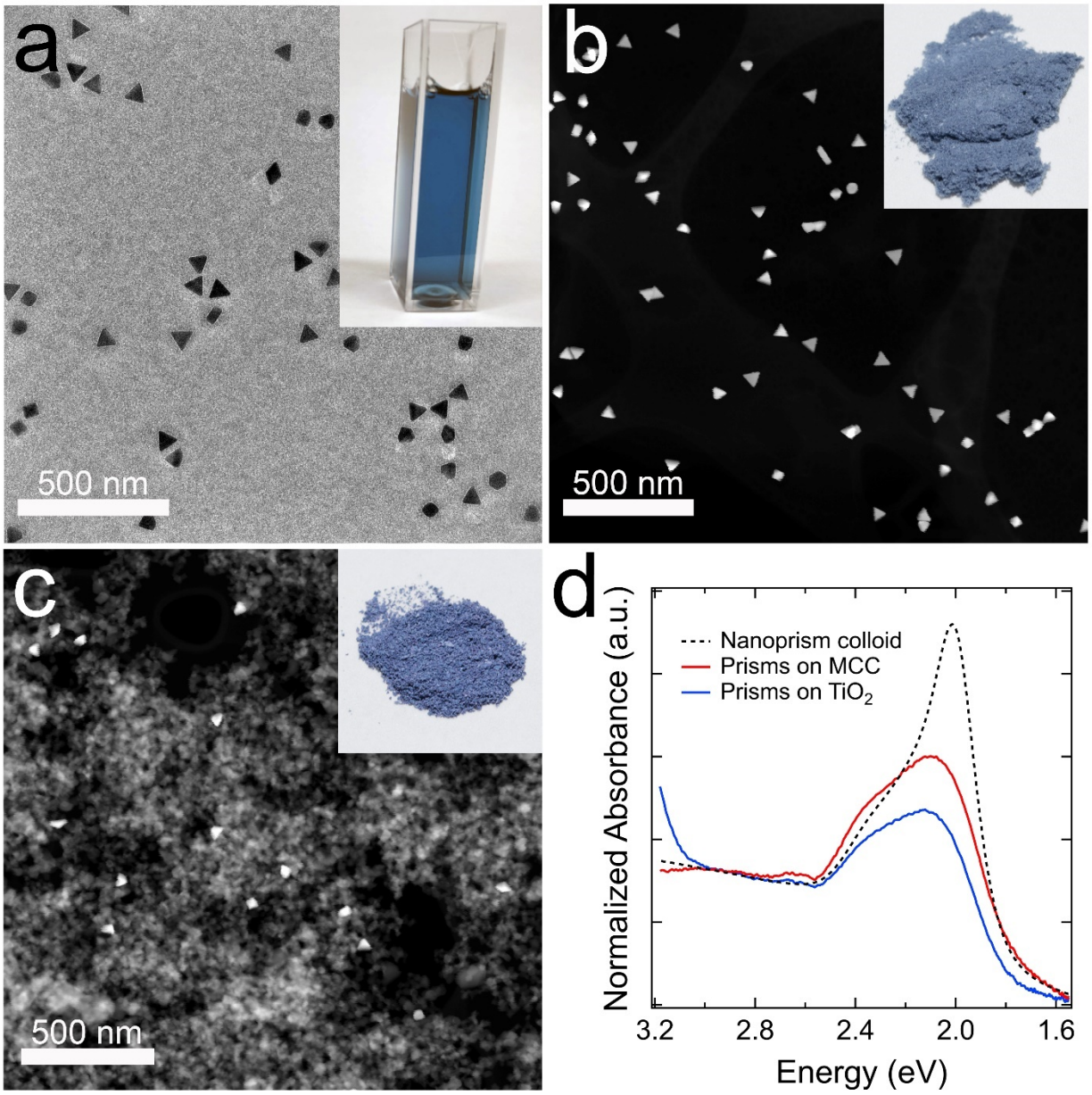

Figure 2.26 Supported Au nanoprisms made by freeze-drying. (a) TEM image and photograph of the colloidal Au nanoprisms. (b) Dark-field STEM image and photograph of the nanoprisms on MCC (0.6 wt%). (c) Corresponding data for nanoprisms on TiO² (0.6 wt%). (d) Absorbance spectra of the supported and colloidal nanoprisms. All spectra are normalized at λ = 420 nm. (Reprinted with permission from Ref.[163] Copyright 2021 American Chemical Society)

2.4. Conclusion

This paper demonstrates that slurry freeze-drying is a simple, mild, reproducible and scalable method to load pre-made colloidal gold nanocrystals onto several organic and inorganic supports to obtain uniform NC dispersion with tunable NC loading (to at least 20 wt%) and retention of original NC size and shape. We showed that sodium citrate suppresses the clustering of gold NCs on cellulose and TiO_2 and can be subsequently rinsed away to yield supported NCs with cleaner surfaces, avoiding the need for high-temperature calcination that can degrade NC monodispersity. Two model reactions were used to establish the catalytic activity of the supported NCs in water. The generality of the method was demonstrated by depositing triangular Au nanoprisms onto cellulose and TiO_2. Due to its many advantages, slurry freeze-drying should prove useful for making a wide variety of uniform supported NC catalysts from chemically-synthesized colloidal NCs. We anticipate that the freeze-drying of colloidal mixture can be extended beyond metal NCs to load many other types of colloids (inorganic NCs, organic nanoparticles, nanowires, etc.) onto a wide variety of support materials (carbon, metal oxides, polymers, etc.) for applications in catalysis, energy conversion and storage, optoelectronics, and sensing.

Chapter 3. Plasmon-driven Chemical Reactions

3.1. Residual Gas Analyzer

The primary method of detection with high sensitivity and specificity is the SRS300 residual gas analyzer (RGA). This quadrupole mass spectrometer is designed to measure small molecule gaseous signatures from 1 to 300 atomic mass units. Its specific purpose is to detect low molecular impurity species in ultra-high vacuum environments for specialized material deposition methods like sputtering and molecular beam epitaxy. Commonly, RGAs are often deployed to detect leaks in high vacuum systems. Leaks from flanges and imperfect welds are notoriously difficult to locate. RGAs are specifically utilized by sensing non ambient gases like helium because of its specific mass signature relative to atmospheric gases of oxygen, nitrogen, argon, and water vapor.

We have repurposed and modified the Residual Gas Analyzer (RGA) to be mounted directly on a turbomolecular pump dedicated for the detection of gases from reaction outputs. Under a static vacuum, the turbo can sustain a vacuum of ~10^{-8} mbar. Even at base pressure, the RGA can still detect and quantify the species typically found in air due to desorption from the stainless steel surface. For sensing atmospheric pressure gases, a miniscule leak must be used to maintain a substantially low pressure to preserve the lifetime of the filament from oxidation. This was done by fitting a 25 micron diameter capillary tubing to the end flange on the manifold. The pressure sustained by the 25 micron intake is typically around 10^{-7} mbar depending on the type of gas sampled. The sensitivity floor for this mass spectrometer is around 10^{-12} mbar, so the sensitivity for atmospheric sampling is about 100 ppm. To fully utilize the system, the experiment must be adjusted so that the intake gas must be fairly concentrated at

thousands of ppm to percentages. Figure 3.1 shows the makeup of the mass spectrometer sampler. The base is supported by a turbomolecular pump and fitted with the RGA on the left and vacuum gauge on the right. The entire unit is wrapped with heating tape to maintain a constant temperature at 105 ˚C to prevent water vapor adsorption. It is well known that small molecule impurities can adsorb on surfaces and will continuously outgas and contaminate the mass spectrum. The connected 25 micron Peek capillary line is fitted specifically to sample atmospheric pressure. It can sample lower pressure however, but quantifying lower pressures are difficult due to the dynamic range and the noise floor of the spectrometer.

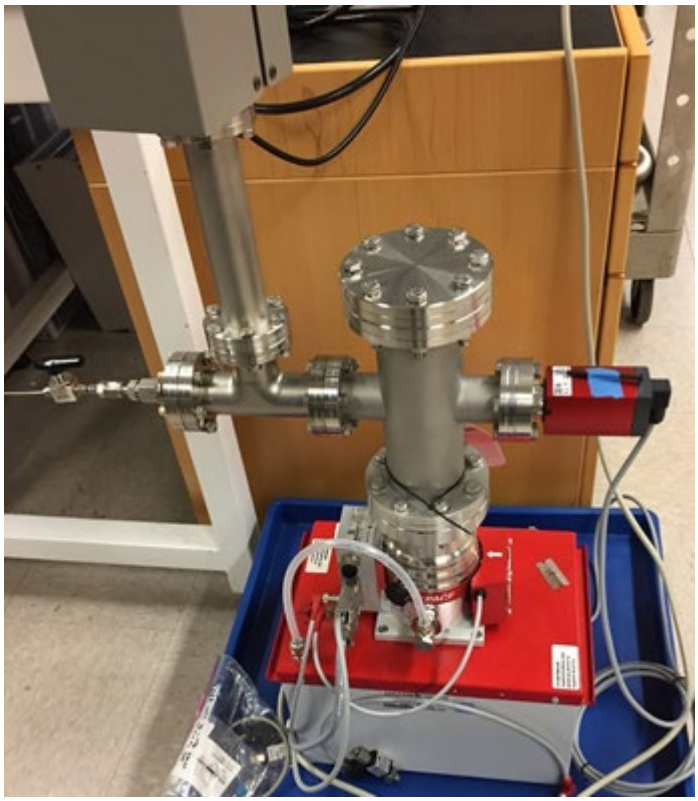

Figure 3.1 Residual Gas Analyzer. Homebuilt modular quadrupole mass spectrometer for real-time online measurement of small molecule gases. The base is a turbomolecular pump that can achieve base pressure of ~10^{-8} mbar. QMS residual gas analyzer RGA300 from Stanford Research Systems. Left of the RGA unit is the

swappable intake capillary line sampling minute quantities from atmospheric pressure to 10^{-7} mbar.

For accurate quantification, the sensitivity factor must be accounted for to equate the raw signal to the true pressures sensed. The sensitivity difference between gaseous species is primarily due to the molecule's ionization potential and its interaction with the electron beam. To properly accelerate the ionic species, a 70 eV electron bombards the incident neutral molecule to ionize electrons. The specific interactions between bound electrons in the molecule and the 70 eV beam determines what proportion of the molecular makeup is ionized. Our purpose is to accurately quantify hydrogen and deuterium gases. Pure hydrogen or deuterium is sampled at atmospheric pressure through the capillary line to yield a steady state RGA signal. A known pressure from a Kurt Lesker gauge was recorded which can be matched with the output current from the RGA. The ratio of the two will yield the sensitivity factor for our RGA for the specific gas. Table 3.1 lists the hydrogen and deuterium sensitivity factors for our RGA. HD's sensitivity factor could not be directly obtained because we did not have a pure source of HD so we can average the H_2 and D_2 factors. There is good agreement as the sensitivity depends on molecular weight of the diatomic hydrogen molecule.

Gas	**Sensitivity Factor (A/mBar)**
Hydrogen	1.06×10^{-4}
Deuterium	8.35×10^{-4}
HD	6.09×10^{-5}

Table 3.1 Sensitivity factors of isotopic hydrogen gases.

3.2. Water Reduction

Applying the supported nanocrystals from the previously developed method in Chapter 2, we can fabricate complex morphologies to harness plasmonic Au

nanocrystals for hydrogen production from water. Our hypothesis was to use platinum decorated Au nanocrystals developed by Engelbrek *et al*. For full synthesis details, refer to Chapter 4.2 Materials and Methods. Hot carriers generated from plasmons dephase at the surface on platinum sites from strong d-electron interactions with gold. High concentrations of hot electrons should be able to quickly transfer to reduce water to diatomic hydrogen with the remaining holes oxidizing isopropyl alcohol to other species.

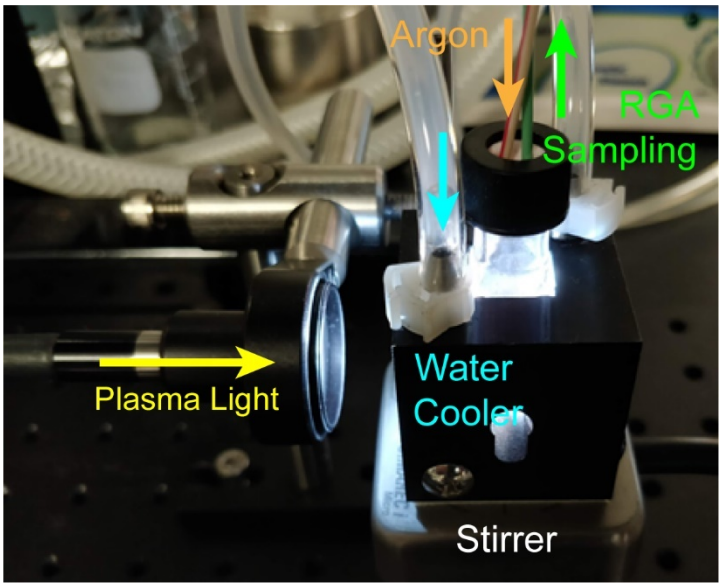

Figure 3.2 Photograph of real-time hydrogen headspace sampling. Photograph of illuminated cuvette for real time sampling of headspace gases. Argon gas is supplied by a Peek tubing to maintain a constant pressure inside the cuvette headspace. A cuvette is housed in a waterblock temperature controlled by a circulator. The base has a magnetic stirrer to continuously stir the catalytic material to maintain a stable suspension. Plasma light is illuminating a window on one side of the cuvette.

The measurement technique utilizes the RGA to continuously monitor the headspace for elevated concentrations of hydrogen. Figure 3.2 shows the reaction condition of plasma light illuminating a stirred cuvette. The beige capillary tubing

samples the headspace at very low rates, approximately 1 microliter per second. Replacing the sample gas is supplied by the green tubing with an abundance of argon flow and pressure. The solution was purged with argon prior to any illumination. This is to remove all excess oxygen from the system. Maintaining an oxygen free environment is crucial because O_2 can act as a strong electron scavenger and neutralize any energetic electrons in the process.

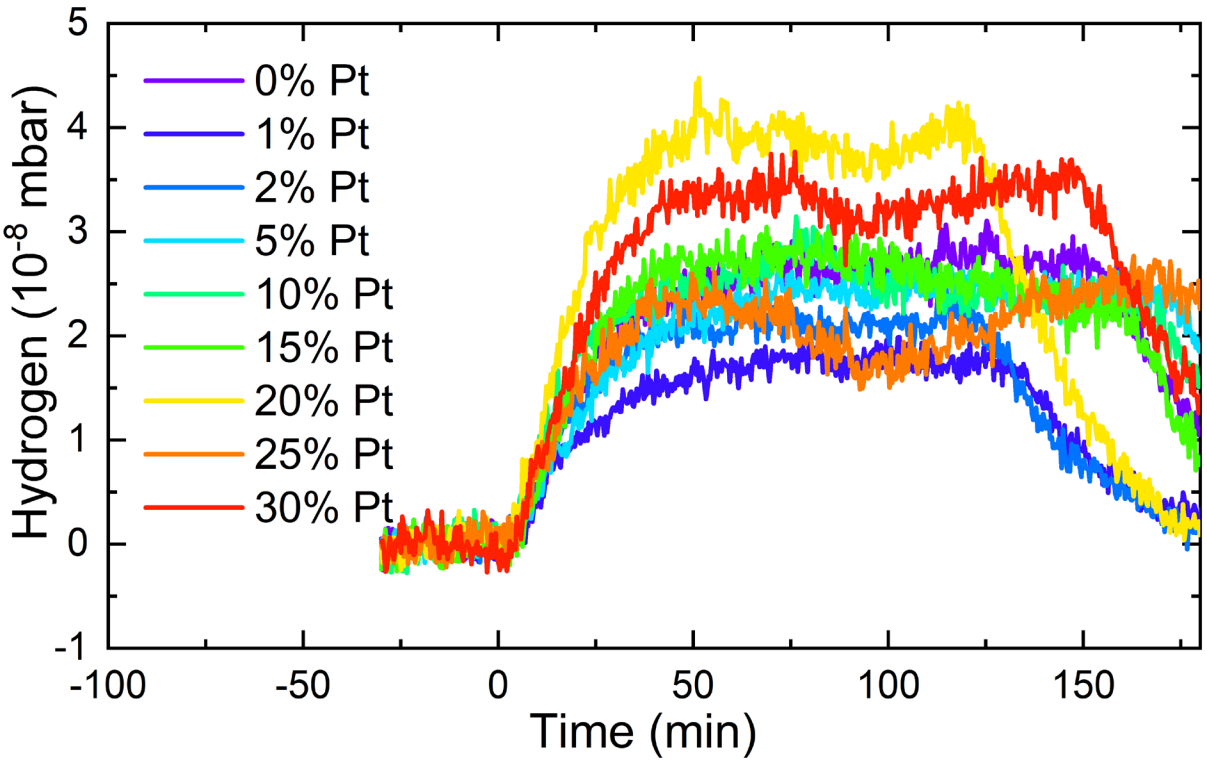

Figure 3.3 RGA traces of platinum decorated Au Nanocrystals. Real time RGA hydrogen traces of a series of platinum decorated Au nanocrystals. At t_0, the plasma light source is turn on to illuminate the particles in the cuvette. The increase in hydrogen signal is observed in real time over 3 hours.

The cuvette solution consists of 0.1 mg/mL nanocrystals in 10% isopropanol in water stirred at 1000 RPM. Illumination used a plasma light source with approximate intensity of 0.3 W/cm^2 for at least 2 hours. Figure shows the increase in hydrogen signal

at t-0 when the sample was illuminated. Samples with increasing concentrations of platinum were tested. All samples show increases in hydrogen signal but had varying levels of saturation. There appears to be no direct dependence on the platinum concentration as the highest hydrogen signal was from 20% and lowest from 1%. The control with pure Au nanoparticles had hydrogen signals in between the rest of the population.

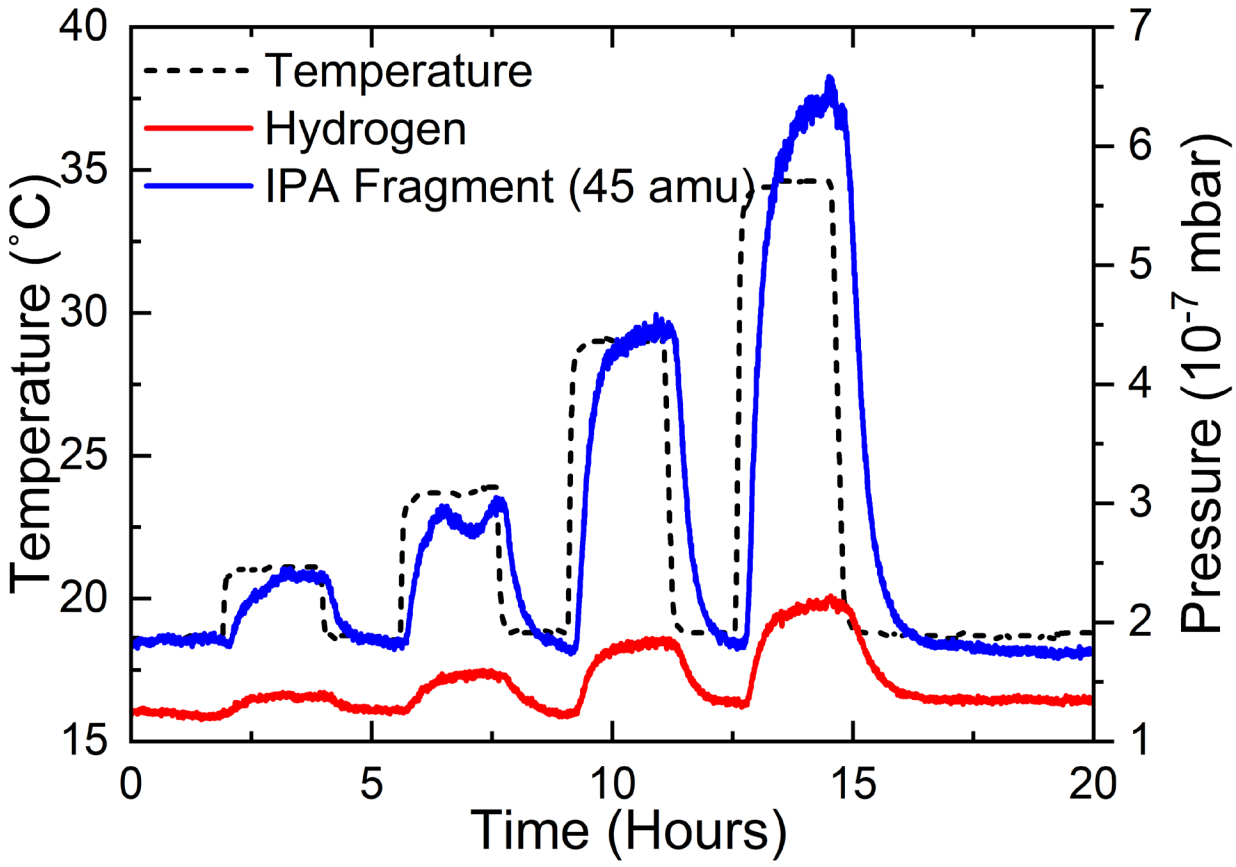

Figure 3.4 RGA traces and temperature of Au nanocrystals. Simultaneous measurements of waterblock temperature with RGA hydrogen and isopropanol pressures. Temperature controlled with circulator was increased in 5 ˚C increments to observe its effect on hydrogen and isopropanol signals. Direct association of thermal effects showing increases hydrogen, convoluting the photochemical reduction of water to hydrogen.

It turns out that the mass spectrometer was picking up a photothermal effect due to solvent evaporation. Figure 3.4 shows the thermal effect of the solvent when no illumination or gold nanocrystals were present. The temperature controller was set to increase in increments of 5 ˚C from the 15 ˚C nominal baseline temperature as indicated by the dashed line. The RGA signal closely follows the increases in temperature for hydrogen at 2 atomic mass units (AMU) and the primary isopropyl alcohol fragment at 45 AMU. This daughter compound $CH3CHOH^{+}$ is a result of a methyl cleavage from the parent molecule. The fragmentation of hydroxyl containing molecules like water and alcohols ionizes and fragments under the electron beam. A fraction of ionized hydrogen atoms recombines in the short window from ionization and striking the detector. It is highly unlikely that simply heating a water/IPA solution produced hydrogen. This indicates that there is a convolution in the hydrogen signal that must be accounted for. This result confirmed that the hydrogen signal seen in Figure 3.4 was mostly or purely due to photothermal effects.

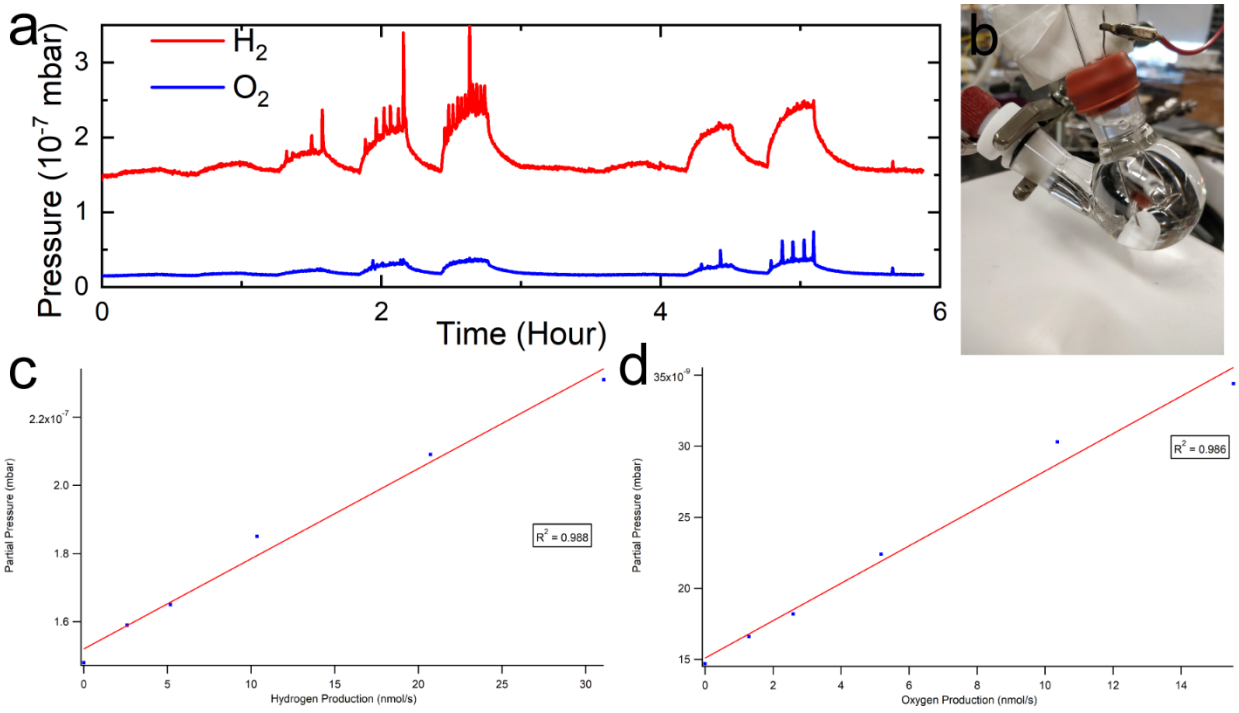

Figure 3.5 Electrolysis of water for real time quantification of headspace hydrogen. (a) Hydrogen and oxygen pressure traces due to chronopoteniometry at 1.5 V for water electrolysis. A series of increasing positive current orders with 0.5, 1.0, 2.0, 4.0, and 6.0 mA followed by negative current of the same order and magnitude. (b) Photograph of the water electrolysis setup. Headspace volume is sampled by RGA while platinum electrodes oxidize and reduce water. Stirring is to help with dislodging gas bubbles on the walls and electrodes. (c) Calibration curve of calculated hydrogen production based on current relative to measured RGA pressures. (d) Calibration curve of calculated oxygen production based on current relative to measured RGA pressures.

To test whether the RGA can detect hydrogen from the headspace of a cuvette, we exercised two methods to split water on command. We used electrolysis and a known photoactive material that is a hydrogen producer. Figure 3.5 details the electrolysis of water to hydrogen and oxygen constituents. Water electrolysis was carried out by applying a 1.5V potential across two platinum electrodes in an acidic electrolyte of 10 mM sulfuric acid. We used a potentiostat in chronopotentiometry mode

to supply a constant current with varying potentials. Figure 3.5a shows the hydrogen and oxygen signals from the RGA. When there is current across the electrodes, an increase in hydrogen and oxygen signals were observed. We hypothesize that the signal spikes were due to dislodging bubbles attached to the electrodes. Stirring was applied during the study, but bubbles were not able to be freed reliably. Figure 3.5(c-d) shows the relationship between supplied current to equilibrated increase in hydrogen and oxygen pressures. Both gases showed good agreement with the supplied current implying that the RGA was capable of measuring headspace hydrogen pressure in a water vapor saturated atmosphere at constant temperature.

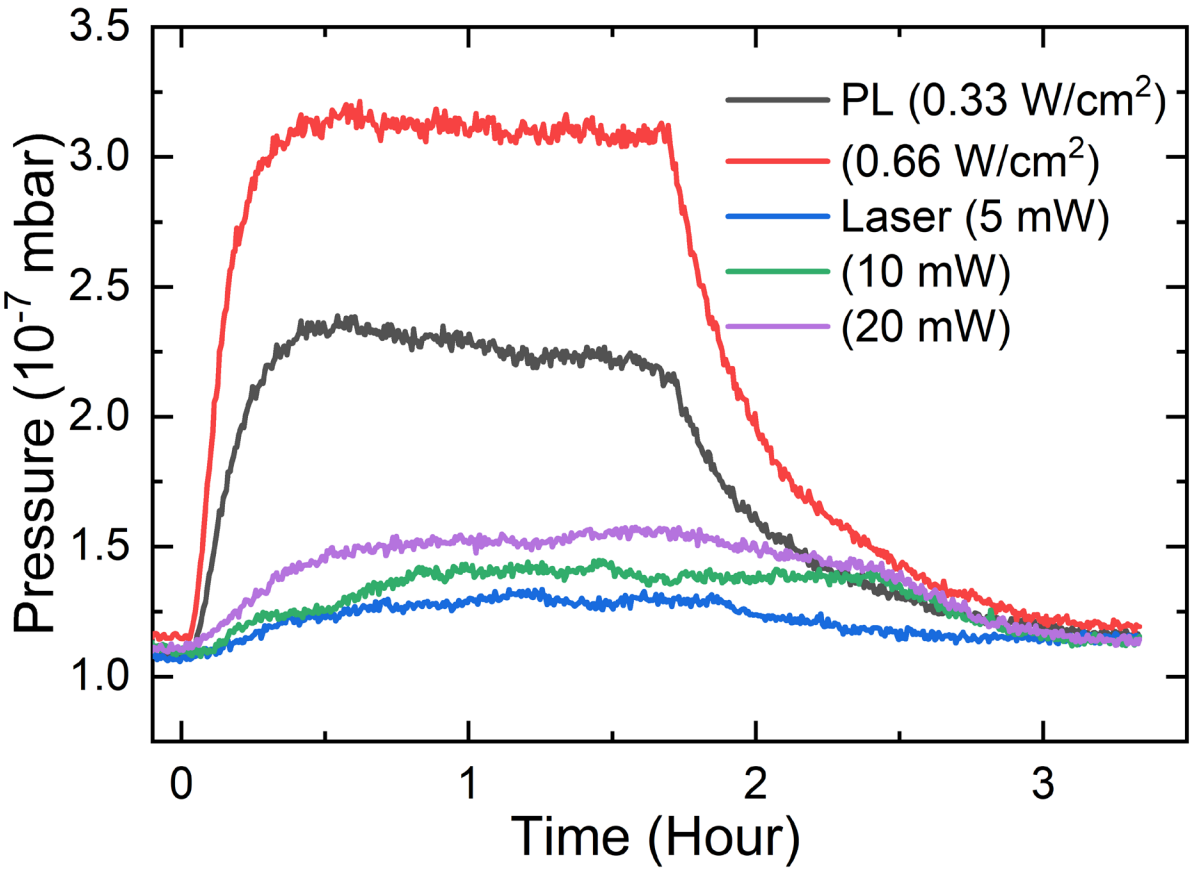

Figure 3.6 Photoinduced hydrogen production from a semiconductor. RGA traces of hydrogen pressure measuring increasing hydrogen signal when light is turned on. Laser and plasma light source are illumining on a suspension of Rh:SrTiO3-Pt

semiconductor with cocatalyst. 5-20 mW of 405 nm laser light produces measurable amounts of hydrogen while plasma light induced photothermal solvent evaporation convoluting the hydrogen signal.

We also used a photoactive material known to produce hydrogen when illuminated to show the RGA was able to measure hydrogen from photoinduced reactions. Rhodium doped strontium titanate with platinum cocatalyst (Rh:$SrTiO_3$-Pt) was used to reduce water in the presence of a hole acceptor methanol. The Rh:$SrTiO_3$ absorbs near UV 405 nm light to excite the band gap of the doped perovskite. The Pt cocatalyst facilitates electron transfer to adsorbed water for more efficient hydrogen production. Holes are quenched by methanol directly on the surface of the $SrTiO_3$. Figure 3.6 shows the effect of relatively low power 405 nm laser illuminations producing hydrogen signals. We believe this is not due to minute photothermal increases of the solvent. We also supplied white light from the plasma light to the material. We know that significant photothermal effects are observed with this light source. The shape of the hydrogen signal possibly indicates a more obvious photothermal effect. Because of the plasma light's spectral output, the vast majority of photons are not absorbed and are likely contributing to heating the solution. Additionally, the power difference between the laser and plasma light is very telling of the mechanisms occurring. We believe if we supplied an equally powerful 405 nm light source similar to the plasma light, the hydrogen signal would easily dwarf the plasma light signals observed.

Our experiments showed that we have the capability to measure headspace hydrogen pressures produced from solution reactions. Quantification is possible by equating the supplied current from chronopotentiometry with the observed hydrogen and oxygen signals. We do not believe we have detected true plasmonic water reduction to hydrogen in this convoluted RGA traces. For future work, we plan to use a

high-powered laser, potentially a white light laser white tunable bandpass selection and a collection of power densities to experiment with. It is possible that higher intensities will yield more efficient plasmonic hot carrier transfer instead of photothermal effects. Additionally, if a dehydration system can be implemented to remove organic solvents and water, it would greatly increase our ability to quantify the hydrogen signal. Other techniques can quantify hydrogen more accurately with the use of a gas chromatograph with a thermal conductivity detector to separate residual gases and quantify its thermal conduction signal. This would however remove the real time measurement aspect of the online sampling with the RGA, so the experiment would need to be converted to batch measurements.

3.3. Nitrogen Fixation

Photofixation of nitrogen to ammonia has been a grand challenge in green energy for decades. The difficulty lies with the number of electrons needed for transfer to completely reduce nitrogen to ammonia. 6 electrons and 6 protons are needed to create 2 units of ammonia while the holes reduce scavengers.

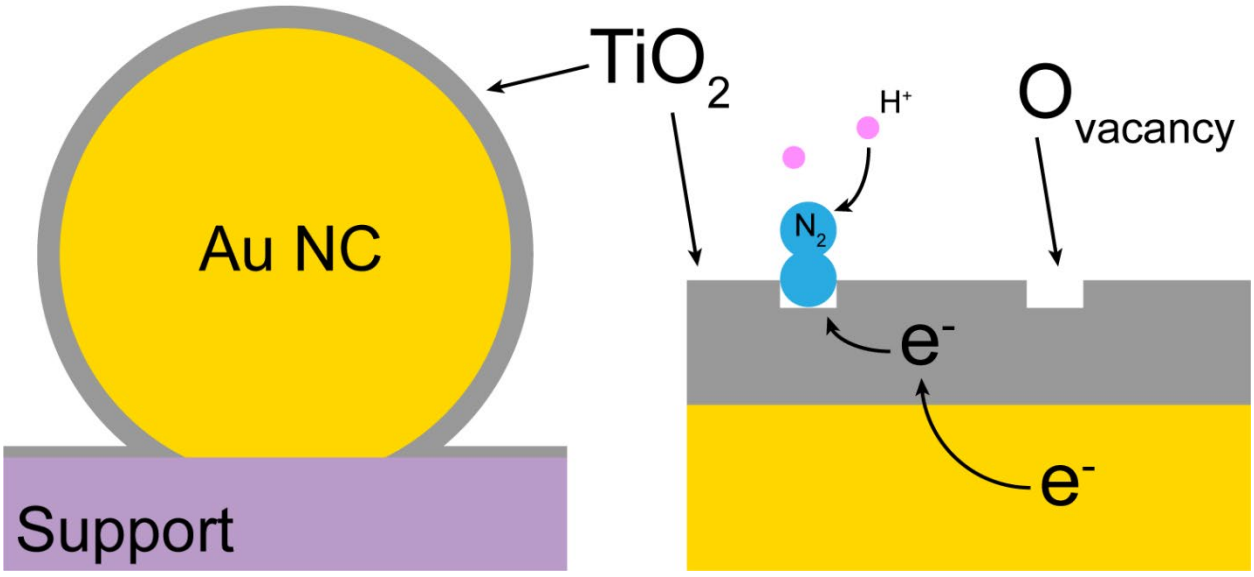

Figure 3.7 Scheme of plasmonic nitrogen fixation mechanism. Atomic layer deposition (ALD) functionalized TiO_2 (grey) shell around supported (purple) Au nanocrystals (yellow). Oxygen vacancies act as binding sites for chemisorbed nitrogen. Hot electrons are injected into the conduction band of the thin TiO_2 overlayer to facilitate electron transfer into the LUMO of bound N_2. N_2^- are protonated from acidic proton sources in solution to generate ammonia in a stepwise process.

We have developed a simple method to fabricate a system for conducting potential nitrogen reduction driven by gold nanocrystals. The system harnesses hot electrons and injects it into the conduction band of TiO_2 which are then subsequently injected into bound nitrogen's antibonding orbitals. This pathway should yield a reasonable transfer of electrons to reduce nitrogen. Figure 3.7 details the electron transfer mechanism to fixate nitrogen. Supported gold nanocrystals are deposited with TiO_2 with atomic layer deposition with a limited number of cycles to create an ultrathin patchy film. Due to the imperfect chemistry of precursor reaction, an abundance of oxygen vacancies should be available to act as binding sites for diatomic nitrogen. Upon an electron injection, a corresponding proton in the form of a hydronium ion, water or other protic acids will be shifted to the bound N_2^- ion. Effectively the electron-proton

pair is equivalent to ½ a H_2 molecule, effectively what the Haber-Bosch reaction from a charge transfer perspective. For ammonia to be synthesized, a complete redox reaction must be completed because there must be constant consumption of holes to balance the charges transported. Holes must be quenched on the surface of the gold to form this cyclic redox electron transfer process. Hole acceptors like methanol, isopropanol, sulfite, or hydroquinone can all be oxidized by hot holes in principle.

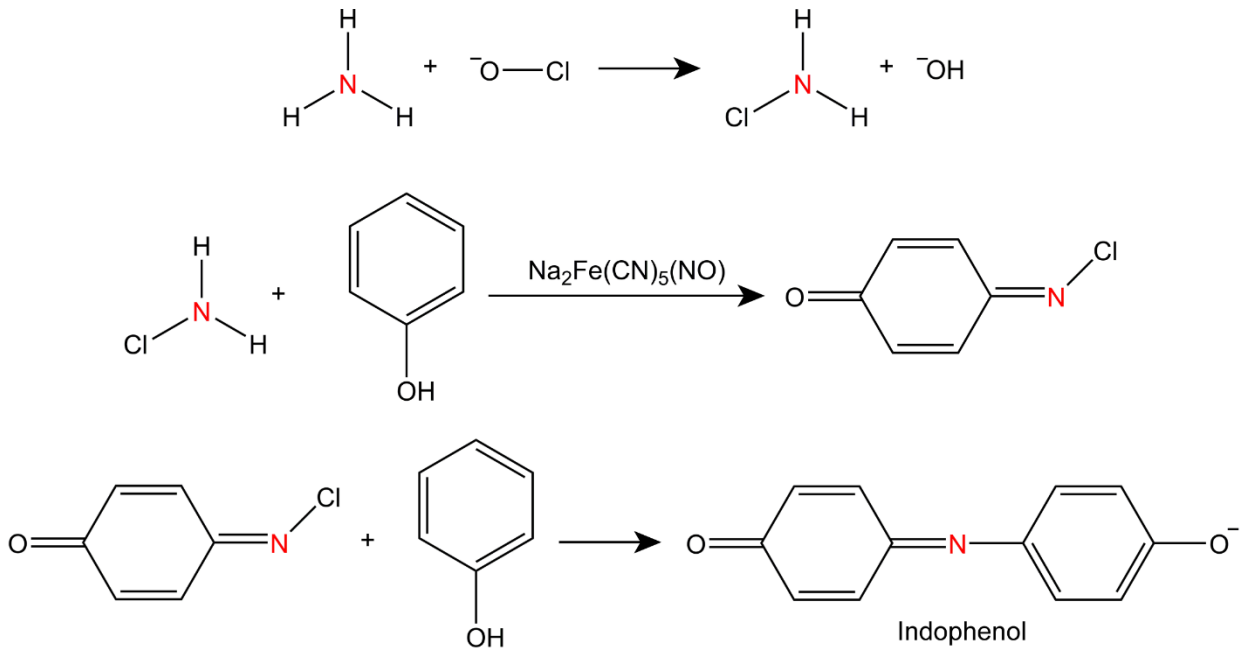

Figure 3.8 Ammonia derivatization reaction to indophenol. The highlighted red nitrogen is carried throughout the indophenol reaction to produce the photoactive indophenol from ammonia. Ammonia reacts with hypochlorite ions to chloramine which then undergoes a catalytic combination reaction with phenol to form the intermediate benzoquinone chloramine. Indophenol is produced when another phenol unit reacts with the intermediate.

Samples of supported 1 wt% Au nanocrystals on crystalline cellulose were fabricated using the forementioned slurry freeze-drying technique. TiO_2 was deposited using ALD from 2 to 20 cycles on the powered material. During deposition, alternating

cycles of $TiCl_4$ and water were pulsed into a nitrogen purged vacuum chamber with sample stage heated to 150 ˚C. 20 ms pulse duration of $TiCl_4$ and water were introduced sufficient precursor to have ample time to react with all surfaces before flushed out by the nitrogen. Ammonia quantification was done spectroscopically after a derivatization reaction with phenol occurred to produce the photoactive molecule indophenol. Figure 3.8 outlines the series of reactions ammonia undergoes to form indophenol. Ammonia is first oxidized in the presence of hypochlorite to chloramine. Phenol and chloramine reaction with a catalyst nitroferricyanide (nitroprusside) to form benzoquinone chloramine. Lastly a second phenol unit further react with benzoquinone chloramine to produce the photoactive compound indophenol. The nitrogen from the original ammonia was preserved throughout the reaction process shown in red from Figure 3.8 signifying that the measured indophenol concentration is a direct measure of ammonia.

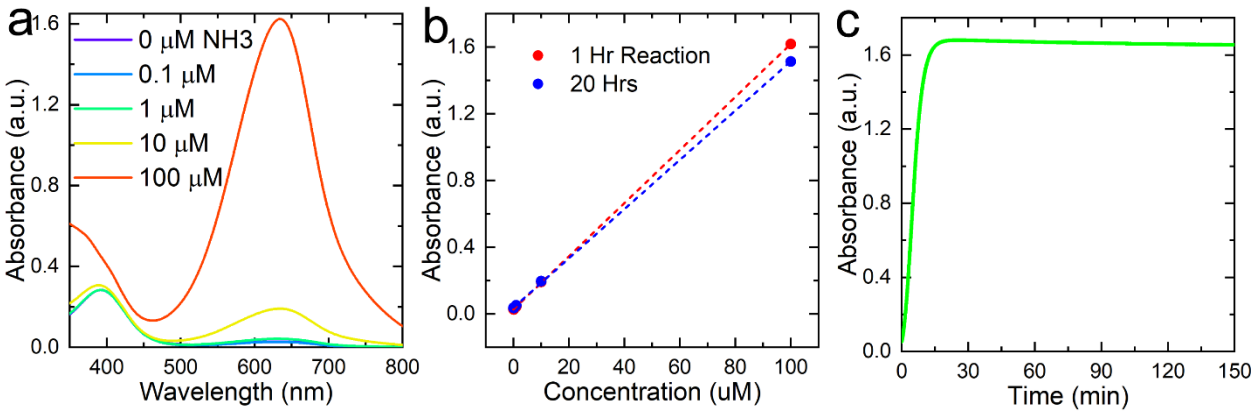

Figure 3.9 Indophenol quantification by UV-vis spectroscopy. (a) UV-vis spectra of ammonia standards and a water blank after the indophenol reaction for 30 minutes. Peak absorption occurs at 630 nm. (b) Calibration curve of absorption at 630 nm of the ammonia standards from (a). (c) Kinetics of the indophenol reaction for a 100 μM ammonia standard monitored at 630 nm.

The derivatization reaction was done by combining 600 μL of the analyte solution, 150 μL phenolic solution, and 150 μL of alkali hypochlorite solution. The

phenolic solution and alkali hypochlorite were premixed solution purchased from Sigma Aldrich specifically formulated for this indophenol reaction. The phenolic solution supplies the phenol and sodium nitroprusside catalyst while the alkali hypochlorite contains a basic solution of sodium hypochlorite. Once mixed, the solution slowly turned a yellow-green color depending on the concentration of ammonia of the original analyte solution. A calibration standard was created by dissolving ammonium chloride in the 10% methanol solution then carried out the indophenol reaction. Figure 3.9a shows the calibration the ammonium chloride standard set from 0.1 μM to 100 μM. The absorbance spectra of the standards are shown in panel (a) of Figure 3.9. We observed a λ_{max} of 630 nm for creating the standard set. A 1 mM solution was created but quantification cannot be completed due to the sensitivity of the UV-vis detector at such significant optical densities. We believe 200 μM ammonia to be the maximum measurable concentration directly measured with this method. Quantifying higher concentrations will require an additional dilution step prior to the reaction. Linear dependence of absorption agrees well shown in Figure 3.9b with coefficient of determination R^2 greater than 0.9999.

The kinetics of the derivatization reaction needs to be determined because any unreacted ammonia will underreport the true concentration. Figure c shows the kinetics of the indophenol assay measured at 630 nm continuously for 150 minutes. Ammonia was completely quenched within 30 minutes with a slow tailing extinction observed. A 24 hour timepoint calibration was compared to the 1 hour reaction in Figure 3.9b. There is a slight decrease in absorption at 630 nm of 6.4% signifying that any measurement of ammonia must have a freshly prepared calibration.

Conditions			Ammonia (μM)			
TiO_2 ALD	Plasma Light	Purge Gas	t_0 Blank	t_0 Filtrate	24 Hours	48 Hours
N/A	Yes	N_2 (50 SCCM)	-0.02		15.67	20.12
1 Cycle			-0.90		11.16	13.41
2 Cycle			-0.88	2.54	9.48	12.54
5 Cycle			-0.97	2.07	14.23	18.17
20 Cycle			-0.76	1.00	5.57	10.59
N/A	No		-1.03	8.74	11.93	14.08
N/A		N/A	-0.84	9.34	7.28	7.87

Table 3.2 Plasmonic nitrogen photofixation. Measured ammonia concentrations for filtrates of 1 wt% Au nanocrystals on MCC at 2 mg/mL concentration in 10% methanol. The light sources used was 3 W plasma light source illuminating 25 mL total volume. A series of TiO_2 ALD was performed with increasing number of cycles. Blank shows the original stock solution of 10% methanol prior to the addition of any catalyst. Three subsequent measurements were at 0 hours illumination, 24 hours, and 48 hours.

The photocatalytic reaction was carried out by suspending the dried supported catalyst at 2 mg/mL concentration in an aqueous 10% methanol solution. 25 mL of this suspension was transferred to a 25 mL two neck round bottom flask capped with rubber septas. The suspension was purged with nitrogen at 50 mL/min for 10 minutes while the stirring rate was set to 800 RPM. During the photochemical reaction, nitrogen was continuously flowing at 50 mL/min. The flask was illuminated by a Thorlab HPLS343 plasma light source with total output of 3 W. A 435 nm longpass filter was used to remove high energy photons that can excite the bandgap of TiO_2 directly. This ensures that only the plasmon excitation is solely responsible for any photo-driven reactions. The suspension was illuminated for 48 hours with samples taken at t-0, 24

and 48 hours for analysis. Samples of the analyte solution were filtered with a 0.22 micron syringe filter to remove all particulates. Table 3.2 details the reaction conditions and sample type for plasmonic nitrogen fixation reaction. Each sample originated from 1 wt% Au on MCC deposited with varying number of layers of TiO_2. Blanks yielded no measurable concentration of ammonia as it was not mixed with the catalyst while the t_0 filtrate was. The higher concentration of ammonia in this could be possibly due to contamination from outside sources or possibly photofixation of ambient nitrogen with water vapor. There is a trend on increasing ammonia levels with 24 and 48 hours of plasma light irradiation showing a possible photoproduction of ammonia. However, the dark sample without TiO_2 ALD also showed increasing trend of ammonia but the increase from background was not as significant as the illuminated samples. Interestingly, when nitrogen was not constantly bubbled, the ammonia concentration did not increase. This control was simply conducting the experiment without catalyst, light or nitrogen. A possible reason could be due to contamination of the phenol and hypochlorite reagents. The TiO_2 ALD cycles did not show a significant trend upwards as the catalyst without TiO_2 yielded the highest ammonia concentration. Interestingly, 20 cycles produced the least ammonia which could possibly show an inability for hot electrons to penetrate the TiO_2 shell. Additional experiment will need to be conducted with more controls and an increased sample size to find any statistical association between ALD cycles, and possible contamination.

Sample	Ammonia (μM)
10% MeOH Blank	-1.17
50 μM Check Standard	50.80
Dark, t_0 Blank	-1.03
Dark, 24 Hrs	11.93
Dark, 48 Hrs	14.08
Dark, t_0 Filtrate	8.74
Dark, No N_2, t_0 Blank	-0.84
Dark, No N_2, 24 Hrs	7.28
Dark, No N_2, 48 Hrs	7.87
Dark, No N_2, t_0 Filtrate	9.34

Table 3.3 Nitrogen fixation controls. Mock experiments in the dark on 10% methanol with and without continuous 50 mL/min nitrogen flow for up to 48 hours.

A series of control experiments listed in Table 3.3 was conducted to potentially deduce any contamination or impurities from the nitrogen gas or outside sources. The blank and check standard are within error of the method. However, the solvent under continuous nitrogen flow showed increasing ammonia demonstrating that the ultra-high purity nitrogen used contains very low levels of ammonia impurities. A possible remedy might be to use an inline gas purifier to scrub the gas to sub parts per trillion levels of amine containing impurities. Other methods involve improving the efficiency of the plasmonic photofixation by using a 520 nm laser with high power density.

We believe this project has future work potential. We have developed a method to quantify ammonia through a robust and quick method with the indophenol derivatization reaction. Our next step would be to use a different light source to excite

the plasmons in a range that could exhibit a higher rate of hot carrier effects. There are additional improvements to be done to remove background ammonia signals from ammonia leeching from the material prior to the photochemical reaction and from the nitrogen gas source.

3.4. Hydrogen Deuterium Dissociation

A model reaction using gaseous hydrogen and deuterium mixture can determine catalytic behavior, rates of reaction and mechanisms of platinum group catalysts. Applying thermodynamic and quantum mechanical models on the energy states of hydrogen can produce the thermodynamic equilibrium of a 1:1 molar ratio of hydrogen and deuterium gases as a function of temperature. This can happen regardless of the catalytic material. Our goal into investigating H-D scrambling is to potentially discover the true or dominant mechanism of plasmonic photocatalysis.

This section will be dedicated towards the development of photoinduced H-D scrambling reaction measured by the RGA in real time. We have already developed the synthesis method for creating colloidal core-shell plasmonic nanocrystals and a process for fabricating the supported material into catalysts. We began by simply decorating 2% Pt decorated Au particles onto alumina nanopowder to test for any photoresponse provided by the plasma light source.

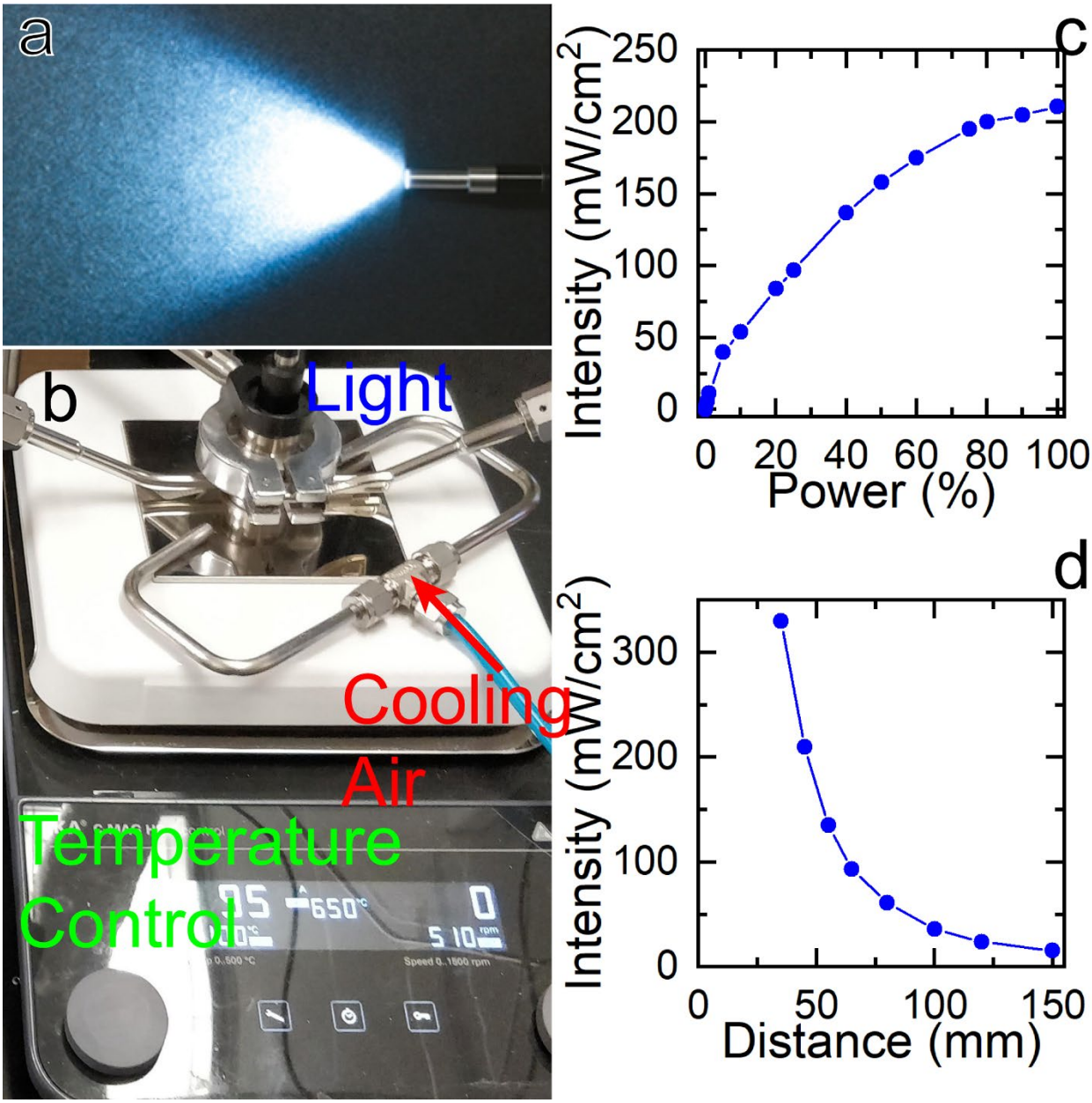

Figure 3.10 Plasma Light Source for H-D Scrambling Reaction. (a) Plasma light source liquid light guide output of white incoherent light. (b) Stainless steel reactor with plasma light guide directed into the top of the reactor. The reactor is on top of a hot plate with a compressed air cooling tube directing air towards the reaction chamber. (c) Power density of the liquid light guide plasma light source dependent on the power setting percentage measured at 35 mm. (d) Distance dependent intensity measurement of the plasma light source liquid guide.

The direct illumination of the liquid light guide into the reaction chamber is shown in Figure 3.10a. The output of the light is extremely divergent which makes it especially difficult to focus into a tight beam required for high intensity photocatalytic studies. For much of the development work, the unfocused output beam was used to measure photoinduced signal increases in HD. Panel b of Figure 3.10 shows the reactor set up for introducing light and heat to the reaction chamber. Plasma light was directed from the top from the liquid light guide while the reactor sits on top of a hot plate with temperature control. The distance from the end of the light guide to the sample is approximately 35 mm. So, Figure 3.10c shows the power density measurement as a function of power setting of the lamp at 35 mm distance from the guide. The light intensity was measured by a LaserProbe Rk-5710 power meter. Lastly, light intensity was measured as a function of distance at full lamp power shown in Figure 3.10. Hydrogen and deuterium gases were delivered by mass flow controllers set to 10 standard cubic centimeter per minute (SCCM). HD concentration was measured by real time RGA at m/z of 3.

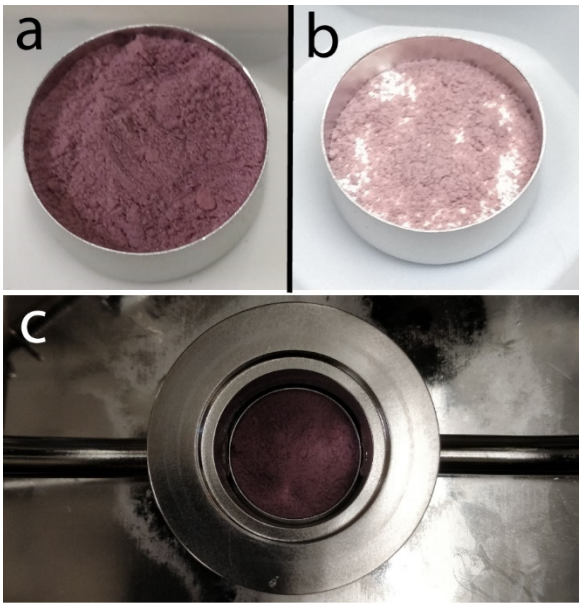

Figure 3.11 Catalyst loading in the reactor. (a) 50 mg of supported 1 wt% Au on alumina in a 20 mm aluminum dish for sample loading into the reactor. (b) 25 mg of the same catalyst with coarse white alumina powder beneath for sample support. (c) 50 mg catalyst in 20 mm aluminum dish loaded in the reaction chamber.

1 wt% nanocrystal with 2% platinum decoration supported on alumina was used as the initial study point. Figure 3.11a shows the sample loading into 20 mm an aluminum dish. Panel a shows 50 mg of catalyst while panel b shows 25 mg of catalyst. Each sample was prepared with 2 grams of coarse alumina powder (visible in panel b) as a powder bed under the catalyst for sample elevation. The 50 mg catalyst sample was lowered into the reactor shown in figure c. The reactor inlet and outlet are near the level of the top of the powder bed to maximize direct contact between the fresh gas and the active material surface. Prior to any HD measurement, the catalyst was annealed at 300 ˚C for 1 hour in air to remove all organic ligands.

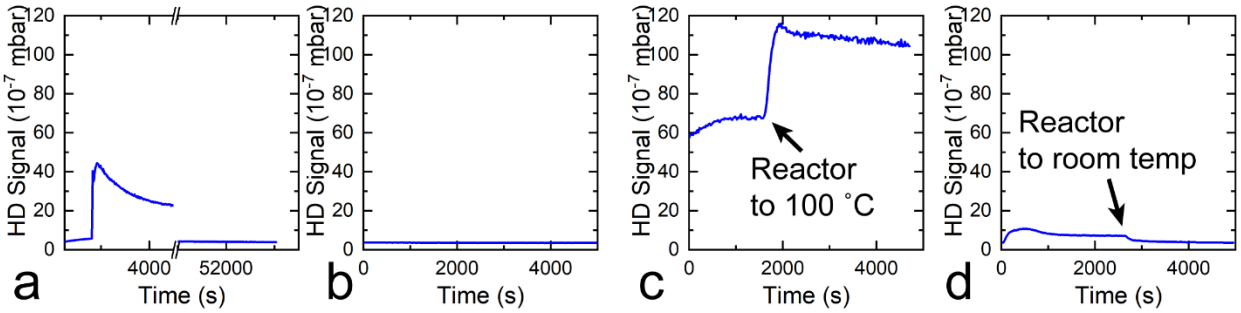

Figure 3.12 RGA HD measurements. (a) Pristine sample of 50 mg 1 wt% (2% Pt on Au) nanocrystals on alumina measuring dark HD scrambling over 15 hours. (b) HD measurement of the same sample after purging with argon overnight. (c) HD measurement of the same sample after 300 ˚C anneal in air for 1 hour. Midway through the measurement, the reactor temperature was increased to 100 ˚C (d) HD rate after an overnight of hydrogen exposure at 100 ˚C reactor temperature.

Background HD production was observed in the dark at room temperature shown in Figure 3.12. This initial rate of HD production was not constant as the rate exponentially decreased until no additional HD was detectable above the background levels. This was a peculiar observation since there was no obvious reason to explain the rate degradation over time. This sample was flushed under argon overnight, then placed under hydrogen and deuterium flow to see any noticeable change in HD formation rate. Negligible increases in HD were observed in Figure 3.12b. The sample was annealed at 300 ˚C for 1 hour in air before remeasuring. Here, the sample appeared to show HD formation rate significantly above the pristine sample from panel a. Not only was the poisoned catalyst recovered, but an enhancement had occurred. Increasing the hotplate temperature to 100 ˚C showed increased HD scrambling rate suggesting this reaction is temperature sensitive. The experiment showed that poisoning was occurring to the platinum on the surface that was reversible by thermal annealing in air. This poisoning was reproducible after the thermal treatment between Figure 3.12b-c.

ID	Pt Decoration	Ligand Type	Catalyst Mass	Annealing Temperature	Annealing Duration	Annealing Gas	Pristine Sample		16 Hours Exposure to Hydrogen	
							Room Temperature	100 ˚C	100 ˚C	Room Temperature
	%		(mg)	(˚C)	(Hours)		RGA HD Signal (10^{-7} mBar)			
P1B1	2	Starch	49.7	300	1	Air	44.1	-	-	3.5
P1B3	2	Starch	49.8	400	1	Air	134	-	-	80.3
P1B4	2	Starch	49.6	300	4	Air	101	-	119	70.9
P1C1	2	Starch	24.9	300	10	Air	31.3	-	9.83	3.5
P1C4	2	Starch	49.8	300	10	Air	162	-	82.7	12.8
P2A1	2	Starch	50.2	350-300	10	Air	190	199	182	104
P2A2	2	Starch	50.1	300	1	O_2	16.8	-	-	-
P2A3	2	Starch	25.4	350	10	Air	176	-	93	18.1
P2B1	2	Starch	25.5	500	1	Air	86.3	140	15.6	4.28
P2B2	2	Starch	25.2	500	10	Air	79.5	142	12.5	4.27
P2B3	0	Citrate	50.8	300	1	Air	3.1	-	-	-
P2B4	2	Citrate	51.1	300	1	Air	201	210	56.1	11.6
P2C1	2	Citrate	25.3	300	10	Air	17.9	24.7	5.05	3.43
P2C2	2	Citrate	25.6	350	10	Air	116	158	12.4	3.8
P2C3	2	Citrate	49	300	1	Air	156	185	48	10.2
P2C4	2	Citrate	25.3	300	1	Air	20.4	62.3	-	-
P3A1	2	Citrate	25	500	1	Air	8	11	4.24	3.44

Table 3.4 Dark RGA HD signals from alumina supported Au@Pt catalysts.

A series of experiments was conducted to investigate this behavior more by testing samples with various thermal treatments, plasma cleaning, and Au nanocrystal synthesis methods. Table 3.4 list the results of a variety of experiments conducted. The last four columns list the RGA signals in the dark with reactor temperature set to either room temperature or 100 ˚C. Each sample was measured initially at room temperature to record the HD signal, then the hot plate was set to 100 ˚C for 16 hours to let the sample immerse in hydrogen. After 16 hours, the sample was measured again initially when the reactor is at 100 ˚C, then again once the reactor has cooled to room temperature. This way, we can have a picture of the behavior of each sample's HD production in the pristine and poisoned state. Nearly every sample test showed a decrease in HD rate over the course of the measurement. The mass of the catalyst clearly affects the overall HD scrambling. It appears that the anneal temperature does have an effect on the initial rate, but it did not prevent the drop-off after 16 hours. Two types of nanoparticles synthesis methods were tested with the stabilization by starch or citrate. These two methods seemed to show negligible differences in preventing poisoning suggesting surface chemistry is playing a key role. A control sample was measured with any platinum decoration which showed no HD scrambling at room temperature or at 100 ˚C. The 3.1×10^{-7} mbar RGA signal is the same as the background signal with a clean reactor.

ID	Substrate	Ligand Type	Catalyst Thickness	Annealing Temperature	Annealing Duration	Annealing Gas	Pristine Sample		16 Hours Exposure to Hydrogen	
							Room Temperature	100 ˚C	100 ˚C	Room Temperature
			(nm)	(˚C)	(Hours)		RGA HD Signal (10^{-7} mBar)			
P3A2	Disk	-	20	-	-	Air	211	213	200	160
P3A3	Disk	-	1.4	-	-	Air	97.6	-	-	-
P3A4	Disk	-	-	-	-	Air	3.64	-	-	-
P3B1	Disk	-	1.0	-	-	Air	176	192	98.7	20.1
P3B2	Disk	-	1.0	-	-	Air	70.2	159	113	28.2
P3B3	Disk	Citrate	1.1	300	1	Air	34	92.3	20.5	4.05
P3B4	Disk	Starch	1.1	300	1	Air	49.2	99.2	22.6	4.02
P3C1	Disk	Starch	1.1	-	-	O_2	146	168	18.6	4.7
P3C2	Disk	Starch	1.1	-	-	Air	-	-	-	-

Table 3.5 Dark RGA HD signals from sputtered Pt/Pd on disc substrate.

To eliminate additional variables, a stainless steel substrate disc was sputter coated with platinum/palladium 85%/15% alloy to mimic nanoparticles without any surface ligands. Only 1 nm of sputtered material was necessary to produce significant HD scrambling rates on the 20 mm diameter substrate. The background HD signal was measured on control sample without any sputtered metal which showed no HD reaction detected by the RGA. Table 3.5 lists the sample preparation conditions with its HD reaction signal similar to Table 3.4. These samples had identical measurement pathway with the initial measurement at room temperature followed by heating to 100 ˚C. Then, the samples were exposed to hydrogen under 100 ˚C for 16 hours and measured again at 100 ˚C and room temperature. A similar behavior was observed for these sputter samples compared to the powder nanoparticle catalyst. Starch and citrate ligands were applied to the sputtered surface to test for ligand coverage possibly moderating hydrogen adsorption. The few samples tested showed no such behavior. The organic ligands did not seem to impact the hydrogen binding measured in the initial HD rates. The hypothesis that ligand coverage was impeding catalysis was also invalidated by evidence from samples P2B4 comparing citrate to starch.

We explored alternative methods to prevent the poisoning by using a different platinum group metal. Iridium was chosen because we had the ability to compare it to iridium sputter coated samples. Iridium sputtered on glass was measured for HD formation which showed overall lower rates compared to Pt/Pd at the same thickness, but it was overall more robust to maintain its rate over the 16 hours tested. Next iridium decorated Au nanocrystals were synthesized to test this behavior. The iridium particles were synthesized using the identical method to synthesize platinum decorated Au particles with the H_2PtCl_6 replaced by a 5 mM $IrCl_3$ solution. We also discovered that plasma cleaning the powder catalyst removes organics to improve overall efficiency without going to high temperature annealing which can alter the atomic landscape of

the particle's surface. One potential undesired consequence to plasma treatment is the formation of oxides. A possible method to manage this is to anneal under hydrogen atmosphere at high temperatures. Annealing under pure hydrogen at 300 °C for 12 hours gives ample time for all surface oxides to reduce to metallic iridium and for oxides to convert to water and desorb. A few samples listed in Table 3.6 underwent this treatment and it does seem to increase autocatalytic HD production. The Table 3.6 lists samples with three levels of iridium decoration each with plasma treatment and thermal anneal in air or hydrogen. The samples with O_2 plasma treatment and hydrogen seemed to yield the highest HD production at room temperature. The rest of the samples did not show any detectable HD scrambling. Additionally, photoinduced HD scrambling rates were measured alongside the thermocatalytic measurements. The samples were irradiated with plasma source white light at 211 mW/cm^2 over the 20 mm diameter sample dish. Only minor increases in HD signal were observed for all signal above the background concentration. Such a low increase in rates is not sufficient to study intricacies in plasmonic photocatalysis mechanism. A high-power laser must be used to focus the beam to high power densities to generate a measurable signal to deduce trends and behaviors.

ID	Ir Decoration	Catalyst Mass	Plasma Treatment	Annealing Temperature	Annealing Duration	Annealing Gas	Pristine Sample			16 Hours Exposure to Hydrogen		
							Room Temperature	Light ON	100 ˚C	Room Temperature	Light ON	100 ˚C
	%	(mg)		(˚C)	(Hours)		RGA HD Signal (10^{-7} mBar)					
P7B3	2	25.3	-	300	1	Air	5.66	11.9	118	6.81	54.4	51.3
P7B4	2	25.6	O_2	-	-	-	4.1	4.1	10.5	8.34	11.6	8.76
P7C1	2	26.9	O_2	300	12	H_2	16.4	18.9	108	4.58	10.8	11.1
P7C2	2	25.8	O_2	300	1	Air	4.98	5.08	58.9	5.26	35	36.2
P7C3	5	25.2	-	-	-	-	5.3	5.57	116	10.2	106	110
P7C4	5	25.3	O_2	300	12	H_2	41.4	66.3	172	_	-	-
P8A1	5	26.1	O_2	300	1	Air	6.86	10.1	175	_	132	146
P8A2	0.2	24.8	O_2	-	-	-	4.31	4.27	4.22	-	-	-
P8A3	0.2	26.5	O_2	300	1	Air	4.97	4.89	4.61	4.2	4.37	4.46
P8A4	0.2	26	O_2	300	12	H_2	4.35	4.36	4.91	4.05	4.13	4.13

Table 3.6 Dark RGA HD signals from sputtered iridium on disc substrate.

The plasma light source was replaced with a monochromatic 1.25 W 520 nm continuous wave laser. The typical use for this laser is for engraving or etching flat material but the Au nanocrystal's plasmons strongly resonate with the 520 nm light. Figure 3.13a shows the overhauled photocatalytic reaction set up with a laser enclosure to contain any potential scattered beam. Two plane mirrors redirect the beam towards the sample chamber that can be centered to each sample. Filters can be placed within the beam path to attenuate or focus the beam to the desired spot size and intensity at nearly any power below the 1.25 W rated maximum output. With the beam focused to a tight spot, much of the catalyst mass is wasted. So, we have developed a couple of new methods for irradiating much lower masses of catalyst. Figure 3.13b shows approximately 2 mg of catalyst without a support bed contained in an aluminum pan centered in the larger 20 mm aluminum dish. Using a loose powder proved to be difficult as the focused laser deformed the surface of the power and created a crater. Our hypothesis is that the gases surrounding the loose powder superheated so quickly that a high-pressure environment formed and rapidly expanded to scatter material outwards to form a crater. When measuring the rate of HD scrambling using this system, there was a rapid decline in the HD signal which likely is due to this material excavating issue. In extended trials, the beam tunneled a cavity to the bottom of the pan such that very little material was exposed. This likely caused the drop in catalytic performance since the illumination was not irradiating much of the catalyst surface directly.

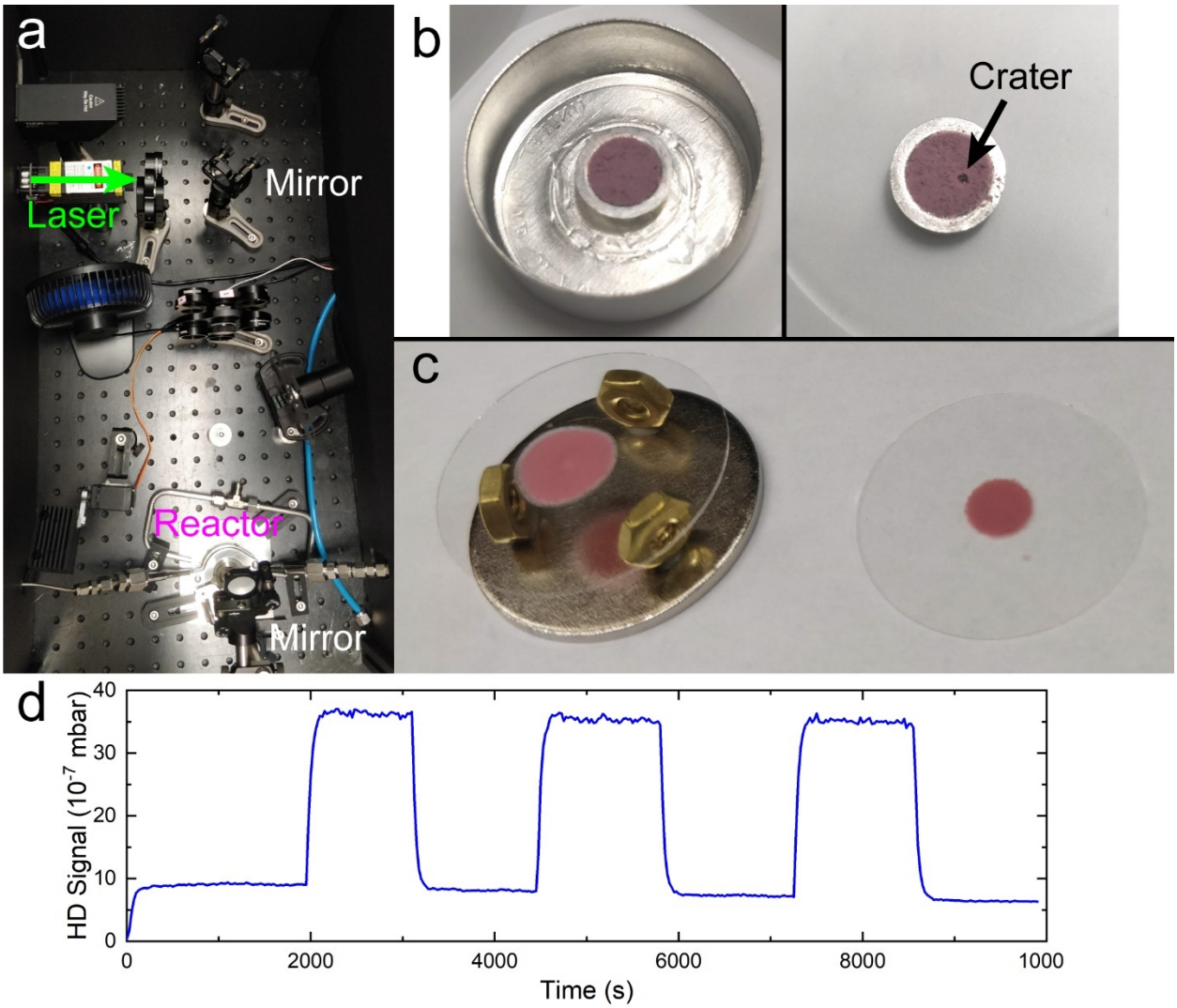

Figure 3.13 520 nm Laser Set up. (a) Laser enclosure for photocatalytic studies. 520 nm laser is focused and redirected into the reaction chamber. (b) 2 mg samples of alumina supported Au nanocrystal catalyst. Laser irradiated loose powder creating a crater in the sample. (c) Dried dropcast of concentrated catalyst slurry on circular glass discs. Left sample (1000 μg) is on a raised platform to be lowered into the reaction chamber. Right sample mass is 500 μg dropcasted from 10 μL of 50 mg/mL slurry. (d) HD pressure trace of laser-illuminated dropcasted sample with sharp increases in HD signal when laser was turned on.

To correct this issue, we resorted to dropcasting concentrated slurries of the catalyst onto 18 mm circular glass cover slides. Figure 3.13c shows the dropcasted samples which formed a densely packed puck of catalyst. There are several upsides to this sample preparation method. *i*) Precise control of the catalyst mass for each measurement. *ii*) Dropcasted area can be tuned with the volume of water during dropcasting. *iii*) The sample was not scattered or destroyed during the laser irradiation. *iv*) The sample platform is easily controlled by using a platform shown in Figure 3.13c. Panel e shows the HD signal of 1000 μg of dropcasted catalyst illuminated by the laser. The pressure trace produced very clean and distinct signals distinguishing illuminated and dark cycles. This is ideal for designing experiments around to generate clean, reproducible, and quantitative data.

Quantifying the hydrogen pressure was done by converting the RGA signal in amps into outside pressure of the reaction exhaust. We did this by using a Kurt Lesker hot filament vacuum gauge to measure the internal pressure under a dynamic vacuum when sampling pure gases. The gauge was calibrated to nitrogen, so a conversion factor was used to normalize the reading to true pressure in hydrogen or deuterium atmospheres. A constant flow of pure hydrogen or deuterium was sampled while measuring the RGA signal and pressure. The RGA's sensitivity factor was calculated with the ratio of the signal (Amps) to the pressure (mbar). We applied the sensitivity factor to quantify any hydrogen/deuterium/HD mixture by applying the sensitivity factors to the raw signals. The HD sensitivity factor was not determined experimentally, but rather by averaging the hydrogen and deuterium factors then multiplying by a constant. This is to normalize the calculated pressure to atmospheric pressure. Once applied, we can calculate exactly how much HD was formed during laser ON cycles relative to the dark measurement.

The following chapter explores the platinum and iridium decorated Au nanocrystals for hydrogen dissociation. We studied the core-shell decoration concentration, power dependence of illumination, and explored quantum yield. Additionally, we revisited investigating the platinum stability issue observed as shown from Figure 3.12.

Chapter 4. Core-shell Nanocrystal Catalysis

4.1. Introduction

Plasmonic photocatalysis is a growing field within the sustainability research area.[182,183] The desirability to use plasmonics is largely driven by its tunable absorption of photons of specific wavelengths to drive chemical reactions.[184] Metallic nanocrystals like gold[185], silver[3], copper[14], aluminum[83], and other non-noble metals[186] offer exceptional plasmonic performance and flexibility. Gold nanocrystals offer remarkable chemical and structural stability along with a range of geometric manipulation to harness light within the visible and infrared spectrum.[187,188] Plasmonics are great because they act as engines that drives light capture, but their range of chemical transformations are bound by the limiting number of chemical interactions between these few plasmonic metals and molecules.[28] Much of the more active catalytic metals are not plasmonically active or not active in a region deemed usable. To merge a plasmonic metallic nanocrystal and a catalytic material, heterostructures have been created to enhance catalytic activity of meaningful reactions.[189] This set up is commonly denoted the "antenna" and "reactor" system in plasmonic photocatalysis. The area of work that plasmonic gold nanocrystals encompasses is vast, with only a small sector of research dedicated towards photocatalysis. Much of the applications surrounding gold nanocrystals are in the fields of sensing and biomedical applications.[31,190] Plasmonic application in energy has gained traction as there exists research in photovoltaics[32], photocatalysis[191], and thermoplasmonics.[98,99] There is significant motivation to enhance light capture and increase efficiency by creating designer catalysts. However, the true dominant mechanism is still not fully understood and is currently debated within the

community.[15] A core-shell heterostructure can offer a straightforward testable method to potentially expose the nature of excited electrons compared to photothermal effects.[96]

In this study, we developed and studied a bimetallic core-shell iridium and platinum decorated gold nanocrystals for driving plasmonic photocatalysis. We used a model reaction consisting of hydrogen and deuterium gases to measure plasmonic activity of the supported core-shell particles illuminated by a high-powered laser.[81,83] This heterostructure gives us controllability of the surface decoration to measure additional catalytic activity compared to their non-decorated counterparts. High magnification STEM imaging allowed us to map the elemental composition and spatial distribution of Au, Ir, and Pt of the core-shell structure. Our homebuilt photoreactor system gives us the ability to continuously monitor real-time reaction products to quantify reaction rates and quantum yield. We showed that increasing the shell decoration leads to an improvement in the photocatalytic rates of hydrogen-deuterium scrambling except for the 0.2% Pt, which can be explained by alloyed Pt acting as decoherence sites. Additionally, Au@Pt particles will undergo room temperature catalytic hydrogen dissociation in the dark which gradually decreases in rate over several hours through a poisoning process. The samples were returned to pristine levels of activity by annealing at 100 ˚C in air and oxygen plasma treatment.

There is significant motivation to enhance light capture and increase efficiency by creating designer catalysts. However, the true dominant mechanism is still not fully understood and is currently debated within the community. The plasmon resonance decay pathway is straightforward and settled within the field, but much more work is needed to understand the experimental pathways. A core-shell heterostructure can offer a straightforward testable method to potentially expose the nature of excited electrons compared to photothermal effects. Platinum is known the dampen the plasmons of Au nanocrystals because platinum act as decoherence sites and accelerate the dephasing

rate. Here, we compare low decoration concentrations at 0.2 mol% differ in HD scrambling rates. Au only and 0.2% Ir produce HD at similar rates while 0.2% Pt is significantly lower signifying Pt alloys with Au under high intensity light. Subsurface Pt atoms act as dephasing sites leading to energy dissipating within the core of the particle rather than on surface atoms leading to a decrease in observed rate. Photothermal effects would not show a meaningful change let alone a decrease in rate between the pure Au and Pt decorated particles.

4.2. Materials and Methods

4.2.1. Chemicals

All chemicals were used as received unless otherwise noted. 18.2 MΩ water (Millipore Milli-Q Gradient) was used throughout the study. Hydrogen tetrachloroaurate(III) trihydrate ($HAuCl_4 \bullet 3H_2O$, 99.99%) was purchased from Alfa Aesar. Aluminum(III) oxide nanopowder (Al_2O_3 <50 nm), Starch (Zulkowsky, 85642), D-(+)-glucose (G8270), 2-(N-morpholino)ethanesulfonic acid hydrate ($MES \bullet xH_2O$, M8250), and hexachloroplatinic(IV) acid hydrate ($H_2PtCl_6 \bullet xH_2O$, ≥99.9%) were purchased from Sigma Aldrich. Iridium(III) chloride hydrate ($IrCl3 \bullet xH_2O$, I0616) was purchased from TCI. Sodium hydroxide (NaOH, E584 reagent grade) 10 N solution was purchased from Amresco. Hydrochloric acid (HCl 36.5-38.0%, 2612-14) and nitric acid (HNO_3 68-70%, 1409-04) were purchased from Macron Fine Chemicals. Hydrogen (Ultra high purity 99.999%) and Deuterium (Research grade, DT R80) gases were purchased from Airgas.

4.2.2. Nanocrystal Synthesis

The synthesis of Pt decorated Au nanocrystals was based on a previously published method.[192] A 100 mM MES solution was adjusted to pH 8.0 with NaOH. Colloidal Au NCs were synthesized by combining 114 mL of water, 20 mL of 100 mM glucose, 30 mL 4 wt% starch solution, and pH 8.0 adjust 100 mM MES solution in a 250

mL three-neck round-bottom flask. A stirbar was added and set to 800 RPM while the temperature was set to 95 ˚C. Once the solution reached 95 ˚C, 16 mL of 25 mM $HAuCl_4$ was quickly pipetted to the hot mixture. The temperature was maintained at 95 ˚C for 1 hour before chilled with an ice bath to room temperature.

For the synthesis of Pt and Ir decorated Au nanocrystals, 50 mL of the Au nanocrystals was combined with water to reach 200 mL total volume in a 250 mL three neck round-bottom flask. This dispersion was heated to 95 ˚C before injecting the remaining volume of 5 mM H_2PtCl_6 to reach the 200 mL total volume. The suspension was allowed to react for 90 minutes before being cooled to room temperature with an ice bath. The Iridium decorated Au nanocrystals was synthesized using this identical method except a 5 mM $IrCl_3$ solution was used.

4.2.3. Preparation of Supported Photocatalysts

The NCs were purified by dialysis filtration using Amicon Ultra-15 Centrifugal Filter Units (UFC905024, 50 kDa cutoff) to remove solutes and loosely-bound ligands (i.e., oxidized MES byproducts, excess glucose, starch, MES, ions and other impurities) without subjecting the NCs to precipitation and redispersion cycling that can cause incomplete NC recovery and an altered size distribution. Briefly, 12.5 mL aliquots of the reaction mixture (Au only and core-shell suspensions) were centrifuge filtered at 3000 RCF (relative centrifugal force) for three minutes and the resulting concentrated colloidal retentate (<1 mL volume) was re-diluted to 12.5 mL with water. Each aliquot was filtered again, diluted again, and filtered a third time to give a >2000-fold reduction in solute concentrations with negligible loss of NCs. The purified aliquots were then combined and diluted with water to a total volume of 20 mL (final NC concentration of ~1 mg/mL).

To fabricate 1 wt% supported NCs, 500 mg of Al_2O_3 nanopowder was combined with 45 mL of water to briefly suspend the particles. While the mixture was suspended,

5 mL of purified 1 mg/mL NC dispersion was transferred to the Al_2O_3 slurry. The mixture was capped and briefly shaken to homogenize the NCs. This mixture was centrifuged at 3000 RCF for 3 minutes to separate the particles from the solvent followed by removal of the supernatant. The remaining thick slurry was oven dried at 100 ˚C for 16 hours. The resulting dried material formed large aggregates which was broken by mortar and pestle to a loose powder. To fabricate 10 wt% supported NCs, 100 mg of Al_2O_3 nanopowder was combined with 10 mL of the purified NC suspension. This slurry was frozen in a -20˚C freezer until fully frozen and then thawed before centrifuging. The rest of the process was identical to the 1 wt% catalyst.

100 mg of the catalyst powder was combined with 2.5 mL water to create a 40 mg/mL suspension. A microstirbar was added to stir the suspension for at least 90 minutes to break up the aggregates even more. 5 μL of the stirred slurry was dropped onto an 18 mm glass cover slide (VWR, 48382-042). The droplet was let undisturbed for at least 3 hours to dry and form a circular disk (200 μg total catalyst mass). Anneal samples were place in a furnace at 200 ˚C or 400 ˚C for 1 hour in air prior to measurement.

4.2.4. Hydrogen-Deuterium Dissociation Reaction

The 200 μg sample was transferred and centered into our homemade stainless steel photoreactor. Mirrors were adjusted to align the beam to the center of the sample under 10 mW 520 nm illumination to not cause any changes. Our MFCs (Aalborg) and laser were controlled by an Arduino system to conduct repeated measurements of multiple samples. Argon was flushed for 5 minutes at 50 SCCM by and MFC to remove any air in the reaction chamber. While the argon MFC was turned off, equal flow rates of hydrogen and deuterium were supplied by MFCs were turned on. A 1.18 W 520 nm laser was cycled on and off during the measurement period. Exhaust gases was measured in real time by an SRS300 quadrupole mass spectrometer. A sample

measurement consists of a five minute wait period in the dark after the RGA initial data collection, 5 minutes of laser on and 5 minutes of off time. The on-off cycle was repeated four more times to conclude one measurement cycle. Two measurement cycles were conducted per sample. Rate calculations was done on the second measurement.

4.2.5. Dark HD Catalytic Reactions

20% platinum decorated Au NCs were tested for stability under 10 SCCM flows of hydrogen and deuterium. 200 μg of the catalyst was placed in the reaction chamber in the dark for five hours while monitored by the RGA. Then the sample was treated with several methods. Annealed samples were placed in a 100 ˚C furnace for 1 hour in air or nitrogen before remeasured. Plasma cleaned sample was exposed to O_2 plasma for 1000 seconds under 0.3 mbar O_2 atmosphere in between measurements. One sample was placed under vacuum at 20 mbar base pressure for 72 hours at room temperature before remeasurement. One sample was placed in ambient atmosphere for 72 hours at room temperature before remeasuring.

4.2.6. ICP-MS Quantification of Au, Ir, and Pt

A stock solution of freshly prepared aqua regia was created by combining 15 mL of concentrated HCl with 5 mL of concentrated HNO_3. 50 μL of each purified 1 mg/mL NC dispersion was combined with 1 mL of aqua regia solution. This was diluted with water to 20 mL total volume. This solution was then diluted with water by a factor of 10. Standards were diluted from a stock 10 μg/mL multi-metal standard for Au, Ir, and Pt (Inorganic Ventures CMS-2). The stock solution standard was serially diluted by combining 1 mL of the stock standard to 9 mL of water. Subsequent levels of standards were diluted 10-fold using this 1:9 volume ratio. A total of six different standards were used for the measurement ranging from 10 μg/mL (100 ppm) to 0.1 ng/mL (0.1 ppb). The standards and unknown solutions were injected into a Thermo Scientific™ iCAP™

RQ single quadrupole ICP-MS. Concentrations were calculated on the integrated Qtegra™ ISDS software.

4.2.7. Materials Characterization

Transmission electron microscopy was performed on a JEOL JEM-CF300 TEM at 300 kV accelerating voltage. Samples were prepared by drop casting and drying 7 μL of the supported nanocrystal suspension on a TEM grid (Ted Pella, 01896) in air. Images of the dropcasted catalysts were taken with an Olympus BX53M optical microscope at 2.5x-10x magnification (dark-field at 600 ms exposure), and 20x-100x magnification (bright-field at auto exposure). Absorbance of the NC colloids were measured in 4.5 mL polystyrene cuvettes (759071D, BrandTech) on a PerkinElmer 950 spectrophotometer. Supported catalyst absorbance for quantum yield calculations were measured using a 60 mm integrating sphere illuminated by a 4.2 mW 520 nm Thorlabs laser with an Ocean Optics photodetector. Optical absorbance was calculated using the following equation: absorbance $= -\log(R + T)$. A spectrum of the high powered 520 nm laser used to drive photocatalytic reactions was measured by the Ocean Optics spectrophotometer.

4.3. Results and Discussion

4.3.1. Synthesis and Characterization of Core-shell Catalysts

Colloidal synthesis of Pt decorated Au nanocrystals was adapted from a green synthetic method by the reduction of MES.[192] Iridium decorated particles were identical to the Pt shell synthesis. Although the method was tailored to Pt, it was sufficient for lower concentrations of Ir up to 20 mol%. Figure 4.1a outlines the colloidal synthesis pathway of the core-shell particles followed by immobilization onto alumina nanopowder support. Excess organics from the starting material and byproducts post-synthesis were removed by dialysis filtration.[163] This removed the need to anneal in

oxygen or air atmospheres at high temperatures to remove surface ligands prior to illuminated photocatalytic measurements. After preparing the dried material, large aggregates were broken up with a mortar and pestle to a fine powder to maximize surface area for gas diffusion. Additionally, when the slurry is freshly made, it was stirred with a stirbar to ensure medium sized aggregates are further broken down.

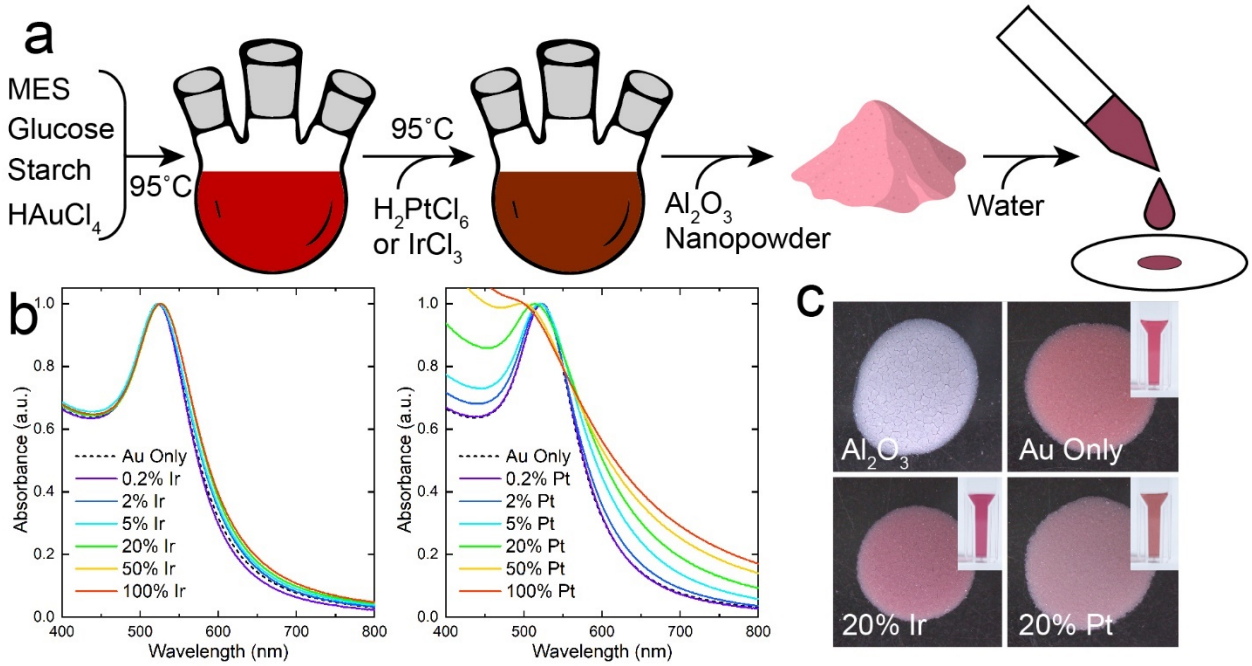

Figure 4.1 Synthesis and fabrication of supported core@shell catalysts. (a) Colloidal synthesis of Au nanocrystals by combining 2-(N-morpholino) ethanesulfonic acid (MES), D-(+) glucose, starch, and $HAuCl_4$ at 95 ˚C. The shell reaction was conducted in a separate reaction from the products of the first. A diluted dispersion was combined with an aqueous solution of $IrCl_3$ or H_2PtCl_6 and reacted at 95 ˚C. The final purified nanocrystals were loaded onto alumina nanopowder support to produce the final catalyst. A dropcasted slurry of the catalyst was dropped onto a glass disk for photocatalytic measurements. (b) Optical absorbance spectra of purified core-shell colloids. No significant coupling was observed for the Ir decorated nanostructure. Au@Pt particles showed significant plasmonic coupling that altered the absorption spectra compared to the Au only (dashed) suspension. (c) Dark-field optical microscope

images of the dropcasted catalyst on glass cover slides with inset showing photographs of its respective colloids.

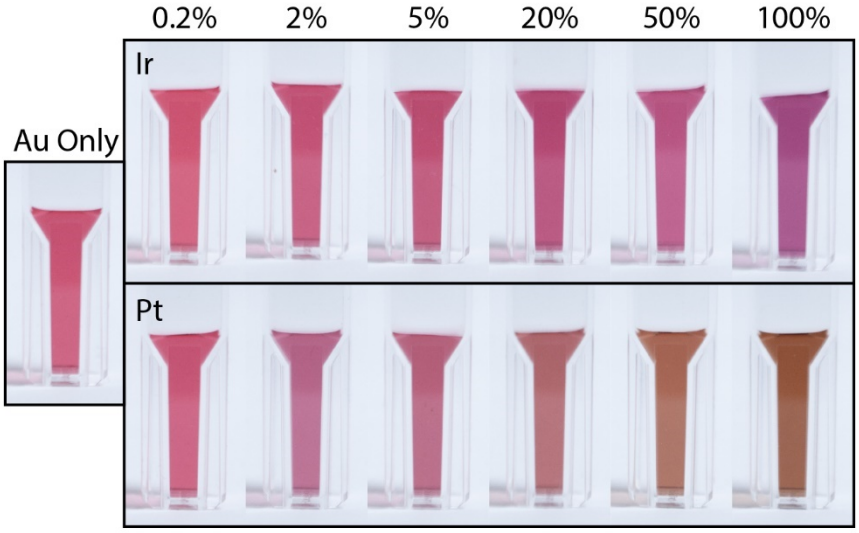

Figure 4.2 Photographs of colloidal Ir and Pt decorated nanocrystals. Dispersions of nanocrystals are diluted to approximately the same concentration. All images taken were at identical exposure. The Ir decorated Au NCs change color slightly towards a violet color with increasing decoration. Au@Pt particles show an increasingly brown color due to strongly plasmonic interactions.

We've synthesized a range of Ir and Pt decorated particles from 0.2 to 100 mol% relative to Au and then quantified the elemental composition with ICP-MS of all the heterostructures listed in Table 4.1. The supported nanocrystal catalysts were prepared by dropcasting the premade slurry onto a circular glass coverside to ensure the minimum amount of material was used for maximal mass efficiency. We found that pipetting 5 μL of 40 mg/mL (200 μg total) slurry was the optimum amount before a decrease in rate was observed. All catalytic measurements conducted in this study were using 200 μg total catalyst mass (NCs + alumina support). The optical extinction spectra of all colloidal nanocrystals are shown in Figure 4.1b with their photographs shown in Figure 4.2. The Ir core-shell particles show intact plasmonic behavior to that of the

original Au core unlike the Pt where there is significant optical coupling. The inset photos of colloidal suspension showed color differences between the Ir and Pt core-shell colloids. Final prepared dropcasted catalyst on glass highlights the color similarities to the colloid. The lack of clustering helps to maintain its original engineered absorptivity. From our previous study, we showed that the NCs on support is uniformly distributed without significant aggregation.[163]

Sample	Shell/Core Molar %
Au Only	0.00
0.2% Ir	0.13
2% Ir	1.26
5% Ir	2.28
20% Ir	4.13
50% Ir	4.23
100% Ir	4.16
0.2% Pt	0.25
2% Pt	2.44
5% Pt	6.09
20% Pt	20.27
50% Pt	50.21
100% Pt	85.20

Table 4.1 List of core/shell ratios by ICP-MS of nanocrystals. Core-shell particles with increasing Ir and Pt decorations were digested with aqua regia before diluting with water. 50 μL of the purified stock was digested with 1 mL of aqua regia. Once the metallic particle has fully dissolved (color change from red to yellow), the digested stock was diluted with 18.95 mL of water. Serial dilution was performed on 10 μg/mL (10 ppm) stock standards by combining 9 mL of water to 1 mL of the standard. A total of 5 serial dilutions were performed to a final concentration of 0.1 ng/mL (100 ppt). The final standard used was 1% HNO_3 as the null concentration. All concentrations measured were within the standard range for Au, Ir and Pt.

Single particle high Angle Annular Dark Field Scanning Transmission Microscopy (HAADF-STEM in the inset) images and elemental mappings of the 100 mol% Ir and Pt decorated particles depicted in Figure 4.3a. The Au only particle EDS map showed low level background concentrations of Ir and Pt. We believe this signal does not originate from Ir and Pt impurities but from background noise imparted from the Au Lα peak. Figure 4.3b shows the integrated normalized counts of x-ray signals from the EDS maps from Figure 4.3a. The background signal from Au Lα (9.71 keV) can interfere with the Pt Lα (9.44 keV) and Ir Lα (9.18 keV) signals are presented in the Au only maps.

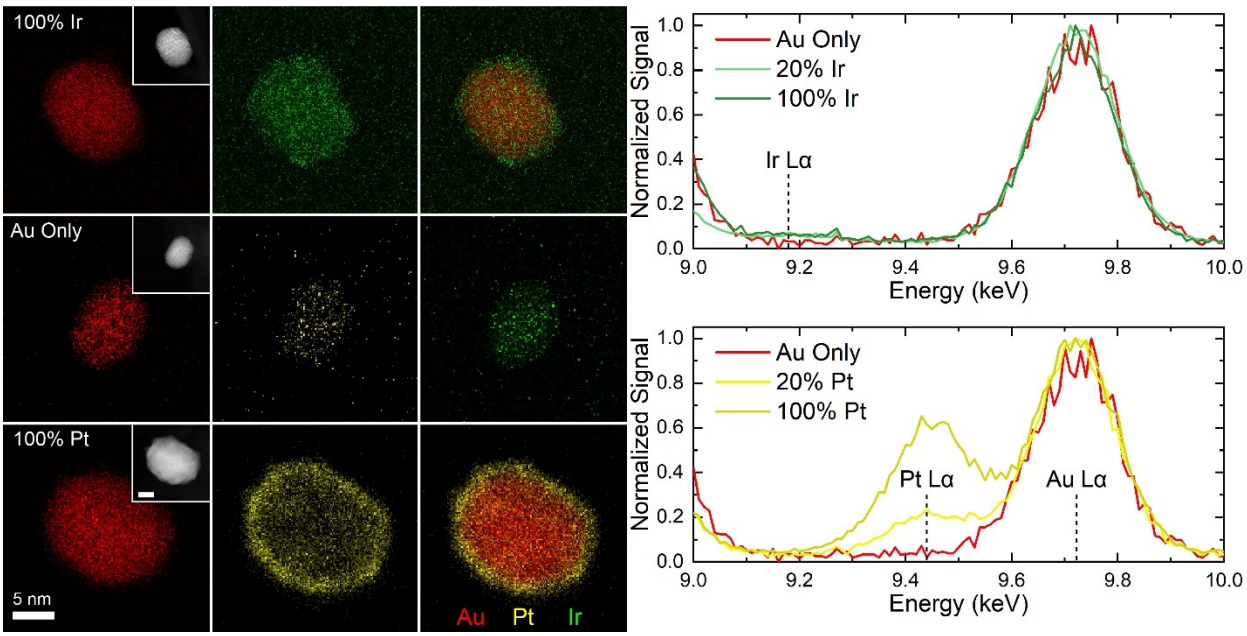

Figure 4.3 Elemental maps and energy dispersive spectrographs of Ir and Pt core-shell single particles. Maps of Au (red), Ir (green), and Pt (yellow) of the highest core-shell % synthesized with inset showing DF STEM images with scalebar at 5 nm. The maps show individual elements of Au, Ir and Pt for its respective core-shell particles. The clear difference in shapes between the Au and Ir outlines indicates the Au core and Ir shell (composite image). The 100% Pt decorated particle map shows a clear shell outline heavily encrusted with a ~2 nm layer of Pt atoms over the Au core. Respective

Au normalized EDS spectra shown correspond with the elemental maps. Only a minimal Ir signal was observed for the Ir core-shell particle. The bottom spectra show the Pt decorated particle showing clearly the increasing Pt signal with respect to the shell concentrations.

The 100% Ir decorated particle showed coverage across the entire particle as the shape of the EDS map (in green) does not completely align with its corresponding Au map. Interestingly, the uniformity of the shell is not conformal as there are a few Ir clusters scattered around the Au core as seen in the composite map. The 100% Pt particle decorates uniformly around the Au core creating a conformal shell of uniform thickness (~2 nm) around the Au core. The brighter map corresponds to higher intensity signal at Pt Lα as shown in Figure 4.3b where the intensity trends with the concentration of the decoration percentage. Differences observed between Ir and Pt maps indicates that reaction conditions and rates are not comparable for this synthesis method. It is likely that $IrCl_3$ requires a stronger reducing agent to rapidly nucleate around the Au NC.

wt% Loading	Shell Metal	Shell Metal %	Absorptance (%)	Std Dev. (%)
1	N/A	0	79.2	0.5
1	Ir	0.2	72.3	2.2
1	Ir	2	73.7	1.6
1	Ir	5	76.7	0.2
1	Ir	20	76.1	1.1
1	Pt	0.2	69.3	1.5
1	Pt	2	60.8	2.8
1	Pt	5	68.1	1.2
1	Pt	20	66.4	2.1
1	Pt	50	70.2	1.5
1	Pt	100	68.8	2.5
10	N/A	0	97.7	0.2
10	Ir	0.2	97.6	0.1

10	Ir	20	96.0	1.6
10	Pt	0.2	97.6	0.3
10	Pt	20	97.3	0.4

Table 4.2 Absorptance of supported catalyst at 520 nm. Samples were measured by integrating sphere absorbance spectroscopy. Samples were prepared by dropcasting the standard 5 μL of 40 mg/mL catalyst slurry onto 1 × 3 inch microscope glass coverslides. Measurements were carried out by measuring transmission and reflectance modes with a 60 mm integrating sphere. The samples were illuminated by a 4.2 mW 520 nm laser focused with a plano convex lens and an aperture to condense the beam to within the sample diameter. Triplicate measurements were conducted for each sample. Absorbance measurements were used for the calculation of quantum yield.

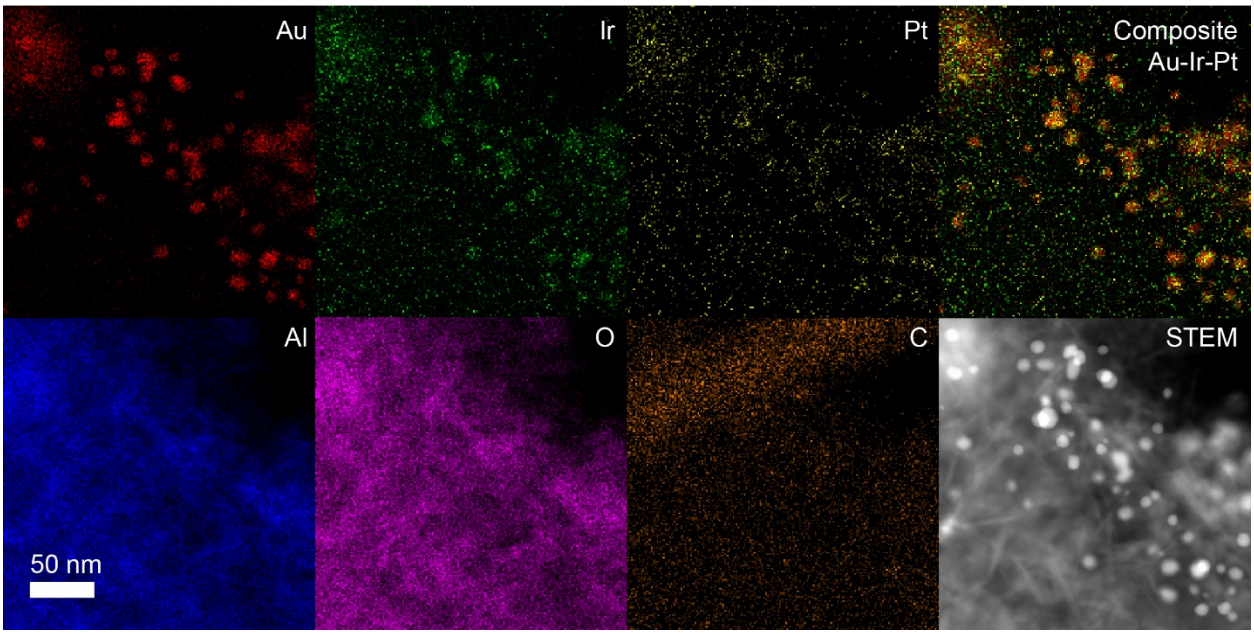

Figure 4.4 Low magnification elemental maps of Au only nanocrystals on alumina. This series of elemental maps show the corresponding signal of Au Lα to the STEM image. There is a faint outline in the green (Ir Lα) and yellow (Pt Lα) which represents the background noise from the spectra integration. The composite shows no outline nucleated Ir or Pt particles without Au signal. The alumina support are show in blue (Al Kα) and violet (O Kα) that closely match the hazy white diffuse background on the

STEM image. The non-aligned orange (C Kα) is from the thin lacey carbon film from the TEM grid.

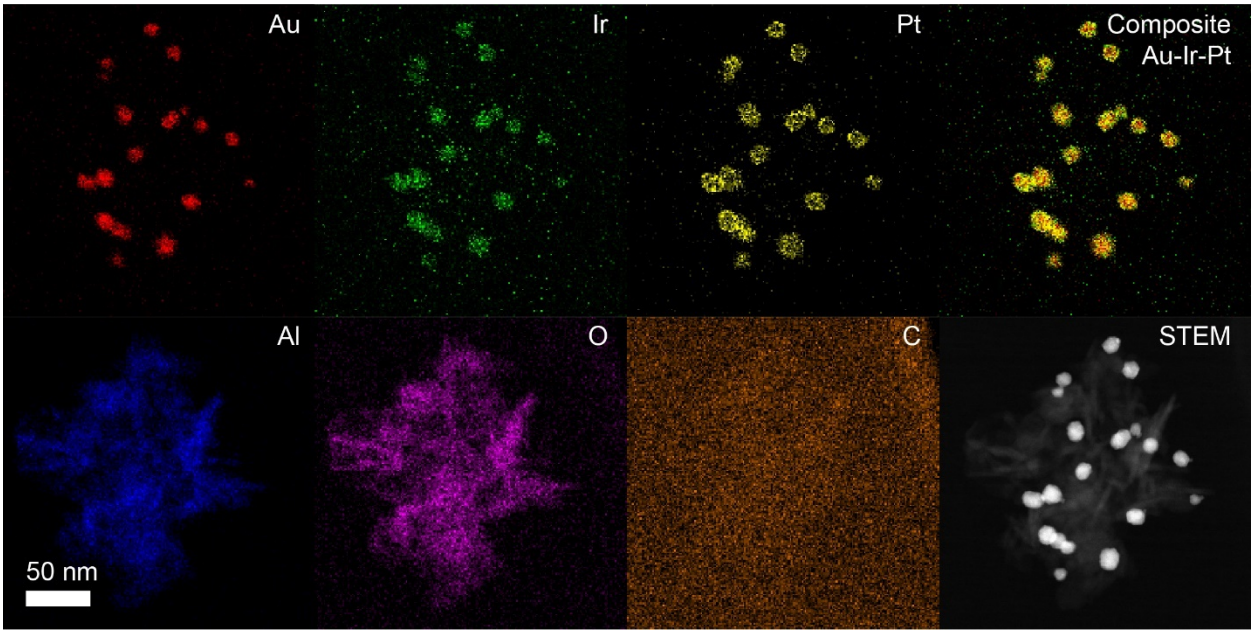

Figure 4.5 Low magnification STEM elemental maps of 100% Pt decorated catalyst. The Ir and Pt maps align well with the Au map showing the absence of homonucleated Pt. There are slight outlines of shell structure visible in the Pt panel. The Al and O maps align well with the alumina support as seen in the STEM image.

Because of the small particle sizes, we are only able to observe a clear distinction of spatial elemental differences for the high concentration Ir and Pt decorations. Lower Ir and Pt percentage decorated particle's EDS mapping are shown in Figure 4.7 and Figure 4.8. A fainter outline of Pt can be observed as the core-shell feature similar to that of the 100% decoration from Figure 4.3b. It is inferred that the lower concentration behaves similarly in its heterogeneity with the higher loadings. The corresponding normalized total energy-dispersive X-ray spectra (EDS) are presented in Figure 4.3b. Additional low magnification EDS maps were conducted to visualize if any homonucleation occurred during synthesis in Figure 4.4, Figure 4.5, and Figure 4.6 for

the Au only, 100% Pt decorated particles and Ir respectively. There does not appear to be any clearly visible Pt or Ir particles absent of Au signal. We can confidently say with the EDS maps and ICP-MS results that the catalyst has a uniform distribution and consistently heterogeneously core-shell for the particle's nanostructure.

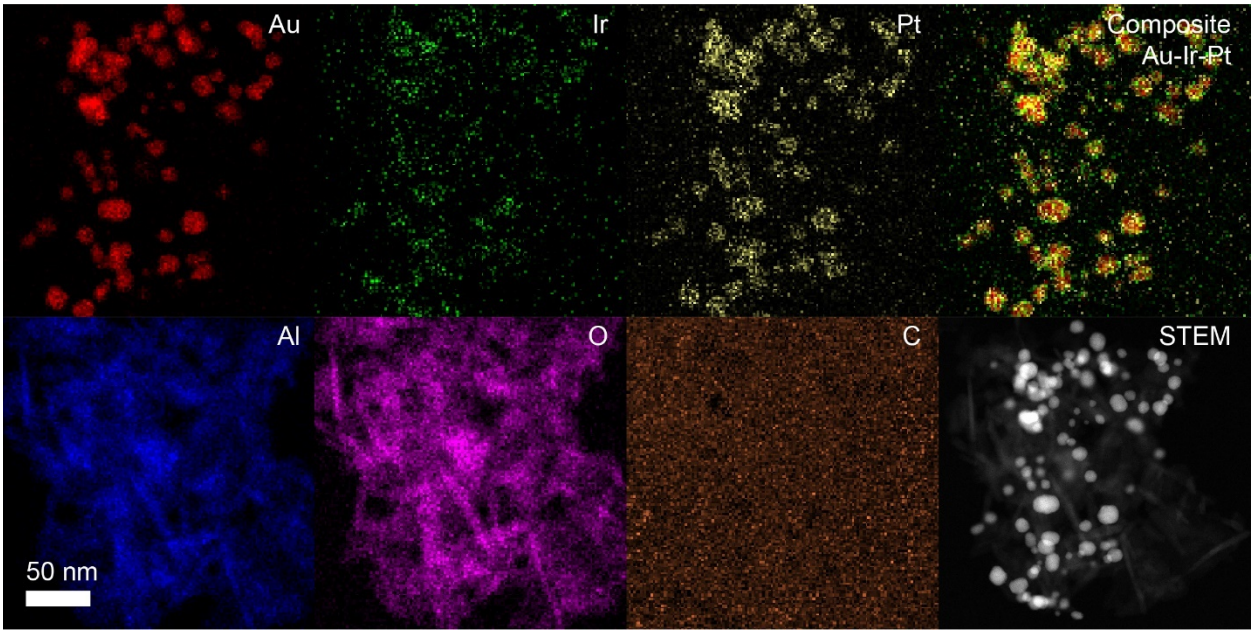

Figure 4.6 Low magnification STEM elemental maps of 100% Ir catalyst.

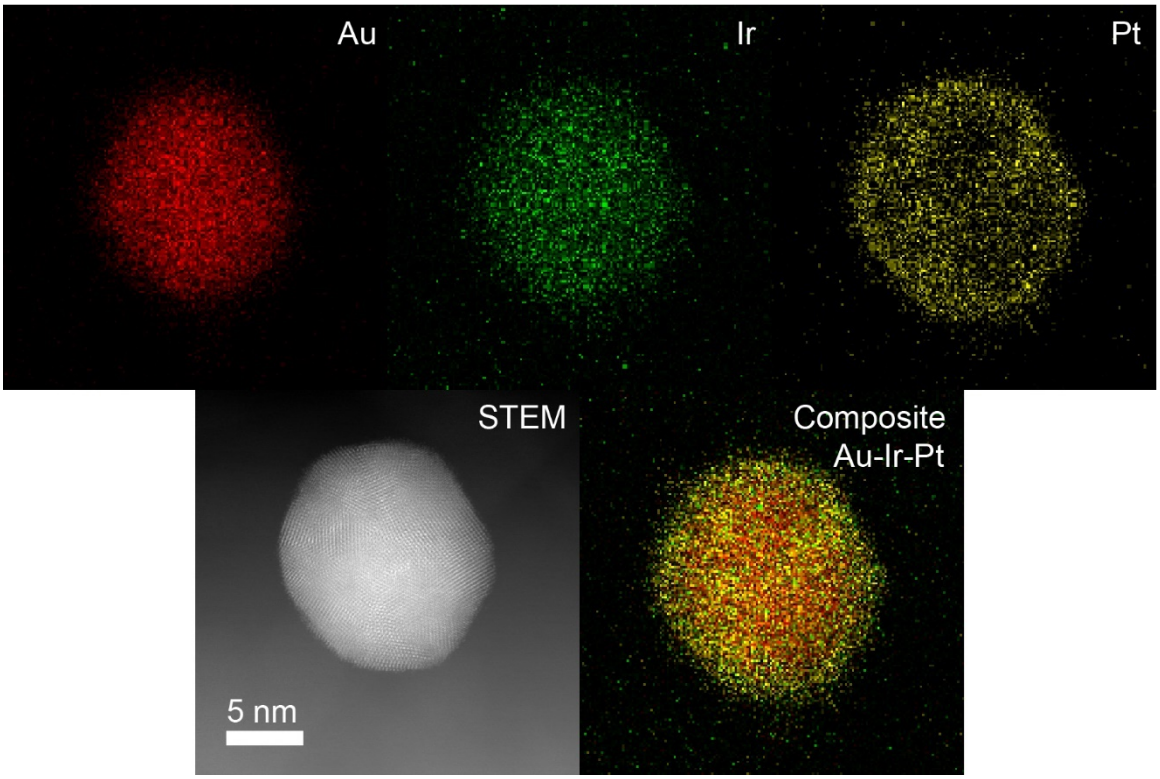

Figure 4.7 High magnification STEM elemental maps of a single 20% Pt nanocrystal. The Pt map show a slight outline that resembles the shell structure as the shape does not match with the Au map. The Ir map closely matches the Au outline but there is no significant concentration of Ir in the sample measured by ICP-MS. The similarities are due to the noise around the Ir Lα.

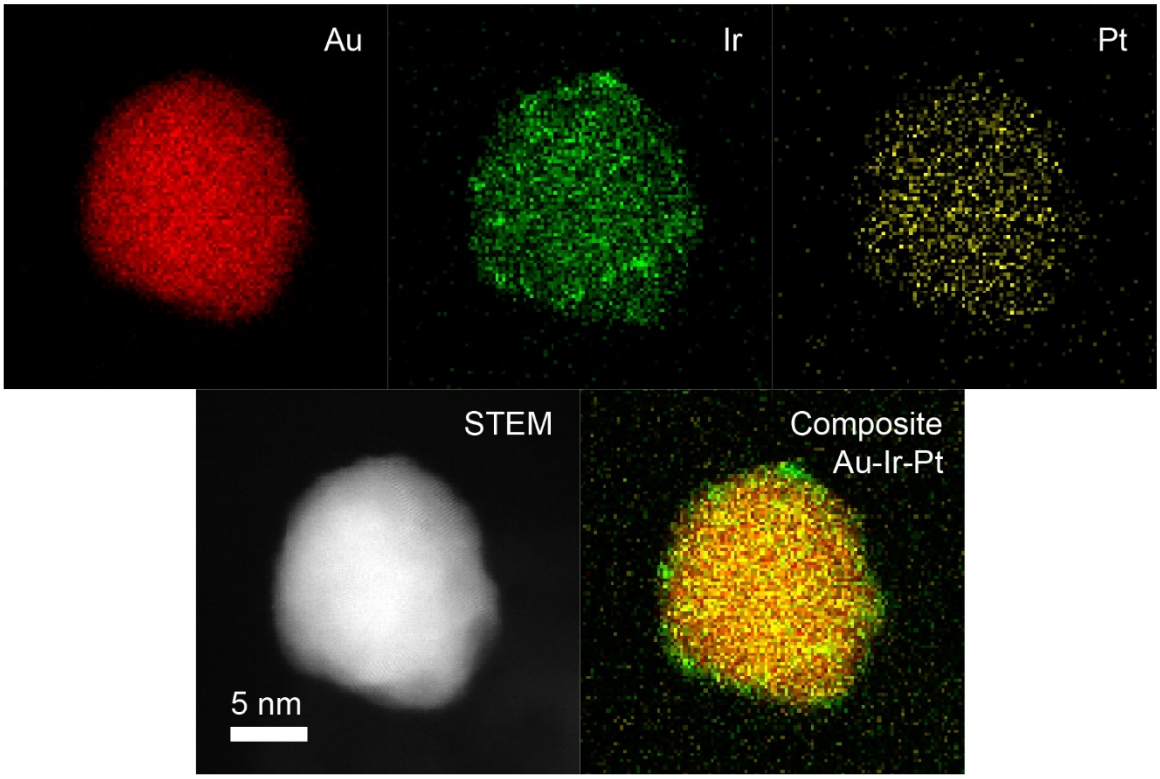

Figure 4.8 High magnification STEM elemental maps of a single 20% Ir nanocrystal. Visible bright spots are visible on the Ir map that show a non-conformal shell on the surface of the Au core. It is likely a patchy island morphology with a low density of surface Ir atoms distributed throughout the surface.

4.3.2. Photocatalytic Hydrogen-Deuterium Dissociation

Catalytic measurements were conducted in real time with a quadrupole mass spectrometer (QMS) show in Figure 4.9a. High purity hydrogen and deuterium gases were controlled by mass flow controllers (MFCs) set from 10 to 80 standard cubic cm per minute (SCCM) depending on the experiment. Flow rates of each gas are mixed at equal ratios for optimal HD signal detection. Other proportions of equal total flow rates were evaluated but yielded lower HD rates for the same experimental condition. Online mass spectrometer continuously monitored the HD (m/z = 3) signal throughout the photocatalytic process. RGA pressure traces was converted into HD rate showing the signal increases during illumination at 20.4 W/cm^2 for 20% decorated core-shell

particles, Au only and alumina blank control. Five minutes of illumination followed by 5 minutes under dark conditions were enough for the signal to plateau and baseline respectively to yield reliable quantification of rates. This condition was kept for all photocatalytic measurements in this study. A slight tailing can be observed in the 20% Ir particles which can be attributed to slow desorption under dark conditions or potentially carryover from residual thermal accelerated reactions.

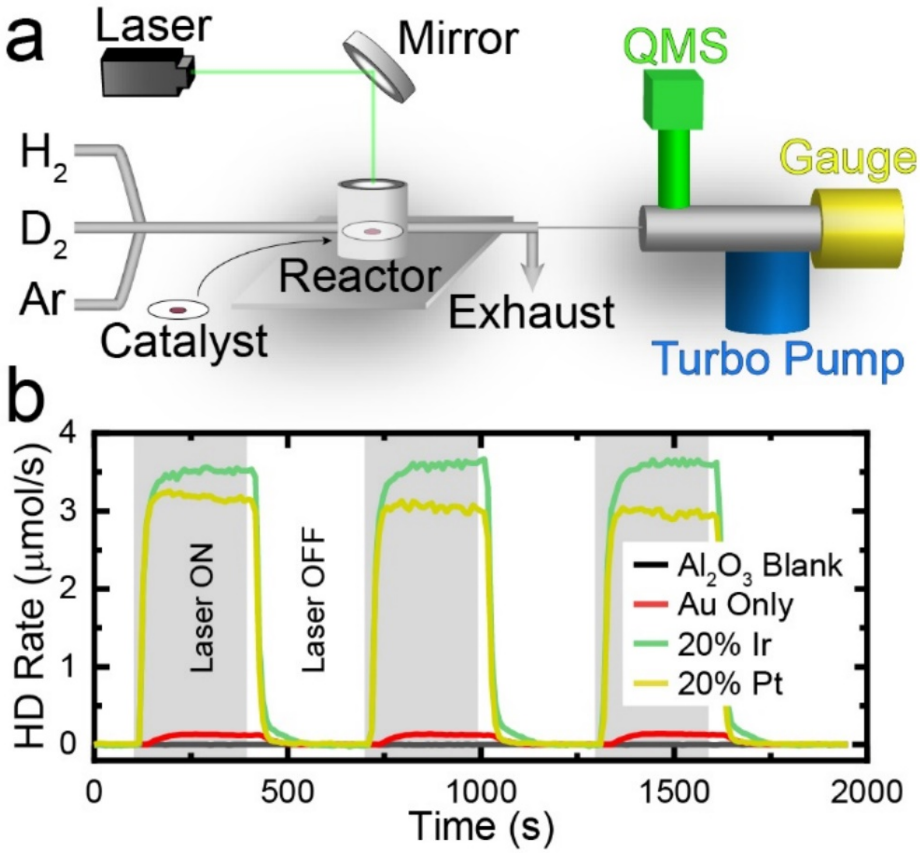

Figure 4.9 Photocatalytic reactor system for measuring HD scrambling rates. (a) Hydrogen, deuterium and argon gases are fed by mass flow controllers into the reaction chamber that houses the dropcasted catalyst. The high power 520 nm laser beam is redirected through the glass viewport to the catalyst. Exhaust gases are measure by a quadrupole mass spectrometer in real time. (b) HD pressure traces of illuminated at 20.4 W/cm^2 (1.18 W total power) and dark catalysts during the measurement process. HD (m/z = 3) rates are quantified by the differential steady-state pressures between the

background dark and illuminated instances. Ir and Pt decorated catalysts significantly increases the HD production rate relative to the Au only material and the alumina only blank.

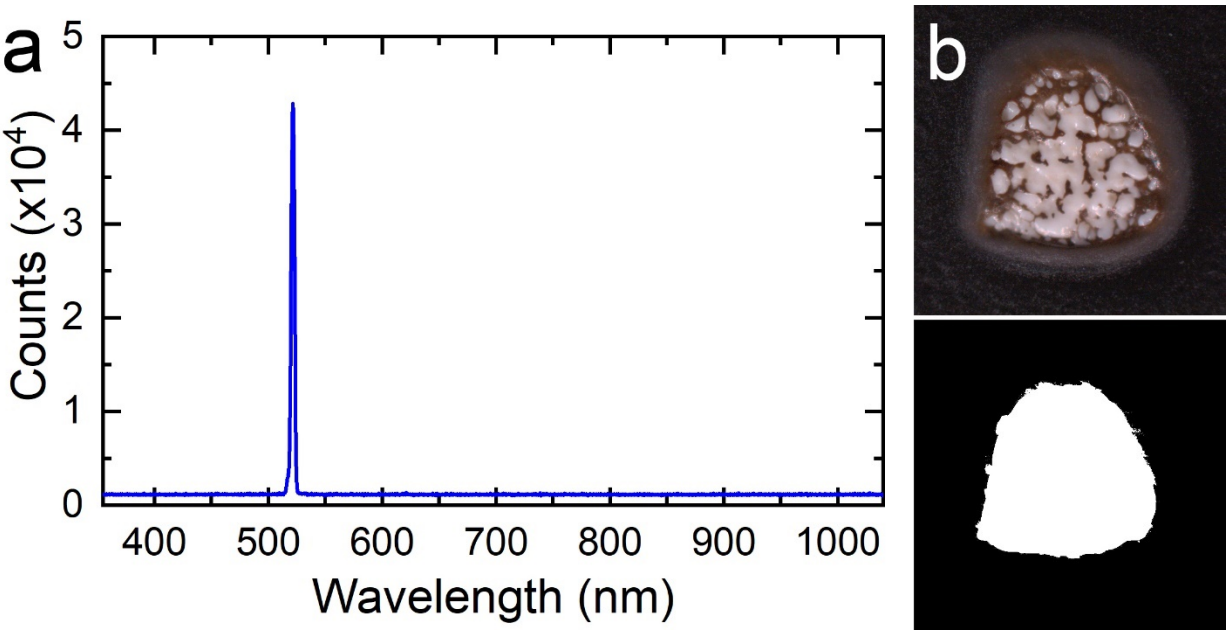

Figure 4.10 Characteristics of the 520 nm CW. (a) Spectra of the laser output measured by an Ocean Optics spectrometer. Only a single wavelength was detected at 518.9 nm. (b) Optical microscope image of a burn spot on laser paper. The beam area was measured from the outline traced from the burn spot. 12 burn spots were used to calculate the average beam area of 5.77 mm^2.

Neutral Density Filter (O.D.)	Laser Power (mW)
1.0	117
0.9	161
0.8	193
0.7	233
0.6	293
0.5	371
0.4	462
0.3	621
0.2	752
0.1	920
0	1180

Table 4.3 List of laser power measurements passed through neutral density filters.

The full power illuminated onto the sample was measured to be 1180 mW of 520 nm light. This measurement was conducted with the transparent glass viewport to account for any spectral reflection from the glass. Subsequent lower laser powers were measured with neutral density filters in the beam path from 0.1 to 0.6 and 1.0 optical density. Optical densities 0.7-0.9 used multiple ND filters, specifically 0.6 + 0.1 (0.7 OD), 0.6 + 0.2 (0.8 OD), and 0.6 + 0.3 (0.9 OD) optical densities.

Photocatalytic measurements are conducted in a homemade photoreactor using a 1.18 W continuous wave 520 nm laser focused to 5.7 sq mm spot area (Figure 4.10). Laser paper was used to quantify beam area by burning the exposed area with the full power beam for 300 ms with an optical chopper for pulsed illumination. We assumed the beam intensity to be spatially distributed evenly for all measurements and this constant focus was kept for the entire duration of this study to maintain the same beam area. Power density dependence experiments were conducted with neutral density filters from an optical density of 0.1 to 1.0. Table 4.3 lists the exposed intensities of the sample filtered by the ND filters. The range encompasses one order of magnitude as lower powers did not show any measurable HD signals. Much of the studies within this

area encompasses only a low range of power densities. This challenge makes it tricky to determine photocatalytic behavior over several orders of light intensities.

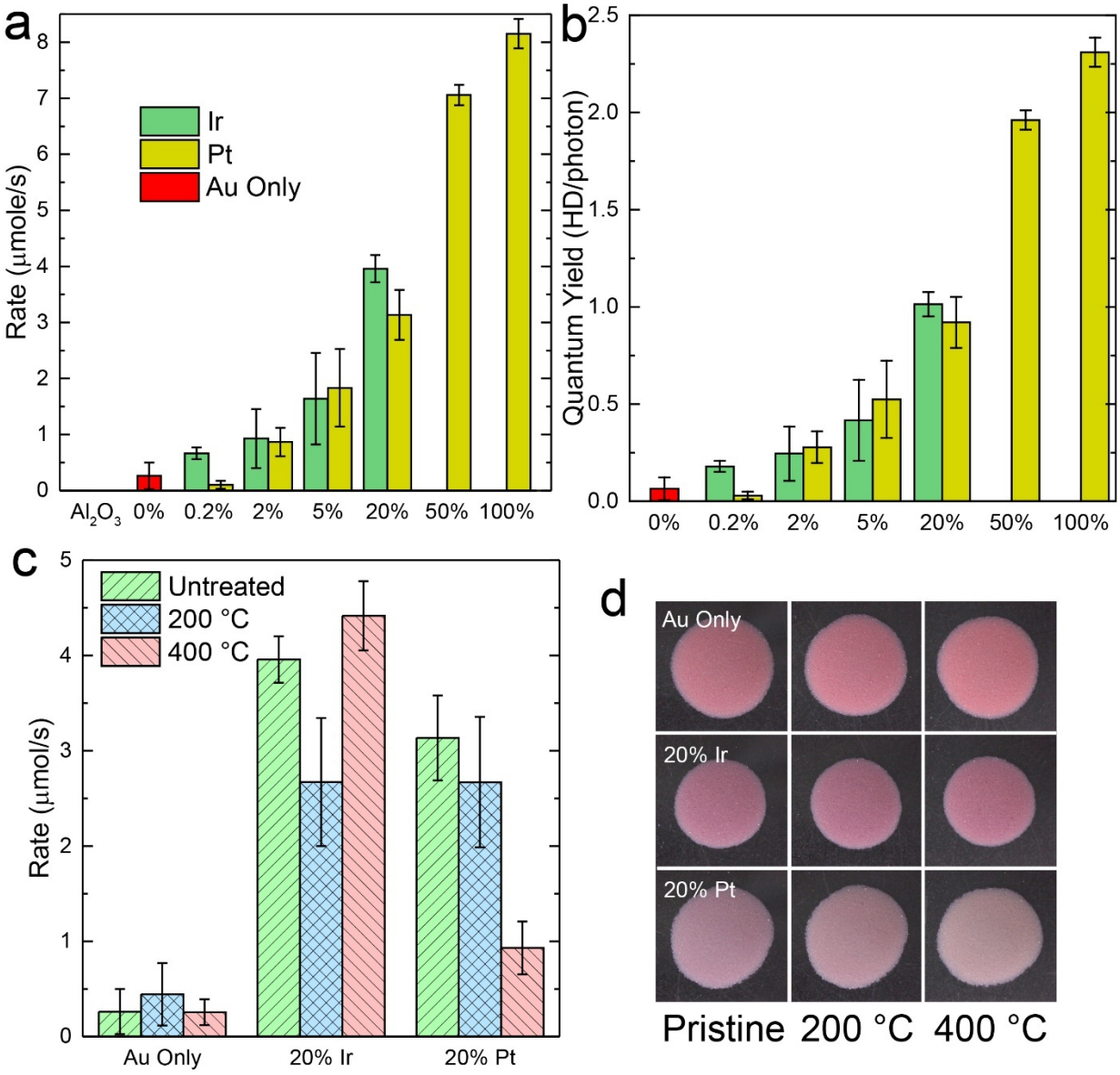

Figure 4.11 Shell decoration comparison on HD scrambling rate. Comparison of shell decoration for Au@Ir and Au@Pt catalysts and the behavior after annealing. (a) H_2/D_2 scrambling rates comparing increasing Ir and Pt shell loadings at 20.4 W/cm^2 (1.18 W total power) with a 520 nm laser. Increased rates were observed for all Ir (green) and Pt (yellow) decoration except for 0.2% Pt compared to the Au only (red) catalyst. The

alumina blank measure is present, the rate was significant enough to appear on the graph. (b) Shell loading dependent quantum yield upon excitation with 20.4 W/cm^2 laser. (c) Pure Au and 20% decorated Ir and Pt catalyst HD rate scrambling after thermal anneal in air for 1 hour at 200 ˚C and 400 ˚C. (d) Dark-field optical microscope images of 1 wt% catalyst before and after annealing. Error bars in this figure were calculated based on triplicate standard deviation.

A series of decoration mole percentages of core-shell particles were synthesized, and its HD rates were compared in Figure 4.11a. Ir and Pt will accelerate HD rates compared to the Au only catalyst except for the 0.2% Pt. We will discuss the implications of the 0.2% Pt decreased rate later in the results. Quantum yield (Figure 4.11b) was calculated with the measured rates combined with absorbance measurements of dropcasted catalysts with and integrating sphere (Table 4.2). After the first illumination of platinum decorated particles, the dark rate drastically reduced to near the level of the Au only dark baseline signifying a significant change of the surface composition of the heterostructure. Figure 4.11c shows the effect of thermal anneal at 200 ˚C and 400 ˚C on the HD rates for 20% decorated catalysts and Au only. We chose these temperatures to compare a mild sub-sintering, sub-combusting temperature to 400 ˚C, above the Au Tammand temperature (395 ˚C).[181] Mild annealing at 200 ˚C appeared to have diminished some performance of the Ir and Pt core-shell particles while 400 ˚C showed dramatic differences. We believe the Au@Pt particles are alloying or diffusing to subsurface at 400 ˚C and under 20.4 W/cm^2 illumination while the Au@Ir particles are not. There was a subtle color differences in Pt decorated particles after annealing at 400 ˚C with a duller brown hue and less purple while the Ir catalyst remained unchanged.

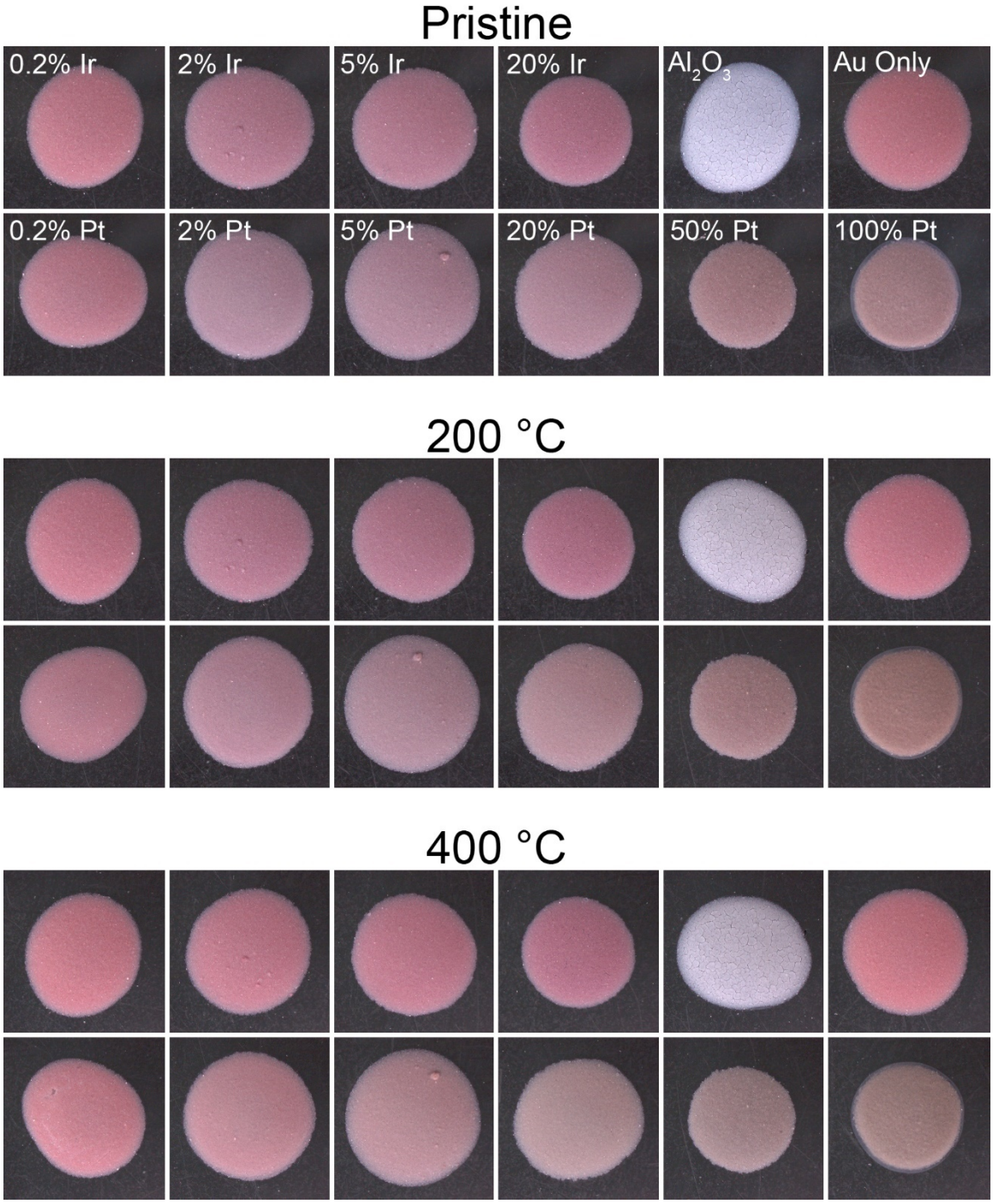

Figure 4.12 Dark Field Microscope images of thermal anneal of 1 wt% dropcasted catalysts. The top panel shows pristine series of 200 μg dropcasted catalyst used in the photocatalytic measurements. The middle panel shows the same samples after annealing at 200 ˚C in air for 1 hour. The sample remain nearly identical to the pristine

state signifying no noticeable sintering of the nanocrystals. The third panel shows the same samples after annealing at 200 ˚C and 400 ˚C in air for 1 hour at each condition. Color differences are difficult to perceive but there are slight changes in the higher Pt decorated catalysts. The 20-100% Pt decorated catalysts appear more of a dull purple and brown than the original slight violet. This is likely due to alloying between Au and Pt. There does not appear to any noticeable differences between the Au@Ir series.

A complete set of images can be viewed in Figure 4.12. Internal migration of Pt atoms to the Au core would explain the change the optical behavior of the plasmon resonance.[193] Hydrogen chemisorption on Au is fairly weak due to the d-orbitals energy below the fermi level.[96,194] The addition of Ir and Pt atoms acting as catalytic sites for hydrogen binding increases the energy transfer efficiency from plasmons to hydrogen dissociation and desorption. It has been shown that dark catalysis does occur at room temperature for supported platinum catalysts for hydrogen dissociation.[195–197] We also have observed dark catalysis in Pt samples at room temperature shown in Figure 4.13.

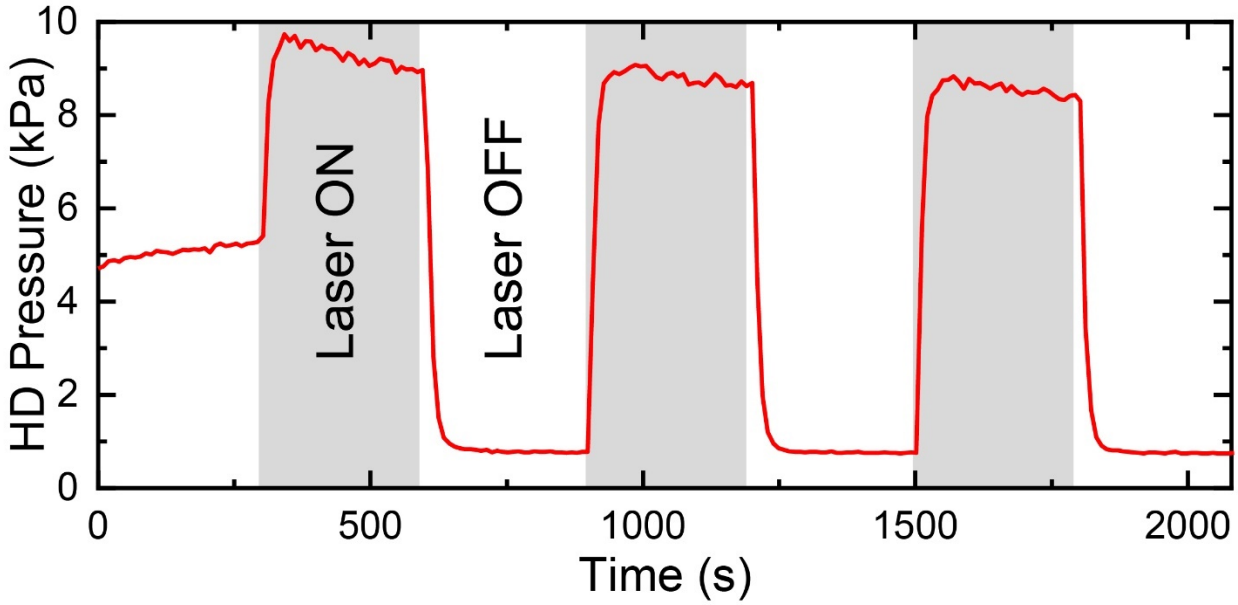

Figure 4.13 HD rate of a pristine sample of 1 wt% loaded 20% Pt decorated catalyst. Significant background HD signal was measured due to the catalyst. The rate increases

upon illumination with the 520 nm laser at 20.4 W/cm^2. In dark conditions, the baseline drops significantly lower than the pristine sample suggesting significant morphological changes occurred while the sample was illuminated. All subsequent measurements showed this much lower baseline of dark hydrogen dissociation rate. H_2 and D_2 flow rates were set to 40 SCCM. Laser ON/OFF cycles were in 5 minute periods.

4.3.3. Intensity Dependent Mechanisms

The catalyst's intensity dependence was studied to elucidate plasmonic mechanism. There have been numerous studies showing a linear relationship to signify hot carrier mechanism while supralinear relationship revolves around photothermal dominated mechanism.[3,113] Here, we observed two regimes that transition from photothermal to hot carrier dominated mechanism that transitions at approximately 5-6 W/cm^2. Figure 4.14a-b shows the linear and logarithmic plots of HD rates for Ir and Pt decorated particles along with bare Au. Interestingly, pure Au particles only experienced exponential behavior over two orders of magnitude in rates between 6 and 20.4 W/cm^2. At the low intensity regime, we can attribute the steeper slope of Au@Pt catalyst to the intrinsic activity of Pt analogizing to a kinetic rate constant of psedo-first-order kinetics assuming the temperature linearly scales with the intensity. The similarities between the "kinetic rates constants" between 20% Ir and Au only is striking as the raw magnitudes are widely apart. We hypothesize that the HD rate for the Au only catalyst must collapse into a linear dependence between 15.9-20.4 W/cm^2, otherwise the exponential rate will very quickly exceed the HD rate by the 20% Ir and Pt decorated catalysts. It might be that the 20.4 W/cm^2 is already on the verge of transitioning since including this point would bring the R^2 down to 0.9974 from 0.9998, a much less remarkable linear behavior. The similarity in the rate region this transition happens is also interesting, especially comparing it with the core-shell catalysts. This transition appears to occur when the rate is ~ 0.1 μmol/s regardless of sample type.

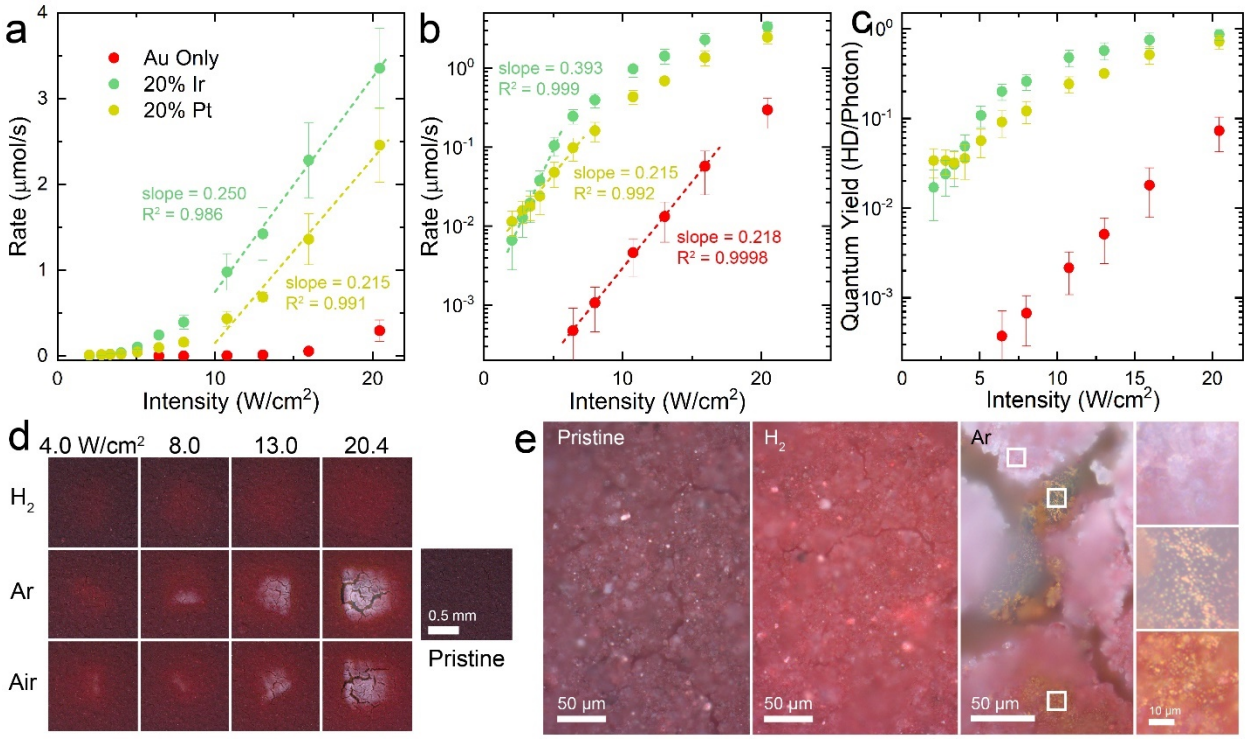

Figure 4.14 Intensity dependence H_2/D_2 scrambling rates of catalysts. (a) 1 wt% loaded core only and core-shelled catalysts intensity dependence plotted on a linearly scaled rate. Linear regression fits are overlayed with the four highest intensities for the core-shelled catalysts in green and yellow. (b) Logarithmically scaled rates of the same data. Core-shelled catalyst have linear regression fits of the first 5 intensity measurements from 2 to 5 W/cm^2. Linear regression for the Au only (red) catalyst of all the data points. (c) Intensity dependent quantum yield plots of the same samples. All error bars in this figure are standard deviation from triplicate measurements. (d) Dark-field optical microscope images of 10 wt% Au only loaded catalysts irradiated with a 520 nm laser at varying intensities for 5 minutes under hydrogen, argon or dry air. (e) High magnification bright-field optical microscope images of pristine and irradiated sample at 20.4 W/cm^2. All images except the pristine sample are of irradiated spots of the catalyst. The stack of 3 images on the right are magnified region of depleted catalyst

(top), bulk gold micro particles (middle), and scattered bulk gold particles on undamaged material (bottom).

The core-shell catalysts are linearly increasing with respect to the intensity beyond 10 W/cm^2, hot carrier dominated regime. It has been well studied that linear dependence in intensity/rate plots are a fingerprint for carrier driven mechanism because the population of excited carriers is directly proportional to the number of incident photons.[116] Our data agrees well with published findings on hydrogen dissociation by plasmonic Cu particles, specifically where the intensity the exponential regime ends and the linear regime starts around ~5-6 W/cm^2.[113] It is particularly interesting to note that if the presumed photothermal mechanism were to continue, the HD rate would far exceed the observed trend. The transition from exponential to linear can be explained by higher concentration of hot carriers catalyzing the desorption of chemisorbed hydrogen species through desorption induced by electronic transition (DIET).[198–200]

Consequently, the energy efficiency of this process is projected by the quantum yield dependence. The signature S-shaped dependence appears except for intensities under 4 W/cm^2 for the 20% Pt catalyst. We observe a near constant quantum yield while the 20% Ir and Au only samples showed no evidence of this behavior between 2-5 W/cm^2. Exceeding unity in quantum yield was observed in the 50% and 100% Pt samples with 1.96 and 2.31 HD/photon respectively. Such an excess above 1 can be explained by electron-electron scattering effectively creating a higher population of elevated energy electrons e.g., hot carrier multiplication. It is also possible that a higher population of lower average energy hot electrons can collectively excite vibrational states in the bound H* adsorbates enough to overcome the desorption barrier.[113] It is experimentally reported that the Pt shell of Au@Pt nanocrystals have enhanced

dephasing of the plasmons, thereby increasing plasmon-electron scattering at the Pt sites to accelerate hot carrier creation.

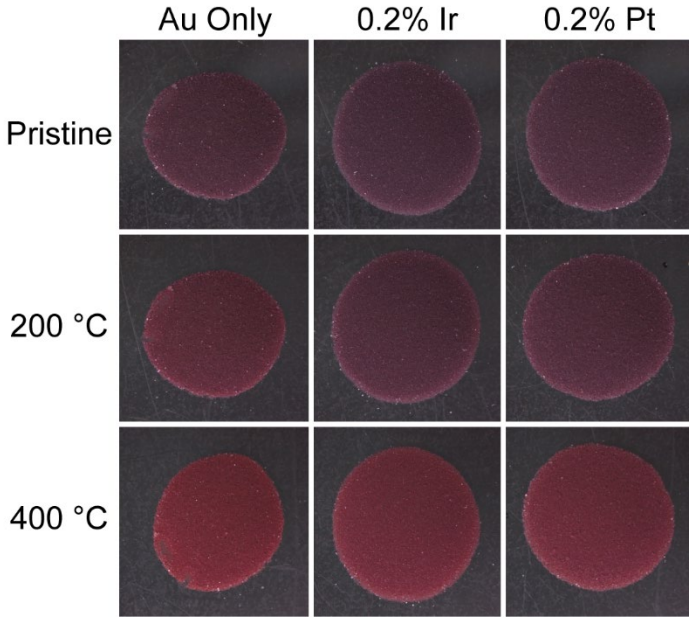

Figure 4.15 Dark-field optical microscope images of 10 wt% loaded catalyst before and after annealing. Dropcasted catalysts of Au only, 0.2% Ir, and 0.2% Pt samples were imaged before and after annealing at 200 ˚C and 400 ˚C in air for 1 hour. After annealing at 200 ˚C, minor optical differences occurred (reddening of the catalyst). The 400 ˚C treatment produced bright red material likely due to mild nanocrystal sintering.

Additionally, we observed the illuminated samples under optical microscopy (Figure 4.14d-e). Significant morphological differences were seen after irradiation for five minutes under hydrogen, argon, or air atmospheres. Surprisingly, a white spot developed that is visible by eye and under dark field optical microscopy for samples irradiated under Ar and Air. Higher magnifications showed the true extent of the damage for Ar samples (Figure 4.14e). Illuminated samples under H_2 only changed color to a brighter red hue from the pristine dark violet. This color change was also consistent with thermal annealing at 400 ˚C in air (Figure 4.15). We can get a sense of the bulk temperature this catalyst endured from this color change. The brighter red

color in the H_2 illuminated samples and the halo around the white spots also signifies temperature approaching or exceeding 400 ˚C as 200 ˚C was not enough to induce a color change. High magnification revealed the depletion of Au NCs from the alumina support (Figure 4.14e inset) seen in white at the top. As a result, bulk gold was seen at the bottom of the catalyst on the substrate as visible small microdots of gold. This gold splatter can also be seen on the adjacent catalyst at the bottom of the image. We hypothesize that hydrogen acts as an energy sink to efficiently remove energy from the NC so photothermal effects are suppressed and temperatures does not increase enough to vaporize gold. Under chemically inert (Argon and Air) atmospheres, no such pathways for energy dissipation exists, so all the absorbed photons are converted to heat via plasmon-electron-phonon interactions.

4.3.4. Low Concentration Core-shell Performance

Increasing the shell concentration increases the dissociation rate under illumination except for the 0.2% Pt from Figure 4.11. We have investigated this further by doubling the sample size to 6 shown in Figure 4.16. In the 1 wt% NC loading (orange), there is a considerably lower rate compared to the Au only and 0.2% Ir catalysts. We believe this decrease in rate is caused by subsurface Pt atoms syphoning plasmon energy away from the surface. It has been experimentally measured that Au@Pt structures exhibit an accelerated plasmon scattering off of the Pt d orbitals, thus preferentially hastening the plasmon damping process to thermal energy. If Pt were to be subsurface and alloyed within the core, the NC would experience homogenous and isotropic plasmon damping. This effectively limits the hot electron concentration on surface sites that consequently decrease overall catalytic efficiency. Of course, because more energy is funneled inwards, there should be an increase in lattice temperature to drive photothermal dissociation. Naturally, all Au@Pt core-shell catalysts should experience alloying under such intense illumination, but we do not see any diminished

rates. This is likely due to the relative catalytic activities between Au and Pt. At 0.2% Pt, the number of surface Pt atoms on an 8 nm particle is only 32 atoms. After alloying, this number drops to 5 with the 27 atoms buried throughout the core. The 5 surface Pt atoms is likely not enough to compete with the rest of the Au surface atoms. We do not see any drop in Ir decorated particles either because Ir does not easily alloy or diffuse subsurface or Ir sites do not decohere plasmons efficiency enough to spatially change energy deposition.

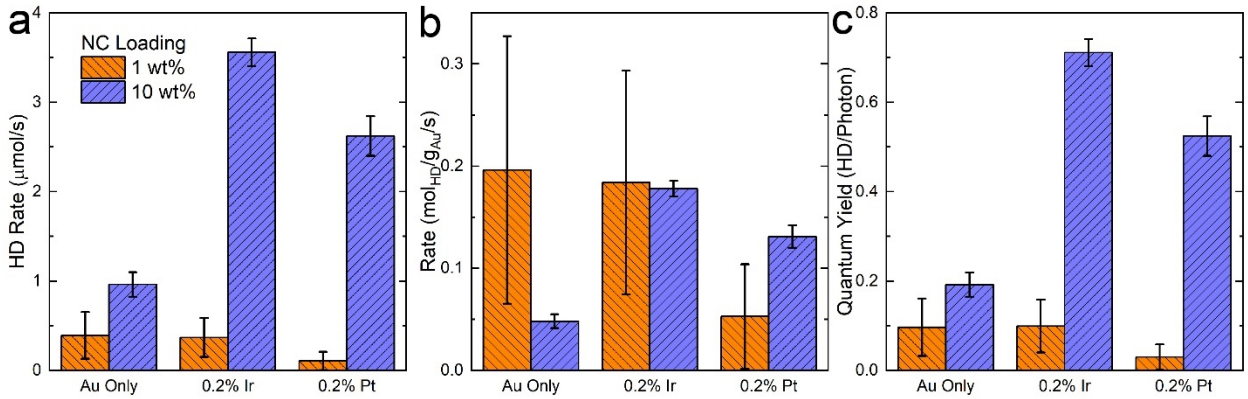

Figure 4.16 Mass loading and low shell decoration comparison of H_2/D_2 scrambling rates. (a) HD rate from core only to 0.2% decorated Ir and Pt shell content at 1 wt% (orange) and 10 wt% (blue) loading on alumina. (b) Au mass normalized rate of the same samples. (c) Quantum yield comparison of the same series. Measurements illustrated in this figure were from N = 6 sample size and error bars are standard deviations.

Comparing the mass efficiencies of NC loading revealed a surprising behavior. All samples HD scrambling rate improved when increasing the NC loading from 1% to 10%, but relative mass efficiency decreased across the board except Au@Pt. We believe this was due to far field competition for light as NC-NC proximities shortened. Plasmonic NCs can interfere with electromagnetic waves far from its physical perimeter. Increasing the concentration of NC disrupts the far field interaction,

effectively limiting the plasmon intensity of the NC. This limitation can in principle change the mechanistic regime between hot carrier to photothermal. The striking increase in quantum yield by the 0.2% core-shell catalysts is interesting compared to the moderate increase from the Au only catalyst (Figure 4.16c). We saw from Figure 4.14c that quantum yield increase as intensity increase but it was

4.3.5. Poisoning and Recovery of Au@Pt Catalyst

We have also observed pristine Au@Pt catalyst undergo dark hydrogen dissociation (Figure 4.17). 20% Pt decorated catalyst were monitored in the dark for five hours to observe the time dependent rate change of HD production at room temperature. All pristine samples behaved similarly with an initial "induction period" of plateau of HD rate followed by a steady decline over the five hours. We attempted several recovery methods to bring the sample to near pristine levels of activities again by annealing at mild temperatures in air and nitrogen, applying vacuum, leaving under ambient conditions, and oxygen plasma cleaning. Only annealing in air and plasma treatment managed to revive the catalyst to their original activity levels. Leaving the sample under ambient conditions for three days also seemed to improve slightly. In the absence of oxygen, the samples did not recover, in fact, a worsening behavior were observed for the vacuum and N_2 annealed samples.

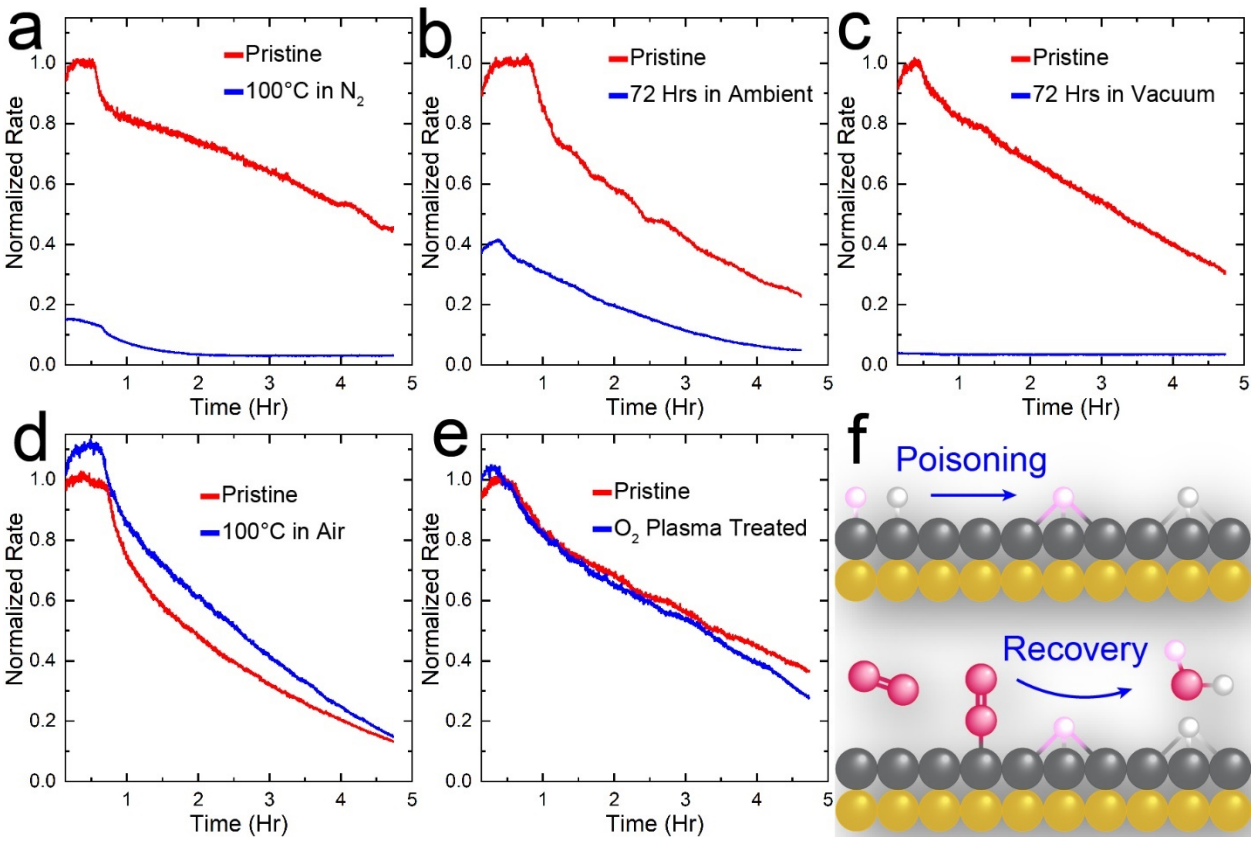

Figure 4.17 Dark H_2/D_2 scrambling rates. HD rates in the dark of 1 wt% loaded 20% Pt shell catalyst and subsequent recovery attempts. (a) Normalized HD rates of a pristine (red) in the dark for nearly 5 hours at 10 SCCM flow rates for H_2 and D_2. The same sample was then annealed at 100 ˚C in N_2 for 1 hour before remeasurement in the dark. Panels b-e had the same experimental workflow with different treatments. (b) The sample was left in ambient conditions, in air at room temperature for 72 hours, before remeasurement. (c) The sample was left under high vacuum (turbo pump with a base pressure of 2.5×10^{-8} mbar) for 72 hours. A turbo pump was used because it eliminated the possibility of oil vapor contamination from traditional rotary vain pumps. (d) The sample was annealed at 100 ˚C in air for 1 hour before remeasurement. The treated sample showed slightly elevated dark HD rate relative to the pristine sample. (e) The sample was plasma treated in 0.3 mbar O_2 pressure for 1000 seconds before remeasurement. The original HD rate was recovered. (f) An illustration of a poisoning

and recovery mechanism on Pt (grey) decorated Au (yellow) nanocrystal. Chemisorbed hydrogen (white) and deuterium (pink) atoms on Pt rearranged to a more stable (lower energy) state more strongly chemisorbed over time. In the presence of O_2 (red), weakly and strongly chemisorbed H and D are oxidized by adsorbed O_2 to water. Eventually, the adsorbed H_2O desorbs and leaves the Pt site pristine.

This set of experiment lead us to hypothesize that oxygen to be an important contributor to the recovery of the poisoned catalyst. Weakly chemisorbed and physisorbed hydrogen species can undergo surface diffusion to rearrange into a lower energy (strongly bonded) state with a single or multiple Pt atoms. In literature, these different binding states are classified as α, β, γ, and δ states each with its own distinct desorption temperature.[196] The conversion towards δ states explains the decrease in activity over time and why there is no recovery in the N_2 anneal and vacuum experiments. N_2 does not undergo catalytic binding and dissociation unlike O_2 can on Pt, and the 72 hours under vacuum is ample time for the adsorbed hydrogen atoms to diffuse on the surface and reconfigure to lower energy states. We have observed that samples at slightly elevated temperatures (up to 100 $^{\circ}$C) under H_2 and D_2 showed accelerated poisoning rates, further supporting a reaction-based poisoning by hydrogen.

4.4. Conclusion

We have demonstrated a method to synthesize Pt-group decorated core-shell Au nanocrystals for plasmonic photocatalysis. High magnification EDS maps show clear core-shell structure of the pristine core-shell catalyst. By applying a hydrogen dissociation reaction as a model reaction, we deduced possible mechanistic behaviors of the driving forces for photocatalysis. Two mechanistic regimes were found to govern reaction rates, a low intensity regime where photothermal dominates and a high

intensity regime driven by hot carriers. Optical microscope images showed changes in morphology depending on illumination under argon or hydrogen suggesting energy can be dissipated under a reactive gas. Low concentration Pt decorated catalyst obstructed energy flow outwards, thereby diminishing overall reaction rates relative to undecorated Au. Overall, evidence from this study suggests that hot carriers can be a dominant mechanism for plasmonic photocatalysis.

Chapter 5. Conclusion

5.1. Summary of Dissertation

The work described in this dissertation is meant to serve as a basis for future work in plasmonic photocatalysis. We have demonstrated a complete systematic method for synthesis of colloidally produced Au nanocrystals with good reproducible behavior. Using the diafiltration method instead of the commonly used centrifuge and decant technique, we improved the efficiency of the purification process to retain with high yield stable Au particles in suspension. The purified particles are immobilized on a wide variety of organic and inorganic powdered support material including crystalline cellulose, TiO_2, alumina, and carbon. We believe this method of freeze-drying is superior to the traditional deposition-precipitation and co-precipitation methods of synthesizing supported nanocrystals. We showed with extensive TEM work, the uniform loading, and effects of additives like citrate on the distribution of the particles. Catalytic behavior was quantized by applying a model reaction, measuring the kinetics of 4-nitrophenol reduction to 4-aminophenol. Additionally, we have demonstrated the generalization of this freeze-drying method by immobilizing Au nanoprisms on support. The color of the material is remarkably close to the colloid color suggesting that the anisotropic nanocrystal maintained its geometry and distribution. We hope the scientific community adopt this method of fabricating supports because of its flexibility to colloidally control the particle's size, shape, and material composition.

Then, our work moved to characterization of the fabricated material. Specifically, we wanted to explore the plasmonic behavior of photocatalysis. A model reaction using hydrogen and deuterium was adopted to assess the performance of the supported nanocrystals. This hydrogen scrambling reaction itself has no industrial utility, but it

will give us insight onto the working mechanisms of photothermal or hot charged carrier dominated trends. We applied a known method of creating core-shell nanostructures for this work. The platinum and iridium decorated particles showed energy dissipation pathways which are important in assessing fundamental mechanisms. Hydrogen dissociation reaction rates were measured with a quadrupole mass spectrometer sampling exhaust gases in real time to provide the clearest observations of any photoactivity. We found that increasing the shell decoration percentage drastically increased the rate of reaction and the quantum efficiency of dissociating hydrogen when illuminated with a 520 nm laser at 20.4 W/cm^2. Power density dependence measurements revealed two distinct regimes, an exponential regime at low intensities indicating photothermal dominated mechanism and a linear regime at higher intensities signifying excited carrier dominated region. This was a comforting result because it corresponded well to published data regarding plasmonic hydrogen dissociation. Quantum yield measurements showed increasing efficiencies with increasing decoration, even well exceeding 1 HD/photon for the 50% and 100% decorated core-shell catalysts.

Measurements on low platinum decorated core-shell catalysts showed energy dissipation into the nanocrystal's core. This was observed by unexpectedly low hydrogen dissociation rates compared to the Au only catalyst. We know that Pt will accelerate the rate, but a decreased rate must point to a depletion of energy around the shell towards the core where hot carrier cannot catalyze dissociation and desorption processes. While this should not happen in the pristine core-shell material, we realized that the alloyed structure was created due to the high intensity of illumination. Additionally, we observed a decreasing hydrogen dissociation rate in the dark for Au@Pt catalysts. Subsequent recovery attempts showed that oxygen was an important aspect for revival of the pristine level of performance. We hypothesized that in the

presence of oxygen, water was forming from the adsorbed hydrogen and oxygen species. Upon desorption of water, surface poisoning was removed, and rates of hydrogen dissociation were recovered.

Lastly, we tried to apply the core-shell platinum decorated particles for water reduction. We showed that we are able to detect in real time hydrogen synthesized in illuminated conditions, but the signal was contaminated by volatile organic solvents. Future work is needed to resolve this issue to remove the convoluted signal so quantification of the true hydrogen signal can be done. We have also investigated plasmonic nitrogen fixation into ammonia, a very important industrial chemical for the synthesis of fertilizer. The supported catalysts can be deposited with TiO_2 by atomic layer deposition to generate binding sites for N_2. We showed that the measurement technique for quantifying ammonia. No statistical difference was seen between the illuminated and dark measurements. We believe we need to apply much higher intensities to drive the reaction with hot carriers. More work is required on developing a clean way to deliver ammonia free nitrogen to the solution to rule out any environmental contamination.

Overall, we believe the work carried out showed the viability of this project for catalysis, basic science studies, and solar fuels production. We are optimistic on the outlook of this project for providing high quality data for important fundamental science discoveries into chemistry at the nanoscale and femtosecond timescale.

5.2. Future Work

The next step following the core-shell nanoparticle work would be to focus on trying to elucidate the dominant mechanism of plasmonic photocatalysis. Having a photoreactor with heating capabilities would be immensely useful for showing background thermocatalytic behavior of Pt decorated Au particles. We know that Pt has significant background hydrogen dissociation dependent on the temperature. So,

upgrading the currently used homebuilt reactor to a commercial reactor would be the next step. The candidate for this is the Harrick high temperature reaction chamber with a built-in temperature controller. The benefits of this unit are the thermocouple, heating element feedback to precisely maintain an internal sample temperature up to 900 ˚C with a modular optical window. Various optical adapters are available to conduct *in situ* measurements with diffuse reflectance infrared spectroscopy (DRIFTS) and Raman to study chemisorbed species' vibrational states. In addition, the reaction chamber has reduced headspace volume to minimize the equilibration time for online mass spectrometry measurement. This increases throughput by requiring less waiting time for laser on/off cycles to reach steady state. The reaction chamber is also engineered to flow reaction gas directly through the sample compartment decreasing the time it takes to reach steady state even more. Reaction products desorbed directly flow out of the reaction chamber's outstream port towards the exhaust and mass spectrometer. Having this will outright reduce any dwell time the reaction product spends in the chamber to potentially react again or reduce catalytic efficiency by mixing with fresh reagent gases. This reactor is the same model used by the Linic and Halas groups to conduct ethylene epoxidation and hydrogen dissociation reactions respectively.[3,81]

Another piece of equipment upgrade would be to use a white light laser. We currently use a monochromatic diode laser that outputs 1.25 W of 520 nm light to conduct the photocatalytic illuminations. Power attenuation was conducted with neutral density filters at 0.1 OD increments for power density dependent studies. With a white light laser, we have broadband capabilities from 300 nm to 2000 nm which can excite a variety of plasmonic nanostructures. A proposal in our group was to synthesize high concentrations of gold nanoparticle dimers to use for photocatalysis. Dimers are excited longitudinally at 620 nm and beyond so having a selection of wavelengths significantly upgrade our currently capabilities. Hotspots at the nanojunction of dimers

are known to enhance Raman signals immensely which can be also applied to catalysis. So, by combining out previous work on supported nanocrystal fabrication and photoreactors, we should be able to enhance chemical reactions with supported dimers. The decoration of a shell around the hotspot could drive reactions not feasible with Au which can extend the utility of the catalyst for a wide variety of applications.

In fundamental science research, the hot carrier versus photothermal effect can conclusively be determined. Using the hydrogen dissociation reaction, we can devise a contraption to measure the nanoscopic temperature of the particles. The equilibrium constant of the hydrogen-deuterium-HD system is temperature dependent, specifically on the catalyst temperature. We can quantify the pressures of the hydrogen isotopes to deduce the equilibrium constant of the system. The catalyst will be the supported Au core-shell nanocrystals illuminated by the 520 nm laser. By illuminating at a certain power density, we can correlate this with the equilibrium constant, thus calculating the local temperature of the catalyst. This is an improvement on currently devised methods of measuring temperature because it can infer the direct local temperature, not the bulk temperature of the active material.

BIBLIOGRAPHY

(1) Ye, W.; Long, R.; Huang, H.; Xiong, Y. Plasmonic Nanostructures in Solar Energy Conversion. *J. Mater. Chem. C* **2017**, *5* (5), 1008–1021. https://doi.org/10.1039/c6tc04847a.

(2) Mubeen, S.; Lee, J.; Singh, N.; Krämer, S.; Stucky, G. D.; Moskovits, M. An Autonomous Photosynthetic Device in Which All Charge Carriers Derive from Surface Plasmons. *Nat. Nanotechnol.* **2013**, *8* (4), 247–251. https://doi.org/10.1038/nnano.2013.18.

(3) Christopher, P.; Xin, H.; Linic, S. Visible-Light-Enhanced Catalytic Oxidation Reactions on Plasmonic Silver Nanostructures. *Nat. Chem.* **2011**, *3* (6), 467–472. https://doi.org/10.1038/nchem.1032.

(4) Zha, R.; Nadimicherla, R.; Guo, X. Ultraviolet Photocatalytic Degradation of Methyl Orange by Nanostructured TiO2/ZnO Heterojunctions. *J. Mater. Chem. A* **2015**, *3* (12), 6565–6574. https://doi.org/10.1039/c5ta00764j.

(5) Brian O'Regan, M. G. A Low-Cost, High-Efficiency Solar Cell Based on Dye-Sensitized Colloidal Ti02 Films. *Nature* **1991**, *353*, 737–740. https://doi.org/10.1016/0146-5724(84)90144-4.

(6) Davis, S. J.; Lewis, N. S.; Shaner, M.; Aggarwal, S.; Arent, D.; Azevedo, I. L.; Benson, S. M.; Bradley, T.; Brouwer, J.; Chiang, Y. M.; et al. Net-Zero Emissions Energy Systems. *Science (80-.).* **2018**, *360* (6396). https://doi.org/10.1126/science.aas9793.

(7) Kumari, G.; Zhang, X.; Devasia, D.; Heo, J.; Jain, P. K. Watching Visible Light-Driven CO 2 Reduction on a Plasmonic Nanoparticle Catalyst. *ACS Nano* **2018**, *12* (8), 8330–8340. https://doi.org/10.1021/acsnano.8b03617.

(8) Yang, J.; Guo, Y.; Jiang, R.; Qin, F.; Zhang, H.; Lu, W.; Wang, J.; Yu, J. C. High-Efficiency "Working-in-Tandem" Nitrogen Photofixation Achieved by Assembling Plasmonic Gold Nanocrystals on Ultrathin Titania Nanosheets. *J. Am. Chem. Soc.* **2018**, *140* (27), 8497–8508. https://doi.org/10.1021/jacs.8b03537.

(9) Munnik, P.; De Jongh, P. E.; De Jong, K. P. Recent Developments in the Synthesis of Supported Catalysts. *Chem. Rev.* **2015**, *115* (14), 6687–6718. https://doi.org/10.1021/cr500486u.

(10) Brongersma, M. L.; Halas, N. J.; Nordlander, P. Plasmon-Induced Hot Carrier Science and Technology. *Nat. Nanotechnol.* **2015**, *10* (1), 25–34.

https://doi.org/10.1038/nnano.2014.311.

(11) Zhang, Y.; He, S.; Guo, W.; Hu, Y.; Huang, J.; Mulcahy, J. R.; Wei, W. D. Surface-Plasmon-Driven Hot Electron Photochemistry. *Chem. Rev.* **2018**, *118* (6), 2927–2954. https://doi.org/10.1021/acs.chemrev.7b00430.

(12) West, P. R.; Ishii, S.; Naik, G. V.; Emani, N. K.; Shalaev, V. M.; Boltasseva, A. Searching for Better Plasmonic Materials. *Laser Photonics Rev.* **2010**, *4* (6), 795–808. https://doi.org/10.1002/lpor.200900055.

(13) Bastús, N. G.; Merkoçi, F.; Piella, J.; Puntes, V. Synthesis of Highly Monodisperse Citrate-Stabilized Silver Nanoparticles of up to 200 Nm: Kinetic Control and Catalytic Properties. *Chem. Mater.* **2014**, *26* (9), 2836–2846. https://doi.org/10.1021/cm500316k.

(14) Zhou, L.; Swearer, D. F.; Robatjazi, H.; Alabastri, A.; Christopher, P.; Carter, E. A.; Nordlander, P.; Halas, N. J. Quantifying Hot Carrier and Thermal Contributions in Plasmonic Photocatalysis. *Science (80-.).* **2019**, *364* (6439), 69–72. https://doi.org/10.1126/science.aaw9545.

(15) Y. Silvan, J. Baraban, I. W. Un, Y. D. Comment on "Quantifying Hot Carrier and Thermal Contributions in Plasmonic Photocatalysis." *Science (80-.).* **2019**, *364*. https://doi.org/10.1063/1.1139125.

(16) Zeng, S.; Baillargeat, D.; Ho, H. P.; Yong, K. T. Nanomaterials Enhanced Surface Plasmon Resonance for Biological and Chemical Sensing Applications. *Chem. Soc. Rev.* **2014**, *43* (10), 3426–3452. https://doi.org/10.1039/c3cs60479a.

(17) Raether, H. *Surface Plasmons on Smooth and Rough Surfaces and on Gratings, Vol. 111 of Springer Tracts in Modern Physics*; 1988.

(18) Wang, L.; Cesar, C.; Huba, Z.; Carroll, K. J.; Carpenter, E. E.; Gu, D.; Lukaszew, R. A. Plasmonics and Enhanced Magneto-Optics in Core - Shell Co - Ag Nanoparticles. **2011**, 1237–1240.

(19) Willets, K. A.; Van Duyne, R. P. Localized Surface Plasmon Resonance Spectroscopy and Sensing. *Annu. Rev. Phys. Chem.* **2007**, *58*, 267–297. https://doi.org/10.1146/annurev.physchem.58.032806.104607.

(20) Maier, S. A. *Plasmonics Fundamentals and Applications*; Springer International Publishing: Bath, 2007. https://doi.org/10.1007/978-0-387-37825-1.

(21) He, S.; Sha, W. E. I.; Jiang, L.; Choy, W. C. H.; Chew, W. C.; Nie, Z. Finite-Element-Based Generalized Impedance Boundary Condition for Modeling Plasmonic Nanostructures. *IEEE Trans. Nanotechnol.* **2012**, *11* (2), 336–345. https://doi.org/10.1109/TNANO.2011.2171987.

(22) Zhang, X.; Chen, Y. L.; Liu, R. S.; Tsai, D. P. Plasmonic Photocatalysis. *Reports Prog. Phys.* **2013**, *76* (4). https://doi.org/10.1088/0034-4885/76/4/046401.

(23) M. Fleischmann, P. J. Hendra, A. J. M. Raman Spectra of Pyridine Adsorbed at a Silver Electrode. *Chem. Phys. Lett.* **1974**, *26* (2), 163–166.

(24) Jeanmaire, D. L.; Van Duyne, R. P. Surface Raman Spectroelectrochemistry: Part I. Heterocyclic, Aromatic, and Aliphatic Amines Adsorbed on the Anodized Silver Electrode. *J. Electroanal. Chem. Interfacial Electrochem.* **1977**, *84* (1), 1–20. https://doi.org/10.1016/S0022-0728(77)80224-6.

(25) Barnes, W. L.; Dereux, A.; Ebbesen, T. W. Surface Plasmon Subwavelength Optics. *Nature* **2003**, *424* (6950), 824–830. https://doi.org/10.1038/nature01937.

(26) Bohren, C. F. How Can a Particle Absorb More than the Light Incident on It? *Am. J. Phys.* **1983**, *51* (4), 323–327. https://doi.org/10.1119/1.13262.

(27) Fan, X.; Zheng, W.; Singh, D. J. Light Scattering and Surface Plasmons on Small Spherical Particles. *Light Sci. Appl.* **2014**, *3* (November 2013), 1–14. https://doi.org/10.1038/lsa.2014.60.

(28) Zhang, Y.; He, S.; Guo, W.; Hu, Y.; Huang, J.; Mulcahy, J. R.; Wei, W. D. Surface-Plasmon-Driven Hot Electron Photochemistry. *Chem. Rev.* **2018**, *118* (6), 2927–2954. https://doi.org/10.1021/acs.chemrev.7b00430.

(29) Wang, F.; Li, C.; Chen, H.; Jiang, R.; Sun, L. D.; Li, Q.; Wang, J.; Yu, J. C.; Yan, C. H. Plasmonic Harvesting of Light Energy for Suzuki Coupling Reactions. *J. Am. Chem. Soc.* **2013**, *135* (15), 5588–5601. https://doi.org/10.1021/ja310501y.

(30) Xiao, M.; Jiang, R.; Wang, F.; Fang, C.; Wang, J.; Yu, J. C. Plasmon-Enhanced Chemical Reactions. *J. Mater. Chem. A* **2013**, *1* (19), 5790–5805. https://doi.org/10.1039/c3ta01450a.

(31) Jiang, N.; Zhuo, X.; Wang, J. Active Plasmonics: Principles, Structures, and Applications. *Chem. Rev.* **2018**, *118* (6), 3054–3099. https://doi.org/10.1021/acs.chemrev.7b00252.

(32) Jang, Y. H.; Jang, Y. J.; Kim, S.; Quan, L. N.; Chung, K.; Kim, D. H. Plasmonic Solar Cells: From Rational Design to Mechanism Overview. *Chem. Rev.* **2016**, *116* (24), 14982–15034. https://doi.org/10.1021/acs.chemrev.6b00302.

(33) Santbergen, R.; Temple, T. L.; Liang, R.; Smets, A. H. M.; Van Swaaij, R. A. C. M. M.; Zeman, M. Application of Plasmonic Silver Island Films in Thin-Film Silicon Solar Cells. *J. Opt.* **2012**, *14* (2). https://doi.org/10.1088/2040-8978/14/2/024010.

(34) Morawiec, S.; Holovský, J.; Mendes, M. J.; Müller, M.; Ganzerová, K.; Vetushka, A.; Ledinský, M.; Priolo, F.; Fejfar, A.; Crupi, I. Experimental Quantification of

Useful and Parasitic Absorption of Light in Plasmon-Enhanced Thin Silicon Films for Solar Cells Application. *Sci. Rep.* **2016**, *6* (June 2015), 1–10. https://doi.org/10.1038/srep22481.

(35) Kale, M. J.; Avanesian, T.; Christopher, P. Direct Photocatalysis by Plasmonic Nanostructures. *ACS Catal.* **2014**, *4* (1), 116–128. https://doi.org/10.1021/cs400993w.

(36) Boerigter, C.; Aslam, U.; Linic, S. Mechanism of Charge Transfer from Plasmonic Nanostructures to Chemically Attached Materials. *ACS Nano* **2016**, *10* (6), 6108–6115. https://doi.org/10.1021/acsnano.6b01846.

(37) Boerigter, C.; Campana, R.; Morabito, M.; Linic, S. Evidence and Implications of Direct Charge Excitation as the Dominant Mechanism in Plasmon-Mediated Photocatalysis. *Nat. Commun.* **2016**, *7*. https://doi.org/10.1038/ncomms10545.

(38) Kelly, K. L.; Coronado, E.; Zhao, L. L.; Schatz, G. C. The Optical Properties of Metal Nanoparticles: The Influence of Size, Shape, and Dielectric Environment. *J. Phys. Chem. B* **2003**, *107* (3), 668–677. https://doi.org/10.1021/jp026731y.

(39) Kang, H.; Buchman, J. T.; Rodriguez, R. S.; Ring, H. L.; He, J.; Bantz, K. C.; Haynes, C. L. Stabilization of Silver and Gold Nanoparticles: Preservation and Improvement of Plasmonic Functionalities. *Chem. Rev.* **2019**, *119* (1), 664–699. https://doi.org/10.1021/acs.chemrev.8b00341.

(40) Zong, C.; Xu, M.; Xu, L. J.; Wei, T.; Ma, X.; Zheng, X. S.; Hu, R.; Ren, B. Surface-Enhanced Raman Spectroscopy for Bioanalysis: Reliability and Challenges. *Chem. Rev.* **2018**, *118* (10), 4946–4980. https://doi.org/10.1021/acs.chemrev.7b00668.

(41) Langer, J.; de Aberasturi, D. J.; Aizpurua, J.; Alvarez-Puebla, R. A.; Auguié, B.; Baumberg, J. J.; Bazan, G. C.; Bell, S. E. J.; Boisen, A.; Brolo, A. G.; et al. Present and Future of Surface-Enhanced Raman Scattering. *ACS Nano* **2020**, *14* (1), 28–117. https://doi.org/10.1021/acsnano.9b04224.

(42) K. Lance Kelly, Eduardo Coronado, Lin Lin Zhao, and G. C. S. The Optical Properties of Metal Nanoparticles: The Influence of Size, Shape, and Dielectric Environment. *J. Phys. Chem. B* **2003**, *107*, 668–677.

(43) Uwe Kreibig, M. V. *Optical Properties of Metal Clusters*; Springer, Berlin, Heidelberg, 1995. https://doi.org/https://doi.org/10.1007/978-3-662-09109-8.

(44) Novak, J. P.; Brousseau, L. C.; Vance, F. W.; Johnson, R. C.; Lemon, B. I.; Hupp, J. T.; Feldheim, D. L. Nonlinear Optical Properties of Molecularly Bridged Gold Nanoparticle Arrays [18]. *J. Am. Chem. Soc.* **2000**, *122* (48), 12029–12030. https://doi.org/10.1021/ja003129h.

(45) Bian, X.; Dunn, R. C.; Xie, X. S. Single Molecule Emission Characteristics in Near-Field Microscopy Randy. *Phys. Rev. Lett.* **1995**, *75* (26), 4772–4776.

(46) Solís, D. M.; Taboada, J. M.; Obelleiro, F.; Liz-Marzán, L. M.; García De Abajo, F. J. Optimization of Nanoparticle-Based SERS Substrates through Large-Scale Realistic Simulations. *ACS Photonics* **2017**, *4* (2), 329–337. https://doi.org/10.1021/acsphotonics.6b00786.

(47) Cortie, M. B.; McDonagh, A. M. Synthesis and Optical Properties of Hybrid and Alloy Plasmonic Nanoparticles. *Chem. Rev.* **2011**, *111* (6), 3713–3735. https://doi.org/10.1021/cr1002529.

(48) Turkevich, J.; Stevenson, P. C.; Hillier, J. A Study of the Nucleation and Growth Processes in the Synthesis of Colloidal Gold. *Discuss. Faraday Soc.* **1951**, *11* (c), 55–75. https://doi.org/10.1039/DF9511100055.

(49) Kimling, J.; Maier, M.; Okenve, B.; Kotaidis, V.; Ballot, H.; Plech, A. Turkevich Method for Gold Nanoparticle Synthesis Revisited. *J. Phys. Chem. B* **2006**, *110* (32), 15700–15707. https://doi.org/10.1021/jp061667w.

(50) Calderón-Jiménez, B.; Johnson, M. E.; Montoro Bustos, A. R.; Murphy, K. E.; Winchester, M. R.; Baudrit, J. R. V. Silver Nanoparticles: Technological Advances, Societal Impacts, and Metrological Challenges. *Front. Chem.* **2017**, *5* (Feb), 1–26. https://doi.org/10.3389/fchem.2017.00006.

(51) Samadi, A.; Klingberg, H.; Jauffred, L.; Kjær, A.; Bendix, P. M.; Oddershede, L. B. Platinum Nanoparticles: A Non-Toxic, Effective and Thermally Stable Alternative Plasmonic Material for Cancer Therapy and Bioengineering. *Nanoscale* **2018**, *10* (19), 9097–9107. https://doi.org/10.1039/c8nr02275e.

(52) Scarabelli, L.; Coronado-Puchau, M.; Giner-Casares, J. J.; Langer, J.; Liz-Marzán, L. M. Monodisperse Gold Nanotriangles: Size Control, Large-Scale Self-Assembly, and Performance in Surface-Enhanced Raman Scattering. *ACS Nano* **2014**, *8* (6), 5833–5842. https://doi.org/10.1021/nn500727w.

(53) Scarabelli, L.; Grzelczak, M.; Liz-Marzán, L. M. Tuning Gold Nanorod Synthesis through Prereduction with Salicylic Acid. *Chem. Mater.* **2013**, *25* (21), 4232–4238. https://doi.org/10.1021/cm402177b.

(54) Finney, E. E.; Finke, R. G. Nanocluster Nucleation and Growth Kinetic and Mechanistic Studies: A Review Emphasizing Transition-Metal Nanoclusters. *J. Colloid Interface Sci.* **2008**, *317* (2), 351–374. https://doi.org/10.1016/j.jcis.2007.05.092.

(55) Pong, B. K.; Elim, H. I.; Chong, J. X.; Ji, W.; Trout, B. L.; Lee, J. Y. New Insights on the Nanoparticle Growth Mechanism in the Citrate Reduction of Gold(III) Salt:

Formation of the Au Nanowire Intermediate and Its Nonlinear Optical Properties. *J. Phys. Chem. C* **2007**, *111* (17), 6281–6287. https://doi.org/10.1021/jp068666o.

(56) Polte, J.; Ahner, T. T.; Delissen, F.; Sokolov, S.; Emmerling, F.; Thünemann, A. F.; Kraehnert, R. Mechanism of Gold Nanoparticle Formation in the Classical Citrate Synthesis Method Derived from Coupled in Situ XANES and SAXS Evaluation. *J. Am. Chem. Soc.* **2010**, *132* (4), 1296–1301. https://doi.org/10.1021/ja906506j.

(57) Kuo, C. H.; Chiang, T. F.; Chen, L. J.; Huang, M. H. Synthesis of Highly Faceted Pentagonal- And Hexagonal-Shaped Gold Nanoparticles with Controlled Sizes by Sodium Dodecyl Sulfate. *Langmuir* **2004**, *20* (18), 7820–7824. https://doi.org/10.1021/la049172q.

(58) Sun, Y.; Xia, Y. Shape-Controlled Synthesis of Gold and Silver Nanoparticles. *Science (80-.).* **2002**, *298* (5601), 2176–2179. https://doi.org/10.1126/science.1077229.

(59) Barnard, A. S.; Chen, Y. Kinetic Modelling of the Shape-Dependent Evolution of Faceted Gold Nanoparticles. *J. Mater. Chem.* **2011**, *21* (33), 12239–12245. https://doi.org/10.1039/c1jm11677k.

(60) Shrivastav, A. M.; Cvelbar, U.; Abdulhalim, I. A Comprehensive Review on Plasmonic-Based Biosensors Used in Viral Diagnostics. *Commun. Biol.* **2021**, *4* (1), 1–12. https://doi.org/10.1038/s42003-020-01615-8.

(61) Lee, C.; Lawrie, B.; Pooser, R.; Lee, K. G.; Rockstuhl, C.; Tame, M. Quantum Plasmonic Sensors. *Chem. Rev.* **2021**, *121* (8), 4743–4804. https://doi.org/10.1021/acs.chemrev.0c01028.

(62) Stewart, M. E.; Anderton, C. R.; Thompson, L. B.; Maria, J.; Gray, S. K.; Rogers, J. A.; Nuzzo, R. G. Nanostructured Plasmonic Sensors. *Chem. Rev.* **2008**, *108* (2), 494–521. https://doi.org/10.1021/cr068126n.

(63) Tang, L.; Li, J. Plasmon-Based Colorimetric Nanosensors for Ultrasensitive Molecular Diagnostics. *ACS Sensors* **2017**, *2* (7), 857–875. https://doi.org/10.1021/acssensors.7b00282.

(64) Mauriz, E. Clinical Applications of Visual Plasmonic Colorimetric Sensing. *Sensors (Switzerland)* **2020**, *20* (21), 1–31. https://doi.org/10.3390/s20216214.

(65) Zhou, X. L.; Yang, Y.; Wang, S.; Liu, X. W. Surface Plasmon Resonance Microscopy: From Single-Molecule Sensing to Single-Cell Imaging. *Angew. Chemie - Int. Ed.* **2020**, *59* (5), 1776–1785. https://doi.org/10.1002/anie.201908806.

(66) Abdulhalim, I.; Zourob, M.; Lakhtakia, A. Surface Plasmon Resonance for Biosensing: A Mini-Review. *Electromagnetics* **2008**, *28* (3), 214–242. https://doi.org/10.1080/02726340801921650.

(67) Taylor, A. B.; Zijlstra, P. Single-Molecule Plasmon Sensing: Current Status and Future Prospects. *ACS Sensors* **2017**, *2* (8), 1103–1122. https://doi.org/10.1021/acssensors.7b00382.

(68) Rangnekar, A.; Sarma, T. K.; Singh, A. K.; Deka, J.; Ramesh, A.; Chattopadhyay, A. Retention of Enzymatic Activity of α-Amylase in the Reductive Synthesis of Gold Nanoparticles. *Langmuir* **2007**, *23* (10), 5700–5706. https://doi.org/10.1021/la062749e.

(69) Pillai, Z. S.; Kamat, P. V. What Factors Control the Size and Shape of Silver Nanoparticles in the Citrate Ion Reduction Method? *J. Phys. Chem. B* **2004**, *108* (3), 945–951. https://doi.org/10.1021/jp037018r.

(70) Yang, S.; Dai, X.; Stogin, B. B.; Wong, T. S. Ultrasensitive Surface-Enhanced Raman Scattering Detection in Common Fluids. *Proc. Natl. Acad. Sci. U. S. A.* **2016**, *113* (2), 268–273. https://doi.org/10.1073/pnas.1518980113.

(71) Syme, C. D.; Sirimuthu, N. M. S.; Faley, S. L.; Cooper, J. M. SERS Mapping of Nanoparticle Labels in Single Cells Using a Microfluidic Chip. *Chem. Commun.* **2010**, *46* (42), 7921–7923. https://doi.org/10.1039/c0cc02209h.

(72) Matschulat, A.; Drescher, D.; Kneipp, J. Surface-Enhanced Raman Scattering Hybrid Nanoprobe Multiplexing and Imaging in Biological Systems. *ACS Nano* **2010**, *4* (6), 3259–3269. https://doi.org/10.1021/nn100280z.

(73) Choe, A.; Yeom, J.; Shanker, R.; Kim, M. P.; Kang, S.; Ko, H. Stretchable and Wearable Colorimetric Patches Based on Thermoresponsive Plasmonic Microgels Embedded in a Hydrogel Film. *NPG Asia Mater.* **2018**, *10* (9), 912–922. https://doi.org/10.1038/s41427-018-0086-6.

(74) Pan, H.; Li, D.; Liu, J.; Li, J.; Zhu, W.; Zhao, Y. Sensing Thermally Denatured DNA by Inhibiting the Growth of Au Nanoparticles: Spectral and Electrochemical Studies. *J. Phys. Chem. C* **2011**, *115* (30), 14461–14468. https://doi.org/10.1021/jp201396j.

(75) Lin, S. Y.; Chen, C. H.; Lin, M. C.; Hsu, H. F. A Cooperative Effect of Bifunctionalized Nanoparticles on Recognition: Sensing Alkali Ions by Crown and Carboxylate Moieties in Aqueous Media. *Anal. Chem.* **2005**, *77* (15), 4821–4828. https://doi.org/10.1021/ac050443r.

(76) Han, M. S.; Lytton-Jean, A. K. R.; Mirkin, C. A. A Gold Nanoparticle Based Approach for Screening Triplex DNA Binders. *J. Am. Chem. Soc.* **2006**, *128* (15), 4954–4955. https://doi.org/10.1021/ja0606475.

(77) Liu, J.; Lu, Y. A Colorimetric Lead Biosensor Using DNAzyme-Directed Assembly

of Gold Nanoparticles. *J. Am. Chem. Soc.* **2003**, *125* (22), 6642–6643. https://doi.org/10.1021/ja034775u.

(78) Rosi, N. L.; Mirkin, C. A. Nanostructures in Biodiagnostics. *Chem. Rev.* **2005**, *105* (4), 1547–1562. https://doi.org/10.1021/cr030067f.

(79) Peternel, I. T.; Koprivanac, N.; Božić, A. M. L.; Kušić, H. M. Comparative Study of UV/TiO2, UV/ZnO and Photo-Fenton Processes for the Organic Reactive Dye Degradation in Aqueous Solution. *J. Hazard. Mater.* **2007**, *148* (1–2), 477–484. https://doi.org/10.1016/j.jhazmat.2007.02.072.

(80) Wu, C. H.; Chang, C. L. Decolorization of Reactive Red 2 by Advanced Oxidation Processes: Comparative Studies of Homogeneous and Heterogeneous Systems. *J. Hazard. Mater.* **2006**, *128* (2–3), 265–272. https://doi.org/10.1016/j.jhazmat.2005.08.013.

(81) Mukherjee, S.; Libisch, F.; Large, N.; Neumann, O.; Brown, L. V; Cheng, J.; Lassiter, B.; Carter, E. A.; Nordlander, P.; Halas, N. J.; et al. Hot Electrons Do the Impossible: Plasmon-Induced Dissociation of H2 on Au. *Nano Lett.* **2013**, *13*, 240–247.

(82) Swearer, D. F.; Robatjazi, H.; Martirez, J. M. P.; Zhang, M.; Zhou, L.; Carter, E. A.; Nordlander, P.; Halas, N. J. Plasmonic Photocatalysis of Nitrous Oxide into N2 and O2 Using Aluminum-Iridium Antenna-Reactor Nanoparticles. *ACS Nano* **2019**, *13* (7), 8076–8086. https://doi.org/10.1021/acsnano.9b02924.

(83) Zhou, L.; Zhang, C.; McClain, M. J.; Manjavacas, A.; Krauter, C. M.; Tian, S.; Berg, F.; Everitt, H. O.; Carter, E. A.; Nordlander, P.; et al. Aluminum Nanocrystals as a Plasmonic Photocatalyst for Hydrogen Dissociation. *Nano Lett.* **2016**, *16* (2), 1478–1484. https://doi.org/10.1021/acs.nanolett.5b05149.

(84) Wu, D. Y.; Liu, X. M.; Huang, Y. F.; Ren, B.; Xu, X.; Tian, Z. Q. Surface Catalytic Coupling Reaction of P-Mercaptoaniline Linking to Silver Nanostructures Responsible for Abnormal SERS Enhancement: A DFT Study. *J. Phys. Chem. C* **2009**, *113* (42), 18212–18222. https://doi.org/10.1021/jp9050929.

(85) Huang, Y.; Fang, Y.; Yang, Z.; Sun, M. Can p, P′-Dimercaptoazobisbenzene Be Produced from p-Aminothiophenol by Surface Photochemistry Reaction in the Junctions of a Ag Nanoparticle- Molecule-Ag (or Au) Film? *J. Phys. Chem. C* **2010**, *114* (42), 18263–18269. https://doi.org/10.1021/jp107305z.

(86) Zhou, B.; Ou, W.; Shen, J.; Zhao, C.; Zhong, J.; Du, P.; Bian, H.; Li, P.; Yang, L.; Lu, J.; et al. Controlling Plasmon-Aided Reduction of p-Nitrothiophenol by Tuning the Illumination Wavelength. *ACS Catal.* **2021**, *11* (24), 14898–14905. https://doi.org/10.1021/acscatal.1c04091.

(87) Warren, S. C.; Thimsen, E. Plasmonic Solar Water Splitting. *Energy Environ. Sci.* **2012**, *5* (1), 5133–5146. https://doi.org/10.1039/c1ee02875h.

(88) Wu, B.; Liu, D.; Mubeen, S.; Chuong, T. T.; Moskovits, M.; Stucky, G. D. Anisotropic Growth of TiO2 onto Gold Nanorods for Plasmon-Enhanced Hydrogen Production from Water Reduction. *J. Am. Chem. Soc.* **2016**, *138* (4), 1114–1117. https://doi.org/10.1021/jacs.5b11341.

(89) Kumar, A.; Choudhary, P.; Kumar, A.; Camargo, P. H. C.; Krishnan, V. Recent Advances in Plasmonic Photocatalysis Based on TiO2 and Noble Metal Nanoparticles for Energy Conversion, Environmental Remediation, and Organic Synthesis. *Small* **2022**, *18* (1). https://doi.org/10.1002/smll.202101638.

(90) Zhu, H.; Ke, X.; Yang, X.; Sarina, S.; Liu, H. Reduction of Nitroaromatic Compounds on Supported Gold Nanoparticles by Visible and Ultraviolet Light. *Angew. Chemie - Int. Ed.* **2010**, *49* (50), 9657–9661. https://doi.org/10.1002/anie.201003908.

(91) Lin, S. C.; Hsu, C. S.; Chiu, S. Y.; Liao, T. Y.; Chen, H. M. Edgeless Ag-Pt Bimetallic Nanocages: In Situ Monitor Plasmon-Induced Suppression of Hydrogen Peroxide Formation. *J. Am. Chem. Soc.* **2017**, *139* (6), 2224–2233. https://doi.org/10.1021/jacs.6b09080.

(92) Xiao, Q.; Sarina, S.; Waclawik, E. R.; Jia, J.; Chang, J.; Riches, J. D.; Wu, H.; Zheng, Z.; Zhu, H. Alloying Gold with Copper Makes for a Highly Selective Visible-Light Photocatalyst for the Reduction of Nitroaromatics to Anilines. *ACS Catal.* **2016**, *6* (3), 1744–1753. https://doi.org/10.1021/acscatal.5b02643.

(93) Sarina, S.; Zhu, H.; Jaatinen, E.; Xiao, Q.; Liu, H.; Jia, J.; Chen, C.; Zhao, J. Enhancing Catalytic Performance of Palladium in Gold and Palladium Alloy Nanoparticles for Organic Synthesis Reactions through Visible Light Irradiation at Ambient Temperatures. *J. Am. Chem. Soc.* **2013**, *135* (15), 5793–5801. https://doi.org/10.1021/ja400527a.

(94) Xiao, Q.; Sarina, S.; Bo, A.; Jia, J.; Liu, H.; Arnold, D. P.; Huang, Y.; Wu, H.; Zhu, H. Visible Light-Driven Cross-Coupling Reactions at Lower Temperatures Using a Photocatalyst of Palladium and Gold Alloy Nanoparticles. *ACS Catal.* **2014**, *4* (6), 1725–1734. https://doi.org/10.1021/cs5000284.

(95) Aslam, U.; Chavez, S.; Linic, S. Controlling Energy Flow in Multimetallic Nanostructures for Plasmonic Catalysis. *Nat. Nanotechnol.* **2017**, *12* (10), 1000–1005. https://doi.org/10.1038/nnano.2017.131.

(96) Engelbrekt, C.; Crampton, K. T.; Fishman, D. A.; Law, M.; Apkarian, V. A. Efficient Plasmon-Mediated Energy Funneling to the Surface of Au@Pt Core-Shell

Nanocrystals. *ACS Nano* **2020**, *14* (4), 5061–5074. https://doi.org/10.1021/acsnano.0c01653.

(97) Swearer, D. F.; Leary, R. K.; Newell, R.; Yazdi, S.; Robatjazi, H.; Zhang, Y.; Renard, D.; Nordlander, P.; Midgley, P. A.; Halas, N. J.; et al. Transition-Metal Decorated Aluminum Nanocrystals. *ACS Nano* **2017**, *11* (10), 10281–10288. https://doi.org/10.1021/acsnano.7b04960.

(98) Wang, C. F.; Wu, C. L.; Kuo, S. W.; Hung, W. S.; Lee, K. J.; Tsai, H. C.; Chang, C. J.; Lai, J. Y. Preparation of Efficient Photothermal Materials from Waste Coffee Grounds for Solar Evaporation and Water Purification. *Sci. Rep.* **2020**, *10* (1), 1–10. https://doi.org/10.1038/s41598-020-69778-2.

(99) Dongare, P. D.; Alabastri, A.; Neumann, O.; Nordlander, P.; Halas, N. J. Solar Thermal Desalination as a Nonlinear Optical Process. *Proc. Natl. Acad. Sci. U. S. A.* **2019**, *116* (27), 13182–13187. https://doi.org/10.1073/pnas.1905311116.

(100) Baffou, G.; Polleux, J.; Rigneault, H.; Monneret, S. Super-Heating and Micro-Bubble Generation around Plasmonic Nanoparticles under Cw Illumination. *J. Phys. Chem. C* **2014**, *118* (9), 4890–4898. https://doi.org/10.1021/jp411519k.

(101) Jauffred, L.; Samadi, A.; Klingberg, H.; Bendix, P. M.; Oddershede, L. B. Plasmonic Heating of Nanostructures. *Chem. Rev.* **2019**, *119* (13), 8087–8130. https://doi.org/10.1021/acs.chemrev.8b00738.

(102) Setoura, K.; Okada, Y.; Hashimoto, S. CW-Laser-Induced Morphological Changes of a Single Gold Nanoparticle on Glass: Observation of Surface Evaporation. *Phys. Chem. Chem. Phys.* **2014**, *16* (48), 26938–26945. https://doi.org/10.1039/c4cp03733b.

(103) Merabia, S.; Shenogin, S.; Joly, L.; Keblinski, P.; Barrat, J. L. Heat Transfer from Nanoparticles: A Corresponding State Analysis. *Proc. Natl. Acad. Sci. U. S. A.* **2009**, *106* (36), 15113–15118. https://doi.org/10.1073/pnas.0901372106.

(104) Kim, M.; Lee, J. H.; Nam, J. M. Plasmonic Photothermal Nanoparticles for Biomedical Applications. *Adv. Sci.* **2019**, *6* (17). https://doi.org/10.1002/advs.201900471.

(105) Qiu, J.; Wei, W. D. Surface Plasmon-Mediated Photothermal Chemistry. *J. Phys. Chem. C* **2014**, *118* (36), 20735–20749. https://doi.org/10.1021/jp5042553.

(106) Fasciani, C.; Alejo, C. J. B.; Grenier, M.; Netto-Ferreira, J. C.; Scaiano, J. C. High-Temperature Organic Reactions at Room Temperature Using Plasmon Excitation: Decomposition of Dicumyl Peroxide. *Org. Lett.* **2011**, *13* (2), 204–207. https://doi.org/10.1021/ol1026427.

(107) Abadeer, N. S.; Murphy, C. J. Recent Progress in Cancer Thermal Therapy Using

Gold Nanoparticles. *J. Phys. Chem. C* **2016**, *120* (9), 4691–4716. https://doi.org/10.1021/acs.jpcc.5b11232.

(108) Wu, P.; Gao, Y.; Zhang, H.; Cai, C. Aptamer-Guided Silver-Gold Bimetallic Nanostructures with Highly Active Surface-Enhanced Raman Scattering for Specific Detection and near-Infrared Photothermal Therapy of Human Breast Cancer Cells. *Anal. Chem.* **2012**, *84* (18), 7692–7699. https://doi.org/10.1021/ac3015164.

(109) Ke, H.; Yue, X.; Wang, J.; Xing, S.; Zhang, Q.; Dai, Z.; Tian, J.; Wang, S.; Jin, Y. Gold Nanoshelled Liquid Perfluorocarbon Nanocapsules for Combined Dual Modal Ultrasound/Ct Imaging and Photothermal Therapy of Cancer. *Small* **2014**, *10* (6), 1220–1227. https://doi.org/10.1002/smll.201302252.

(110) Maiti, A.; Maity, A.; Satpati, B.; Large, N.; Chini, T. K. Efficient Excitation of Higher Order Modes in the Plasmonic Response of Individual Concave Gold Nanocubes. *J. Phys. Chem. C* **2017**, *121* (1), 731–740. https://doi.org/10.1021/acs.jpcc.6b11018.

(111) Kazuma, E.; Jung, J.; Ueba, H.; Trenary, M.; Kim, Y. Real-Space and Real-Time Observationof a Plasmon-Induced Chemicalreaction of a Single Molecule. *Science (80-.).* **2018**, *526* (May), 521–526.

(112) Huang, J.; Zhao, X.; Huang, X.; Liang, W. Understanding the Mechanism of Plasmon-Driven Water Splitting: Hot Electron Injection and a near Field Enhancement Effect. *Phys. Chem. Chem. Phys.* **2021**, *23* (45), 25629–25636. https://doi.org/10.1039/d1cp03509f.

(113) Zhou, L.; Lou, M.; Bao, J. L.; Zhang, C.; Liu, J. G.; Martirez, J. M. P.; Tian, S.; Yuan, L.; Swearer, D. F.; Robatjazi, H.; et al. Hot Carrier Multiplication in Plasmonic Photocatalysis. *Proc. Natl. Acad. Sci. U. S. A.* **2021**, *118* (20), 1–6. https://doi.org/10.1073/pnas.2022109118.

(114) Kip, B. J.; Meier, R. J. Determination of the Local Temperature at a Sample during Raman Experiments Using Stokes and Anti-Stokes Raman Bands. *Appl. Spectrosc.* **1990**, *44* (4), 707–711. https://doi.org/10.1366/0003702904087325.

(115) Dongare, P. D.; Zhao, Y.; Renard, D.; Yang, J.; Neumann, O.; Metz, J.; Yuan, L.; Alabastri, A.; Nordlander, P.; Halas, N. J. A 3D Plasmonic Antenna-Reactor for Nanoscale Thermal Hotspots and Gradients. *ACS Nano* **2021**, *15* (5), 8761–8769. https://doi.org/10.1021/acsnano.1c01046.

(116) Baffou, G.; Bordacchini, I.; Baldi, A.; Quidant, R. Simple Experimental Procedures to Distinguish Photothermal from Hot-Carrier Processes in Plasmonics. *Light Sci. Appl.* **2020**, *9* (1). https://doi.org/10.1038/s41377-020-00345-0.

(117) Jia, C. J.; Schüth, F. Colloidal Metal Nanoparticles as a Component of Designed Catalyst. *Phys. Chem. Chem. Phys.* **2011**, *13* (7), 2457–2487. https://doi.org/10.1039/c0cp02680h.

(118) Corma, A.; Garci, H. Supported Gold Nanoparticles as Catalysts for Organic Reactions. *Chem. Soc. Rev.* **2008**, *37* (9), 2096–2126. https://doi.org/10.1039/b707314n.

(119) Ma, Z.; Dai, S. Design of Novel Structured Gold Nanocatalysts. *ACS Catal.* **2011**, *1* (7), 805–818. https://doi.org/10.1021/cs200100w.

(120) Stratakis, M.; Garcia, H. Catalysis by Supported Gold Nanoparticles: Beyond Aerobic Oxidative Processes. *Chem. Rev.* **2012**, *112* (8), 4469–4506. https://doi.org/10.1021/cr3000785.

(121) Nakamura, T.; Yamada, Y.; Yano, K. Direct Synthesis of Monodispersed Thiol-Functionalized Nanoporous Silica Spheres and Their Application to a Colloidal Crystal Embedded with Gold Nanoparticles. *J. Mater. Chem.* **2007**, *17* (35), 3726–3732. https://doi.org/10.1039/b705209j.

(122) Haruta, M.; Yamada, N.; Kobayashi, T.; Iijima, S. Gold Catalysts Prepared by Coprecipitation for Low-Temperature Oxidation of Hydrogen and of Carbon Monoxide. *J. Catal.* **1989**, *115* (2), 301–309. https://doi.org/10.1016/0021-9517(89)90034-1.

(123) S. Tsubota, D.A.H. Cunningham, Y. B. and M. H.; Osaka. Preparation of Nanometer Gold Strongly Interacted with TiO 2 and the Structure Sensitivity in Low-Temperature Oxidation of CO. *Stud. Surf. Sci. Catal.* **1995**, 227–235.

(124) Bitter, J. H.; Van Der Lee, M. K.; Slotboom, A. G. T.; Van Dillen, A. J.; De Jong, K. P. Synthesis of Highly Loaded Highly Dispersed Nickel on Carbon Nanofibers by Homogeneous Deposition-Precipitation. *Catal. Letters* **2003**, *89* (1–2), 139–142. https://doi.org/10.1023/A:1024744131630.

(125) Haruta, M. Size- and Support-Dependency in the Catalysis of Gold. *Catal. Today* **1997**, *36* (1), 153–166. https://doi.org/10.1016/S0920-5861(96)00208-8.

(126) Liu, X.; Glasser, B.; Khinast, J. Impact of Impregnation and Drying on the Metal Distribution in Supported Catalysts. *2007 AIChE Annu. Meet.* **2007**, *56*, 4473–4487.

(127) Mondloch, J. E.; Bayram, E.; Finke, R. G. A Review of the Kinetics and Mechanisms of Formation of Supported-Nanoparticle Heterogeneous Catalysts. *J. Mol. Catal. A Chem.* **2012**, *355*, 1–38. https://doi.org/10.1016/j.molcata.2011.11.011.

(128) Prati, L.; Martra, G. New Gold Catalysts for Liquid Phase Oxidation. *Gold Bull.* **1999**, *32* (3), 96–101. https://doi.org/10.1007/BF03216617.

(129) Porta, F.; Prati, L.; Rossi, M.; Coluccia, S.; Martra, G. Metal Sols as a Useful Tool for Heterogeneous Gold Catalyst Preparation: Reinvestigation of a Liquid Phase Oxidation. *Catal. Today* **2000**, *61* (1), 165–172. https://doi.org/10.1016/S0920-5861(00)00370-9.

(130) Formation, S. W.; Tai, B. Y.; Watanabe, M.; Kaneko, K.; Tanemura, S.; Miki, T.; Murakami, J. Preparation of Gold Cluster / Silica Nanocomposite. **2001**, No. 21, 1611–1614.

(131) Tai, Y.; Murakami, J.; Tajiri, K.; Ohashi, F.; Daté, M.; Tsubota, S. Oxidation of Carbon Monoxide on Au Nanoparticles in Titania and Titania-Coated Silica Aerogels. *Appl. Catal. A Gen.* **2004**, *268* (1–2), 183–187. https://doi.org/10.1016/j.apcata.2004.03.039.

(132) Rossi, L. M.; Fiorio, J. L.; Garcia, M. A. S.; Ferraz, C. P. The Role and Fate of Capping Ligands in Colloidally Prepared Metal Nanoparticle Catalysts. *Dalt. Trans.* **2018**, *47* (17), 5889–5915. https://doi.org/10.1039/c7dt04728b.

(133) Grunwaldt, J. D.; Kiener, C.; Wögerbauer, C.; Baiker, A. Preparation of Supported Gold Catalysts for Low-Temperature CO Oxidation via "Size-Controlled" Gold Colloids. *J. Catal.* **1999**, *181* (2), 223–232. https://doi.org/10.1006/jcat.1998.2298.

(134) Comotti, M.; Li, W. C.; Spliethoff, B.; Schüth, F. Support Effect in High Activity Gold Catalysts for CO Oxidation. *J. Am. Chem. Soc.* **2006**, *128* (3), 917–924. https://doi.org/10.1021/ja0561441.

(135) Chou, J.; McFarland, E. W. Direct Propylene Epoxidation on Chemically Reduced Au Nanoparticles Supported on Titania. *Chem. Commun.* **2004**, *4* (14), 1648–1649. https://doi.org/10.1039/b403213f.

(136) Lee, I.; Morales, R.; Albiter, M. A.; Zaera, F. Synthesis of Heterogeneous Catalysts with Well Shaped Platinum Particles to Control Reaction Selectivity. *Proc. Natl. Acad. Sci. U. S. A.* **2008**, *105* (40), 15241–15246. https://doi.org/10.1073/pnas.0805691105.

(137) Biella, S.; Porta, F.; Prati, L.; Rossi, M. Surfactant-Protected Gold Particles: New Challenge for Gold-on-Carbon Catalysts. *Catal. Letters* **2003**, *90* (1–2), 23–29. https://doi.org/10.1023/a:1025808024943.

(138) Pietron, J. J.; Stroud, R. M.; Rolison, D. R. Using Three Dimensions in Catalytic Mesoporous Nanoarchitectures. *Nano Lett.* **2002**, *2* (5), 545–549. https://doi.org/10.1021/nl025536s.

(139) Zheng, N.; Stucky, G. D. A General Synthetic Strategy for Oxide-Supported Metal Nanoparticle Catalysts. *J. Am. Chem. Soc.* **2006**, *128* (44), 14278–14280.

https://doi.org/10.1021/ja0659929.

(140) Lopez-Sanchez, J. A.; Dimitratos, N.; Hammond, C.; Brett, G. L.; Kesavan, L.; White, S.; Miedziak, P.; Tiruvalam, R.; Jenkins, R. L.; Carley, A. F.; et al. Facile Removal of Stabilizer-Ligands from Supported Gold Nanoparticles. *Nat. Chem.* **2011**, *3* (7), 551–556. https://doi.org/10.1038/nchem.1066.

(141) Morris, C. A.; Anderson, M. L.; Stroud, R. M.; Merzbacher, C. I.; Rolison, D. R. Silica Sol as a Nanoglue: Flexible Synthesis of Composite Aerogels. *Science (80-.).* **1999**, *284* (5414), 622–624. https://doi.org/10.1126/science.284.5414.622.

(142) Kónya, Z.; Puntes, V. F.; Kiricsi, I.; Zhu, J.; Ager, J. W.; Ko, M. K.; Frei, H.; Alivisatos, P.; Somorjai, G. A. Synthetic Insertion of Gold Nanoparticles into Mesoporous Silica. *Chem. Mater.* **2003**, *15* (6), 1242–1248. https://doi.org/10.1021/cm020824a.

(143) Rioux, R. M.; Song, H.; Hoefelmeyer, J. D.; Yang, P.; Somorjai, G. A. High-Surface-Area Catalyst Design: Synthesis, Characterization, and Reaction Studies of Platinum Nanoparticles in Mesoporous SBA-15 Silica. *J. Phys. Chem. B* **2005**, *109* (6), 2192–2202. https://doi.org/10.1021/jp048867x.

(144) Song, H.; Rioux, R. M.; Hoefelmeyer, J. D.; Komor, R.; Niesz, K.; Grass, M.; Yang, P.; Somorjai, G. A. Hydrothermal Growth of Mesoporous SBA-15 Silica in the Presence of PVP-Stabilized Pt Nanoparticles: Synthesis, Characterization, and Catalytic Properties. *J. Am. Chem. Soc.* **2006**, *128* (9), 3027–3037. https://doi.org/10.1021/ja057383r.

(145) Kosmulski, M. Journal of Colloid and Interface Science The PH Dependent Surface Charging and Points of Zero Charge . VI . Update. *J. Colloid Interface Sci.* **2014**, *426* (1), 209–212. https://doi.org/10.1016/j.jcis.2014.02.036.

(146) Xu, Y.; Cao, Q.; Svec, F.; Fréchet, J. M. J. Porous Polymer Monolithic Column with Surface-Bound Gold Nanoparticles for the Capture and Separation of Cysteine-Containing Peptides. *Anal. Chem.* **2010**, *82* (8), 3352–3358. https://doi.org/10.1021/ac1002646.

(147) Cao, Y.; Lv, M.; Xu, H.; Svec, F.; Tan, T.; Lv, Y. Planar Monolithic Porous Polymer Layers Functionalized with Gold Nanoparticles as Large-Area Substrates for Sensitive Surface-Enhanced Raman Scattering Sensing of Bacteria. *Anal. Chim. Acta* **2015**, *896*, 111–119. https://doi.org/10.1016/j.aca.2015.09.018.

(148) Hua, T.; Liu, B.; Zhang, H. *Front Matter*; Woodhead Publishing Limited: Cambridge, 2010. https://doi.org/10.1533/9781845697471.frontmatter.

(149) Lévy, R.; Thanh, N. T. K.; Christopher Doty, R.; Hussain, I.; Nichols, R. J.;

Schiffrin, D. J.; Brust, M.; Fernig, D. G. Rational and Combinatorial Design of Peptide Capping Ligands for Gold Nanoparticles. *J. Am. Chem. Soc.* **2004**, *126* (32), 10076–10084. https://doi.org/10.1021/ja0487269.

(150) Abdelwahed, W.; Degobert, G.; Stainmesse, S.; Fessi, H. Freeze-Drying of Nanoparticles: Formulation, Process and Storage Considerations. *Adv. Drug Deliv. Rev.* **2006**, *58* (15), 1688–1713. https://doi.org/10.1016/j.addr.2006.09.017.

(151) Zhang, L.; Li, P.; Li, D.; Guo, S.; Wang, E. Effect of Freeze-Thawing on Lipid Bilayer-Protected Gold Nanoparticles. *Langmuir* **2008**, *24* (7), 3407–3411. https://doi.org/10.1021/la703737q.

(152) Khlebtsov, B. N.; Panfilova, E. V.; Terentyuk, G. S.; Maksimova, I. L.; Ivanov, A. V.; Khlebtsov, N. G. Plasmonic Nanopowders for Photothermal Therapy of Tumors. *Langmuir* **2012**, *28* (24), 8994–9002. https://doi.org/10.1021/la300022k.

(153) Alkilany, A. M.; Abulateefeh, S. R.; Mills, K. K.; Bani Yaseen, A. I.; Hamaly, M. A.; Alkhatib, H. S.; Aiedeh, K. M.; Stone, J. W. Colloidal Stability of Citrate and Mercaptoacetic Acid Capped Gold Nanoparticles upon Lyophilization: Effect of Capping Ligand Attachment and Type of Cryoprotectants. *Langmuir* **2014**, *30* (46), 13799–13808. https://doi.org/10.1021/la504000v.

(154) Gupta, A.; Moyano, D. F.; Parnsubsakul, A.; Papadopoulos, A.; Wang, L. S.; Landis, R. F.; Das, R.; Rotello, V. M. Ultrastable and Biofunctionalizable Gold Nanoparticles. *ACS Appl. Mater. Interfaces* **2016**, *8* (22), 14096–14101. https://doi.org/10.1021/acsami.6b02548.

(155) Vergunst, T.; Kapteijn, F.; Moulijn, J. A. Monolithic Catalysts - Non-Uniform Active Phase Distribution by Impregnation. *Appl. Catal. A Gen.* **2001**, *213* (2), 179–187. https://doi.org/10.1016/S0926-860X(00)00896-6.

(156) Xi, X.; Nie, Z.; Jiang, Y.; Xu, X.; Zuo, T. Preparation and Characterization of Ultrafine Cobalt Powders and Supported Cobalt Catalysts by Freeze-Drying. *Powder Technol.* **2009**, *191* (1–2), 107–110. https://doi.org/10.1016/j.powtec.2008.09.017.

(157) Bastús, N. G.; Comenge, J.; Puntes, V. Kinetically Controlled Seeded Growth Synthesis of Citrate-Stabilized Gold Nanoparticles of up to 200 Nm: Size Focusing versus Ostwald Ripening. *Langmuir* **2011**, *27* (17), 11098–11105. https://doi.org/10.1021/la201938u.

(158) Johnsen, E.; Brandtzaeg, O. K.; Vehus, T.; Roberg-Larsen, H.; Bogoeva, V.; Ademi, O.; Hildahl, J.; Lundanes, E.; Wilson, S. R. A Critical Evaluation of Amicon Ultra Centrifugal Filters for Separating Proteins, Drugs and Nanoparticles in Biosamples. *J. Pharm. Biomed. Anal.* **2016**, *120*, 106–111.

https://doi.org/10.1016/j.jpba.2015.12.010.

(159) Bastús, N. G.; Comenge, J.; Puntes, V. Kinetically Controlled Seeded Growth Synthesis of Citrate-Stabilized Gold Nanoparticles of up to 200 Nm: Size Focusing versus Ostwald Ripening. *Langmuir* **2011**, *27* (17), 11098–11105. https://doi.org/10.1021/la201938u.

(160) Johnsen, E.; Brandtzaeg, O. K.; Vehus, T.; Roberg-Larsen, H.; Bogoeva, V.; Ademi, O.; Hildahl, J.; Lundanes, E.; Wilson, S. R. A Critical Evaluation of Amicon Ultra Centrifugal Filters for Separating Proteins, Drugs and Nanoparticles in Biosamples. *J. Pharm. Biomed. Anal.* **2016**, *120*, 106–111. https://doi.org/10.1016/j.jpba.2015.12.010.

(161) Luan, Z.; Salk, T.; Abelson, A.; Jean, S.; Law, M. Reversible Aggregation of Covalently Cross-Linked Gold Nanocrystals by Linker Oxidation. *J. Phys. Chem. C* **2019**, *123* (38). https://doi.org/10.1021/acs.jpcc.9b06976.

(162) Sweeney, S. F.; Woehrle, G. H.; Hutchison, J. E. Rapid Purification and Size Separation of Gold Nanoparticles via Diafiltration. *J. Am. Chem. Soc.* **2006**, *128* (10), 3190–3197. https://doi.org/10.1021/ja0558241.

(163) Yang, A. Y.; Law, M. Uniform Supported Metal Nanocrystal Catalysts Prepared by Slurry Freeze-Drying. *Chem. Mater.* **2021**, *33* (1), 256–265. https://doi.org/10.1021/acs.chemmater.0c03615.

(164) Jana, N. R.; Gearheart, L.; Murphy, C. J. Seeding Growth for Size Control of 5-40 Nm Diameter Gold Nanoparticles. *Langmuir* **2001**, *17* (22), 6782–6786. https://doi.org/10.1021/la0104323.

(165) Gao, W. G.; Liu, X. C.; Chen, M. F. In Situ ATR-FTIR Investigation and Theoretical Calculation of the Interactions of Chromate and Citrate on the Surface of Haematite (α-Fe2O3). *RSC Adv.* **2017**, *7* (65), 41011–41016. https://doi.org/10.1039/c7ra04587e.

(166) Max, J. J.; Chapados, C. Infrared Spectroscopy of Aqueous Carboxylic Acids: Comparison between Different Acids and Their Salts. *J. Phys. Chem. A* **2004**, *108* (16), 3324–3337. https://doi.org/10.1021/jp036401t.

(167) Rodríguez-Fernández, J.; Pérez-Juste, J.; Mulvaney, P.; Liz-Marzán, L. M. Spatially-Directed Oxidation of Gold Nanoparticles by Au(III)-CTAB Complexes. *J. Phys. Chem. B* **2005**, *109* (30), 14257–14261. https://doi.org/10.1021/jp052516g.

(168) Etchegoin, P. G.; Le Ru, E. C.; Meyer, M. An Analytic Model for the Optical Properties of Gold. *J. Chem. Phys.* **2006**, *125* (16). https://doi.org/10.1063/1.2360270.

(169) Chen, H.; Kou, X.; Yang, Z.; Ni, W.; Wang, J. Shape- and Size-Dependent

Refractive Index Sensitivity of Gold Nanoparticles. *Langmuir* **2008**, *24* (10), 5233–5237. https://doi.org/10.1021/la800305j.

(170) Jeon, H. Bin; Tsalu, P. V.; Ha, J. W. Shape Effect on the Refractive Index Sensitivity at Localized Surface Plasmon Resonance Inflection Points of Single Gold Nanocubes with Vertices. *Sci. Rep.* **2019**, *9* (1), 13635. https://doi.org/10.1038/s41598-019-50032-3.

(171) Kasarova, S. N.; Sultanova, N. G.; Ivanov, C. D.; Nikolov, I. D. Analysis of the Dispersion of Optical Plastic Materials. *Opt. Mater. (Amst).* **2007**, *29* (11), 1481–1490. https://doi.org/10.1016/j.optmat.2006.07.010.

(172) A Bendavid, P.J Martin, Å Jamting, H. T. Structural and Optical Properties of Titanium Oxide Thin Films Deposited by Filtered Arc Deposition. *Thin Solid Films* **1999**, *C* (355–356), 6–11.

(173) Heuer-Jungemann, A.; Feliu, N.; Bakaimi, I.; Hamaly, M.; Alkilany, A.; Chakraborty, I.; Masood, A.; Casula, M. F.; Kostopoulou, A.; Oh, E.; et al. The Role of Ligands in the Chemical Synthesis and Applications of Inorganic Nanoparticles. *Chem. Rev.* **2019**, *119* (8), 4819–4880. https://doi.org/10.1021/acs.chemrev.8b00733.

(174) Grzelczak, M.; Pérez-Juste, J.; De Abajo, F. J. G.; Liz-Marzán, L. M. Optical Properties of Platinum-Coated Gold Nanorods. *J. Phys. Chem. C* **2007**, *111* (17), 6183–6188. https://doi.org/10.1021/jp0671502.

(175) Straney, P. J.; Marbella, L. E.; Andolina, C. M.; Nuhfer, N. T.; Millstone, J. E. Decoupling Mechanisms of Platinum Deposition on Colloidal Gold Nanoparticle Substrates. *J. Am. Chem. Soc.* **2014**, *136* (22), 7873–7876. https://doi.org/10.1021/ja504294p.

(176) Gilroy, K. D.; Ruditskiy, A.; Peng, H. C.; Qin, D.; Xia, Y. Bimetallic Nanocrystals: Syntheses, Properties, and Applications. *Chem. Rev.* **2016**, *116* (18), 10414–10472. https://doi.org/10.1021/acs.chemrev.6b00211.

(177) Ortiz, N.; Zoellner, B.; Hong, S. J.; Ji, Y.; Wang, T.; Liu, Y.; Maggard, P. A.; Wang, G. Harnessing Hot Electrons from Near IR Light for Hydrogen Production Using Pt-End-Capped-AuNRs. *ACS Appl. Mater. Interfaces* **2017**, *9* (31), 25962–25969. https://doi.org/10.1021/acsami.7b05064.

(178) Hervés, P.; Pérez-Lorenzo, M.; Liz-Marzán, L. M.; Dzubiella, J.; Lu, Y.; Ballauff, M. Catalysis by Metallic Nanoparticles in Aqueous Solution: Model Reactions. *Chem. Soc. Rev.* **2012**, *41* (17), 5577–5587. https://doi.org/10.1039/c2cs35029g.

(179) Wang, Y.; Widmann, D.; Behm, R. J. Influence of TiO2 Bulk Defects on CO

Adsorption and CO Oxidation on Au/TiO2: Electronic Metal-Support Interactions (EMSIs) in Supported Au Catalysts. *ACS Catal.* **2017**, *7* (4), 2339–2345. https://doi.org/10.1021/acscatal.7b00251.

(180) Tauster, S. J. Strong Metal-Support Interactions. *Acc. Chem. Res.* **1987**, *20* (11), 389–394.

(181) Chakraborty, S.; Ansar, S. M.; Stroud, J. G.; Kitchens, C. L. Comparison of Colloidal versus Supported Gold Nanoparticle Catalysis. *J. Phys. Chem. C* **2018**, *122* (14), 7749–7758. https://doi.org/10.1021/acs.jpcc.8b00664.

(182) Qu, Y.; Duan, X. Progress, Challenge and Perspective of Heterogeneous Photocatalysts. *Chem. Soc. Rev.* **2013**, *42* (7), 2568–2580. https://doi.org/10.1039/c2cs35355e.

(183) Linic, S.; Christopher, P.; Ingram, D. B. Plasmonic-Metal Nanostructures for Efficient Conversion of Solar to Chemical Energy. *Nat. Mater.* **2011**, *10* (12), 911–921. https://doi.org/10.1038/nmat3151.

(184) Dhiman, M. Plasmonic Nanocatalysis for Solar Energy Harvesting and Sustainable Chemistry. *J. Mater. Chem. A* **2020**, *8* (20), 10074–10095. https://doi.org/10.1039/d0ta03114c.

(185) Wang, C.; Astruc, D. Nanogold Plasmonic Photocatalysis for Organic Synthesis and Clean Energy Conversion. *Chem. Soc. Rev.* **2014**, *43* (20), 7188–7216. https://doi.org/10.1039/c4cs00145a.

(186) Sayed, M.; Yu, J.; Liu, G.; Jaroniec, M. Non-Noble Plasmonic Metal-Based Photocatalysts. *Chem. Rev.* **2022**. https://doi.org/10.1021/acs.chemrev.1c00473.

(187) Hartland, G. V. Optical Studies of Dynamics in Noble Metal Nanostructures. *Chem. Rev.* **2011**, *111* (6), 3858–3887. https://doi.org/10.1021/cr1002547.

(188) Adam M. Schwartzberg, J. Z. Z. Novel Optical Properties and Emerging Applications of Metal Nanostructures. *J. Phys. Chem. C* **2008**, *112* (28), 10323–10337. https://doi.org/10.1021/jp801770w.

(189) Sytwu, K.; Vadai, M.; Dionne, J. A. Bimetallic Nanostructures: Combining Plasmonic and Catalytic Metals for Photocatalysis. *Adv. Phys. X* **2019**, *4* (1). https://doi.org/10.1080/23746149.2019.1619480.

(190) Amini, S. M. Gold Nanostructures Absorption Capacities of Various Energy Forms for Thermal Therapy Applications. *J. Therm. Biol.* **2019**, *79* (December 2018), 81–84. https://doi.org/10.1016/j.jtherbio.2018.12.007.

(191) Marye Anne Fox, M. T. D. Heterogeneous Photocatalysis. *Chem. Re* **1993**, *93* (1), 341–357. https://doi.org/10.1021/cr00017a016.

(192) Engelbrekt, C.; Sørensen, K. H.; Zhang, J.; Welinder, A. C.; Jensen, P. S.; Ulstrup, J. Green Synthesis of Gold Nanoparticles with Starch-Glucose and Application in Bioelectrochemistry. *J. Mater. Chem.* **2009**, *19* (42), 7839–7847. https://doi.org/10.1039/b911111e.

(193) He, W.; Han, X.; Jia, H.; Cai, J.; Zhou, Y.; Zheng, Z. AuPt Alloy Nanostructures with Tunable Composition and Enzyme-like Activities for Colorimetric Detection of Bisulfide. *Sci. Rep.* **2017**, *7* (October 2016), 1–10. https://doi.org/10.1038/srep40103.

(194) Huang, H.; Zhang, L.; Lv, Z.; Long, R.; Zhang, C.; Lin, Y.; Wei, K.; Wang, C.; Chen, L.; Li, Z. Y.; et al. Unraveling Surface Plasmon Decay in Core-Shell Nanostructures toward Broadband Light-Driven Catalytic Organic Synthesis. *J. Am. Chem. Soc.* **2016**, *138* (21), 6822–6828. https://doi.org/10.1021/jacs.6b02532.

(195) Yasunobu Inoue, Seiji Hacho, Eizo Miyazaki, I. Y. Hydrogen-Deuterium Equilibration Reaction over Platinum Supported on Polyamide-6. *Bull. Chem. Soc. Jpn.* **1979**, *52* (11), 3258–3264.

(196) Tsuchiya, S.; Amenomiya, Y.; Cvetanović, R. J. Study of Metal Catalysts by Temperature Programmed Desorption. III. Hydrogen-Deuterium Exchange on Platinum. *J. Catal.* **1971**, *20* (1), 1–9. https://doi.org/10.1016/0021-9517(71)90002-9.

(197) Greenlief, C. M.; Akhter, S.; White, J. M. Temperature-Programmed Desorption Study of H2-D2 Exchange on Pt(111) and the Role of Subsurface Sites. *J. Phys. Chem.* **1986**, *90* (17), 4080–4083. https://doi.org/10.1021/j100408a049.

(198) Spata, V. A.; Carter, E. A. Mechanistic Insights into Photocatalyzed Hydrogen Desorption from Palladium Surfaces Assisted by Localized Surface Plasmon Resonances. *ACS Nano* **2018**, *12* (4), 3512–3522. https://doi.org/10.1021/acsnano.8b00352.

(199) Christopher, P.; Xin, H.; Marimuthu, A.; Linic, S. Singular Characteristics and Unique Chemical Bond Activation Mechanisms of Photocatalytic Reactions on Plasmonic Nanostructures. *Nat. Mater.* **2012**, *11* (12), 1044–1050. https://doi.org/10.1038/nmat3454.

(200) Steven A. Buntin, Lee J. Richter, Richard R. Cavanagh, and D. S. K. Optically Driven Surface Reactions: Evidence for the Role of Hot Electrons. *Phys. Rev. Lett.* **1988**, *61* (11), 1321–1324.